RELIABILITY-BASED SEISMIC ASSESSMENT OF MASONRY ARCH BRIDGES

by

Semih Gönen

B.S., Civil Engineering, Middle East Technical University, 2011

M.S., Advanced Masters in Structural Analysis of Monuments and Historical Constructions , Polytechnic University of Catalonia, 2012

Submitted to the Institute for Graduate Studies in
Science and Engineering in partial fulfillment of
the requirements for the degree of
Doctor of Philosophy

Graduate Program in Civil Engineering

Boğaziçi University

2020

Aileme ve Güneş'ime...

ACKNOWLEDGEMENTS

Here we are, on the first page, that is last to be written. This Ph.D. has been a long journey with many ups and downs: finding joy in little discoveries and unveiling the unknown, or getting frustrated but working on the same thing over and over again; learning new things and opening up to new horizons, or forgetting what you knew and feeling pity for it, but always keep improving. I am entitled to say that it has been a satisfactory journey because I finally completed it. While sealing this life-changing chapter in my life, I would like to express my sincere gratitude to my supervisor, Prof. Serdar Soyöz, for his invaluable guidance and help during the dissertation work. He was always patient and encouraging with me. I also would like to thank the thesis committee members Prof. Alper Ilki and Prof. Kutay Orakçal, for their support and contribution. Their knowledge and valuable insights, together with the strong criticism of my work, pushed my performance up and resulted in better work. I also would like to acknowledge that this study was partially supported by the financial support provided by Boğaziçi University Research Fund [Grant Number 12782].

I am grateful to Prof. Nilüfer Özyurt Zihnioğlu for her kindness and support. She has always been an exemplary considerate person towards all of her students. I am also thankful to Prof. Hilmi Luş for the fruitful discussions and his recommendations related to both work and life.

Thank you very much to all my friends and colleagues, whose names are too many to be listed here without the fear of leaving someone out. I am truly thankful to all of you who were with me throughout this process, or helped me and touched my life, somehow, at some point.

I would like to express my appreciation for the continuous support and encouragement from three special people: Elspeth R.M. Dusinberre, David T. Biggs, and H. Gökhan Güler. Without their presence, this work would not have been possible. I also

cannot thank these kind souls enough for how much they enrich my life.

The exclusive gratitude goes to my wife and, at the same time, my sunshine Güneş. Her exceptional personality always brings me joy and makes my life better. Thank you for being with me, loving me, enduring me (sometimes), encouraging and supporting me. Your presence makes everything easier. Love you.

To close up this unique opportunity to thank so many people at the same time, I must mention that I am always indebted to my mother and father, Fatma and Celal, to my sister, brother-in-law and beloved nephew, Seçil, Selim and Yağız. Thank you very much for your unconditional love and never-ending support. Your presence warms my heart.

ABSTRACT

RELIABILITY-BASED SEISMIC ASSESSMENT OF MASONRY ARCH BRIDGES

Masonry arch bridges form a noteworthy portion of road and railway networks in the world, especially in Europe and Turkey. Structural assessment of such bridges is required because of their vulnerability to seismic actions. A realistic and rigorous structural assessment is important in terms of protecting cultural heritage and using resources carefully. However, there are no standardized or widely accepted procedures. This study presents an overarching reliability-based seismic assessment methodology based on analytical modeling, laboratory testing, and probabilistic assessment. It investigates the seismic behavior of masonry arch bridges and the uncertainties in the assessment methods by using different existing seismic analysis techniques. The Finite Element (FE) macro-modeling approach is used in modeling the behavior of the structure. System identification and model updating of the bridge enabled obtaining a reliable analytical model. Next, the seismic assessment is performed using Nonlinear Static Analysis (NSA), Nonlinear Dynamic Analysis (NDA), and Incremental Dynamic Analysis (IDA). This study also examines the uncertainties in obtaining the elasticity modulus of masonry by using several experiments, numerical modeling, and empirical equations. It then combines the knowledge acquired from analysis and testing for the reliability-based seismic assessment. Because there are no performance criteria available for masonry arch bridges, performance limit states for the investigated masonry arch bridge are defined. In the end, the probability of exceedance (or failure) for each limit state is calculated by integrating the performance criteria and the results of NDA and probabilistic seismic analyses. This reliability-based seismic assessment study of a masonry arch bridge is the first example that considers the uncertainties in material properties and uses a detailed 3D FE model to obtain reliability indexes.

ÖZET

YIĞMA TAŞ KEMER KÖPRÜLERİN DEPREM PERFORMANSININ GÜVENİLİRLİK-TABANLI DEĞERLENDİRİLMESİ

Yığma kemer köprüler, Avrupa ve Türkiye başta olmak üzere, dünyada karayolu ve demiryolu ulaşım ağlarının önemli bölümünü oluşturmaktadır. Bu köprülerin yapısal değerlendirmesi, özellikle deprem etkilerine karşı zayıflıklarından gereklidir. Ne yazık ki bu alanda standart veya genel kabul gören prosedürler bulunmamaktadır. Bu çalışma, analitik modelleme, laboratuvar testleri ve olasılıksal değerlendirmeye dayalı kapsamlı bir güvenilirlik-tabanlı performans değerlendirme metodolojisi sunmayı hedefler. Yığma kemer köprülerin deprem davranışı ve bunun belirlenmesinde kullanılan yöntemlerdeki belirsizlikler mevcut teknikler kullanılarak araştırılmıştır. Yapının modellenmesinde Sonlu Elemanlar (FE) makro-modelleme yaklaşımı kullanılmıştır. Sistem tanımlaması ile bulunan yapısal parametreler ile güncellenen FE modeli üzerinde Nonlineer Statik Analiz (NSA), Nonlineer Dinamik Analiz (NDA) ve Artımsal Dinamik Analiz (IDA) kullanılarak yapının deprem performansı değerlendirilmiştir. Ayrıca, bu çalışmada yığma yapıların elastisite modülündeki belirsizlikler birçok farklı yaklaşımla araştırılmıştır. Analiz ve testlerden elde edilen bilgi ve çıktılar sonrasında birleştirilerek deprem performansının güvenilirlik-tabanlı değerlendirmesinde kullanılmıştır. Yığma kemer köprüler için performans kriterleri bulunmadığından, bu yapılar için performans sınır durumları tanımlanmıştır. Sonunda, performans kriterleri ile NDA ve olasılıksal nonlineer analizlerin sonuçları entegre edilerek her bir sınır durum için aşılma (veya başarısızlık) olasılığı hesaplanmıştır. Yığma kemer köprülerin malzeme özelliklerindeki belirsizlikleri dikkate alan ve güvenilirlik indekslerini elde eden bu güvenilirlik-tabanlı performans değerlendirme çalışması literatürdeki ilk örnektir.

TABLE OF CONTENTS

ACKNOWLEDGEMENTS iv
ABSTRACT vi
ÖZET vii
LIST OF FIGURES xii
LIST OF TABLES xxii
LIST OF SYMBOLS xxiv
LIST OF ACRONYMS/ABBREVIATIONS xxvii
1. INTRODUCTION 1
1.1. General Information and Research Objectives 1
1.2. Content of the Chapters 7
2. SYSTEM IDENTIFICATION 11
2.1. Bridges and Ambient Vibration Survey 12
2.2. Dynamic Identification 14
2.2.1. Preprocessing 14
2.2.2. Enhanced Frequency Domain Decomposition (EFDD) 15
2.2.3. Auto-Regressive (AR) Model 18
2.2.4. Multiple Signal Classification (MUSIC) Method 23
2.3. Results and Discussion 24
3. MODEL UPDATING 30
3.1. System Identification of Bridge 41 30
3.2. Information on Bridge 41 32
3.3. Model Updating Study of Bridge 41 37
4. NONLINEAR ANALYSIS 44
4.1. Modeling Strategy and Material Properties 47
4.2. Modal Analysis 51
4.3. Nonlinear Model Properties 52
4.3.1. Frictional Contact Elements 52
4.3.2. Nonlinear Materials 54

4.3.3. Nonlinear Solution Controls 59
4.4. Model Verification and the Issues Raised 60
4.5. Nonlinear Static Analysis 61
4.5.1. The Methodology 62
4.5.2. Sensitivity Study 65
4.5.2.1. Sensitivity of Results to the Modulus of Elasticity of Masonry 66
4.5.2.2. Sensitivity of Results to the Tensile Strength of Masonry 67
4.5.2.3. Sensitivity of Results to the Shear Crack Coefficients . 67
4.5.2.4. Sensitivity of Results to the Elasticity Modulus of Fill Material 68
4.5.2.5. Sensitivity of Results to the Friction Coefficient of Contacts 69
4.5.3. Partial Performance Assessment 71
4.5.4. Multi-directional MPP 76
4.6. Nonlinear Dynamic (Time-History) Analysis 78
4.6.1. Model Setup 79
4.6.2. Earthquake Record Selection 80
4.6.3. Results 84
4.6.3.1. NDA in Transverse Direction Only 84
4.6.3.2. NDA in Horizontal and Vertical Directions Combined . 88
4.6.4. Comparison of NSA with NDA 90
4.7. Incremental Dynamic Analysis 93
4.7.1. Intensity and Damage Measures 93
4.7.2. Record Selection and Scaling 94
4.7.3. Results 95
4.7.3.1. Qualitative Observations 95
4.7.3.2. Quantitative Observations 98
5. LABORATORY EXPERIMENTS 104
5.1. Masonry Component Tests 108
5.1.1. Compressive Strength of Stone Units 109

5.1.2. Flexural-Tensile Strength of Stone Units 111
5.1.3. Flexural-Tensile and Compressive Strength of Mortar 112
5.2. Empirical Equations 116
5.3. Masonry Wallettes 117
5.4. Masonry Panel Wall 125
5.4.1. Panel Wall Production 125
5.4.2. Tests 127
5.4.3. Modeling 132
5.5. Non-destructive and Minor-destructive Tests 134
5.5.1. Schmidt Hammer Test 134
5.5.2. Ultrasound Test 136
5.5.3. Ambient Vibration Tests and Model Matching 142
5.5.4. Flat-jack Tests 145
5.6. Summary of the Results and Discussion 151
5.7. A Simple Example 153
6. RELIABILITY-BASED SEISMIC ASSESSMENT 155
6.1. Performance Criteria Study 157
6.1.1. General Concept for Masonry Buildings 157
6.1.2. Performance Criteria for Masonry Arch Bridges 160
6.1.3. Defining the Limit States 162
6.2. Seismic Reliability Assessment 166
6.2.1. Material Uncertainty 167
6.2.2. Capacity Distributions 170
6.2.2.1. Functionality (FunC) Limit State 171
6.2.2.2. Life Safety (LS) Limit State 172
6.2.2.3. Near Collapse (NC) Limit State 172
6.2.3. Demand Distribution 173
6.2.4. Reliability Analysis Background 175
6.2.4.1. Limit State Functions 176
6.2.4.2. The first expression of the Probability of Failure, P_F . 177
6.2.4.3. The Concept of Reliability Index 179

6.2.4.4. Monte Carlo Simulation 180
6.2.4.5. First-Order Reliability Method (FORM) 181
6.2.5. Probability of Failure Calculation 182
6.2.5.1. Monte Carlo Simulation 183
6.2.5.2. First-Order Reliability Method (FORM) 184
6.3. Discussion 185
7. CONCLUSIONS 191
REFERENCES 199

LIST OF FIGURES

Figure 1.1. The percentage of masonry arch railway bridges in the railway network of some European countries (adapted from [3]). 1

Figure 1.2. Some of the famous masonry arch bridges and aqueducts around the world (images obtained from the web). 2

Figure 1.3. Puente Talca bridge collapsed during Maule, Chile earthquake, 2010 (Source [6]). 4

Figure 1.4. The methodology presented in this study. 7

Figure 2.1. Dynamically identified bridges: (a) Bridge 13, (b) Bridge 41 and (c) Bridge 5. 13

Figure 2.2. Sensor layout of the bridges: (a) Bridge 13, (b) Bridge 41, (c) Bridge 5. 14

Figure 2.3. Example of the processed ambient vibration data - in the bare condition. 14

Figure 2.4. Auto-spectrum of the whole data for Bridge 5. 16

Figure 2.5. Experimental out-of-plane mode shapes for Bridge 13. 17

Figure 2.6. Experimental first vertical mode shape for Bridge 13. 18

Figure 2.7. Example of the impulse response function and damping envelope for damping identification, Bridge 13 out-of-plane mode, ζ=0.58%. 18

Figure 2.8. The ARX model. 21

Figure 2.9. Stabilization diagram for Bridge 5-Sensor 1 out-of-plane data. . . . 23

Figure 2.10. Frequency response spectra comparison for out-of-plane data of Bridge 5. 26

Figure 3.1. Auto-spectrum of the Bridge 41 data. 31

Figure 3.2. Identified out-of-plane mode shapes of the Bridge 41. 31

Figure 3.3. Identified vertical mode shape of Bridge 41. 32

Figure 3.4. Typical structure of a double-span masonry arch railway bridge illustrating the bridge terminology (Adapted from [29]). 33

Figure 3.5. Location of the Bridge, plan view and North Anatolian Fault line. 34

Figure 3.6. Borehole samples between (a) 12-17 m and (b) 17-21 m from the trackwork level. 35

Figure 3.7. Dimensions of Bridge 41. 36

Figure 3.8. (a) FE Model of Bridge 41, (b) FE model of Bridge 41 with different material assignments. 39

Figure 3.9. MAC matrix representation with a 3D bar chart. 40

Figure 3.10. Frequency pairing between updated and measured data. 41

Figure 3.11. Error length obtained for each model (iteration). 43

Figure 4.1. FE modeling approaches for masonry structures. 48

Figure 4.2. (a) Parts of the FE model, (b) FE mesh of the model. 51

Figure 4.3. From (a) to (d): the first four out-of-plane modes of the FE model. 51

Figure 4.4. Example figure showing the frictional contact between spandrel and the fill. 53

Figure 4.5. The friction model [63]. 54

Figure 4.6. The elasto-plastic nonlinear behavior and tension yielding in the spandrel wall. 55

Figure 4.7. (a) Tensile stress-strain, and (b) compressive stress-strain diagrams for the masonry material. 56

Figure 4.8. (a) Strength of cracked section, (b) 3D failure surface in principal stress space [63]. 58

Figure 4.9. Hypothetical load distribution in 2D. 64

Figure 4.10. Pushover curves obtained using the CM and TOP control points. . 65

Figure 4.11. Pushover curves obtained for different elasticity modulus of masonry values. 66

Figure 4.12. Pushover curves obtained for different tensile strength values of masonry. 67

Figure 4.13. Pushover curve comparison for different values of shear crack coefficients. 68

Figure 4.14. Pushover curve comparison for different elasticity modulus values of the fill material. 69

Figure 4.15. Contact status at the end of the PO analysis (last converged step). 70

Figure 4.16. Pushover curve comparison for the different coefficient of friction values. 70

Figure 4.17. Elastic demand vs. capacity curves for CM and TOP nodes. . . . 72

Figure 4.18. Finding D_{max} using TOP node data. 72

Figure 4.19. Equivalent total strain plot for the last step of the MPP analysis in the transverse-direction. 74

Figure 4.20. Vector principal strain plots. 75

Figure 4.21. Stress-strain plot of a node in a cracked region. 75

Figure 4.22. Equivalent total strain plot for the MPP in the X-direction. 77

Figure 4.23. Total strain plot for the MPP in Z-0.3X direction. 77

Figure 4.24. Total strain plot for the MPP in Z+0.3X+0.3Y direction. 78

Figure 4.25. Total strain plot for the MPP in Z+0.3X-0.3Y direction. 78

Figure 4.26. Scaled spectra of the records vs. target design spectrum. 82

Figure 4.27. FAS of the scaled records. 83

Figure 4.28. RSN 1161 – Kocaeli earthquake response at specific time instants. 86

Figure 4.29. NDA maxima vs. spectral first mode accelerations. 87

Figure 4.30. Examples for the effects of higher modes using qualitative total strain plots. Results from different earthquake motions and IDA analyses: (a) RSN1161-IDA2, (b) RSN 4213-IDA3, (c) RSN 6928-IDA6. 88

Figure 4.31. Equivalent total strain plot to show the damage distribution after RSN 285 Irpinia-Italy earthquake. 89

Figure 4.32. Principal stresses at the time of the damage occurred during RSN 285 Irpinia-Italy earthquake. 90

Figure 4.33. Results of the RSN1102 Kobe Japan earthquake. 91

Figure 4.34. Pushover curve vs. NDA results for the CM node. 92

Figure 4.35. First three transverse mode shapes - plan view. 96

Figure 4.36. Third mode behavior observed during RSN 6928 IDA9 (plan view). 96

Figure 4.37. (a) First mode displacements, (b) MPP displacements. 97

Figure 4.38. Multiple spandrel cracks from max principal stress plot - two subsequent steps (RSN 6928 IDA8). 98

Figure 4.39. Change in the displacement time-history of "RSN 1161 Kocaeli" earthquake. 99

Figure 4.40. FAS of the acceleration responses of RSN 2627 IDA. 100

Figure 4.41. Peaks becoming more significant in RSN2627 IDA. 100

Figure 4.42. IDA curves for CM node using spectral acceleration as IM. 101

Figure 4.43. Characteristic IDA and PO curves for the CM node. 102

Figure 5.1. Stone specimen before and after the test. 109

Figure 5.2. Force-displacement graphs of stone specimens under compression. 110

Figure 5.3. Stone specimens before and after the flexural tests. 111

Figure 5.4. Force-displacement graphs of the prism specimens. 111

Figure 5.5. Mortar specimens before and after the bending test. 113

Figure 5.6. Force-displacement graphs of the NHL mortar prism specimens under bending. 113

Figure 5.7. NHL mortar specimens before and after the compression test. . . . 114

Figure 5.8. Force-displacement graphs of the NHL mortar specimens under compression. 115

Figure 5.9. (a) dimensions, (b) displacement measurements as per EN 1052-1. 118

Figure 5.10. Specimens of (a) the first campaign; (b) the second campaign. . . 119

Figure 5.11. Cracks and spalls of the second specimen after the test: (a) front, (b) back, (c) disintegrating masonry constituents. 119

Figure 5.12. (a) The test setup used in compression tests, (b) crushed Specimen 8 front, (c) crushed Specimen 8 back. 120

Figure 5.13. Stress-strain graphs obtained from LVDT measurements for the second specimen. 120

Figure 5.14. Comparison of stress-strain graphs obtained from LVDT and full height measurements (the third specimen). 121

Figure 5.15. Stress-average strain graphs for the selected specimens. 122

Figure 5.16. Panel wall construction in the laboratory. 126

Figure 5.17. (a) Panel wall specimen right after its construction, and (b) during the curing process. 126

Figure 5.18. Instrumentation of the front face of the wall. 128

Figure 5.19. Instrumentation of the backside of the wall. 128

Figure 5.20. (a) Front face of the wall specimen and the test setup, (b) backside of the wall, and the test setup. 129

Figure 5.21. Front view of the wall panel after the test. 130

Figure 5.22. Lateral displacement-lateral load hysteresis curve. 130

Figure 5.23. Positive, negative and the average envelope curves. 131

Figure 5.24. Average envelope curve and EEEP curve. 132

Figure 5.25. Comparison of the analytical and experimental curves. 133

Figure 5.26. Schmidt Hammer test. 135

Figure 5.27. (a) Measuring the surface waves during ultrasound testing, (b) test points and distances for the indirect measurements. 137

Figure 5.28. The best fit for the indirect pulse velocity transmission of the panel wall to determine V_R. 139

Figure 5.29. (a) the instrumentation and (b) the test setup. 143

Figure 5.30. Auto-spectrum of the wall data before the cyclic test. 143

Figure 5.31. Mode shapes found using the analytical model. 144

Figure 5.32. Single flat-jack test procedure. 145

Figure 5.33. Preparation for the double flat-jack tests. 147

Figure 5.34. Execution of the double flat-jack test. 148

Figure 5.35. Stress-strain graphs under different vertical stress levels. 149

Figure 5.36. Initial and “plastic” tangent moduli. 150

Figure 5.37. Pushover curve comparison for different elasticity modulus values. 154

Figure 6.1. The relative error between the prescribed mean and the mean of first j realizations. 169

Figure 6.2. Histograms and distributions for the elasticity modulus values for masonry and arch. 169

Figure 6.3. Acceleration-CM displacement results of the probabilistic and deterministic pushover analyses. 170

Figure 6.4. MPP analyses results and the limit states (green: FunC, blue: LS, red: NC). 171

Figure 6.5. Transverse drift of the CM node at the performance limit states. . 171

Figure 6.6. Bridge response to MPP at the FunC limit state – equivalent total strains. 172

Figure 6.7. Bridge response to MPP at the LS limit state – equivalent total strains. 172

Figure 6.8. Bridge response to MPP at the NC limit state – equivalent total strains. 173

Figure 6.9. Histogram of the CM max displacements of NDA and the lognormal distribution fit. 174

Figure 6.10. Probability integration using a two-dimensional example: (a) isometric view and (b) projected view on the $x_1 - x_2$ plane (Retrieved from [163]). 177

Figure 6.11. Densities of R and S: the first form of P_F (Retrieved from [165]). 177

Figure 6.12. Transformation of random variables from X to U space, using a two-dimensional example: (a) PDF and projected contours in X-space, and (b) standard normal distribution in U-space (Retrieved from [163]). 181

Figure 6.13. Approximation of failure probability integration using a two-dimensional example: (a) PDF and projected contours in U-space and (b) projected view on the $u_1 - u_2$ plane (Retrieved from [163]). 182

Figure 6.14. Probability Density Distributions of the demand and capacity. . . 182

Figure 6.15. Probability of failure for each limit state vs. number of iterations. 184

Figure 6.16. R and S distributions for the Near Collapse limit state and demand, $F_R(\cdot)f_S(\cdot)$ representation 185

Figure 6.17. NDA results for RSN 763 Loma-Prieta earthquake record. 189

Figure 6.18. Displacement time-histories obtained for different elasticity modulus values. 189

Figure 6.19. (a) The first mode dominant behavior and (b) the higher mode effects. 190

LIST OF TABLES

Table 1.1. Properties of the bridges presented in Figure 1.2. 3

Table 2.1. List of presented bridges in this section. 13

Table 2.2. Dynamic identification results for Bridge 13. 25

Table 2.3. Dynamic identification results for Bridge 41. 25

Table 2.4. Dynamic identification results for Bridge 5. 25

Table 3.1. Comparison of analytical and measured frequencies and mode shapes. 40

Table 4.1. Summary of the material properties. 50

Table 4.2. Strong ground motion records. 82

Table 4.3. NDA results: the maximum displacements for the CM and TOP nodes. 84

Table 5.1. Compression tests results of stone specimens. 110

Table 5.2. Flexural-tensile tests results of stone specimens. 112

Table 5.3. Flexural-tensile test results of NHL mortar specimens. 114

Table 5.4. Compression test results of NHL mortar specimens. 115

Table 5.5. Compressive strength and modulus of elasticity values. 123

Table 5.6. Elasticity modulus when the vertical loading is $P_v = 25$ tons. . . . 139

Table 5.7. Elasticity modulus when the vertical loading is $P_v = 15$ tons. . . . 140

Table 5.8. Static elasticity moduli when the Poisson's ratio is 0.19. 141

Table 5.9. Summary of the results. 152

Table 6.1. Probability of Failure and Reliability Index values. 184

Table 6.2. Proposed target reliability index values in different countries and international bodies (at member level for ultimate limit state, moderate consequences of failure and reference period of one year, adapted from [130]. 186

LIST OF SYMBOLS

A	SDOF acceleration
$\mathbf{c}$	Damping matrix in the equation of motion of a MDOF system
D	SDOF displacement
D_{max}	Maximum SDOF displacement
E	Modulus of elasticity
$E_{1/3}$	Elasticity modulus calculated using the 1/3 of the maximum stress
$E_i(\theta)$	i'th objective function
E_{ave}	Average value of the elasticity modulus
E_D	Dynamic elasticity modulus
E_{mas}	Modulus of elasticity of masonry
E_S	Static elasticity modulus
E_{si}	Elastic modulus at any instant on stress-strain curve
f_c	Compressive strength
$f_{c,mas}$	Compressive strength of masonry
$f_{c,mo}$	Compressive strength of masonry mortar
$f_{c,st}$	Compressive strength of stone
f_i	Simulated modal frequency of the i'th mode
f_i^*	Measured modal frequency of the i'th mode
f_k	Characteristic compressive strength of masonry
f_{mi}	Compressive stress at any instant
f_t	Tensile strength of masonry
G	Shear modulus
G	Limit state function
G_{yy}	Estimate of the output PSD
h_i	Weighting coefficient for i'th modal assurance criteria
K	Constant used in the calculation of the compressive strength of masonry

K_a	Calibration factor considering the physical characteristic of jacks
K_m	Ratio of measured area of the flat-jack to the area of the slot
$\mathbf{k}$	Stiffness matrix in the equation of motion of a MDOF system
k_i	Weighting coefficient for i'th modal frequency
M	Total mass of the structure
M	Safety margin
M_p	P-wave modulus
$\mathbf{m}$	Mass matrix in the equation of motion of a MDOF system
P	Flat-jack pressure
P_F	Probability of failure
P_S	Probability of safety
R	Resistance
$\mathbf{R_{xx}}$	Auto-correlation matrix
S	Load
S_1	spectral acceleration at one second period
S_i	i'th eigenvector
$\mathbf{S_j}$	diagonal matrix containing the scalar singular values
S_s	spectral acceleration at short period
u_i	Gaussian space variables
$\mathbf{U_j}$	Orthonormal matrix containing singular vectors
U_{max}	Maximum physical displacement
U_r	Physical displacement
V_b	Base shear force
V_{mo}	Volumetric content of mortar
V_P	Pressure wave velocity
V_R	Surface wave velocity
V_S	Shear wave velocity
V_{st}	Volumetric content of stone
Γ	Modal participation factor

Φ	Standard normal probability
α	Coefficient of the mass matrix
β	Reliability index
β	Coefficient of the stiffness matrix
β_c	Shear transfer coefficient for closed cracks
β_t	Shear transfer coefficient for open cracks
γ	Specific weight
γ_{mas}	Specific weight of masonry
γ_{st}	Specific weight of stone
γ_{mo}	Specific weight of mortar
ζ_i	Damping ratio of the i'th mode
η	Masonry efficiency
θ	Updating parameters
ε_{mi}	Compressive strain at any instant
μ	Mean
μ	Poisson's ratio
μ_{mas}	Poisson's ratio of masonry
μ_{st}	Poisson's ratio of stone
μ_{mo}	Poisson's ratio of mortar
ρ	Density of material
σ	Stress
σ	Standard deviation
σ_m	Flat-jack pressure level
ϕ	Mode shape vector of the structure
ψ	Complex mode shape vector
ω	Natural angular frequency

LIST OF ACRONYMS/ABBREVIATIONS

2D	Two Dimensional
3D	Three Dimensional
AR	Auto Regressive
ASCE	American Society of Civil Engineers
CDF	Cumulative Distribution Function
CM	Center of Mass
DM	Damage Measure
DT	Destructive Testing
EFDD	Enhanced Frequency Domain Decomposition
EN	European Norms
ERA	Eigen-system Realization
FAS	Fourier Amplitude Spectrum
FBA	Force-Balance Accelerometer
FDD	Frequency Domain Decomposition
FE	Finite Element
FEMA	Federal Emergency Menagement Agency
FFT	Fast Fourier Transform
FORM	First-Order Reliability Method
FunC	Functionality
GPa	Giga Pascal
IDA	Incremental Dynamic Analysis
IFFT	Inverse Fast Fourier Transform
IM	Intensity Measure
IRF	Impulse Response Function
LHS	Latin Hypercube Sampling
LS	Life Safety
LVDT	Linear Variable Displacement Transducer
MAC	Modal Assurance Criteria

MCS	Monte Carlo Simulation
MPa	Mega Pascal
MPP	Mass Proportional Pushover
MUSIC	Multiple Signal Classification
NAF	North Anatolian Fault
NC	Near Collapse
NDA	Nonlinear Dynamic Analysis
NDT	Non-Destructive Testing
NHL	Natural Hydraulic Lime
NSA	Nonlinear Static Analysis
NZSEE	New Zealand Society for Earthquake Engineering
MDOF	Multi Degree of Freedom
MDT	Minor-Destructive Testing
MPP	Mass Proportional Pushover
PC	Performance Criteria
PDF	Probability Density Function
PEER	Pacific Earthquake Engineering Research
PGA	Peak Ground Acceleration
PO	Pushover
PSD	Power Spectral Density
SDOF	Single Degree of Freedom
SORM	Second-Order Reliability Method
SRSS	Square Root of Sum of Squares
SSI	Stochastic Subspace Identification
SVD	Singular Value Decomposition
TBDY	Turkish Building Seismic Code
TOP	Top Point

1. INTRODUCTION

1.1. General Information and Research Objectives

Masonry arch bridges comprise a significant portion of the road and railway bridges in Europe. More than 40% of 220000 railway bridges and 25% of the existing road bridges are masonry arch bridges, according to the Sustainable Bridges project [1, 2]. For certain countries, the ratio of the masonry arch bridges to the existing railway bridges is even higher, as can be seen from Figure 1.1, which is adapted from [3]. Also, more than 1600 masonry arch bridges constitute a part of the US transportation infrastructure system [4]. Similarly, there are about 9000 masonry arch bridges in the railway network of Iran [5].

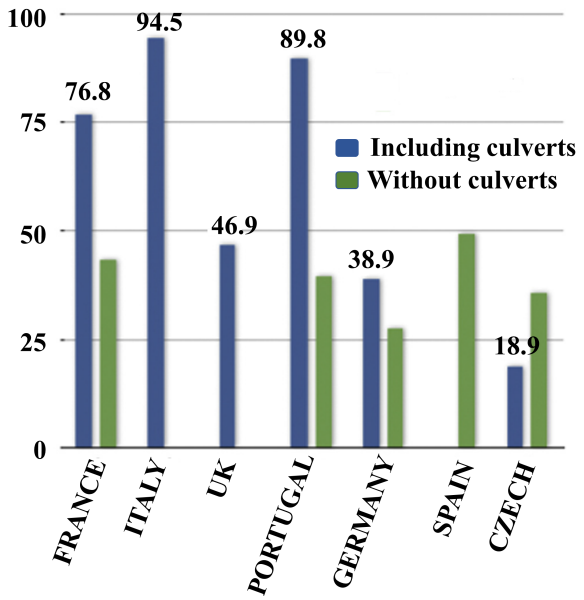

Figure 1.1. The percentage of masonry arch railway bridges in the railway network of some European countries (adapted from [3]).

Statistical data for Turkey indicate a significant percentage of masonry arch bridges in the railway network, such that 245 of the 2012 railway bridges (12.2%) and 6966 of the 24196 culverts (28.8%) are made of masonry. There are also 2063 masonry arch bridges in the road network. These bridges are invaluable as they are not only vital to the road and railway network but also form part of the architectural

and cultural heritage. The architectural and cultural value of some bridges even transcends their strategic value. Some of the famous masonry arch bridges and viaducts around the world are presented in Figure 1.2, and their properties are given in Table 1.1. Along with the beauty of these structures, the figure also displays a wide variety of geometry, morphology, and material types of masonry arch bridges.



Figure 1.2. Some of the famous masonry arch bridges and aqueducts around the world (images obtained from the web).

Table 1.1. Properties of the bridges presented in Figure 1.2.

	Bridge	**Location**	**Country**	**Year**	**Length (m)**	**Height (m)**	**Width (m)**	**Longest Span (m)**
I	Göltzschtal Viaduct	Netzschkau	Germany	1851	578	78	N/A	30.9
II	Pont du Gard	Gard	France	40-60	275	48.8	6.4	-
III	Solkan Bridge	Nova Gorica	Slovenia	1906	219.7	-	-	85
IV	Ponte Vecchio	Florence	Italy	1345	95	4.4	32	30
V	Irgandi Bridge	Bursa	Turkey	1442	-	-	11	16
VI	Çifte Bridge	Artvin	Turkey	1850(?)	35.5	-	2.8	-
VII	Severan (Cendere) Bridge	Adıyaman	Turkey	200	120	-	7	34.2
VIII	Malabadi Bridge	Diyarbakır	Turkey	1154	150	19	7	38.6
IX	The Mehmed Paša Sokolović Bridge	Višegrad	Bosnia	1577	179.5	15.4	6.3	15
X	Pélussin Viaduct	Pélussin	France	1917	170.8	45	4	55
XI	Varda Viaduct	Adana	Turkey	1916	172	98	-	30
XII	Wiesen Viaduct	Wiesen	Switzerland	1909	210	88.9	3.7	55

Despite the importance of these pieces of infrastructure, their safety and use are in danger due to several factors. These factors are, for instance, the unavoidable decay of materials, fatigue and strength degradation, changes in the boundary conditions and the acting loads from the time they were constructed. However, the most critical integrity risk for this type of structure is typically due to exceptional events like earthquakes, because the historic masonry structures were mainly designed to withstand vertical static loads, and not for seismic effects. For example, Figure 1.3 [6] shows the remains of the Puente Talca bridge, which collapsed during the earthquake that occurred in Maule, Chile, in 2010. Most of the masonry arch bridges are not compatible with their current use and modern design criteria, and many of them are structurally unsafe [7]. Therefore, structural assessment of the masonry arch bridges is essential in order to avoid cultural, economic, and life losses and to guarantee a required safety level.



Figure 1.3. Puente Talca bridge collapsed during Maule, Chile earthquake, 2010 (Source [6]).

Assessment of masonry arch bridges is a difficult task for several reasons. The geometry of the bridge is a key feature determining the behavior and seismic response, but it is often highly variable within the structure. For example, the span length of the arches, the height of the piers, and the thickness of the walls vary significantly. An accurate representation of the geometry might be difficult to obtain, especially for bridges in remote areas. Another important aspect that affects modeling and analysis of masonry arch bridge behavior is the morphology of the bridges. Internal constituents of the bridge, their interaction, and the existing features are very difficult to obtain, particularly because the original design documents usually do not exist, and several non-destructive tests are required for proper characterization.

Similarly, material characterization is a complex issue, especially in the absence of destructive tests on a statistically meaningful number of samples. Describing the proper material behavior is a formidable task in the same way. It is often not possible to obtain enough data to determine the mechanical properties of the material within limited time and budget constraints. Moreover, several parameters may be affecting model behavior depending on the modeling strategy, but at this time, there is limited knowledge of and experience concerning such parameters and their effect on the overall structural behavior. Finally, determining the type of analysis to conduct is a difficult

choice. Nonlinear static analysis procedures are often preferred to dynamic analysis procedures because of their relative simplicity and low computational cost; however, the accuracy of nonlinear static procedures for this type of structure has not been verified. Examples comparing both methods for masonry arch bridge structures are very scarce, and there is not enough evidence that one can be preferred to another.

While these issues present strong research need in those areas, the emerging probabilistic methods also add up to the difficulty in determining the assessment method. For example, the strong ground motions are characterized by their frequency content, seismic intensity, and duration. These uncertainties, combined with the structure's dynamic characteristics, bring about the seismic demand. On the other hand, the capacity is defined by the structural material properties and modeling parameters, which also possess intrinsic variability. Considering these, a probabilistic approach for the seismic vulnerability assessment seems more reasonable compared to the deterministic approach. Due to the reasons presented so far, there are no standardized or widely accepted procedures. To this end, a comprehensive seismic vulnerability assessment methodology is required to evaluate the safety of masonry arch bridges, to determine the strengthening needs, and to base on the post-earthquake decisions such as continuing operation or bridge closure.

The objectives of this research are manifold. The main one is to present all-around aspects of the seismic assessment of the masonry arch bridges and provide an overarching reliability-based assessment methodology for future studies. Thus, this study consists of various research topics, including data analysis, experimental testing, and numerical modeling. As the first step, experimental dynamic identification is performed and the dynamic properties of masonry arch bridges are investigated. Subsequent Finite Element model updating enables obtaining an accurate model that reflects the global behavior of the structure. To improve and contribute to the understanding of the seismic behavior of masonry arch bridges, nonlinear static and dynamic analyses are carried out. Both methods are compared to examine the validity of nonlinear static analysis procedures for masonry arch bridges, as such comparison is lacking

at present. Because of the significant differences in the results, incremental dynamic analysis is implemented. This type of analysis, carried out on a 3D FE model for the first time in literature, allowed to determine a continuous picture of the full range of structural responses. In order to obtain the data to conduct a probabilistic seismic assessment, various laboratory experiments are implemented. The sources of uncertainties in different experimental methods used for determining the elasticity modulus of masonry are investigated and highlighted. Several destructive, minor-destructive, and non-destructive testing results, numerical and empirical approaches are compared on the same masonry structure. Highlighting the advantages and drawbacks of the methods will allow, in the future, choosing the optimal experimental campaign. The information on the uncertain material properties identified from experimental testing is then reflected on the 3D FE model and probabilistic nonlinear analyses are performed. In the absence of performance limit states for masonry arch bridges, the principles of defining the limit states are discussed and combined with the probabilistic analysis results to determine the limit states for the investigated bridge. This also yielded the capacity distributions for each limit state. Demand distribution is obtained from the NDA results. As the last step of the proposed methodology, the probability of failure (or exceedance) for each limit state is calculated, and the corresponding reliability index is compared to the ones given in the standards for contemporary structures. The methodology presented in this study is outlined in Figure 1.4.

In addition to the main objectives of this study, secondary objectives emerged as the derivative of the primary ones. During the nonlinear time-history analyses, the interaction of horizontal and vertical components of earthquake records are investigated, and their importance is analyzed as they have not been investigated on masonry arch bridges before. Also, when researching the uncertainty in the elasticity modulus of masonry, its influence on the numerical analysis results is demonstrated.

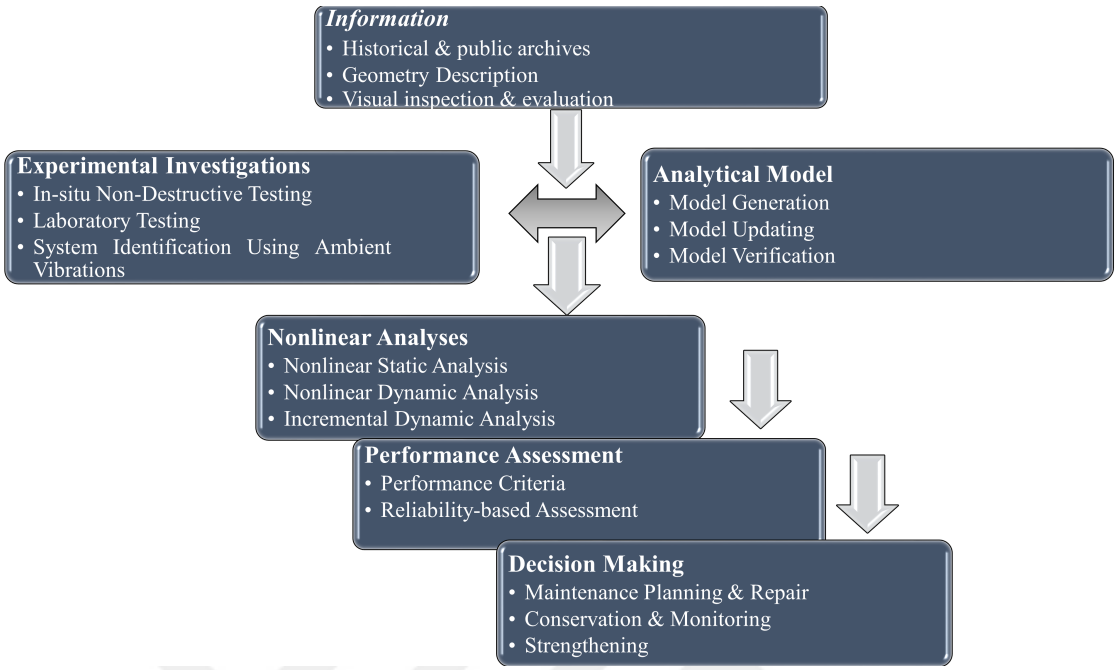

Figure 1.4. The methodology presented in this study.

1.2. Content of the Chapters

This study is structured in five main parts. Within each part, starting with Chapter 2 and ending with Chapter 6, literature research related to the specific topic is presented. Similarly, the results and discussion section is devoted to each chapter as well. The reason for such an organization is to define the research needs clearly and enable following the outcomes of the research easier, as combining all the results from those broad topics at once would be considerably confusing.

The methodology and all the investigations conducted in this research are centered on the example masonry arch bridges that are a part of an important railway route in Turkey. The Samsun-Kalin railway route was built circa 1926 in Central and North Anatolia, part of the newly established Turkish Republic. The railway had strategic importance as an alternative route to the Mediterranean Sea, and it continues to play a significant logistical role in the nation's transport network [8]. Modernization of the 378-km-long route necessitated assessing 78 bridges on the railway, 41 of which were registered as historical structures. Preservation and strengthening measures will

be taken, should structural assessment results require them. Thus, realistic and rigorous structural assessment becomes more important in terms of both protecting cultural heritage and using resources carefully. Structural vulnerability assessment is to be performed using only finite element analysis; however, finite element modeling of masonry structures includes significant uncertainties in terms of material properties, boundary conditions and different modeling assumptions [9]. Since these uncertainties affect the results significantly and make generating an accurate FE model a challenging task, they should be reduced as much as possible. In this context, one of the most efficient and novel approaches is system identification using ambient vibrations and the use of modal parameters for updating FE models.

Chapter 2 starts with the description of the bridges and the ambient vibration surveys carried out on site. The theoretical background of the dynamic identification methods used in this study is then presented. The collected signals were preprocessed for system identification. Next, modal parameters of the structures were identified by processing the data separately in the frequency and time domains, using Enhanced Frequency Domain Decomposition (EFDD), Auto-Regressive Model (AR Model) and Multiple Signal Classification (MUSIC) methods. All of the algorithms were implemented via the codes written by the author in MATLAB software. The results are presented and compared for three of the representative bridges, consisting of three, four, and five arches, respectively.

In Chapter 3, one of the bridges presented in the previous chapter, Bridge 41, is selected for the model updating study. The results of the system identification study specific to Bridge 41 are displayed. Background information that is necessary to generate a 3D FE model is presented. An in-house developed code employing MATLAB interface and SAP2000 OAPI software was used to update the analytical model. The elasticity modulus of the masonry elements and the fill material are selected as updating parameters. Dynamic identification and model updating studies in Chapter 2 and Chapter 3, respectively, are essential to the methodology presented in this research. They introduce new information and valuable discussion, albeit there is no substantial

contribution to the literature. Chapter 4 includes all-around aspects of the nonlinear analyses. The adopted modeling strategy and the reasons behind this choice are justified. Nonlinear model properties that control the structural behavior and the solution are discussed in detail and implemented to the updated bridge model. As the nonlinear static analysis is relatively the simpler of the analysis methods, the sensitivity of the model parameters and the structural performance of the bridge are investigated using this method first. Then, increasing the complexity, nonlinear dynamic analyses are performed using 14 real acceleration time-histories, scaled with respect to the target design spectrum. The results of the nonlinear static and dynamic analyses are compared. Because of the significant differences observed, incremental dynamic analysis is performed despite its major computational cost. After performing the structural seismic assessment using multiple methodologies, the results are evaluated and compared to each other, and the conclusions are drawn.

In Chapter 5, the sources of uncertainties in determining the elasticity modulus of masonry are investigated and highlighted. Masonry panel walls are constructed with similar stone and mortar types to that of Bridge 41. First, the stone and mortar components are tested for mechanical characterization. The results are then used in empirical equations provided by international standards. Masonry wallettes are also built and tested to calculate the elasticity modulus. Schmidt Hammer, ultrasound, ambient vibration, and flat-jack tests are performed on the masonry panel wall. Later, the panel wall is tested under cyclic in-plane shear-compression loading. A 3D FE model of the wall is generated in order to determine the elasticity modulus by matching the experimental and numerical results. Therefore, several destructive, minor-destructive, and non-destructive testing results, numerical and empirical approaches are compared on the same masonry structure. The advantages and drawbacks of the methods are highlighted.

The knowledge gained about the uncertain material properties from experimental testing is afterward applied to the reliability assessment of the bridge in Chapter 6. Uncertainty in the elasticity modulus values is represented as a probability distribution

and implemented to the 3D FE model. This way, probabilistic nonlinear analyses are performed. Because there are no performance limit states available for masonry arch bridges, the main aspects and principles of defining the limit states are discussed and combined with the probabilistic analysis results. The capacity distributions for the investigated bridge are obtained from the distribution of limit state values in probabilistic nonlinear analysis results. The demand distribution, on the other hand, is obtained from the nonlinear dynamic analyses carried out in Chapter 4. Before moving to the final part, background information regarding the reliability analysis is presented. In the end, the joint probability distribution of the capacity and demand distributions is utilized to calculate the probability of failure (or exceedance) for each limit state. The reliability index for each limit state is also calculated and compared to the values given in the international standards.

In Chapter 7, the present research is summarized and the major conclusions are presented. In addition, the recommendations for future studies are given.

2. SYSTEM IDENTIFICATION

In this chapter of the thesis, the ambient vibration tests that were carried out on site are explained. After a quick overview of the bridges forming the focus of this study, the manner of data collection is defined. Then, the methods by which the data were manipulated and analyzed are outlined, and the theoretical background is given. The data obtained from the bridges is presented, and the modal parameters gained from the multiple interpretive methodologies are compared. This chapter concludes with a discussion of the various identification methodologies and emphasizes the benefit of using multiple approaches to enable accurate analysis.

Dynamic identification tests were carried out under ambient vibration, hammer impact loading, and train passing conditions. The collected signals were preprocessed for system identification. Then, modal parameters of the structures were identified by processing the data separately in the frequency and time domains, using MATLAB software. The results, obtained using the data under ambient vibration condition, were presented for three of the representative bridges, consisting of three, four, and five arches, respectively. Because historical masonry structures are often more complicated and have higher stiffness than the standard shear-type buildings, dynamic identification presents a more challenging task for these structures. Thus, it is good practice not to rely on a single method but to confirm the identification results with other methods based on different principles. For this reason, Enhanced Frequency Domain Decomposition (EFDD) was performed in the frequency domain, and the modal values were found with the methods using the Cross Power Spectral Density (CPSD) graphs and decay of the autocorrelation, whereas, in the time domain Auto-Regressive Model (AR Model) and Multiple Signal Classification (MUSIC) methods were employed. Finally, the results were compared to each other and recommendations were derived for future work.

It is possible to find examples of similar work in the literature, and others have also emphasized the importance of using multiple methodologies in the analysis. Costa *et al.* [10] performed the operational modal analysis of three different masonry arch bridges using different techniques such as EFDD and Stochastic Subspace Identification (SSI), and subsequently did numerical model updating. Aoki *et al.* [11] carried out a series of non-destructive, destructive, and dynamic tests to determine the dynamic properties of the long masonry arch bridge. After finding the modal properties of the bridge via the Eigensystem Realization Algorithm (ERA) technique, the numerical model was fed with these values and the inverse Eigen-sensitivity method was utilized for a model updating procedure. Andersen *et al.* [12] carried out rigorous ambient vibration tests of a concrete box girder bridge and investigated the performance of various system identification methods like Peak-Picking, Polyreference LSCF method, SSI, and Auto-Regressive Moving Average Vector models. Magalhães and Cunha [13] explained the topic of operational modal analysis by using three output-only modal identification algorithms on the data from a 280-meter long concrete arch bridge. Their use of different methods based on distinct principles revealed the uncertainty of the modal damping estimates and demonstrated the need for further research on the subject. Gentile and Saisi [14] focused on the dynamic identification and variations in the modal characteristics of a historical iron bridge under different levels of traffic excitation. In addition to the dynamic identification studies on bridges, various instances that employ operational modal analysis for structural dynamic identification of monumental historical structures are available to the reader as well [15–18].

This part of the dissertation work contributes to understanding the dynamic properties of a large number of historical arch bridges built in the same period while highlighting the capabilities and drawbacks of the identification methods used.

2.1. Bridges and Ambient Vibration Survey

All 41 historical masonry arch bridges of the 378 km Samsun-Kalin railway — all built between 1926-1932 —are grouped after the preliminary inspection in terms

of their total length, maximum height from the foundation to the top of the spandrel, number of spans and the longest span. They represent a similar design: barrel arches, sandstone or limestone, mortar and infill as a building material, and a similar deck width of around four to five meters. Properties of the bridges are given in Table 2.1, and they are shown in Figure 2.1. Of those, Bridge 13 (three arches), Bridge 41 (four arches), and Bridge 5 (five arches) have been selected as paradigms to present the results obtained from the analysis as they typify their respective groups and produced particularly clear results.



Figure 2.1. Dynamically identified bridges: (a) Bridge 13, (b) Bridge 41 and (c) Bridge 5.

Table 2.1. List of presented bridges in this section.

ID	**Location (km)**	**Spans (m)**	**Total Length (m)**	**Max Height (m)**
5	21+689	6-10-10-6-6	64.3	17.55
13	30+153	8-8-8	40.7	13.70
41	360+292	10-10-10-10	59.3	10.77

Instrumentation was performed using a cabled data acquisition system, force-balance accelerometers (FBA), and 24-bit recorders. Twelve FBA sensors were used for the ambient vibration survey of Bridge 13, while 20 FBA sensors were used in a single setup for Bridges 41 and 5. Sensors have a 155 dB dynamic range and user-selectable ± 0.25g to ± 4g scale range. They were placed over the arches and piers at the lateral edges on the deck in longitudinal, vertical, and out-of-plane (transverse) directions with regard to the bridges' plane. It was thus possible to characterize vertical and transversal movements as well as rotations. The sensor layout for the bridges is provided in Figure 2.2. Approximately one hour of data was collected for each bridge

under the bare condition, and a maximum of seven minutes' data was taken under impact loading and train passing. The system's sampling frequency was configured to 200 Hz.

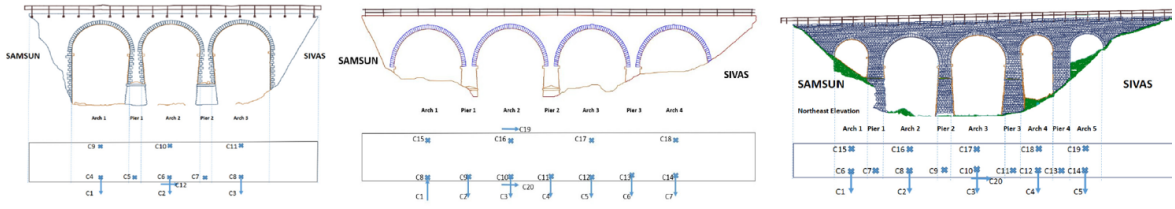

Figure 2.2. Sensor layout of the bridges: (a) Bridge 13, (b) Bridge 41, (c) Bridge 5.

2.2. Dynamic Identification

2.2.1. Preprocessing

For structures with high stiffness such as masonry arch bridges, ambient vibration has small amplitudes and low signal-to-noise ratio. The noise changes the frequency content and the amplitudes of the Fourier spectra, and also introduces spurious resonant peaks [19]. Thus, analysis of the noisy data collected from the bridges presented in this study required signal processing before the identification procedure. Preprocessing included detrending, applying filters, and decimation. An example of the processed data from a few channels is shown in Figure 2.3.

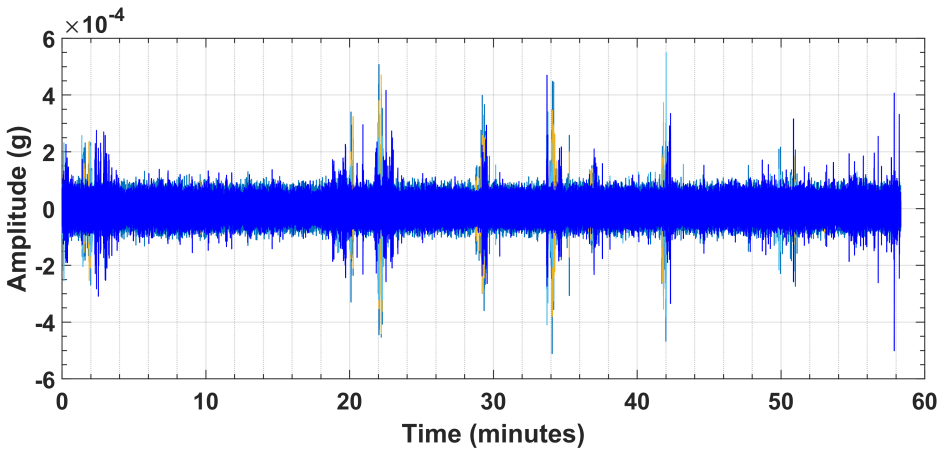

Figure 2.3. Example of the processed ambient vibration data - in the bare condition.

First, existing trends in the data, if there are any, were removed from the data. Second, the acceleration data was integrated twice to find the displacement time histories. The raw data usually has non-zero final displacements, and this should be corrected by removing the low frequencies incrementally via the application of high-pass filters. The suggested increment for correction is 0.05 Hz. Third, it is often a good practice to check the Fourier Amplitude Spectrum of the data as it indicates the quality of the signal and whether the signal is noise dominant or not. If there were any frequencies in the signal dominated by noise, such as those stemming from a working generator or an electrical connection, these frequencies might be eliminated by employing a band-pass filter around them. Finally, decimation was employed when dealing with long records in time-domain methods, as they tend to require more processing time. Decimation enabled shortening the data without losing information.

2.2.2. Enhanced Frequency Domain Decomposition (EFDD)

Frequency Domain Decomposition [20] is a non-parametric output-only modal identification technique. As its name suggests, it operates in the frequency domain and has the advantage of being fast and user friendly. It also gives the user a feeling of the data they are dealing with through the use of spectral density functions. As the first step in implementing the identification algorithm, the Power Spectral Density (PSD) matrix is estimated. In this study, PSD matrix estimation is done with the Welch method, using the number of Fast Fourier Transform (FFT) as 4096 points, a Hanning window and an overlapping of 50%. Then, the estimate of the output PSD, G_{yy}, is decomposed by taking the Singular Value Decomposition (SVD) of the PSD matrix, which is presented by Equation 2.1.

$$\mathbf{G_{yy}}(\omega_j) = \mathbf{U_j S_j U_j^H} \tag{2.1}$$

where $\mathbf{U_j}$ is an orthonormal matrix ($\mathbf{U_j U_j^H = I}$) that contains the singular vectors of $\mathbf{G_{yy}}(\omega_j)$ and $\mathbf{S_j}$ is a diagonal matrix containing the scalar singular values. Now the spectral matrix is decomposed into a set of auto spectral density functions, each

corresponding to a single degree of freedom system. By plotting the first singular values for each frequency, a system's modal frequencies can be obtained via simple peak-picking, and the mode shapes were obtained using the first singular vectors at the corresponding frequency. Figure 2.4 presents an example of the auto-spectrum for Bridge 5.

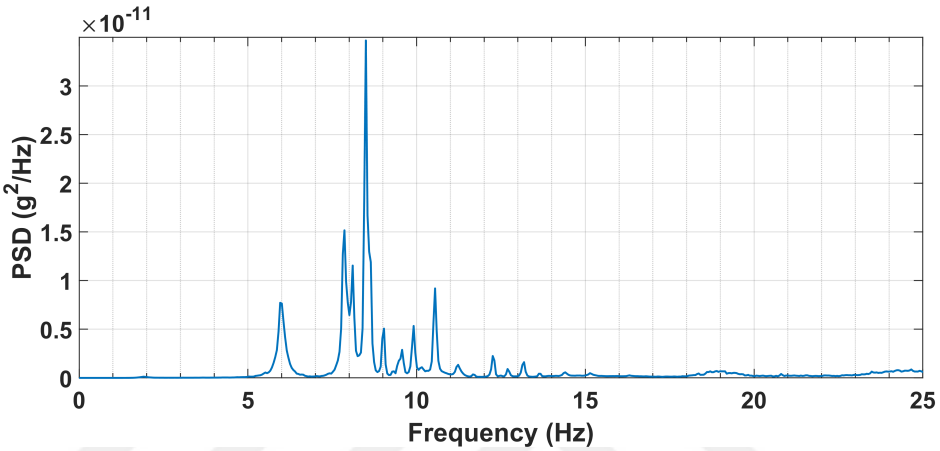

Figure 2.4. Auto-spectrum of the whole data for Bridge 5.

Enhanced Frequency Domain Decomposition [21] is the improved version of the FDD technique and allows the identification of damping ratios. The PSD function is identified around the peak by comparing the mode shape estimate (the singular vector) with the singular vectors for the frequency lines around the peak. This comparison can be made using the Modal Assurance Criterion (MAC) [22], given by Equation 2.2, which measures the correlation between two modal vectors.

$$MAC_{\phi_1,\phi_2} = \frac{(\phi_1^T \phi_2)^2}{(\phi_1^T \phi_1)(\phi_2^T \phi_2)} \tag{2.2}$$

where $\phi_{\mathbf{i}}$ are the modal vectors.

The MAC value ranges between zero and one. As long as the singular vector has a high MAC value with the mode shape, the corresponding singular value belongs to the single degree of freedom (SDOF) density function. If the MAC value drops below the user-defined threshold for a certain frequency, then the search for matching parts of the auto spectral density function is stopped, and the rest of the values (the remaining part

of the function) is set to zero. Then the natural frequency and damping are obtained by taking the spectral density function back to the time domain using Inverse Fast Fourier Transform (IFFT). Since the impulse response of a dynamic system and the system's output correlation when excited by white noise are proportional, the modal damping ratio of the mode under investigation can be estimated by the logarithmic decrement of the free decaying auto-correlation function of the SDOF system. An improved estimate of the natural frequency is found by the crossing times of the function. The method is described in detail by Magalhães and Cunha [13] in a pedagogical way. The examples of the mode shape identification from singular vectors and damping identification from the impulse response function can be seen in Figure 2.5, Figure 2.6, and Figure 2.7. The frequencies identified for the various bridges and the modal damping ratios will be presented in detail later.

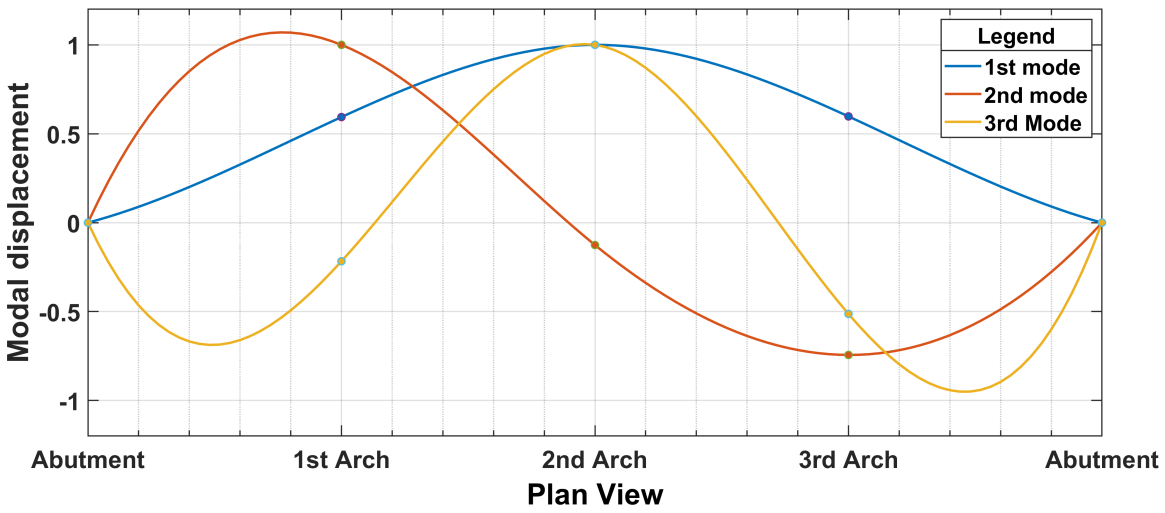

Figure 2.5. Experimental out-of-plane mode shapes for Bridge 13.

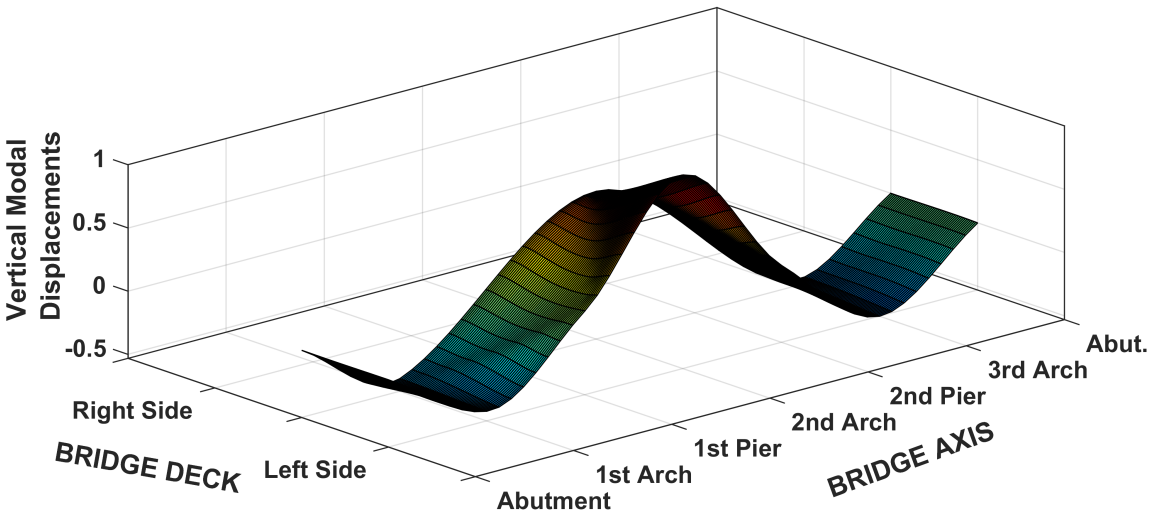

Figure 2.6. Experimental first vertical mode shape for Bridge 13.

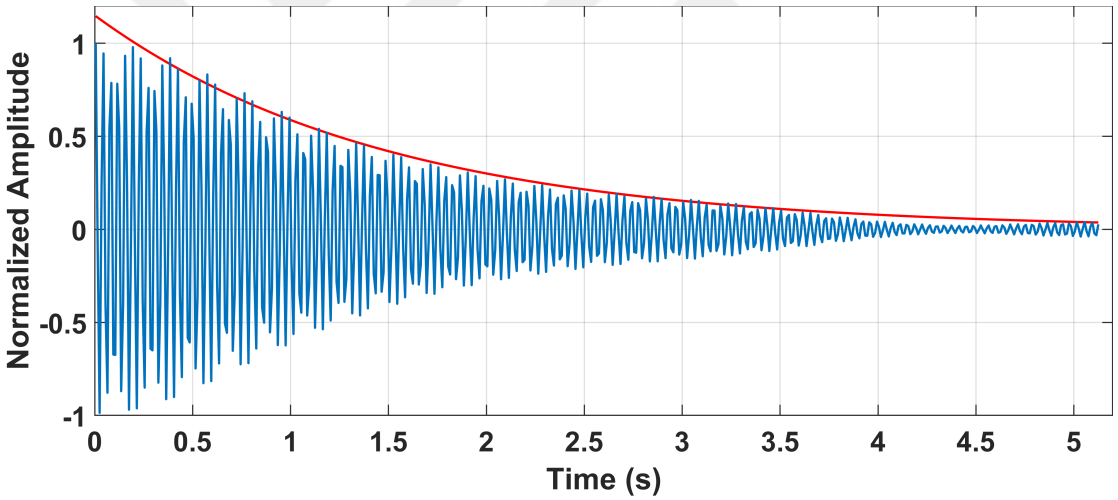

Figure 2.7. Example of the impulse response function and damping envelope for damping identification, Bridge 13 out-of-plane mode, ζ=0.58%.

2.2.3. Auto-Regressive (AR) Model

The time-domain methods available for operational modal analysis, extensively investigated in Peeters [23], are mainly based on discrete-time state-space models and auto-regressive moving average (ARMA) or auto-regressive (AR) models. Both methods are classified as parametric methods, but the subspace identification formulations such as stochastic subspace identification (SSI) use state-space models, whereas the

AR models use modal models. The former method is more commonly used in civil engineering applications, while the latter has been less frequently adopted by the civil engineering community [13].

To understand the AR model, it is necessary first to understand the modal model and discrete-time method. A brief explanation of those is presented below.

If one applies the Laplace transform to the equation of motion of a multi-degree of freedom (MDOF) system with zero initial conditions, they can relate the inputs with the output through a matrix called transfer function, $H(s)$, such that

$$Ms^2X(s) + CsX(s) + KX(s) = F(s) \tag{2.3}$$

$$[Ms^2 + Cs + K]X(s) = F(s) \tag{2.4}$$

$$H(s) = \frac{X(s)}{F(s)} = [Ms^2 + Cs + K]^{-1} \tag{2.5}$$

Algebraic manipulations allow the transfer function in Equation 2.5 to be expressed as the sum of the contribution of the dynamic system modes, as given below for two different cases, each with the load at point i and the displacement at point j.

- For proportional damping:

$$H_{ij} = \frac{X_j(s)}{F_i(s)} = \sum_{k=1}^{n}[\frac{\phi_{\mathbf{jk}}\phi_{\mathbf{ik}}}{m^*_{kk}[s^2 + 2i\zeta_k\omega_k s + \omega_k^2]}] \tag{2.6}$$

  where $\phi_{.\mathbf{k}}$ is the kth mode shape, ω is the natural cyclic frequency, ζ is the modal damping ratio and m is the kth modal mass.

- For non-proportional damping:

$$H_{ij} = \frac{X_j(s)}{F_i(s)} = \sum_{k=1}^{n}[\frac{\psi_{\mathbf{jk}}\psi_{\mathbf{ik}}}{m^*_{kk}(s - \lambda_k)} + \frac{\psi^{\mathbf{c}}_{\mathbf{jk}}\psi^{\mathbf{c}}_{\mathbf{ik}}}{m^*_{kk}(s - \lambda^c_k)}] \tag{2.7}$$

where $\psi_{.\mathbf{k}}$ is the kth complex mode shape, the superscript $[\cdot]^c$ denotes the complex conjugate and λ_k is the kth eigenvalue of the kth modal response [24].

As a side note, the frequency response function, a special form of the transfer function in the frequency domain, can be obtained by substituting $i\omega$ for s.

The discrete-time method for system identification, using discrete-time linear filters, is well known in electrical and systems engineering and can also be used in structural engineering [25].

Discrete-time models for single input single output (SISO) systems can be expressed as:

$$y(t) + a_1 y(t-1) + ... + a_m y(t-m) = b_0 x(t) + b_1 x(t-1) + ... + b_n x(t-n) \quad (2.8)$$

$$y(t) = -a_1 y(t-1) - ... - a_m y(t-m) + b_0 x(t) + b_1 x(t-1) + ... + b_n x(t-n) \quad (2.9)$$

$$y(t) = -\sum_{r=1}^{m} a_r y(t-r) + \sum_{s=1}^{n} b_s x(t-s) \quad (2.10)$$

or, by using the Backward Shift operator, i.e., $q^{(-k)}x(t) = x(t-k)$ and defining the polynomial:

$$A(q) = 1 + a_1 q^{-1} + a_2 q^{-2} + ... + +a_m q^{-m} = 1 + \sum_{r=1}^{m} a_r q^{-r} \quad (2.11)$$

$$B(q) = b_0 + b_1 q^{-1} + b_2 q^{-2} + ... + +b_n q^{-n} = b_0 + \sum_{s=1}^{n} b_s q^{-s} \quad (2.12)$$

$$A(q) \cdot y(t) = B(q) \cdot x(t) \Rightarrow y(t) = H(q) \cdot x(t) \quad (2.13)$$

After defining the modal model and discrete-time method, the ARX Models (Auto-Regressive with Auxiliary Input) for SISO systems can be defined as in Figure 2.8 below:

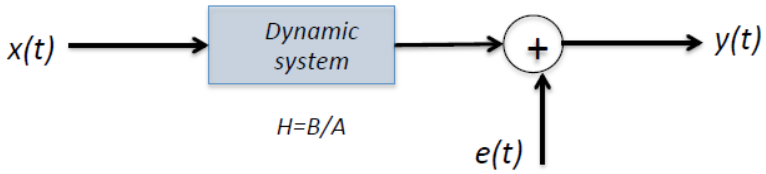

Figure 2.8. The ARX model.

$$y(t) = \frac{B(q)}{A(q)} \cdot x(t) + e(t) \tag{2.14}$$

where $y(t)$ is the output time series, $x(t)$ is the input time series and $e(t)$ corresponds to zero-mean Gaussian noise. $H(q)$=$B(q)/A(q)$ represents the system transfer function. The SISO system can be represented in another way by defining vectors as follows:

$$\varphi(t) = \begin{Bmatrix} -y(t-1) \\ \vdots \\ -y(t-m) \\ x(t) \\ x(t-1) \\ \vdots \\ x(t-n) \end{Bmatrix}_{(m+n+1)\times 1} ; \theta = \begin{Bmatrix} a_1 \\ \vdots \\ a_m \\ b_0 \\ b_1 \\ \vdots \\ b_n \end{Bmatrix}_{(m+n+1)\times 1} \Rightarrow y(t) = \varphi(t)^T \cdot \theta \tag{2.15}$$

Once the SISO system is defined, the system identification can be achieved by using "One-Step Ahead Prediction". That is, if one knows all the parameters up to time $(t-1)$, one-step ahead prediction $\hat{y}(t)$ of the output $y(t)$ at time t is:

$$\hat{y}(t) = \varphi^T(t) \cdot \theta \tag{2.16}$$

The difference between the estimated and recorded values of $y(t)$ — in other words, the error in the prediction $\epsilon(t)$ — can be minimized to predict $\hat{y}(t)$ employing the least-squares approximation (or using other methods such as Burg, Yule-Walker, or Kalman filters inter alia). Differentiating the error function with respect to θ gives the

Equation 2.17:

$$\theta = \frac{\sum_{t=max(m,n)+1}^{N} \varphi(t) \cdot y(t)}{\sum_{t=max(m,n)+1}^{N} \varphi(t) \cdot \varphi^T y(t)} \tag{2.17}$$

After finding the a and b coefficients using these equations, the system's poles (roots of $A(q)$) are found and utilized to determine the natural frequencies and damping ratios of the system [25]. This can either be achieved by using the formulas in the given reference or by using the pole-zero plot feature in MATLAB software. For the AR model estimation, the procedure is essentially the same as the ARX model except that the input is implicitly considered to be white noise.

The AR model method is known to improve the results obtainable from noisy data. However, the results are highly dependent on the chosen model order for the system. The model order theoretically should be twice the number of modes, since, for stable systems (with no negative damping), the poles appear in complex-conjugate pairs. Notwithstanding, higher model orders are required due to the presence of noise in the data. Thus, a practical approach would be to observe the system's frequency response and the change of natural frequencies and damping ratios with increasing model order. For this purpose, a stabilization diagram is an effective and widely-used tool. Figure 2.9 represents an example of a stabilization diagram and the frequency response plot of the system, drawn together.

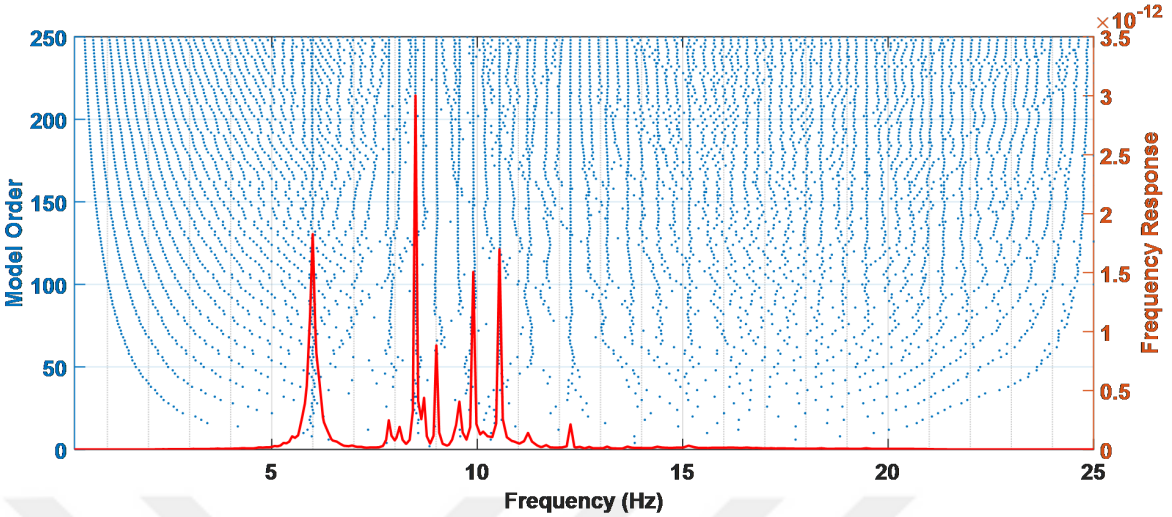

Figure 2.9. Stabilization diagram for Bridge 5-Sensor 1 out-of-plane data.

2.2.4. Multiple Signal Classification (MUSIC) Method

In the MUSIC method, the signal $x(t)$ is assumed to be composed of p complex exponentials in noise. It can be decomposed in terms of its signal and noise subspace components by using the eigenvalues and eigenvectors of the auto-correlation matrix. The auto-correlation matrix $\mathbf{R_{xx}}$ is defined by:

$$R_{xx} = \begin{bmatrix} R(0) & \cdots & R(M) \\ \vdots & \ddots & \vdots \\ R(-M) & \cdots & R \end{bmatrix}_{(m+1)(m+1)} \tag{2.18}$$

$$R(\tau) = \frac{1}{N}\sum_{t=1}^{N} x(t) \cdot x(t-\tau) \tag{2.19}$$

$$\tau = [-M \cdots M] \tag{2.20}$$

Every stationary signal $x(t)$ can be expressed as a linear combination of the eigenvectors of its auto-correlation matrix [26]. Thus, we can write:

$$x(t) = \sum_{i}^{m} c_i \cdot \mathbf{S_i} \tag{2.21}$$

where c_i is a constant and $\mathbf{S_i}$ is the ith eigenvector.

It can be observed that the correlated components of the record $x(t)$, i.e., the signal, have much larger eigenvalues than the uncorrelated components, i.e., the noise. Also, the signal subspace is orthogonal to the noise subspace. Therefore, the signal and the noise can be separated by using the eigenvalues and eigenvectors of the correlation matrix [27].

In addition to the MUSIC method in literature, the Pisarenko Harmonic Decomposition and Rotational Invariance Techniques (ESPRIT) are based on this principle; the theoretical background may be found in various textbooks on signal processing, e.g., Moon and Stirling [27].

Two important points should be noted concerning the MUSIC method. The first is the assumption that $x(t)$ is a stationary signal and hence does not change significantly with time. Therefore, the auto-correlation function R_{xx} is not a function of time, but only of the time lag between two components. Thus, if the record is not of ambient vibrations but rather represents a signal under transient loads such as earthquakes or blasts, this assumption is not valid. The second crucial part is the selection of the filter order (or the number of sinusoids) in the signal, M. The filter order M must be greater than p to represent the signal accurately, but it should not be too large; otherwise, it might represent the noise as well. Selecting the optimal filter order can be made via the simple method proposed by Safak [28].

2.3. Results and Discussion

Dynamic identification results using the three different methods presented above are shown in Table 2.2, Table 2.3, and Table 2.4 for Bridge 13, Bridge 41 and Bridge 5, respectively. The examples of mode shape identification presented in the text previously are representative of all the shapes rendered, which are very similar to each other for different methods; thus, additional examples will not be provided in this section.

For the same reason, a comparison of mode shapes via MAC is not necessary here.

Table 2.2. Dynamic identification results for Bridge 13.

BRIDGE 13					
	AR Model		**EFDD**		**MUSIC**
Mode Shape	f (Hz)	Damping Ratio, ζ (%)	f (Hz)	Damping Ratio, ζ (%)	f (Hz)
1st out-of-plane	6.23	0.38 - 1.33	6.23	0.45 - 1.00	6.20
2nd out-of-plane	8.37	0.73 - 2.40	8.37	0.97 - 1.30	8.40
3rd out-of-plane	9.98	0.43 - 1.11	9.99	0.79 - 1.14	9.96
1st vertical	16.66	0.88 - 1.84	16.68	1.64 - 5.22	N/A

Table 2.3. Dynamic identification results for Bridge 41.

BRIDGE 41					
	AR Model		**EFDD**		**MUSIC**
Mode Shape	f (Hz)	Damping Ratio, ζ (%)	f (Hz)	Damping Ratio, ζ (%)	f (Hz)
1st out-of-plane	5.72	1.80 - 2.78	5.71	1.22 - 4.44	5.96
2nd out-of-plane	8.49	1.06 - 1.88	8.50	1.02 - 1.56	8.50
3rd out-of-plane	12.18	1.04 - 1.99	12.11	1.16 - 3.57	12.11
4th out-of-plane	15.33	0.29 - 0.60	15.33	0.31 - 0.43	15.33
1st vertical	18.44	0.28	18.45	0.03 - 0.67	18.46

Table 2.4. Dynamic identification results for Bridge 5.

BRIDGE 5					
	AR Model		**EFDD**		**MUSIC**
Mode Shape	f (Hz)	Damping Ratio, ζ (%)	f (Hz)	Damping Ratio, ζ (%)	f (Hz)
1st out-of-plane	6.01	1.05 - 1.33	6.01	0.43 - 1.32	5.96
2nd out-of-plane	8.50	0.27 - 0.43	8.50	0.06 - 0.33	8.50
3rd out-of-plane	10.55	0.27 - 0.44	10.55	0.23 - 0.35	10.55
1st vertical	18.90	0.60 - 1.29	18.90	1.34 - 3.16	N/A

The results show that the identified modal frequencies are very close to each other, confirming the reliability of the results. For example, Figure 2.10 presents a frequency response spectra comparison for Bridge 5 data. However, and significantly, the damping estimation turns out to be notably subjective — to the extent that it seems best to provide a range for the damping ratio rather than a single value.

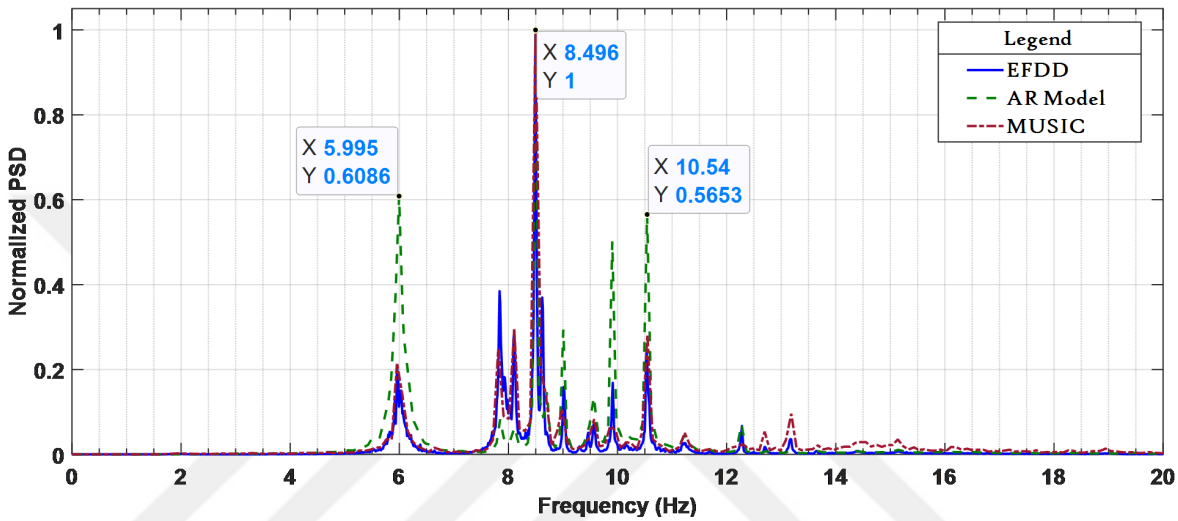

Figure 2.10. Frequency response spectra comparison for out-of-plane data of Bridge 5.

The methodologies used in dynamic identification study present idiosyncratic issues in application and interpretation. In the case of damping estimation from EFDD, the method and data used alter the results. For example, using all the data available from all sensors or using only the out-of-plane data from the sensors in the transverse direction for damping estimation of the out-of-plane modes give different results. The reason for this is the slight change in the auto-spectrum for different data sets; as the auto-spectrum changes so does its IFFT and the damping estimation. Similarly, using an exponential fit to the Impulse Response Function (IRF) or IRF's envelope or using a logarithmic decrement method with the selection of a different number of peaks results in different values. As for the damping estimation from the AR Model, the data used and the model order assigned change the results. Generally, the higher the model order, the smaller is the damping ratio. Also, similar to the previous case, damping ratios estimated from out-of-plane data or vertical data do not match. Thus, utmost care is necessary both in implementing dynamic identification and in presenting the data derived.

In terms of the speed and interpretation of the results, the EFDD method is easy to implement, and it is well-established in the literature. On the other hand, the AR Model and MUSIC methods are computationally demanding because they require the autocorrelation of the input data. Visualization and manipulation of the results are easier in the case of the EFDD method as well. There is no significant change in the EFDD method as the bridges grow in complexity, while the AR Model and MUSIC methods become even more computationally demanding.

The results obtained from the MUSIC method depend on the data used. For long records, e.g., several minutes' worth of data, employing even a moderate number of sensors renders the method impossible due to computational power limitations. Therefore, 60 minutes' worth of data was decimated four times, and the segmentation technique was used afterward. An average of the frequency response spectra obtained via the MUSIC method was then used to estimate the system's fundamental frequencies. Although it was not possible to identify the first vertical modal frequencies from an average spectrum of the segmentation for Bridge 41 and Bridge 5, these frequencies could be determined when particular portions of the data were chosen. This again demonstrates the subjectivity of the method. Another observation is that the filter order and the length of the data do not change the frequency response spectrum significantly; in other words, as both quantities keep increasing, the frequency response stabilizes quickly after the iteration starts. Depending on the data used and filter order chosen, the MUSIC method was capable of identifying the first three fundamental frequencies of Bridge 13 using only two seconds of data. This shows that the method is very promising. Currently, however, the results are subject to the user's methods, and this approach has not yet reached the required robustness for practical structural engineering applications.

Another general observation concerns the sensor layout. As can be seen in other studies referenced at the beginning of Chapter 2, mode shapes of the masonry arch bridges are usually complex and multi-directional. That is, peaks in the frequency response spectrum representing the modal frequencies usually appear in spectra ob-

tained from both out-of-plane and vertical data; therefore, making the engineer's work more difficult to distinguish between the structural modes. Also, observed mode shapes change depending on the bridge geometry. In the case of this study, the first structural modes observed were out-of-plane. In the case of a long bridge span and shallow arches, however, the dominant modes would probably be vertical and horizontal. In general, a careful 3D investigation of modal displacements is necessary since the planar view of the mode shapes can be misleading. Keeping that in mind and also considering that all the methods perform fairly well with a few minutes' worth of data collection, it would be advisable to perform ambient vibration testing with sensors put in horizontal, vertical and out-of-plane directions in a dense grid covering the bridge deck, using multiple setups. It should also be noted the sensors on the piers are necessary, but due to piers' high rigidity, the record becomes very noisy at high frequencies.

Even though the results of dynamic identification under the impact loading and loading during the train passing are not presented in this study, the following comment could be made. For the bridge-train interaction, dynamic identification using the data under train passing reveals a drop in the modal frequencies and an increase in damping. However, it is not possible to deduce a nonlinear behavior from these changes because the data after train passing brings about the same modal parameters as in bare condition. Therefore, the change in the modal frequencies and damping ratios can be attributed to the temporary bridge-train interaction. Moreover, estimating the damping ratio by using the data obtained from the bridge-train interaction might not give correct estimates, as it reflects the forcing nature of the train on the damping. The data, which is taken after the train leaves the bridge, might be used instead.

As this study makes clear, because of the inherent complexity of masonry structures, it is good practice not to rely on a single method but rather to confirm the identification results with other methods based on different principles. The comparison of results reveals that all methods yield reasonable estimates of the natural frequencies and the range of damping ratios, even though the damping estimation tends to be relatively subjective. Mode shape estimation, by contrast, is a difficult task and requires

three-dimensional visualization; therefore, recommendations were given for ambient vibration testing of similar structures in the future. In the meantime, applying multiple methodologies to dynamic identification demonstrates the strengths and weaknesses of each analytical approach, even as it suggests the same for the structures under study.

3. MODEL UPDATING

One of the most efficient and novel approaches to reducing the uncertainties associated with finite element modeling of masonry structures includes system identification using ambient vibrations and employing modal parameters to update the Finite Element (FE) models. In this chapter, to exploit and refine this approach, one of the three bridges, Bridge 41, is chosen as the paradigm. The signals are preprocessed for system identification, and the modal parameters of the structures are identified by processing the data, as presented in Chapter 2. The identified parameters are then used to update the FE model of the structure by minimizing the difference between experimental and numerical modal parameters.

The theory underlying the system identification of the bridges, details of the ambient vibration survey and data processing, and an overview of the results are provided in Chapter 2. In order to avoid repetition, dynamic identification results of the selected bridge will be briefly illustrated in this chapter. The background information necessary for the FE modeling of Bridge 41 will be presented next, and the chapter will be concluded with the details of the model updating study and the results.

3.1. System Identification of Bridge 41

This discussion presents only those results of the system identification study that allow the characterization of the dynamic properties of the Bridge 41 and enable updating of the FE model. As can be seen in Table 2.3 and Figure 3.1, the structure's dynamic response is dominated by five modal frequencies between 0-20 Hz. The first four are out-of-plane modes, characterized by the bending behavior about the bridge's longitudinal axis, while the fifth corresponds to the vertical mode.

The mode shapes represent 3D behavior that is complex to identify when compared with 2D plane frame representation of buildings because the measured points on

the deck move in both the transverse and vertical directions. Although the evaluation of 3D movements is typically required to distinguish between the mode shapes, out-of-plane mode shapes can be represented as the sinusoidal shapes in 2D when looking at the plan view. Figure 3.2 displays the out-of-plane mode shapes in such representation. On the other hand, a 3D representation is necessary to identify the vertical mode shapes, as can be seen in Figure 3.3.

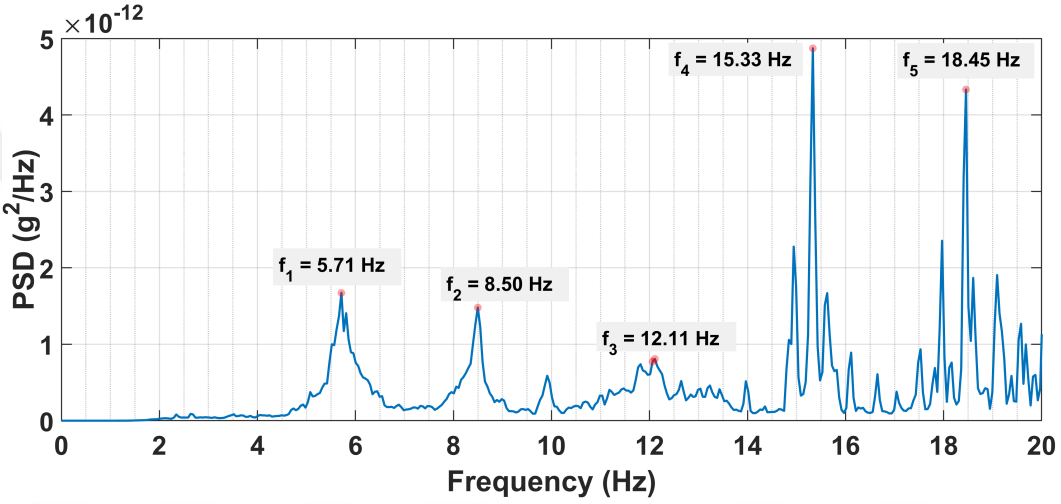

Figure 3.1. Auto-spectrum of the Bridge 41 data.

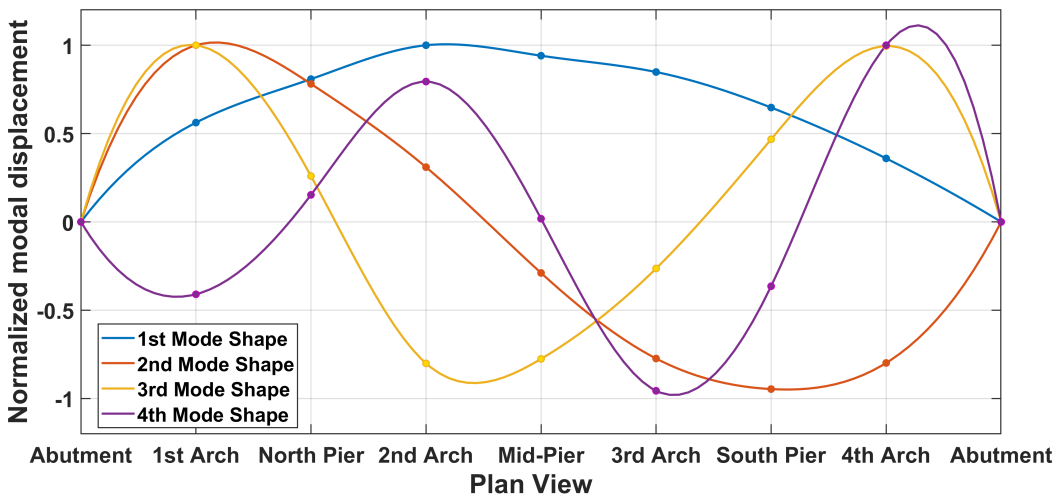

Figure 3.2. Identified out-of-plane mode shapes of the Bridge 41.

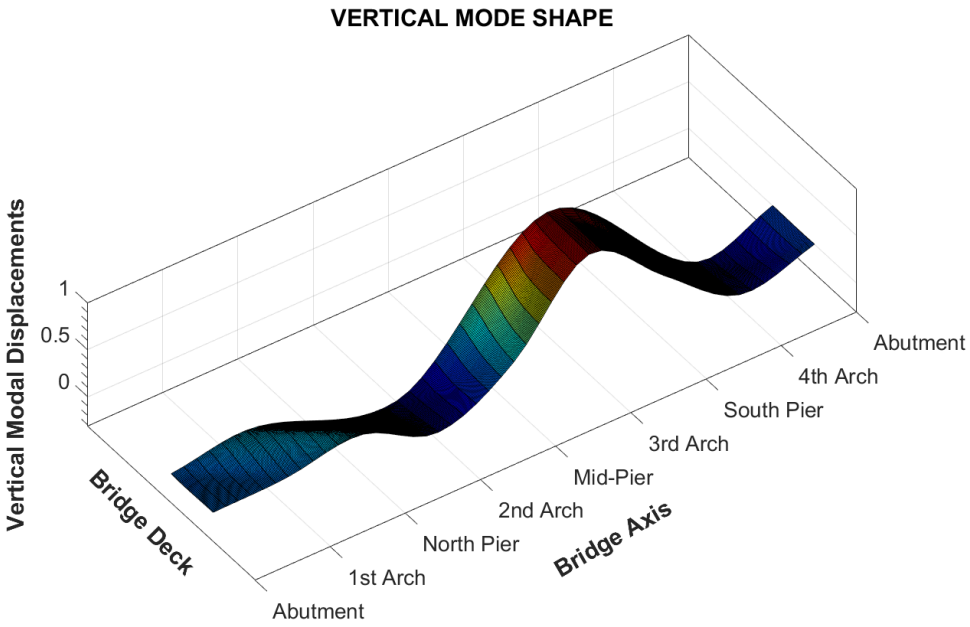

Figure 3.3. Identified vertical mode shape of Bridge 41.

3.2. Information on Bridge 41

The Samsun-Kalın railway was built between 1926 and 1932, according to the historical records [8]. The main components of the railway's masonry arch bridges are arch barrels, piers, abutments, spandrels, backing, and fill materials. Figure 3.4, adapted from [29], illustrates the typical structure of a masonry arch bridge and the related terminology. Amongst the components of masonry arch bridges, arch barrels, piers and spandrels are composed of masonry, which can be distinguished as a series of ashlar stone blocks separated by mortar joints. Together, they form the stone skeleton of the structure [30]. The arch barrels are covered by backing up to varying heights, which increases the arches' load-carrying capacity by pre-stressing the masonry. The backing material is of either masonry or concrete. Lying on top of the backing, fill material is embedded between the spandrel walls and helps distribute the live load from the deck of the bridge. Fill material is usually made of stone rubble, remains of cut stones and earth material available near the construction site; thus, its properties vary significantly between different bridges.

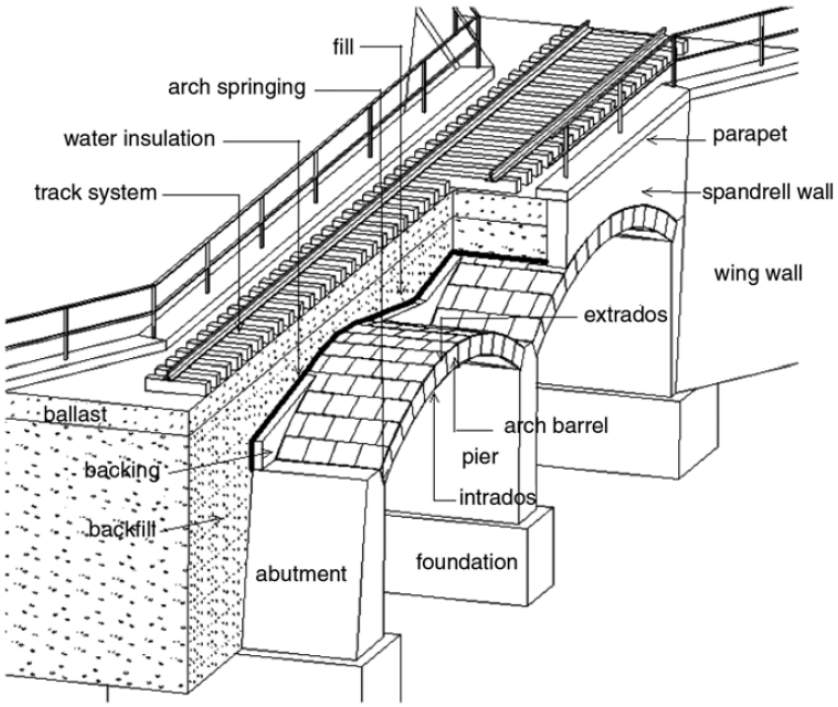

Figure 3.4. Typical structure of a double-span masonry arch railway bridge illustrating the bridge terminology (Adapted from [29]).

Located at the 360+292 km mark of the railway, Bridge 41 (shall be designated as the Bridge hereafter) lies between the modern Yıldızeli and Mentese stations, approximately 80 km away from the seismically very active North Anatolian Fault (NAF) line. Figure 3.5 shows the location of the bridge and the fault line. A German contractor constructed the Bridge. The bridge has four spans over a watercourse and access tracks with no skew, but it is slightly curved in plan. The spans are approximately 10 m, and the structure length and width are 59.3 m and 4.3 m, respectively. The maximum height from the bottom of the piers to the top of the spandrel is 10.7 m.

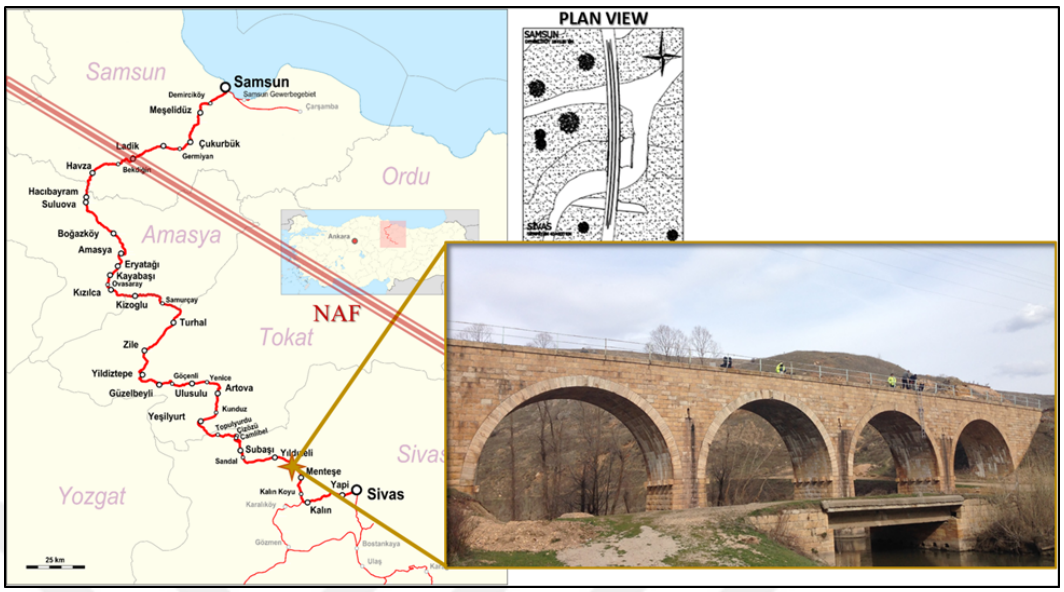

Figure 3.5. Location of the Bridge, plan view and North Anatolian Fault line.

ARUP-Istanbul Office provided the geometric description, on-site visual inspection results, material test results, and the geotechnical information. Drawings of the original design do not exist, as encountered in most situations. The accurate geometric description that is crucial in numerical modeling of masonry arch behavior was determined using 3D laser scanners. The thickness of the spandrel walls was measured 0.65 m at the top, but also visual inspection revealed that the thickness keeps increasing below the track level, making approximately 20 degrees with the vertical. This tapered spandrel shape has generally not been observed or has been ignored in the analysis of similar bridges, but it provides extra stiffness to the bridge.

The foundation of the Bridge 41 is not visible, and none of its parts could be inspected qualitatively. No detail is known about its construction or the bearing stratum. However, it was a general practice to construct masonry arch bridges on rock foundations or the timber piles bearing on a rock, and we expect this was the case here, particularly as the general condition of the foundation shows no signs of distress due to deterioration, defects, movement or settlement. The geotechnical report concerning the Bridge reveals the findings of three boreholes near the bridge location. The geotechnical engineers predicted the foundation level as a massive rock. Still, due to insufficient data, their conservative site classification named it weathered andesite

and marble with a minimum shear wave velocity (V_S) of 750 m/s. The boring logs and photos of the samples, shown in Figure 3.6, corresponding to the foundation level down to nine meters below confirm the assumption that the bridge was built on an approximately solid rock foundation.



(a) **(b)**

Figure 3.6. Borehole samples between (a) 12-17 m and (b) 17-21 m from the trackwork level.

The current condition of the bridge exhibits chronic problems attributed to structures with similar typologies: calcite accumulation due to drainage problems, black crust formation, and vegetation growth. On the other hand, no permanent deformation and damage were noticed during the visual inspection. Identifying the inner morphology of masonry arch bridges is a difficult task. In this case, the level of backing starts at three meters from the top of the spandrel, as determined on-site. Its composition is not known and might be either masonry or concrete. The backing was assumed to be of masonry because there were no traces of cementitious materials on the site, although it is plausible that concrete was used as a backing material since some of the bridges on the same railway were constructed with concrete. Fill material is similarly not known, and no sampling or testing was performed. Figure 3.7 illustrates the dimensions and morphology of the Bridge.

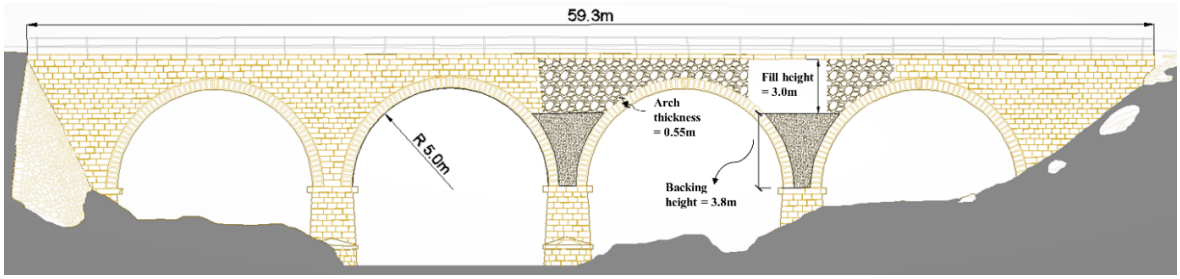

Figure 3.7. Dimensions of Bridge 41.

The materials of the Bridge were investigated using the available tests. A cubic stone sample with an edge length of 50 mm was analyzed via petrography and Scanning Electron Microscopy to determine its composition. The results indicate that this brownish-yellow stone type is limestone with 10-15% sand content. Point loading tests were also conducted on the two samples, and the results were extrapolated to the uniaxial compressive strength of 35.5 MPa. Finally, the specific gravity of the limestone was measured as 2.66 g/cm^3. The chemical composition of the mortar was determined and used to reproduce samples for testing the compressive strength of the natural hydraulic lime (NHL) mortar, which was found to be 1.2-1.9 MPa, and the tensile strength, which ranged between 0.5 MPa and 0.9 MPa. It should be noted, however, that these strength values belong to newly produced and cured samples whose conditions are entirely different from the old and weathered mortar of the Bridge.

There is no record of early repairs conducted on the Bridge, and site inspection revealed that there are no internal spandrel walls or ribs or a saddle over the arch barrels. Haunching at the supports was not observed, and the thickness of the arch seemed to be constant. It is not known whether a common pier construction technique – solid external masonry layer infilled with a lower grade material – was applied in the construction of this bridge. Internal morphology of the bridge parts and invisible defects such as cracks in the extrados of the arches or voids in the fill material cannot be revealed solely by visual inspection, and more sophisticated tools and methods are necessary. In that regard, various test techniques are available to obtain additional information. Although Destructive Testing (DT) is usually essential to define mechanical properties for analysis, DT results are affected by significant uncertainties, and they

only apply to those parts of the structure on which the tests are done. In order to add to its drawbacks, in the case of historical structures, permission to conduct DT is usually hard to obtain from historic preservation boards. Fortunately, Non-destructive Testing (NDT) can provide valuable information about the global condition and characteristics of the structure and its components, and may also supply further input for the numerical analyses [29].

3.3. Model Updating Study of Bridge 41

The experimental modal properties of the Bridge can be used to tune the analytical model after being identified. The common practice is to define various updating parameters in the FE model and check the sensitivity of the modal properties against the changes in the updating parameters so that the most sensitive parameters can be used in model updating, whereas the less sensitive ones are given fixed values to reduce computational cost. From that point, various methods with different degrees of complexity are available to the analyst for updating the FE model. For example, the Inverse Eigen-sensitivity method [31] is an iterative method that is widely used in aerospace and mechanical engineering. Another example is the method applied in this study, using an objective function that minimizes error, where the error is defined as the difference or length between the experimental and measured modal properties. In this method, a range is defined for each updating parameter, and then, all possible combinations of the updating parameters in their defined ranges are used to calculate the error. The combination that gives the minimum error is chosen as the updated FE model, and its parameters are defined as "updated parameters". Thus, in practice, this method scans all the subspaces of updating parameters and chooses the best combination.

Two objective functions that measure the difference between the experimental and analytical frequencies and mode shapes were defined, as Equation 3.1 and 3.2. Specific weighting coefficients were assigned to account for the modal contribution and

the level of uncertainty.

$$E_1(\theta) = \sum \left(k_i \cdot \sqrt{[\frac{f_i^* - f_i}{f_i^*}]^2} + h_i \cdot [1 - MAC_i]^2 \right) \tag{3.1}$$

where, θ is the updating parameters, i is mode number; k_i is the weighting coefficient for i^{th} modal frequency; h_i is the weighting coefficient for i^{th} modal assurance criteria; f_i^* is the measured modal frequency of ith mode; f_i is the simulated modal frequency of ith mode; MAC_i is the modal assurance criteria for i^{th} mode shape.

$$E_2(\theta) = \sum \left(k_i \cdot \sqrt{[\frac{f_i^* - f_i}{f_i^*}]^2} + 0.5 \cdot k_i \cdot [1 - MAC_i]^2 \right) \tag{3.2}$$

where the weighting coefficient is $k_i \in \{0.60, 0.15, 0.10, 0.05, 0.05\}$.

The first term in the objective function represents the difference between the measured experimental and analytical modal frequencies, while the second term gives the error in the mode shapes through the use of MAC values [22], which measures the correlation between two vectors.

The weighting coefficients in E_1 are the modal mass participation factors that are updated at each iteration. One problem associated with this approach is that the second mode has almost zero modal mass participation, thus almost no effect on the results. This might be stemming from a trivial reason, such as the modal vectors on opposite directions canceling out each other. However, second mode shape and modal frequency are some of the most reliable data obtained from the dynamic identification. Therefore, in order not to disregard the second mode, E_2 was defined such that the weighting coefficients were determined based on engineering judgment and the modal displacements obtained from the acceleration records. Also, the contribution of the mode shape term was decreased by half as the modal frequency estimation is done more reliably than the mode shape estimation in general [31].

After defining the methodology, the procedure was applied using SAP2000 OAPI that employs a MATLAB interface. First, the linear 3D FE model of the bridge was generated using SAP2000 software [32]. A macro-modeling approach that considers the masonry as a homogeneous and isotropic continuum element was employed. Solid elements were used to define the geometry of arch, spandrel, fill, and backing materials, as seen in Figure 3.8, reaching approximately 183000 degrees of freedom in total. Soil springs in three directions were assigned at the boundaries, and their limiting values were obtained from the literature [33]. As the model is linear and only an Eigenvalue analysis is required, no contact elements were defined between the spandrel and the fill materials.

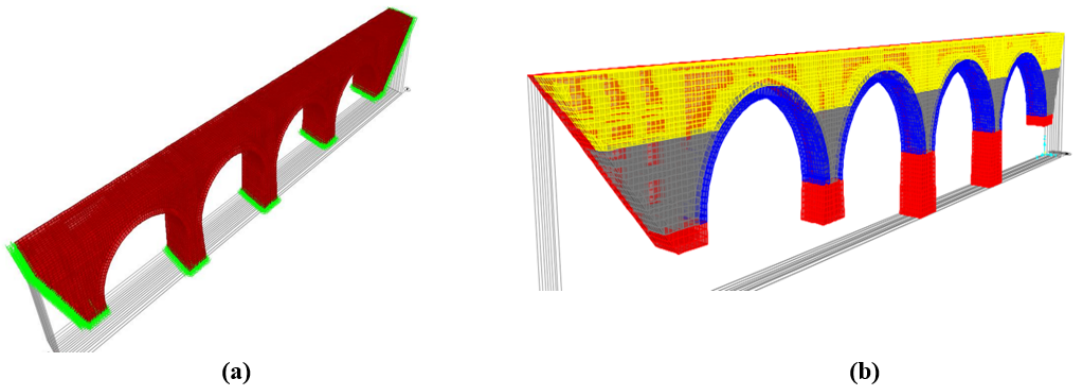

Figure 3.8. (a) FE Model of Bridge 41, (b) FE model of Bridge 41 with different material assignments.

The upper and lower limits of the material properties were assigned using the information given in Chapter 3.2 and similar practices in published studies. The range of the updating parameters, i.e., the Elasticity Moduli of the masonry (arch, spandrel, and the backing) and fill materials, were 2-15 GPa and 0.3-1.5 GPa, respectively. The numerical modal analysis was carried out after defining the necessary input. An in-house developed code transferred the numerical modal analysis results to MATLAB and matched with the experimental values by comparing the mode shapes. If any of the experimental modes cannot be found in the analytical results, then a penalty value is applied. Afterward, the error was calculated using the objective functions. This process was used until all the combinations were covered. Finally, the combination

of updating parameters that provided minimum error was selected and labeled as the "updated parameters". In the end, both error functions yielded very similar results. The updated modulus of elasticity for the masonry of spandrel walls and backing was determined as 6.2 GPa, whereas for the masonry arch it was 6.7 GPa and for the fill material 1.15 GPa. The specific weight of all the masonry elements was determined as 25 kN/m^3 except the masonry arch, whose specific weight is 25.4 kN/m^3. The comparison of analytical and measured frequencies and mode shapes can be seen in Figure 3.9, Figure 3.10, and Table 3.1 below.

Table 3.1. Comparison of analytical and measured frequencies and mode shapes.

	Measured frequencies	**Analytical frequencies**	$\mathbf{\Delta f = (f_a - f_m)/f_m}$	**MAC**
Mode #	$\mathbf{f_m}$**[Hz]**	$\mathbf{f_a}$**[Hz]**	**(%)**	
1	5.71	5.72	0.001	0.91
2	8.49	8.47	0.002	0.75
3	12.11	12.08	0.25	0.78
4	15.33	16.03	-4.67	0.80
5	18.45	17.34	-6.01	0.88

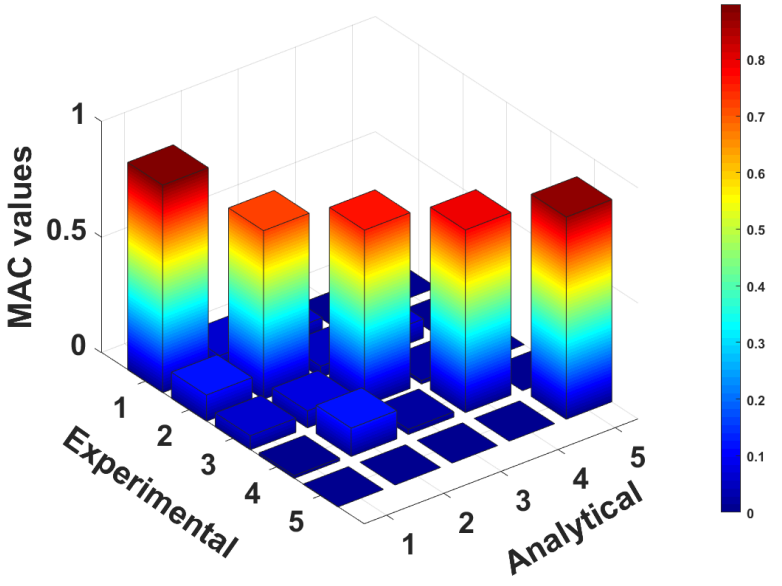

Figure 3.9. MAC matrix representation with a 3D bar chart.

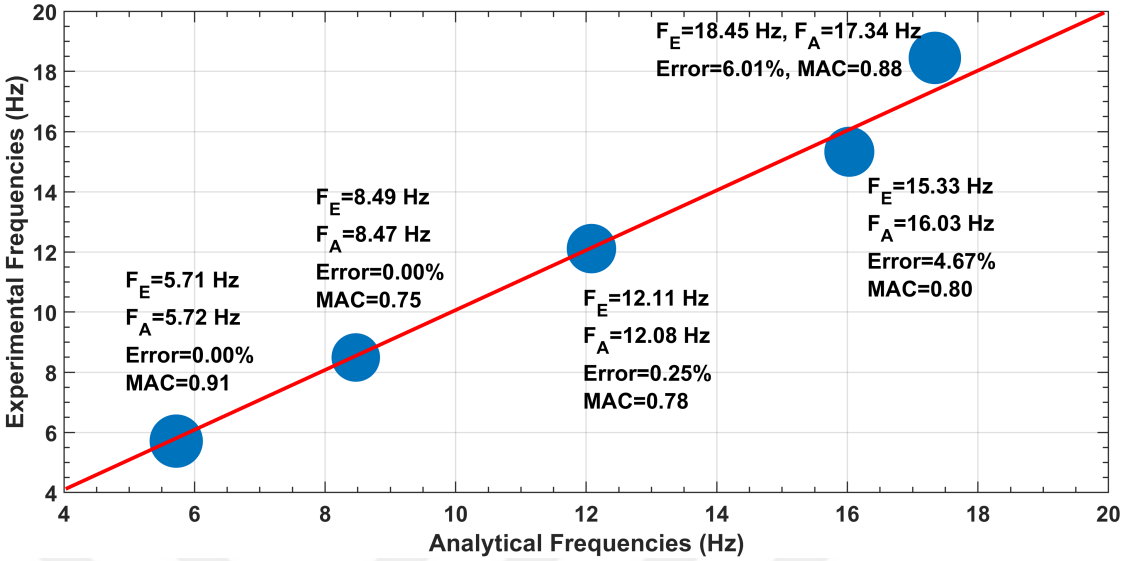

Figure 3.10. Frequency pairing between updated and measured data.

Modal analyses revealed interesting findings, such as the effect of soil springs on the modal analysis results is very significant. A possible explanation is that the ratio of the boundary to the total perimeter of the structure is much bigger in the case of masonry arch bridges compared to other building type structures. It was not possible to converge the analysis to the experimental results using reasonable values for modulus of subgrade reaction or modulus of elasticity of the masonry macro-elements. Analytical frequencies were much lower than the measured frequencies such that the subgrade reaction modulus or masonry elastic modulus had to be increased many folds to match the measured frequencies. Increasing the subgrade modulus too much causes the model to behave in the same manner as the case when the base of the bridge is restrained in all directions. Therefore, in conducting the analysis, the base of the bridge was fixed in the FE model. The only selected updating parameters are the Elasticity Moduli of the masonry for the arch, spandrel, and the backing and fill materials.

Possible explanations for assuming the base of the structural model as fixed boundary are as follows:

- Boundary conditions are very different between the masonry arch bridge and buildings. The ratio of the boundary to the total perimeter (or area) of the structure is much bigger in the case of masonry arch bridges; therefore, the effect

of boundary conditions is more significant.

- Soil investigation report provides the soil shear wave velocity as V_S=750 m/s and states that this value stays on the safe side because there is not enough data or experimental tests. A higher shear wave velocity can be expected, and the findings imply a rock type foundation.

- Scour has not been observed in any of the masonry arch bridges built in the same railroad. The engineers must have known about the scour problem in bridges. It is likely that they dug until the bedrock or used wooden piles to reach the bedrock, before constructing the foundation.

The model updating study shows that a detailed FE model is a must for accurate representation and model updating. Also, manual tuning is required before starting the iterations. As the FE model was very large and the range of values increased the iteration number, this method turned out to be very time-consuming. In this study, thousands of iterations were run because of the wide ranges of the parameters. Because this method may appear a self-contained and analytically opaque method, close inspection and evaluation of results after the analyses is a must for correct updating. In other words, the user experience is very important — a significant element of the methodologies outlined here. It must be acknowledged in this context that the limited extent of the investigations carried out on Bridge 41 resulted in a limited amount of information, which made the work of updating the model rather cumbersome.

Finally, close inspection of the error length reveals that the minimum values correspond to the same elastic modulus for the spandrel walls, whereas the change in elastic modulus of the fill does not have a significant effect. An example can be seen in Figure 3.11 below, where the troughs with the minimum error length correspond to the same elasticity modulus.

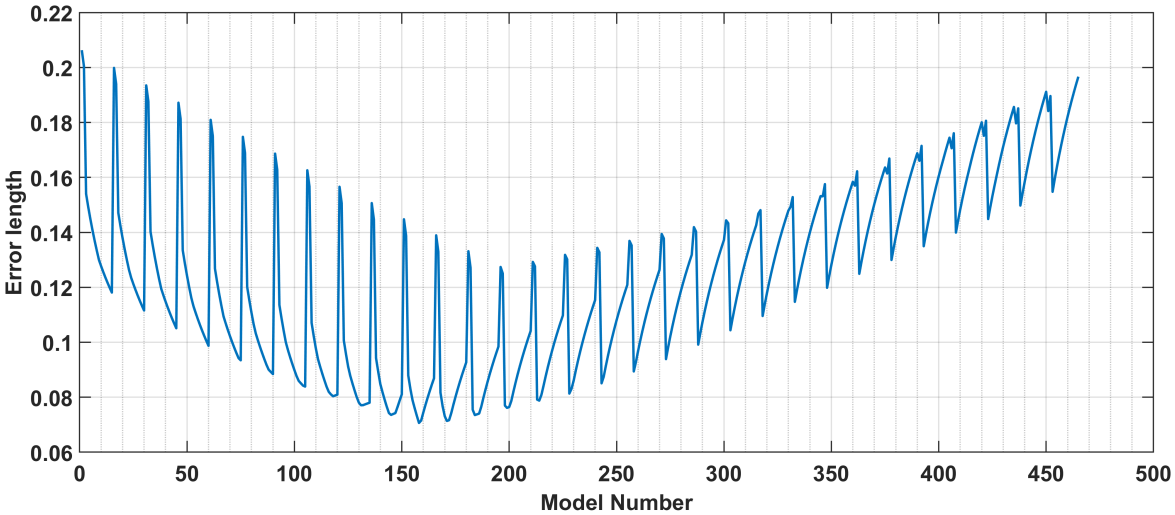

Figure 3.11. Error length obtained for each model (iteration).

4. NONLINEAR ANALYSIS

"Is the exact analysis of an approximate model good enough to qualify as an approximate analysis of the exact structure?"

Mete A. Sozen

Two essential steps in obtaining an accurate FE model are discussed in Chapters 2 and 3. This chapter presents the all-around aspects of the nonlinear analyses conducted in this thesis. The adopted modeling strategy is introduced first. Then the nonlinear structural model of the Bridge, generated using ANSYS v19.2 software [34], is presented. A sensitivity study is performed to observe the influence of the model parameters on the bridge behavior. Following this, a partial performance assessment of the structure is done using mass proportional pushover analysis. The complexity of the analysis method is increased afterward. Nonlinear dynamic analyses are performed using 14 real acceleration time-histories, scaled to the target design spectrum. The results of the nonlinear static and dynamic analyses are compared. Because of the significant differences observed, incremental dynamic analysis is performed. As the structural seismic assessment is performed using multiple methodologies, the chapter is concluded by evaluating and comparing the results to each other.

The force-displacement behavior of masonry is nonlinear, as observed from the tests conducted on masonry structures and masonry samples in laboratories. Generally, the structural response is non-proportional to the applied loading, even for simple loading cases. The material behavior depends on the current deformation state and deformation history. The focus of structural performance assessments of historic structures is often understanding the behavior of the structure in extreme conditions, finding the strength and stability of structures and the causes of structural failure. How much

load or deformation can the structure support before failure occurs? Are the structure's strength and stability compromised under progressive deterioration such as cracking and crushing? Our interest in these issues obliges us to use nonlinear modeling for the performance assessment of historic masonry structures.

Even though the necessity is evident and imperative, the nonlinear assessment of masonry arch bridges is a difficult task for several reasons, and there are no standardized or widely accepted procedures. Modeling and analysis of masonry arch bridge behavior require considerable information in terms of bridge geometry, morphology, materials, and behavior, which is often not possible to obtain within limited time and budget constraints. Moreover, several parameters may be affecting model behavior depending on the modeling strategy, but at this time, there is limited knowledge of and experience concerning such parameters and their effect on the overall structural behavior. Fortunately, research on masonry arch bridge characterization and assessment has increased significantly in the last twenty years, and future research will contribute to understanding masonry arch bridges' behavior and choosing the assessment method most suitable for individual cases.

It is possible to find limited examples of various work on masonry arch bridges in the literature. Amongst those which were devoted to the structural assessment of masonry bridges, Pela *et al.* [35] and Leprotti *et al.* [36] investigated the effectiveness of nonlinear pushover analysis and choice of the control point in conducting seismic performance evaluation. Oliveira *et al.* [7] carried out a comprehensive research about the effect of bridge geometry on the ultimate vertical load capacity of masonry arch bridges. Milani and Lourenço [37] examined the 3D nonlinear behavior of masonry arch bridges under eccentric vertical loading using a non-commercial FEM code. They highlighted the limitations of 2D hypotheses and the importance of transversal effects. Pela *et al.* [38] studied the comparison of nonlinear static analysis with an extensive set of nonlinear dynamic analyses corresponding to different excitation levels. Domede *et al.* [39] performed structural analysis employing an orthotropic damage model and highlighted the importance of taking the whole performance history of a masonry

structure when assessing its current state. Zampieri *et al.* [40] focused on the effect of bridge geometry and proposed a simplified seismic assessment method to determine seismic retrofitting strategies. Modena *et al.* [41] investigated specific problems in common arch bridge types and gave examples of the applicable retrofit strategies. Deng *et al.* [42] reviewed the causes and mechanisms of bridge collapse for various bridge typologies, including masonry arch bridges. Karaton *et al.* [43] and Aydin and Ozkaya [44] present case studies: Karaton investigates the nonlinear seismic performance of a 12th-century historical bridge under different earthquake levels via finite element modeling and nonlinear dynamic analyses, whereas Aydin and Ozkaya search for the vertical collapse loads of a single-span historical masonry arch bridge. Zampieri *et al.* [45] carried out research on the structural behavior of masonry arch bridges subjected to local pier scour. Pulatsu *et al.* [46] examined the behavior of masonry arch bridges under vertical loading using discontinuum analysis and observed the effect of soil infill properties on the strength of the bridges.

Some other research focused more on the experimental investigation and comparative numerical assessment of masonry arch bridges. Fanning and Boothby [47] is one of the first studies on 3D nonlinear FEM modeling of masonry arch bridges, and it presents test results of full-scale in-service bridges and the use of the test data in calibrating the FEM models to understand bridges' behavior. Aoki *et al.* [11] carried out a series of non-destructive, destructive, and dynamic tests to determine the dynamic properties of a long masonry arch bridge and utilized the results for a modal updating procedure. Brencich and Sabia [48] carried out various experimental tests on an 18 span masonry bridge in service conditions as well as throughout its demolition. They compared the results with the ones obtained from the FE analysis. Orban and Gutermann [29] presented non-destructive methods for inspecting and testing masonry arch railway bridges. They state that in-situ load tests are especially useful in providing valuable information for structural analysis and assessment. De Felice and de Santis [49] worked on the experimental and numerical behavior of brick masonry under eccentric vertical loading, simulating the piers of historical masonry arch bridges in Italy. Helmerich *et al.* [2] proposed a methodology for the assessment of European masonry arch bridges,

comprising multiple non-destructive and minor destructive testing and subsequent FE modeling. Pellegrino *et al.* [50] investigated the seismic performance of a vast number of existing bridges and highlighted the contribution of in-situ and laboratory testing to the assessment. Costa *et al.* [10] performed an operational modal analysis of three different masonry arch bridges and subsequent numerical model updating. Sarhosis *et al.* [51] conducted an extensive review of experimental tests and assessment methods for masonry arch bridges, pinpointing important aspects of bridges' behavior. Conde *et al.* [52] implemented a series of non-destructive testing techniques on a historical bridge and used the results to feed the 3D FE model, which was then utilized to assess the bridge's performance under vertical and seismic loading.

4.1. Modeling Strategy and Material Properties

Roca *et al.* [53] and Lourenço [9] present a comprehensive review of computational strategies for historical masonry structures, while Proske and Gelder [54] and Reccia *et al.* [55] also provide overall aspects and methods of masonry bridge analysis. Different methodologies to predict the behavior of masonry arch bridges and several procedures have been developed and applied in the last 25 years. There are various modeling strategies of different complexities available to the analyst: from more straightforward limit analysis to more complex Finite Element and Discrete Element analyses. All of them have advantages and shortcomings, and each may be preferred over to one another in different cases. Simpler methods, usually leading to more conservative results, often underestimate the load-carrying capacity. This may result in unwarranted or uneconomical structural strengthening applications or even complete replacement of bridges. Conversely, advanced and more sophisticated methods usually suffer from the difficulty of providing the necessary input parameters and from the associated computational cost. They may as well overestimate the bridge capacity and jeopardize safety. The choice of the modeling technique will probably lead to different results depending on the adequacy of the numerical tool and the information sought. The best method might be defined as that which reliably provides the information sought while minimizing error and cost [56]. Therefore, different strategies can be utilized

depending on the aim of the analysis and the experience of the analyst.

In this study, Finite Element analysis with a macro-modeling approach was used. In the macro-modeling approach, the units of masonry, i.e., stones and mortar, are homogenized into the material and smeared out in an equivalent continuum, whereas the mechanical properties of the masonry are either determined by experimental tests or derived through homogenization techniques. The other possibilities would have been to use a micro-modeling technique, where masonry units and their interface are modeled separately, or a simplified micro-modeling technique, in which the stones are modeled separately while the mortar and stone-mortar interface are smeared together between the stones. These modeling approaches are illustrated in Figure 4.1. The macro-modeling technique has some limitations, such as the assumptions of isotropic and continuum material, which do not reflect the heterogeneous anisotropic composite nature of masonry. Also, the results heavily depend on the accuracy of the constitutive models, on the material parameters and boundary conditions, and the numerical problems related to mesh dependency [51]. Nevertheless, this approach is more practical for the analysis of large and complex structures when compared to the other methods, since the nonlinear analysis of the selected masonry arch bridge would not be possible due to computational power limitations [57].

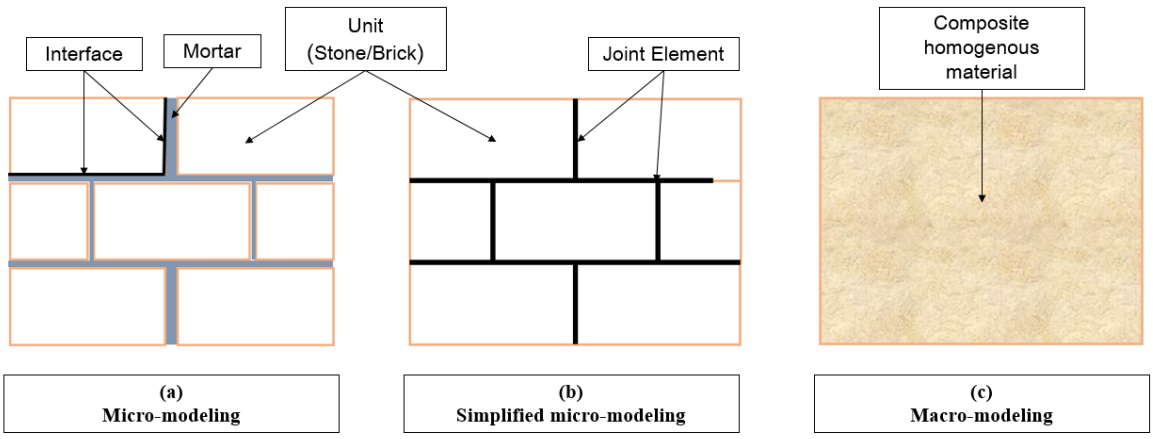

Figure 4.1. FE modeling approaches for masonry structures.

Simplified 3D isotropic nonlinear constitutive laws, with a need to define only a few parameters like modulus of elasticity, compressive and tensile strength, and Poisson's ratio are incorporated in practical studies using FE macro-modeling technique. Nonetheless, these simplifications are indispensable when it comes to the safety evaluation of historical masonry arch bridges, especially because seismic safety assessment cannot be accomplished without taking into account the behavior of masonry in the post-peak regime [58]. The macro-modeling technique has thus been widely utilized in the analysis of masonry structures and is known to perform well [9, 47, 59–61].

After deciding the type of technique to be used, material properties were determined based on available information and published studies. In the absence of operational modal analysis and subsequent model updating, a common approach would be to use the composite material properties of masonry found from the homogenized material properties of masonry units. For example, the masonry compressive strength can be found using the compressive strength of the stone and the mortar in empirical exponential models, as represented in Equation 4.1. Such models are recommended in various literature and standards, including Eurocode 6 Part 1 [62]. However, we followed an inverse methodology as the available data regarding the masonry units was not complete or reliable. Having found the elastic modulus of masonry, the relationship given in EN 1996-1-1 as $E_{mas} = 1000 \cdot f_{c,mas}$ was used to determine the compressive strength of the masonry. Masonry tensile strength in the literature ranges between 5-20% of its compressive strength; therefore, it was taken as 13% of the compressive strength in this study. This, by chance, corresponded to the tensile strength of the newly produced and cured mortar in the laboratory, as stated before. Specific weight (γ) and the Poisson's ratio (μ) of the masonry were calculated by making use of Equations 4.2 and 4.3.

$$f_{c,mas} = K \cdot f_{c,st}^{a} \cdot f_{c,mo}^{b} \tag{4.1}$$

$$\gamma_{mas} = \gamma_{st} V_{st} + \gamma_{mo} V_{mo} \tag{4.2}$$

$$\mu_{mas} = \mu_{st} V_{st} + \mu_{mo} V_{mo} \tag{4.3}$$

All the different parts of the bridge, the spandrel walls, piers, backing, arches, and the fill were modeled with material properties assigned to their specific geometry, as shown in Figure 4.2a. Mechanical properties of the masonry were assumed to be the same for spandrel walls, piers and backing masonry elements whereas the masonry arches' mechanical properties were set as different from the rest due to the different volumetric ratios of stone and mortar and the apparent superior quality of the stones used in the arches. Volumetric ratios were evaluated using available geometrical information and engineering judgment. Poisson's ratios of the stone, mortar, and backfill were determined based on existing literature on masonry arch bridges. Material properties for the materials used in the FE model are summarized in Table 4.1.

Table 4.1. Summary of the material properties.

Material Property	**Masonry Arch**	**Masonry Elements**	**Fill**
Modulus of Elasticity, E	6.7 (GPa)	6.2 (GPa)	1.15 (GPa)
Compressive strength, f_c	6.7 (MPa)	6.2 (MPa)	1.2 (MPa)
Tensile strength, f_t	0.88 (MPa)	0.80 (MPa)	0.10 (MPa)
Volumetric ratio, V_{st}/V_{mo}	0.93/0.07	0.89/0.11	N/A
Specific weight, γ	25.4 (kN/m^3)	25.0 (kN/m^3)	19.0 (kN/m^3)
Poisson's ratio, μ	0.22	0.22	0.27

For the boundary conditions of the bridge, "compression-only support" was used in the vertical direction, whereas the movement was restrained on the transverse and longitudinal directions. Compression only support in ANSYS applies compression only constraint normal to the face selected. It is modeled internally using asymmetric rigid-flexible contact. A rigid target surface is constructed and mirrored from the scoped face of the compression-only support. Therefore, normal contact stiffness is important for nonlinear convergence. A very high value of normal contact stiffness was assigned in this case so that the support allowed no vertical displacement in compression, but there was also no resistance in tension. The compression only support type is only supported with solid elements in ANSYS. The 3D FE model used has approximately 393000 degrees of freedom and a sophisticated mesh with refinements at the critical regions of the structure, as displayed in Figure 4.2b.

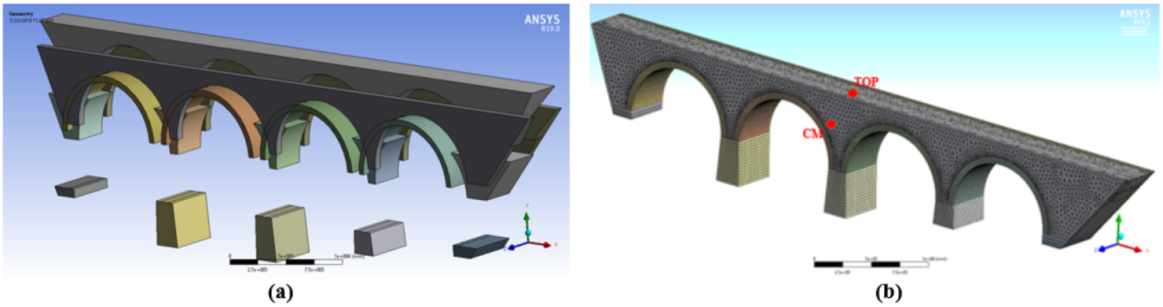

Figure 4.2. (a) Parts of the FE model, (b) FE mesh of the model.

4.2. Modal Analysis

Once the model geometry is generated, the material properties are assigned, and the boundary conditions are set, linear analysis is very useful in determining how the structure behaves and if there are any significant problems with the FE model. To this end, modal analysis was performed to ensure the model worked properly, and the dynamic properties of the structure, seen in Figure 4.3, matched with those obtained from SAP2000 software during the model updating phase. The results show that they match very well with the SAP2000 model results and that the model represents the structure- in the linear range, accurately.

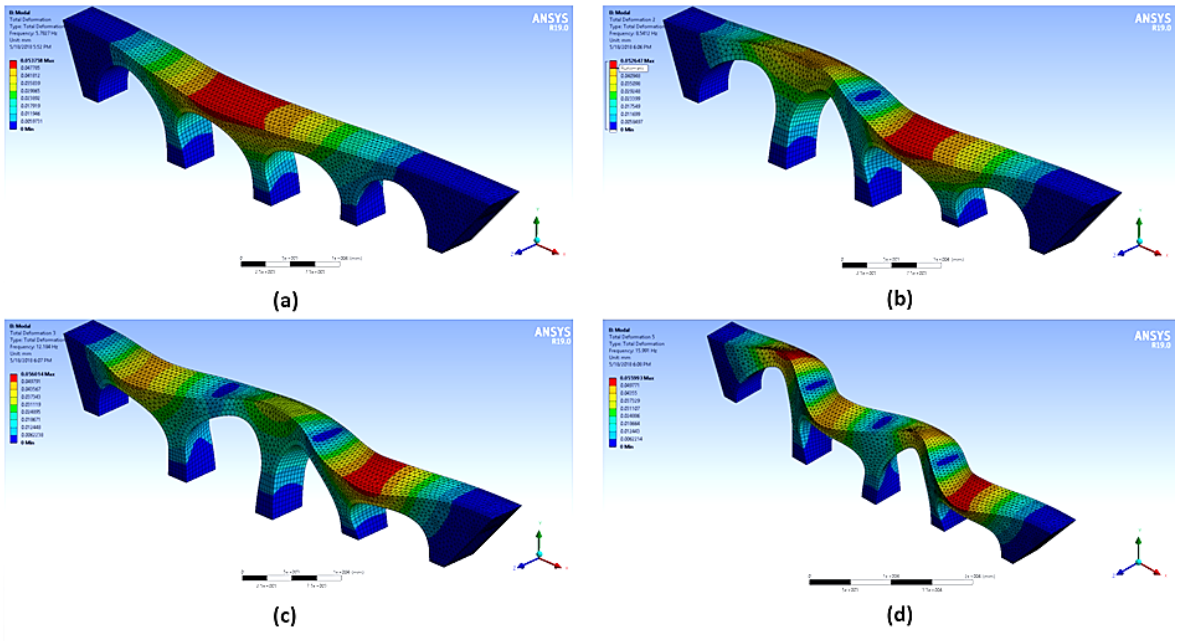

Figure 4.3. From (a) to (d): the first four out-of-plane modes of the FE model.

4.3. Nonlinear Model Properties

The nonlinearity was introduced to the model step-by-step, after the linear model was successfully working, in order to have control over the model response.

4.3.1. Frictional Contact Elements

The 3D models capture the transverse effects and are thus indispensable to compare the actual behavior of masonry bridges with numerical results. These transverse effects include longitudinal cracking in the arch barrels, the transverse deformation of the arches during seismic events, soil pressure of the fill on the spandrel walls, and confinement effect of the spandrel walls. Such effects require the softer and lighter fill material to slide or move relative to the stiffer and denser masonry spandrel and arches without generating significant tensile stresses at the interfaces between these materials. For this purpose, frictional contact elements were used in the nonlinear analyses. These elements were specifically necessary because the vertical loading — including the dead load of the structure itself — introduced at the initial stage of the analysis, creates tension in the masonry elements, which in turn results in early convergence problems due to the low stiffness of the fill material compared to the stiffness of masonry material [47]. However, in reality, the fill must have been constructed in layers of a certain height with compaction of each layer afterward; thus, clearing away any possibility of differential deformation in the bridge body due to self-weight. This artificial phenomenon was also prevented in the model by applying frictional contact surfaces at the interfaces of the fill material with the arches, spandrel walls, and backing. An example illustrating the frictional contact between the spandrel and fill is presented in Figure 4.4 below.

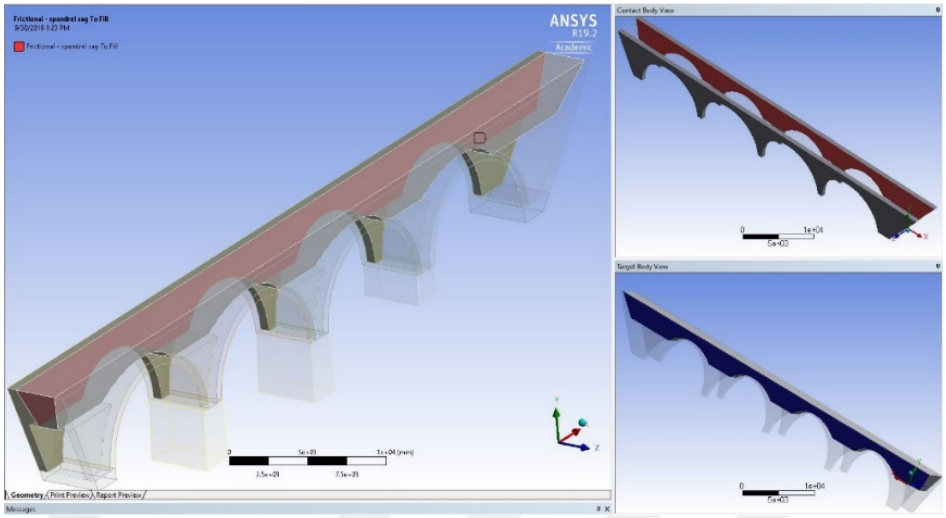

Figure 4.4. Example figure showing the frictional contact between spandrel and the fill.

The parts do not interpenetrate when frictional contact is defined between two bodies. Contacts transfer compression force, perpendicular and tangential friction forces, but have no tensile strength, and thus, the tensile forces are not transferred. Moreover, frictional contact implies changing-status nonlinearity, i.e., the system stiffness changes depending on whether parts are touching or not. In frictional contact settings, contact elements follow the behavior defined by the Coulomb friction model with a slight modification, as shown in Figure 4.5. The two contacting geometries can carry shear stresses up to a certain magnitude across their interface before they start sliding relative to each other. This state is known as "sticking". The model defines equivalent shear stress at which sliding on the geometry begins as a fraction of the contact pressure. Once the shear stress is exceeded, the two geometries will slide relative to each other. Thus, the friction force stays constant as long as the normal force also does. The cohesion value can be defined, but its default value is zero. The coefficient of friction can be given any non-negative value, but its value for the nonlinear analyses of Bridge 41 is unknown [63]. Limited examples from published studies [47, 60, 64, 65] point to its value as ranging between 0.4-0.5. The benchmark value of the friction coefficient was therefore decided as 0.4.

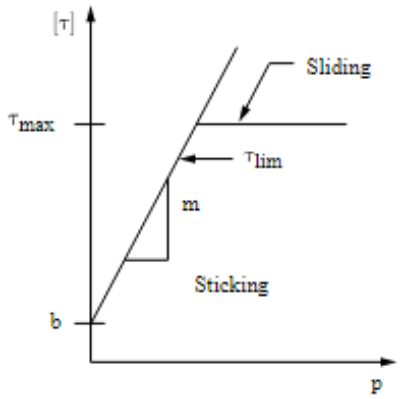

Figure 4.5. The friction model [63].

4.3.2. Nonlinear Materials

All of the materials defined in the FE model of the Bridge possess nonlinear material properties. Although we know that the material model for masonry is not bilinear isotropic (or elasto-plastic) but rather has a softening behavior after cracking and crushing, the testing of material property input in the FE model is essential. It can be done by first testing the material behavior on a simple model. In that sense, the bilinear isotropic material model is simpler and allows the user to assess the problems with the nonlinear model and to observe the trend in nonlinear behavior. Therefore, this approach – using elasto-plastic material and pushover analysis, can be considered as a preliminary assessment. Figure 4.6 below displays the maximum principal stress plot after the pushover analysis. It shows that nonlinearity occurs at the arches and the spandrel walls, and the failure is expected to occur due to the nonlinearity in these elements.

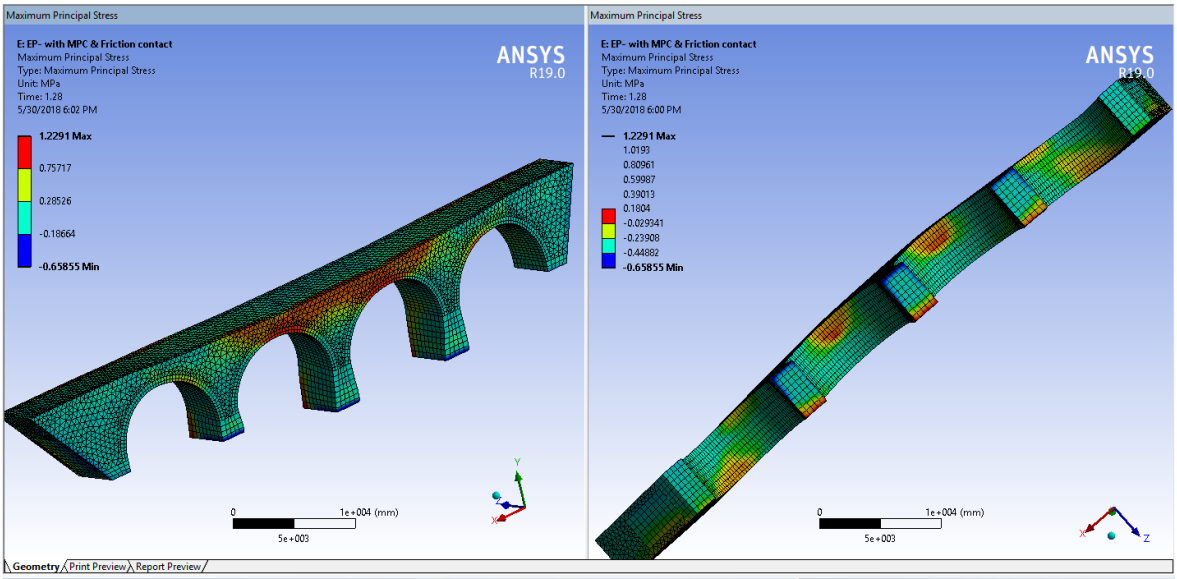

Figure 4.6. The elasto-plastic nonlinear behavior and tension yielding in the spandrel wall.

Defining a constitutive relation for the 3D nonlinear anisotropic nature of the masonry is possible in principle, but its reliability is compromised in the absence of those tests required for a large number of input parameters. Tests to obtain such parameters like Poisson's ratios, elastic moduli, parameters required for the limit domains, and the post-peak response can still not be performed for most bridges in practice [48]. Therefore, resorting to simplified constitutive models that require only a few parameters to be defined is a common approach employed in most 3D FE modeling applications. Knowing that the behavior of masonry has a significant stiffness degradation after cracking and crushing, Solid65 elements defined in ANSYS Element Library were used to model the masonry behavior.

Explicitly developed for concrete material in the ANSYS platform, the Solid65 element is used for 3D modeling of solids and is capable of cracking in tension and crushing in compression. The element is defined by eight nodes having three degrees of freedom at each node: translations in the nodal x, y, and z directions. The element allows for cracking in three orthogonal directions at each integration point, and if cracking occurs at an integration point, the cracking is modeled through an adjustment of material properties that effectively treats the cracking as a "smeared band" of cracks,

rather than discrete cracks. The material is assumed to be initially isotropic [63]. Stress-strain relations are determined from a coordinate system parallel to principal stress directions and perpendicular to the crack face. Figure 4.7 depicts the stress-strain relationships defined for the masonry material in this study.

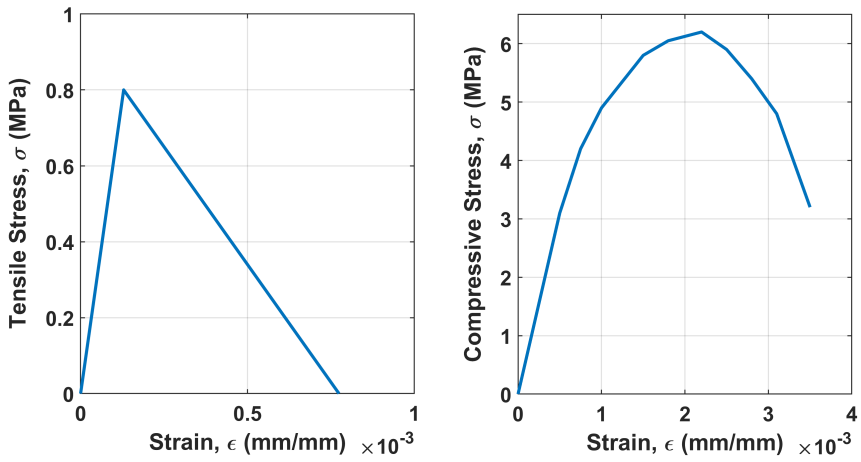

Figure 4.7. (a) Tensile stress-strain, and (b) compressive stress-strain diagrams for the masonry material.

A smeared crack concept considers the cracked solid to be a continuum and allows a description in terms of stress-strain relations. It offers a variety of possibilities, ranging from fixed single to fixed multidirectional and rotating crack approaches. These approaches differ from each other in terms of the orientation of the smeared crack, which is either kept constant, updated in a stepwise manner, or updated continuously. The Solid65 element uses the multidirectional crack model, which is an extension of the fixed-crack model and incorporates sub-decomposition of the crack strain into the separate contributions from a number of multi-directional cracks that simultaneously occur at a sampling point [66]. It is possible to guess the significance of the multi-directional crack model, as it overcomes the restraints posed by the fixed-crack model, in case of biaxial and triaxial tension and the tension-shear conditions, which are typical of fracture/crack propagation problems. On these occasions, the fracture starts in tension and proceeds in tension-shear. Thus, such behavior indicates that the axes of principal stress rotate after crack formation, leading to an increasing discrepancy between the axes of principal stress and fixed crack axes. The multi-directional crack

concept provides an alternative to this problem: whenever the angle of inclination between the existing crack(s) and the current direction of principal stress exceeds a certain threshold value, a new crack is initiated in a system of non-orthogonal cracks. The Smeared-crack approach is known to be mesh sensitive. Therefore, a sensitivity analysis is recommended.

A failure surface, as shown in Figure 4.8b (where the axes represent the ratio of compressive stresses to the strength in three orthogonal directions), determines the cracking or crushing of the masonry. Depending on the direction of the principal stresses, cracking or crushing occurs when the failure surface is surpassed. The failure surface for the Solid65 element is based on the William-Warnke failure criterion [67], which depends on five material parameters. In most practical cases where the hydrostatic stress is limited to $\sqrt{3}$ times the uniaxial compressive strength (f_c), the failure surface is defined using only the uniaxial tensile (f_t) and compressive strength of masonry [68]. A maximum tensile stress criterion describes the tensile failure. The material behavior is linear elastic until tensile failure and follows a nonlinear path until the compression failure. When the failure surface is reached in cracking condition, the stress-strain relations are modified by introducing a plane of weakness in a direction normal to the crack face. The stiffness normal to the crack face becomes zero. In the case of crushing, it is defined as the complete deterioration of the structural integrity of the material (e.g., material spalling). Under conditions where crushing has occurred, material strength is assumed to have degraded to an extent such that the contribution to the stiffness of an element at the integration point in question can be ignored [63]. This makes the softening branch of the compressive stress-strain curve defined in Figure 4.7b irrelevant. Also, until the crushing, the unloading stiffness is equal to the elastic state of the material because there is no damage formulation in this model. Alternatively, Drucker-Prager plasticity could have been defined for softening behavior.

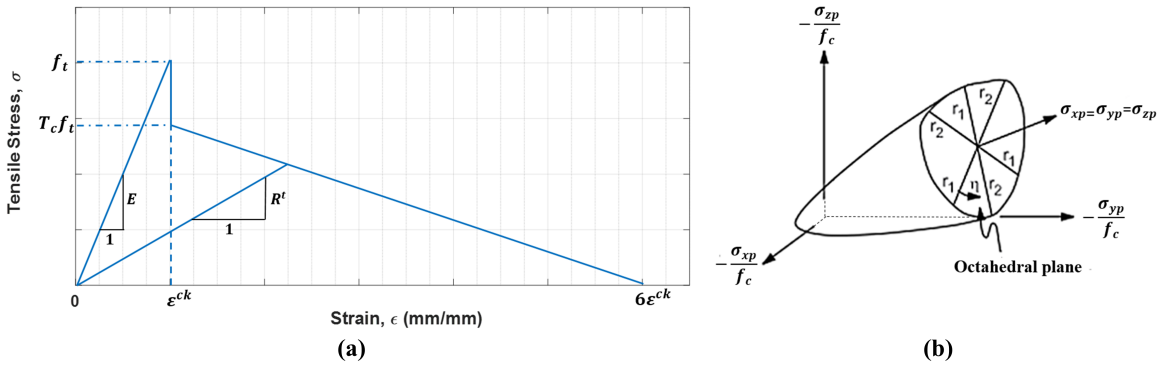

Figure 4.8. (a) Strength of cracked section, (b) 3D failure surface in principal stress space [63].

Information related to the shear transfer coefficients are required in addition to the stress-strain data, uniaxial tensile strength, and uniaxial compressive strength, to complete the material definition. Two shear transfer coefficients, one for open cracks (β_t) and other for closed ones (β_c), are used to consider the retention of shear stiffness or shear strength reduction in cracked concrete/masonry. Typical shear transfer coefficients range from 0.0 to 1.0, with 0.0 representing a smooth crack (complete loss of shear transfer) and 1.0 representing a rough crack (no loss of shear transfer). In the current study, shear transfer coefficient values were determined based on the literature examples [64,68], and considered as 0.3 and 0.8 for β_t and β_c, respectively. Similar material models are available in various FE software, especially for concrete-like materials. For example, Bertolesi *et al.* [69] used ABAQUS software and the Concrete Damaged-Plasticity model with Drucker-Prager tension softening, while Scheibmeir [58] investigated the effects of using different models such as "multidirectional fixed-crack" and "total strain rotating crack" models in DIANA software.

Apart from the masonry material definition, the Drucker-Prager constitutive model is the most commonly used material model for the soil type infill materials in masonry bridges. However, in this study, the bilinear isotropic (or elasto-plastic) material model is used for the fill material. The behavior is very similar to the Drucker-Prager model, but instead of cohesion and internal angle of friction values, only the strength values were needed for the model. Its tensile and compressive strength (0.1

MPa and 1.2 MPa, respectively) were determined based on the literature examples and using engineering judgment.

4.3.3. Nonlinear Solution Controls

Nonlinear analysis is an iterative solution because the relationship between load and response is not known beforehand. ANSYS uses the Newton-Raphson algorithm to obtain a converged solution. The algorithm works well with a smooth changing stiffness, but if there is a contact or softening region in the material model, it may become difficult to obtain convergence. There are various types of algorithms available to the user. The standard Newton-Raphson method works effectively in most cases, but it is not necessarily the most economical solution method and does not always provide rapid and reliable convergence. Modified Newton-Raphson method can provide more rapid and better convergence than the standard one in specific cases [70]. Asymmetric Newton-Raphson method might also be useful in various cases, especially when the Solid65 elements are used because the cracking and crushing damage results in an asymmetric stiffness matrix. The computational expense and the divergence problems due to specified increment size may be considered as the weaknesses of the Newton-Raphson method. Nonetheless, in ANSYS, it is possible to improve the convergence using "line search" and "stabilization" algorithms. Line search is particularly useful for problems involving rapid changes in tangent stiffness, such as cracking of the masonry. In this study, the Modified Newton-Raphson method with a line search algorithm was used. Stabilization was not used because the Solid65 elements do not support this option.

Substep sizes or time-step increments were determined considering the balance between the analysis duration, output size, and the stability of the results. They will be mentioned in the related sections of the nonlinear analysis results.

4.4. Model Verification and the Issues Raised

The most critical aspect of any numerical modeling is the model verification. Ideally, the underlying theory, assumptions and the modeling parameters that govern the model behavior should be verified by comparing the numerical behavior with the actual phenomenon observed on site. Load testing may be useful for model verification, but it is often not possible or feasible to do it in remote sites. Another approach can be simulating the damage and defects observed in the real structure. If the numerical model can predict the observed phenomenon under pre-determined effects, then the reliability of the model may be assured. In our case, neither of these two approaches was possible. Verification of the linear behavior was possible using dynamic identification and model updating, but in the absence of the damage, the nonlinear behavior could be checked only by using engineering judgment and the model's ability to perform the expected behavior. The expected behavior is based on the observation of damaged and collapsed masonry arch bridges. Earthquakes may cause damage in the spandrel walls, as observed after the 1997 Umbria and Marche earthquake in Italy [71] or the 2001 Bhuj earthquake in India [72]. Damage in the arches, arch support systems (springing) and piers are expected to cause a partial or total collapse of the bridges, as observed in 2008 during the Wenchuan earthquake in China [73]. Diagonal or transverse cracks may be observed in the piers, and Figure 1.3 displays this type of damage. Notice that all of these damage types are captured by the FE model of the Bridge and observed during the nonlinear analyses.

Last but not least, we would like to highlight the two issues with FE macro-modeling of masonry arch bridges, which were put forward by Brencich and Sabia [48]. The first one relates to the definition of mechanical properties of the materials and their assigned values. The masonry macro-elements are defined as isotropic and homogenous materials, but the elastic modulus is defined as a local parameter in continuum mechanics. Therefore, the elastic modulus of a macro-element represents the average deformability of the continuous medium, not the individual stones or mortar. So, how many units of stones and mortar should a macro-element include, and what should be

the corresponding mesh size? Also, can the properties of a macro-element be extended to the whole bridge? That brings us to the second issue: the variability of the test results and the material properties. Owing to the difficulties related to testing the whole structure, material properties found from the local tests are often considered to be representative of the remaining parts. This common practice in masonry bridge assessment remains doubtful since the type and quality of materials used for the abutments, arch barrels, spandrels, and backfill can be highly variable. Moreover, different tests applied to the same part of the bridge often give distinct results. Then, which is the reasonable modulus of elasticity value to be used?

If we stipulate that the global behavior of the structure is sought rather than the local mechanisms, and the local tests are supported with the global tests such as Operational Modal Analysis (experimental dynamic identification), these two aforementioned issues might be condoned for the sake of the structural assessment of the masonry arch bridges. The approach adopted in this research complies with the two under-arching principles of engineering emphasized by Mete Sozen, in a presentation titled "Rehumanizing Engineering". They are *i*) *"difficult things must be made simple"*, and *ii*) *"a good solution with today's science, tools, and materials is better than a perfect solution next year or even next week"*.

4.5. Nonlinear Static Analysis

In this section, nonlinear static analyses (NSA) of the Bridge are conducted and several topics are investigated. The Mass-Proportional Pushover (MPP) analysis method is used; therefore, the method is introduced first. The assumptions and the restrictions of the method are underlined. Then, it should be stated that all the properties and parameters outlined so far affect the results of the nonlinear analyses to a certain extent. Therefore, a sensitivity analysis is carried out for the elastic modulus and tensile strength of the masonry, the elastic modulus of the fill, the coefficient of friction for the frictional contacts, and the shear transfer coefficients of Solid65 elements. The sensitivity of the results to these parameters is tested using nonlinear static

pushover analyses. Further, using the benchmark model, the MPP analysis is carried out in the transverse direction of the Bridge, and a partial performance assessment is done. Finally, the MPP analyses are applied in a combination of the horizontal and vertical directions, and their effects are discussed.

Please note that the term "failure" that is mentioned in this chapter represents the physical conditions that the author considers as a failure, and not the non-convergence of the numerical model, as the numerical convergence is significantly affected by several factors. There might be more displacement capacity until the physical failure, but numerically, further spreading of the plasticity is not found physically meaningful. It might be argued that the model can be improved more by playing with the analysis and nonlinear controls of the model, but there should be a compromise between the level of the detailed analysis and the expected physical behavior of the structure.

4.5.1. The Methodology

Pushover analysis incorporates the application of a load/ or displacement pattern to an element/ or system incrementally, enabling the user to draw a continuous picture of the behavior from the elastic region to the collapse. Nonlinear static analysis procedures such as N2 method [74], capacity spectrum method, and the displacement coefficient method [75] usually combine the pushover analysis of an MDOF model with the response spectrum analysis of an equivalent SDOF system. Those procedures are often preferred to nonlinear dynamic analysis (NDA) in the evaluation and design processes, especially for regular building type structures, because of their simplicity and efficiency. Nevertheless, when using NSA methods, it should be kept in mind that those approximate procedures are subject to several limitations. For example, the selection of the lateral load is a crucial step as pushover analysis is based on a time-independent displacement shape assumption. Using the first mode shape as the pattern of lateral forces may be inaccurate for asymmetric and complex structures, or for the structures where higher mode effects are dominant. Moreover, the inelastic demand spectra used are not appropriate in the case of near-fault ground motions, soft soil sites, and hys-

teretic material behavior with significant strength and stiffness degradation – which is the case for unreinforced masonry material. Finally yet importantly, the results of the NSA procedures are intended to represent the mean values for the applied earthquake loading, but they usually scatter from the mean considerably. Therefore, the analyst must be aware of the limitations and drawbacks of the methods while exploiting their advantages.

N2 method is a well-known nonlinear static analysis procedure proposed by Fajfar [74] along with similar procedures in FEMA 356 and ATC 40, and the details can be found there. However, it is important to note that the selection of the lateral load distribution is an important step within the pushover analysis, and no unique solution exists. Any reasonable shape can be used, and this leads to another variation of the procedure, namely the Mass Proportional Pushover analysis [76]. The total seismic mass distributed to the structure at the floor and roof levels is used in MPP analysis. As the mode shape (ϕ) of the structure, the linear-elastic displacement vector obtained by applying the force on the structure is used. In the MPP procedure, the total mass, M, is used in converting the pushover base shear force of the structure, V_b, to the SDOF acceleration, A.

$$A = \frac{V_b}{M} \tag{4.4}$$

Note that using the total mass in the conversion is consistent with the lateral force distribution in the proposed procedure. The SDOF displacement, D is given by:

$$D = \frac{U}{\Gamma} \tag{4.5}$$

where the participation factor Γ, which controls the transformation from MDOF to the SDOF model and vice versa, is calculated as:

$$\Gamma = \frac{\phi^T M 1}{\phi^T M \phi} \tag{4.6}$$

These procedures are all developed and verified for plane frame structures with lumped masses, but also widely used for structures with distributed mass. Therefore, the question remains as to how the transformation of a 3D masonry arch bridge with distributed mass should be configured. What should the lateral displacement vector and the corresponding participation factor be? The method proposed here is to discretize the mass of the structure and obtain the displacement vector from the lateral displacements of the discretized masses along the height of a line drawn from the base to the top of the bridge. Accordingly, in this analysis, the Bridge was discretized in the same way as its finite element model, i.e., base, backing, arch, spandrels, and fill material. If it were a discretized 2D system, then the loading would look like that portrayed in Figure 4.9 below. However, note that the analysis was conducted in a 3D distributed mass system.

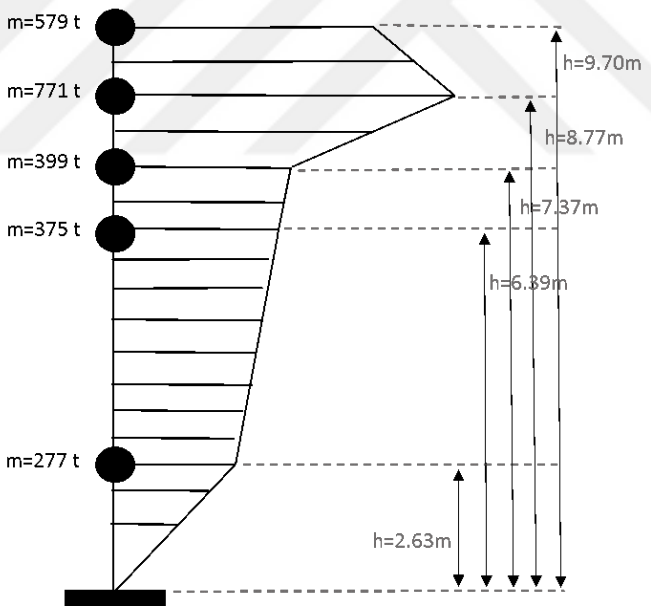

Figure 4.9. Hypothetical load distribution in 2D.

The information above is then used to find the modal participation vector, Γ, and the acceleration and displacement response of the equivalent SDOF system. Finally, the acceleration and displacement response of the SDOF system and the elastic demand spectrum are used to obtain the "performance point", which is transformed back to the physical space to determine how much displacement a particular node will undergo during the design level earthquake.

Pushover curves, i.e., the acceleration-nodal displacement data sets, can be obtained for different control points. The work of Pela *et al.* [35] and Leprotti *et al.* [36] indicate that the results are more conservative, and the method is easier to apply when the center of mass (CM) node is selected as the control point. In this study, the control point was selected as the center of mass or the top displacement of the MDOF system (TOP), which can be seen in Figure 4.2b. The graphs obtained using both approaches are indeed different, as can be seen in Figure 4.10.

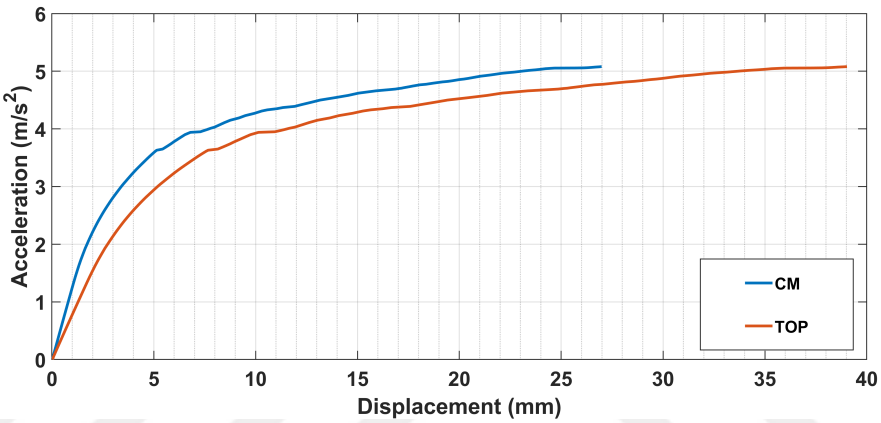

Figure 4.10. Pushover curves obtained using the CM and TOP control points.

Also, there is no degradation or negative slope in the presented PO curves because a force-controlled loading is used, i.e., the force keeps increasing, and the corresponding displacements are obtained.

4.5.2. Sensitivity Study

Nonlinear static analysis of Bridge 41 required many variables about which there is no existing information available. Therefore, it was intended to conduct parametric studies for some variables and observe how the results change. In conducting these analyses, all other parameters were set to their benchmark values presented in Table 4.1 and Chapter 4.3, while the sensitivity to one specific parameter was investigated. All of the figures used for PO curve comparison are drawn using the CM node data.

4.5.2.1. Sensitivity of Results to the Modulus of Elasticity of Masonry. Modulus of elasticity of the masonry is one of the most important parameters in the FE analysis, and high importance has been put on it from the beginning by carrying out dynamic identification and subsequent model updating. It is important to see whether different elasticity modulus values provided in the literature yield similar results, and the stress state or the failure pattern of the Bridge is sensitive to it or not. For this purpose, three different values were used for the elasticity modulus of the masonry elements (spandrel walls, piers, and arches) while keeping the other benchmark values fixed. Used values of the elasticity modulus are experimentally identified value (E), half ($0.5E$), and twice ($2E$) of that value. The results show the importance of dynamic identification and model updating. Extensive literature research presented in this study and the reference values provided by international standards indicate that the range of values of the elastic modulus of masonry could be between 2.5-12.5 GPa.

The results of the analyses are provided in Figure 4.11 graphically. It is observed that the pushover curves change significantly. Especially, attained displacements get much smaller as the elasticity modulus value increases. Also, final acceleration values change slightly. Increasing elasticity modulus values also increase the shear and compressive stresses at the piers significantly.

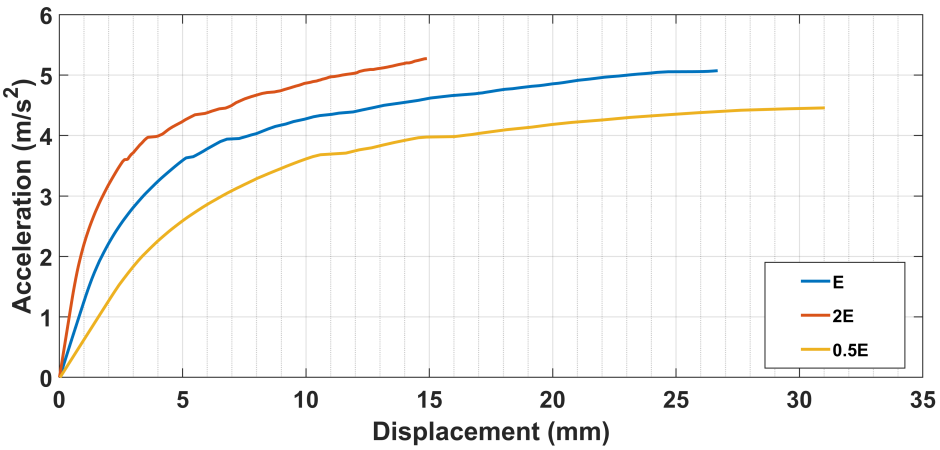

Figure 4.11. Pushover curves obtained for different elasticity modulus of masonry values.

It should be noted that the presented PO curves do not correspond to the same physical limit state, but merely represent the numerically attained converged values. Therefore, physical damage states may be different in each of them at the last converged step. It might be more logical to carry out pushover analyses until a specified damage state for all three cases, but determining the damage limit state for historical structures is a major concern itself.

4.5.2.2. Sensitivity of Results to the Tensile Strength of Masonry. The tensile strength of the masonry is the most influential parameter that affects the results. Not only it changes the displacement capacity of the Bridge significantly, but also it alters the damage mechanisms. The literature research indicates that the tensile strength of masonry is between 1/6 to 1/20 of its compressive strength. Based on this, three values –lower and upper boundary and a mid-value, were selected. The lower boundary value, i.e., 0.3 MPa, resulted in early cracking and non-convergence. On the other hand, the upper bound value, 1.5 MPa, was not found realistic. It causes late cracking initiating at the west spandrel and arches and concentrated plasticity in a small region. Initially considered value, 0.8 MPa, gives physically meaningful results. The pushover graphs for the analyses are provided in Figure 4.12.

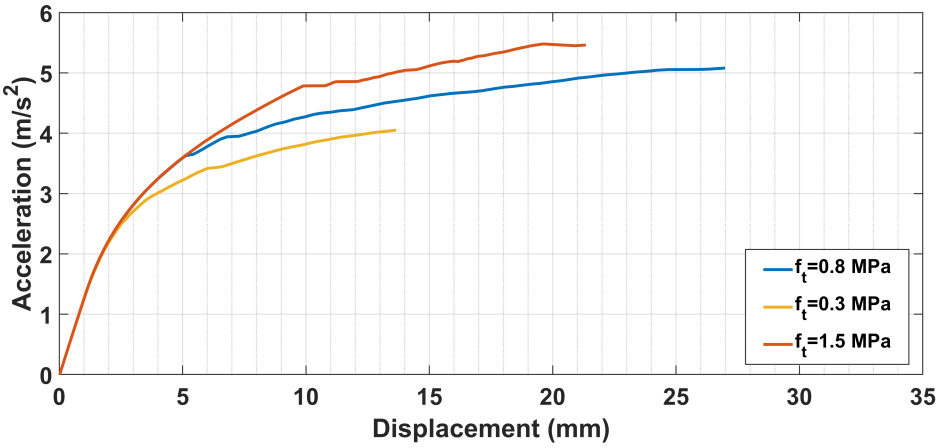

Figure 4.12. Pushover curves obtained for different tensile strength values of masonry.

4.5.2.3. Sensitivity of Results to the Shear Crack Coefficients. The shear crack coefficients modify the shear modulus in the stiffness matrix, and the value of shear modulus

changes with each step. Therefore, the relationship between shear stress and shear strain is not bilinear.

Three additional cases to the benchmark case, i.e., 0.3 & 0.8 for open and closed cracks, are implemented to represent the extreme conditions. The shear transfer coefficient values for the other cases are: 0.1 & 0.8, 0.6 & 0.8, and 0.0 & 1.0. The change is observed after the damage starts. Also, the literature states that the shear retention factor is a very important parameter, even more than the fracture energy on the seismic response [58], and its value alters the results significantly [66]. If the two cases of value sets for shear transfer coefficients, 0.3 & 0.8 and 0.0 & 1.0, are compared regarding their damage states at the last converged steps, their prominent effects might be understood better. The former case displays substantial displacement compared to the latter, as in the latter case, the non-convergence occurs imminently with the first cracks. The results of the analyses are presented in Figure 4.13.

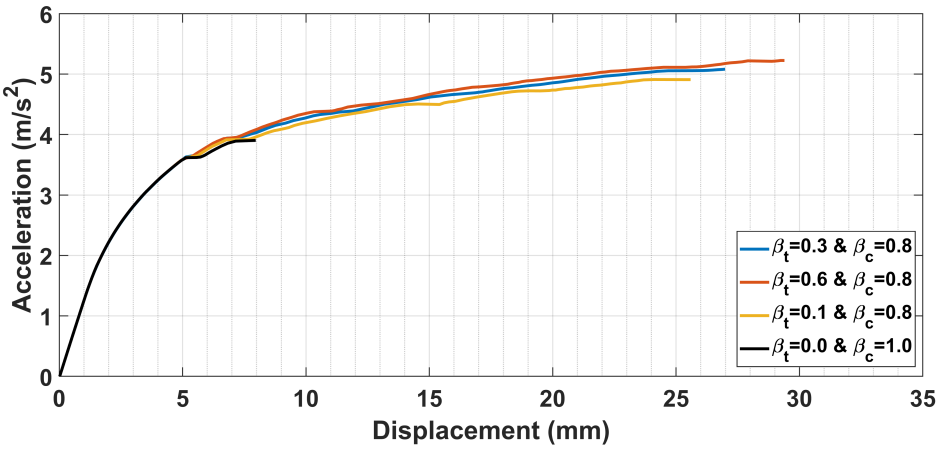

Figure 4.13. Pushover curve comparison for different values of shear crack coefficients.

4.5.2.4. Sensitivity of Results to the Elasticity Modulus of Fill Material. The fill material has considerable mass and volume within the Bridge, and it was one of the updating parameters. The upper and lower boundary values, 2300 MPa and 500 MPa respectively, are used and compared with the benchmark value, 1150 MPa. It is observed that the softer fill material causes more deformation and significantly higher stresses in the piers. However, there is no significant difference between these three

cases on the pushover curves.

In the absence of the fill, i.e., when the fill's stiffness and mass are reduced to an insignificant number, the bridge becomes stiffer, and it can also be observed in the pushover graphs in Figure 4.14. Yet, as the pushing force is in one direction and the main stiffness of the system comes from the arches and piers, there is no tremendous change due to the fill properties. Indeed, the density, elastic modulus, and depth of the fill material are important parameters for vertical loading, but we do not observe the same phenomenon for transverse loading, at least for this bridge.

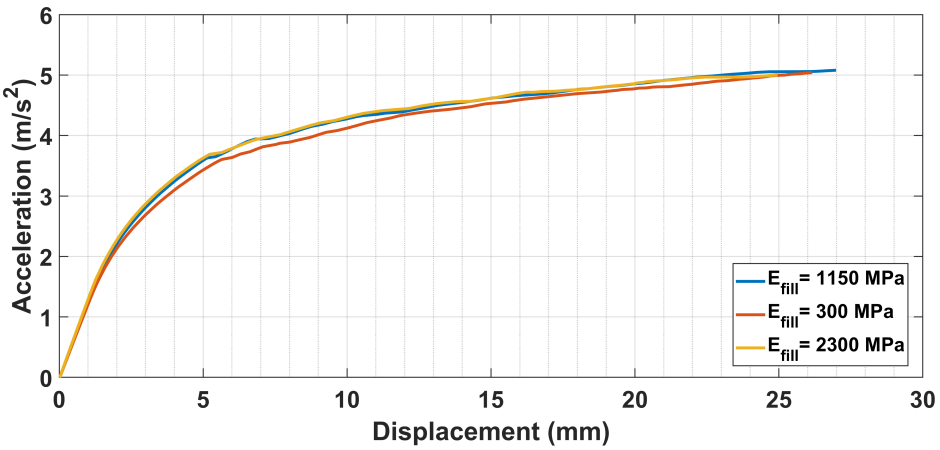

Figure 4.14. Pushover curve comparison for different elasticity modulus values of the fill material.

4.5.2.5. Sensitivity of Results to the Friction Coefficient of Contacts. Apart from the prominent effect of assigning frictional contacts that are mentioned in Chapter 4.3.1, it was aimed to investigate how the frictional contact coefficient changes the structural behavior. In the late stages of the PO analysis, separation of the contacting bodies was observed the most in the middle portion, as can be seen in Figure 4.15. As for the effect of the coefficient of friction in the late stages of the PO analysis, the change in the PO curves, illustrated in Figure 4.16, seems insignificant.

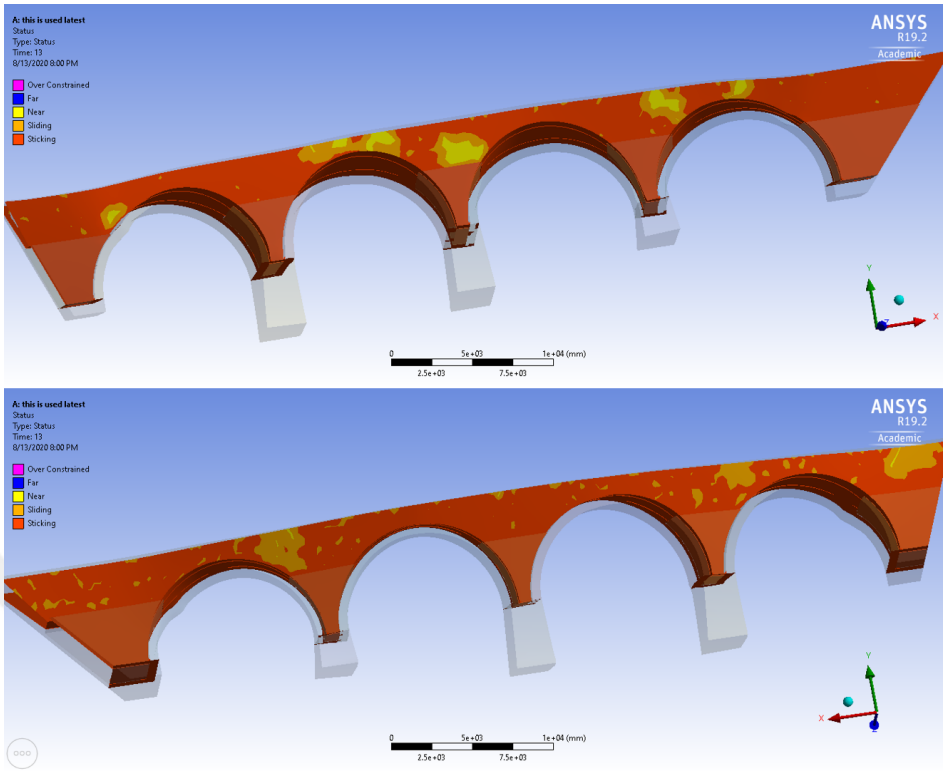

Figure 4.15. Contact status at the end of the PO analysis (last converged step).

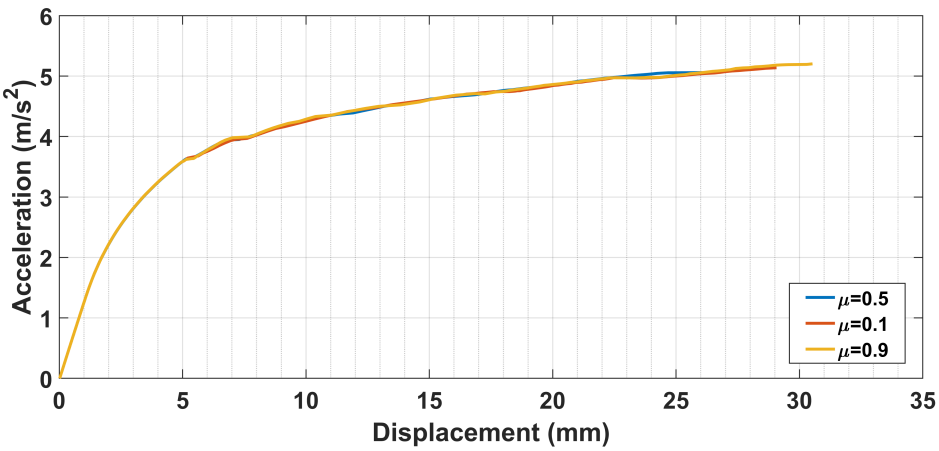

Figure 4.16. Pushover curve comparison for the different coefficient of friction values.

The results of the sensitivity analyses confirm that our findings correspond to those published in the most recent literature. Tensile strength of the masonry and shear retention factors completely alter the nonlinear behavior and have a very significant influence on the results, as stated by Scheibmeir [58] and Pela *et al.* [35]. A similar effect can be observed for the elastic modulus of the masonry elements as it directly affects

the stiffness of the bridge and its structural response. Interestingly, the effects of the coefficient of friction of the frictional contacts and the elastic modulus of the fill material seem to be limited on the pushover curve. However, two things should be recalled here: *i*) these two parameters were found to be very effective for vertical loading cases in previous research by other researchers, *ii*) the mass of the fill is only 24% in this bridge, and the fill depth can be considered small. Therefore, the investigated parameters may be important for another masonry arch bridge with different structural features even though they do not change the PO analysis results significantly for the Bridge model. It should be emphasized that further research is needed on these parameters.

4.5.3. Partial Performance Assessment

Once the effects of different parameters to the results were investigated, the performance assessment of the bridge was done using MPP. The assessment was carried out up to finding the performance point in the pushover curve because there are no performance criteria available for this type of structure. MPP method was described in Chapter 4.5.1, and the steps of the partial assessment are explained in this section.

Partial performance assessment was conducted for two different base shear-nodal displacement data sets, where the control point was selected as the center of mass (CM) or the top displacement of the MDOF system (TOP), as can be seen in Figure 4.2b. As explained before, the reason for this comparison is the work of Pela *et al.* [35], which indicates the results are more conservative, and the method is easier to apply when the CM node is selected as the control point. The resulting elastic demand versus capacity curves for the TOP and CM nodes are given below in Figure 4.17.

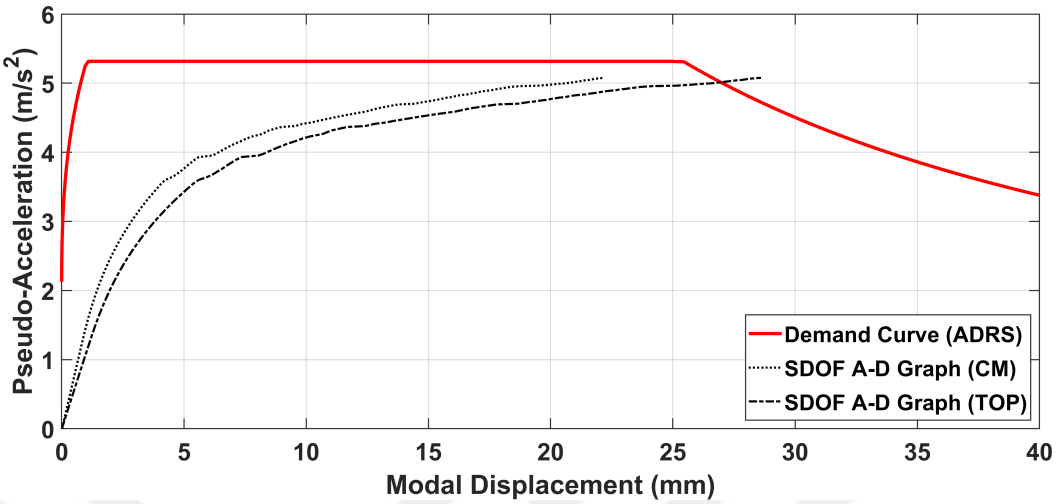

Figure 4.17. Elastic demand vs. capacity curves for CM and TOP nodes.

Continuing further with the procedure, the maximum SDOF displacement (or the performance point), D_{max}, was then found using the iterative bi-linearization procedure described in the Turkish Building Seismic Code [77]. It is illustrated for the TOP node capacity curve in Figure 4.18 below.

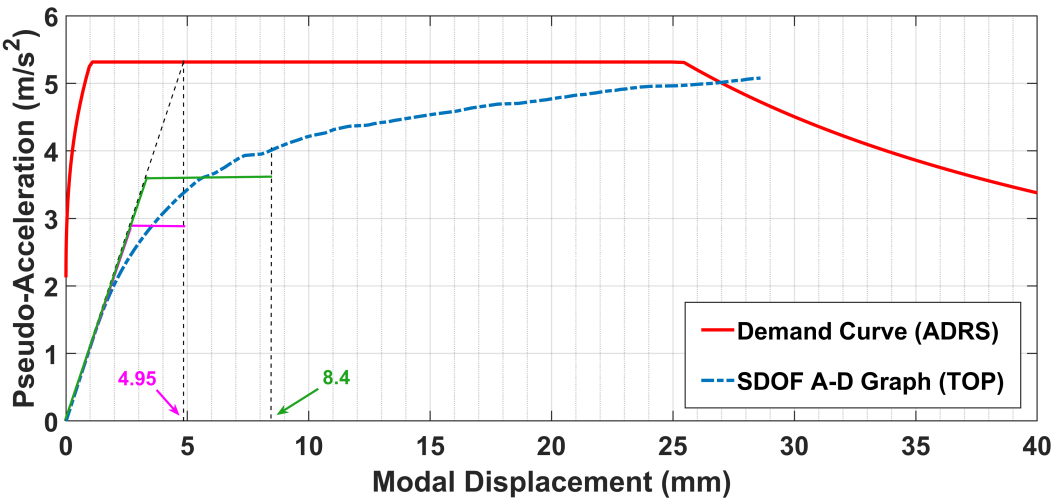

Figure 4.18. Finding D_{max} using TOP node data.

Once the D_{max} is found, MDOF displacements can be calculated using Equation 4.7:

$$\{U_{max}\} = D_{max}\Gamma\{U\} \tag{4.7}$$

$$U_{max} = \{1.60, 5.90, 7.05, 8.74, 9.96\}$$

The maximum displacement in this vector corresponds to the center of mass of the fill body. Thus, the TOP displacement demand was read from the ANSYS analysis results as 11.61 mm when the CM of fill body displaced 9.96 mm in Z-direction. Similarly, the displacement demand for the CM node was found as 7.78 mm. As for the CM node data set, the results were more conservative in that the top of the spandrel reached a target displacement of 7.78 mm, whereas CM node displacement was 5.71 mm.

Pushover analysis of the Bridge in the transverse direction points out possible damage at the arches, arch springing, and spandrel walls. Damage is described here as the cracking of the masonry after being exposed to high tensile stress and the consequent increase and propagation of localized strains afterward. This phenomenon is shown visually in the qualitative total strain plots below in Figure 4.19. Cracking starts at side arches and propagates. Subsequently, the middle arches crack, and the cracks propagate into the arch further as well as the spandrel walls just above the mid-portion of the arches. This behavior can be considered as flexural behavior or out-of-plane bending. While the upper portions of the bridge are damaged, the arch-springing in the middle part of the bridge also suffers damage by cracking, and the cracks propagate diagonally to the pier foundations. This shear-type behavior is usually encountered in shallow and stocky bridges, whereas the out-of-plane bending behavior dominates tall masonry arch bridges. Thus, Bridge 41 can be said to have a complex seismic behavior demonstrating both out-of-plane bending and shearing of the piers.

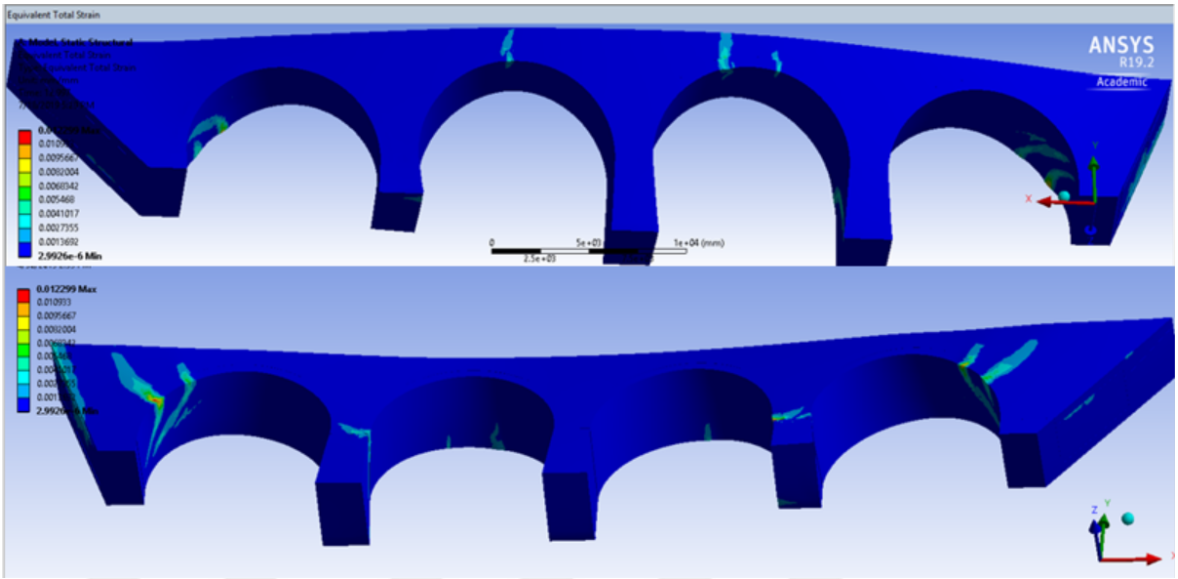

Figure 4.19. Equivalent total strain plot for the last step of the MPP analysis in the transverse-direction.

The Bridge behavior is further investigated, and the displacements under the mid-arches and at the top of the spandrel are checked. They are compared within the elastic and plastic regions of the behavior. The displacement difference below the arch and above the spandrel is around 20%, which shows the stiffness mainly comes from the piers and the arches. Also, the stiffness contribution from the spandrel above the arch and the fill seems very low. This might also be due to the fact that the vertical distance between two points at the top of the spandrel and below the arch and is only 100 cm. It is even 50 cm if a point above the arch stones is considered. Therefore, this might be another factor decreasing the effect of the fill material on the bridge behavior.

MPP analysis procedure claims to give more accurate results for plane frame structures than the N2 procedure while it also includes higher mode effects. However, what draws attention in the model behavior of Bridge 41 is that the normalized displacement vector ϕ, given as $\phi = \{0.16, 0.59, 0.71, 0.88, 1\}$, resembles the first mode shape. Therefore, in contrast with plane frame structures, the effect of higher modes is not considered in MPP analysis for masonry arch bridges.

Other observations are pertinent to the direction and the behavior of cracks. As it can be observed from the equivalent strain plots, crack directions are not constant. They start in a certain direction and then may propagate in a different direction. This phenomenon can be observed in Figure 4.20 below, which shows the vector principal strains in the last step of the PO analysis. Directions of the high strains also correspond to the evolution of cracks during the analysis.

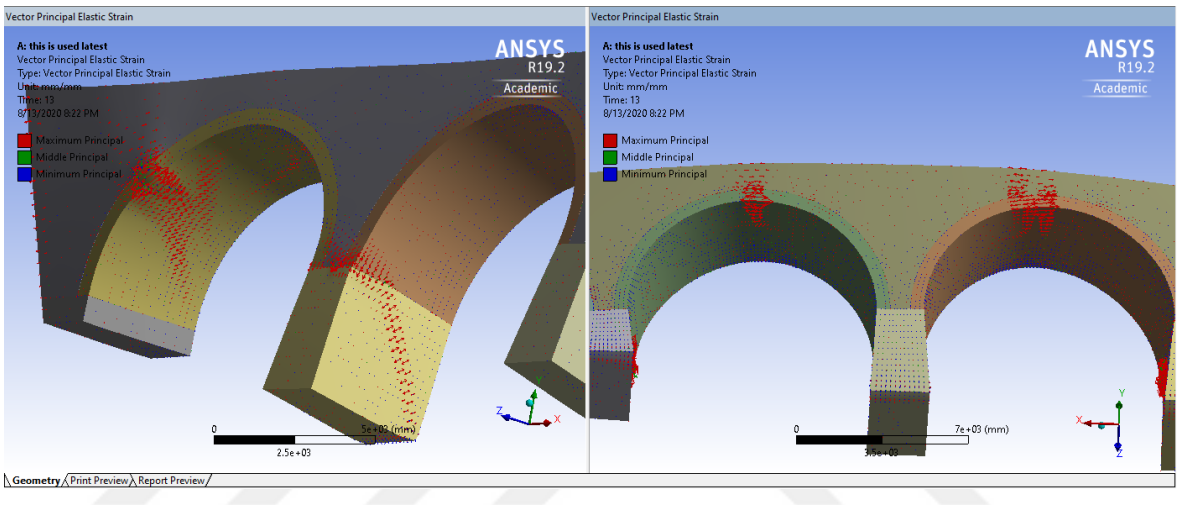

Figure 4.20. Vector principal strain plots.

Figure 4.21 displays the maximum principal stress-strain behavior of the node in a cracked region. Notice that the maximum principal stress does not drop to zero because of the shear retention factors (shear crack coefficients) defined. This behavior is a part of the smeared crack model.

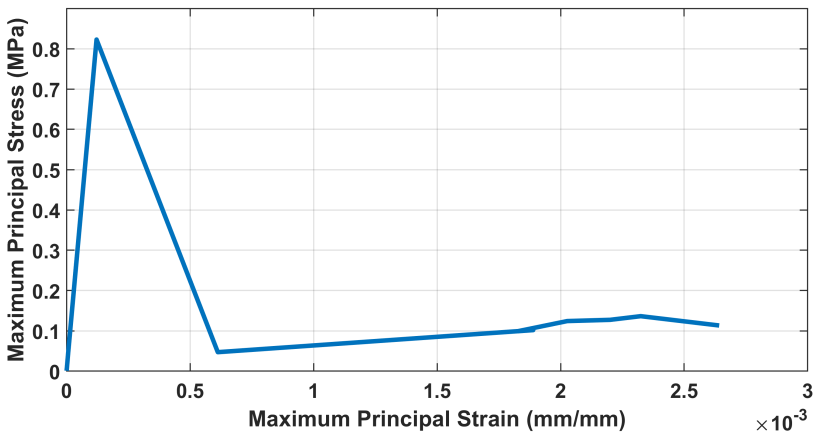

Figure 4.21. Stress-strain plot of a node in a cracked region.

As a final note, approximately 40 mm TOP displacement to reach the failure seems physically reasonable, because that much of out-of-plane displacement also means approximately 0.4% in-plane drift of the piers. The acceptable drift ratios and performance limits given in ASCE 41-17 [78] and NTC 2018 indicate that such a high drift ratio may even cause Collapse Prevention limit state, although those limit states are provided for masonry walls and not for bridge piers.

4.5.4. Multi-directional MPP

The PO analysis - in the transverse direction only, of the Bridge presented so far can be considered as the representative analysis for comparison with other analysis methods. Additionally, MPP analyses in horizontal and vertical directions, as well as their combination, were carried out. As there are no guidelines for PO analysis in multiple directions, in longitudinal and vertical directions, 30% of the loading in the main direction is used. If the transverse direction of the bridge is called Z-direction, longitudinal is X-direction, and the vertical is Y-direction, then the analyses were carried out for the cases below:

- ±Z
- ±X
- Z±0.3X
- Z±0.3X±0.3Y

When the MPP analysis in the longitudinal direction is investigated, differences to MPP analysis in the transverse direction are observed. One of the side-arches cracks along the arch in the transverse direction in a brittle manner, creating a similar mechanism to the well-known four-hinge collapse mechanism of the arch. This is observed in Figure 4.22. The pushover curve starts increasing almost linearly up to the above-mentioned failure point, 5.69 m/s^2 acceleration value. Note that the acceleration value for failure in Z-direction was 5.07 m/s^2.

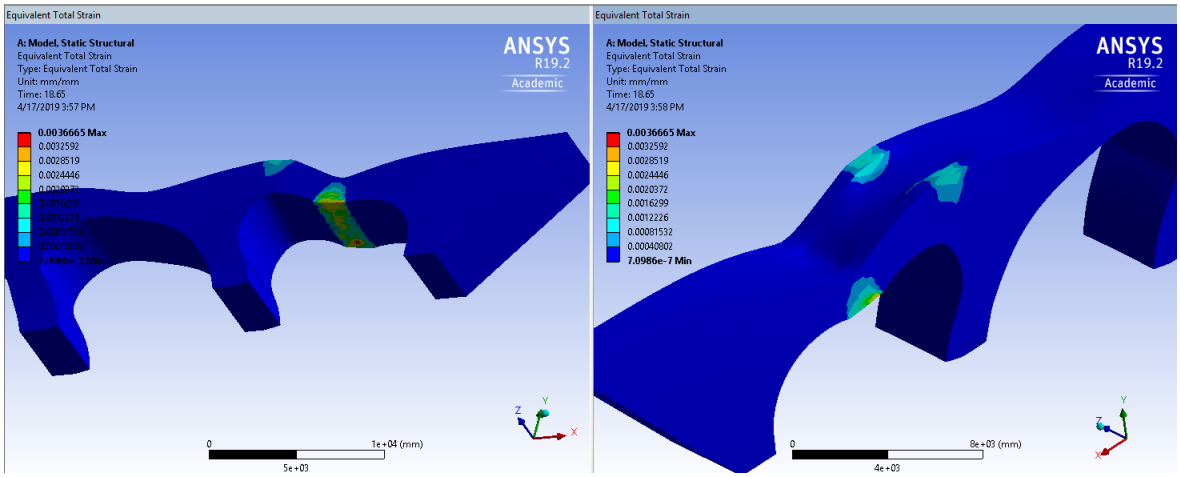

Figure 4.22. Equivalent total strain plot for the MPP in the X-direction.

Analysis of the Z±0.3X directions demonstrated that the strains decreased slightly, but the plasticity (or damage) became more spread compared to Z-direction, as can be observed in Figure 4.23. Also, the increase in the total maximum displacements was insignificant ($< 5\%$), but the total base shear force increased by 5.5% because of the reaction force in the X-direction.

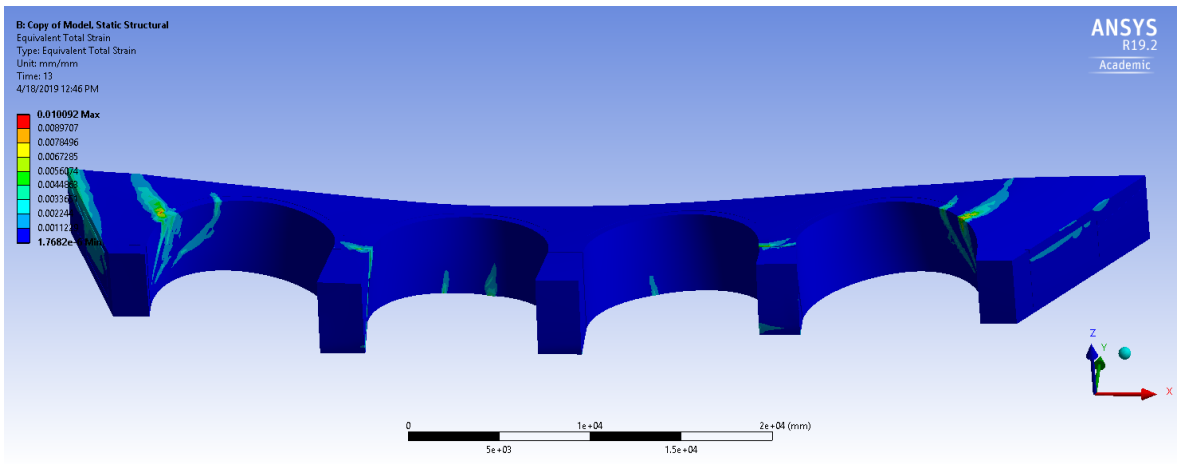

Figure 4.23. Total strain plot for the MPP in Z-0.3X direction.

The analyses in Z±0.3X±0.3Y directions present considerably different results depending on the direction of the vertical force. When the vertical force is in the downward direction, it contributes to the stability of the Bridge as the displacements and the damage decrease. This phenomenon is seen in Figure 4.24 and might be generally accepted for short bridges, such as Bridge 41, with low vertical stress levels.

However, when the vertical force is in an upward direction, Figure 4.25 shows that the displacements increase remarkably, causing an increase in the stresses and spreading of the damage. Although the analysis converges to a solution, it might be stipulated that such a physical condition will lead to the collapse of the bridge.

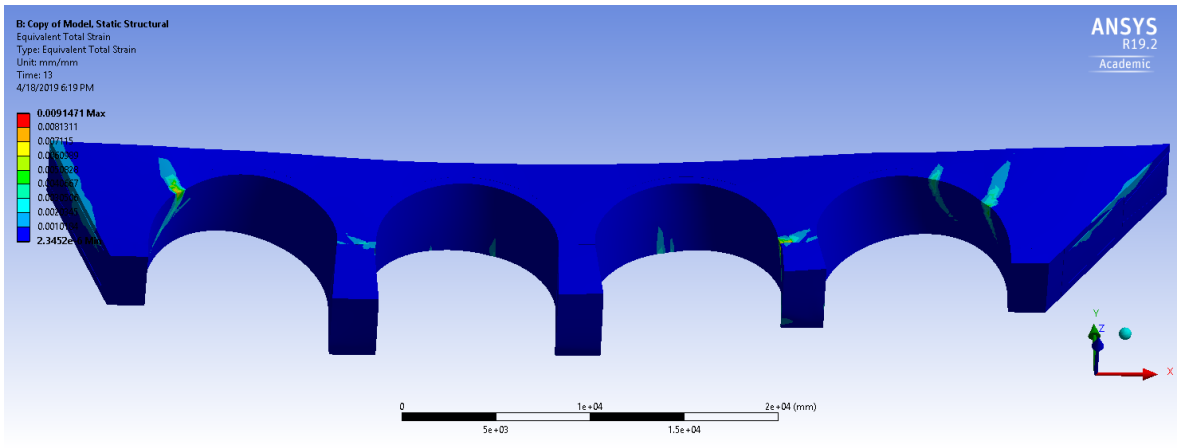

Figure 4.24. Total strain plot for the MPP in Z+0.3X+0.3Y direction.

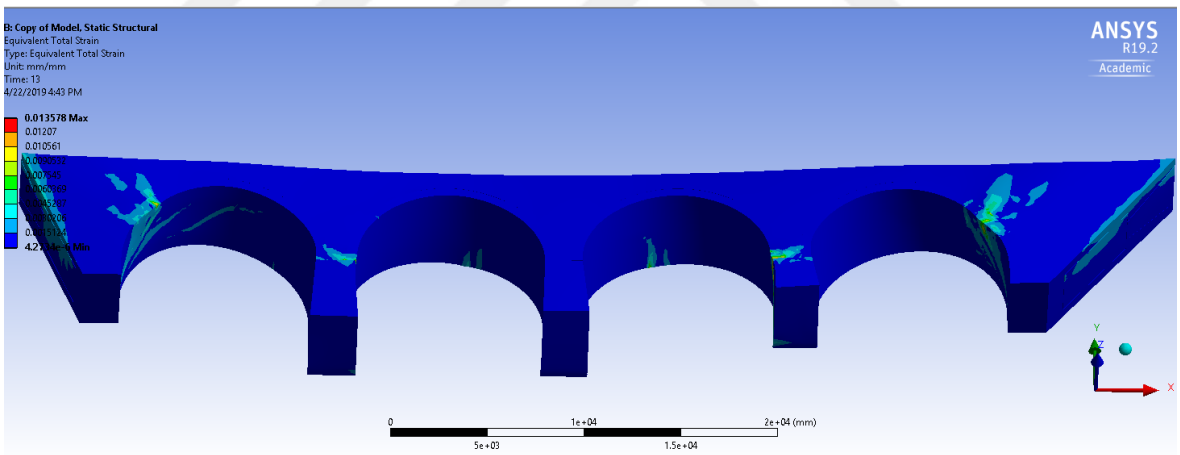

Figure 4.25. Total strain plot for the MPP in Z+0.3X-0.3Y direction.

4.6. Nonlinear Dynamic (Time-History) Analysis

Architectural masonry heritage structures are often overdesigned and capable of resisting vertical loads safely. However, they are usually vulnerable to seismic loads due to some characteristic features such as high seismic mass, a low tensile strength of masonry, and poor connections between structural parts. Therefore, the need for rigorous seismic assessment arises.

Nonlinear dynamic analysis is a comprehensive and effective procedure for studying the complex behavior of structures during an earthquake, and it represents the most advanced deterministic analysis method available [79]. Although it is computationally more expensive, more information about the structural behavior such as damage mechanisms, spatial and momentary distribution of inelasticity, redistribution of forces, and ductility can be obtained than from conventional linear or nonlinear static approaches. Even though not often preferred by practicing engineers, nonlinear dynamic analysis procedures have been included in the various recent standards, thanks to the research conducted in the last few decades. There are still aspects that require further research; for instance, the behavior of the analyzed structure is highly dependent on the ground motion characteristics, so the results are dramatically affected by their choice. Another example is the complex damping mechanisms during earthquakes. As important as the examples mentioned already is the interaction of earthquake components, as in most NDA, only the dominant earthquake direction is considered and the effects of horizontal or vertical components of the earthquake are only taken into account indirectly — or even simply disregarded. Within this study, NDA using the earthquake component in the transverse direction of the bridge were carried out first. The results were then compared to the pushover analysis results. Afterward, the other components of the earthquake records were taken into account one by one, adding the longitudinal component first and the vertical component later. A total of 42 nonlinear time-history analyses were conducted. All analyses were carried out using a Work Station that has Intel(R) Xeon(R) W-2133 CPU @3.60 GHz processor with six cores and 128 GB RAM, and average analysis duration for a single analysis was approximately 18 hours.

4.6.1. Model Setup

Pushover analysis was conducted using the “Static Structural” module of ANSYS Workbench Mechanical; however, inertial effects are taken into account only in the “Transient Structural” module. Therefore, the same geometry was transferred to the following module. Transient structural analysis in ANSYS workbench requires the input for damping constants and the time-steps additionally. For the initial time steps,

auto-time-stepping was used, and the minimum and maximum time step sizes were arranged according to the earthquake record step size. Such that the minimum step size is 1/4 of the maximum step size, which is equal to the step size of the earthquake record.

Evaluating damping is one of the most challenging tasks of civil engineering practice. Besides, the damping mechanisms in stone masonry structures comprise a more complex issue that has not yet been fully investigated [80]. The energy dissipating mechanisms include frictions between the structure and the surrounding media, a material's internal frictions, and the frictions in the joints connecting structural elements and members. In ANSYS Workbench, the input of a constant damping ratio is not allowed for a Transient Analysis, as viscous damping is not considered a global parameter. As the damping coefficient c is not an intrinsic property of the material, and to filter out such factors as geometry, we can use Rayleigh damping, which assumes the coefficient c is a linear combination of the mass (m) and the stiffness (k), represented in Equation 4.8:

$$\mathbf{c} = \alpha\mathbf{m} + \beta\mathbf{k} \tag{4.8}$$

The **m**, **c**, and **k** represent the mass, damping and stiffness matrices in the equation of motion of a multi-degree of freedom system. The other major source of damping, dry friction (or Coulomb friction), was taken into account in this study via the frictional contacts between structural members [81]. The coefficients α and β were calculated as 0.244 and 0.00196 using the average values of the first and third mode damping ratios ζ_1=2.7 and ζ_3=2.2. The friction coefficient for the frictional contact was kept as 0.4, as in the previous analyses.

4.6.2. Earthquake Record Selection

Earthquake demand in NDA is determined using a number of earthquake records, whereas in NSA it was determined using the response spectrum. The uncertainty in

earthquake records decreases as the number of selected records increases, which in turn provides more reliable results. Various databases offer a large amount of real seismic recordings, and they can be scaled with appropriate scaling criteria. Thus, the trend has shifted towards using natural accelerograms, scaled according to the target code requirements. In this study, according to the Turkish Building Seismic Code, at least 11 site-specific earthquake time-histories were required for the nonlinear time history analyses. The earthquake records were selected from the PEER NGA-West2 database and scaled according to the procedure defined in the code. In order to do this, the TDTH Web Interface (AFAD Deprem Tehlike Haritası) was first used by entering the coordinates of the Bridge. The soil type of the location was determined as ZC, and the intensity of seismic ground motion was chosen as DD-2, representing a 10% probability of exceedance in 50 years (or 475 years return period). The distance to the fault was measured as 80 km, and S_s and S_1 values were obtained. Afterward, the design spectrum was generated according to the code and multiplied with 1.3 to obtain the "target design spectrum." Then, it was imported as ".csv" file to PEER search engine. Required fields of the engine were input as follows: fault type was left as "any"; magnitude was set between "6.2-7.6"; the distance to fault was "R_JB: 60-100 km"; the shear wave velocity of the ground as "V_S:600-1000 m/s"; suite selection by "SRSS, 5% damping and Geometric mean"; selection criteria as "Minimize Mean Square Error (MSE)"; and for D5-95, "left blank" as there is no restriction in TBDY 2018; weight points were equally spaced 10 points between 0.2T and 1.5T and weights were 1,1,1,...,1 preferably. This information enables reproducing the same set of results. Within the several records provided by the database, the records with scaling factor smaller than three were chosen, and in between $0.2T_1$ and $1.5T_1$, the average spectra (SRSS combination of directions) was always kept above the target design spectrum. There were at most three records from the same earthquake, as required by the code.

Finally, a set of 14 earthquake records compliant with the design response spectrum was selected and used in the analyses. Information about the records is presented in Table 4.2, and the coherence between the SRSS of scaled response spectra of the earthquake records and target design spectrum is illustrated in Figure 4.26.

Table 4.2. Strong ground motion records.

Record ID	Earthquake Name, Year and Site	Magnitude (Mw)	Distance (km)	PGA (g)	Scale Factor
285	“Irpinia_ Italy-01”, 1980, “Bagnoli Irpinio”	6.90	8.14	0.31	1.63
763	“Loma Prieta”, 1989, “Gilroy - Gavilan Coll”	6.93	9.19	0.23	0.63
1013	“Northridge-01”, 1994, “LA Dam”	6.69	0	0.33	0.77
1102	“Kobe_ Japan”, 1995, “Chihaya”	6.90	49.91	0.24	2.13
1161	“Kocaeli_ Turkey”, 1999, “Gebze”	7.51	7.57	0.37	1.42
2627	“Chi-Chi_ Taiwan-03”, 1999, “TCU076”	6.20	13.04	0.46	0.88
4213	“Niigata_ Japan”, 2004, “NIG023”	6.63	25.33	0.32	0.80
4472	“L’Aquila_ Italy”, 2009, “Celano”	6.30	17.82	0.27	2.91
4858	“Chuetsu-oki_ Japan”, 2007, “Tokamachi Chitosecho”	6.80	25.35	0.22	1.08
4864	“Chuetsu-oki_ Japan”, 2007, “Yoitamachi Yoita Nagaoka”	6.80	4.69	0.27	0.85
5618	“Iwate_ Japan”, 2008, “IWT010”	6.90	16.26	0.22	0.77
5809	“Iwate_ Japan”, 2008, “Minase Yuzawa”	6.90	17.34	0.23	0.94
6928	“Darfield_ New Zealand”, 2010, “LPCC”	7.00	25.21	0.28	0.79
8110	“Christchurch_ New Zealand”, 2011, “MQZ”	6.20	13.91	0.29	1.94

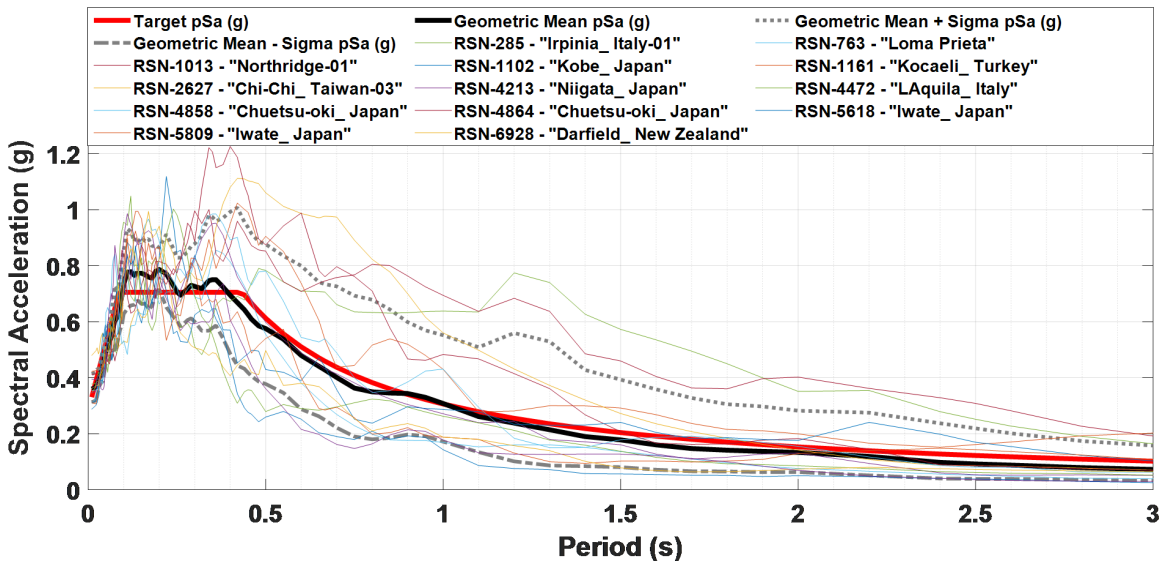

Figure 4.26. Scaled spectra of the records vs. target design spectrum.

The Fourier Amplitude Spectrum (FAS) of the scaled records, shown in Figure 4.27, does not represent anomalies concerning the natural frequencies of the structure.

RSN 285 record is removed from the graph because its amplitudes are relatively larger than the others and make the FAS presentation difficult. It is observed that the first three modes of the structure, which are in between 5-12 Hz, are expected to be affected more, while the fourth and fifth modes between 15-20 Hz are hardly excited by the ground motion.

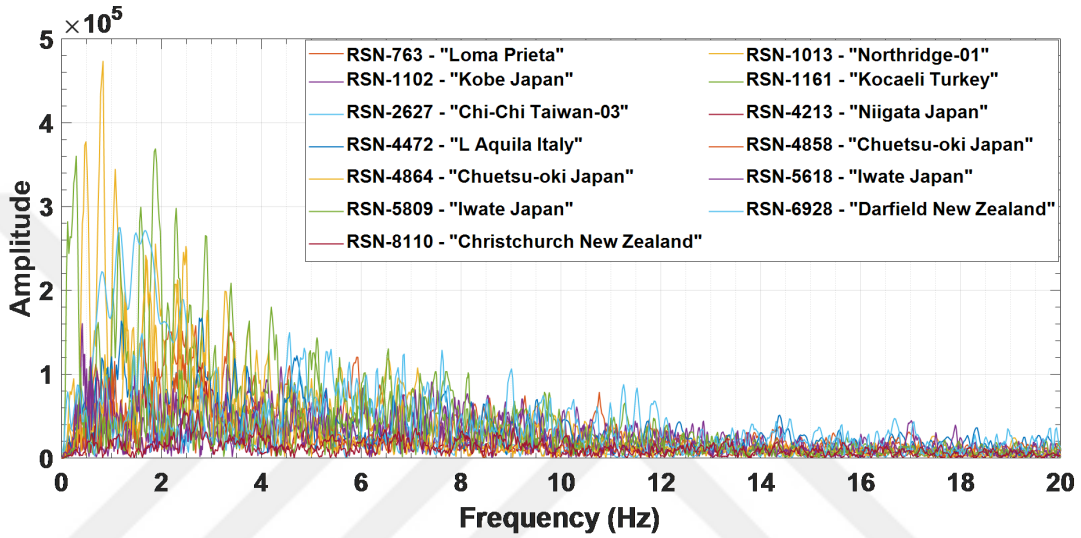

Figure 4.27. FAS of the scaled records.

Please note that the scaling of the vertical component of earthquake records is another research area. There is no "combined spectrum" approach that considers both horizontal and vertical components of earthquake records when selecting the records. So, in this approach, the horizontal components are used to select the earthquake records, and then the vertical records are scaled with the same scale factors. This approach may not be accurate in general, as it might result in very high vertical accelerations. Also, when the same scale factor is used for the vertical component, the content of the record is changed, and it may not be considered as a "natural record" anymore. However, the scale factors used in this study are close to unity (approximately in the range of 0.5-2); thus, the results can be considered as representative and accurate. Another approach would be considering the vertical earthquake load as an equivalent static load in the vertical direction and carrying out the analyses for both directions, which would increase the analysis duration twice.

4.6.3. Results

4.6.3.1. NDA in Transverse Direction Only. Each earthquake record or scenario exhibits different outcomes and a considerable scatter as expected and given in Table 4.3. These differences mainly stem from the earthquake duration, peak ground acceleration, and the acceleration's frequency content.

Table 4.3. NDA results: the maximum displacements for the CM and TOP nodes.

Record ID	**Earthquake Name, Year and Site**	**Max CM displacement (mm)**	**Max TOP displacement (mm)**
285	"Irpinia_ Italy-01", 1980, "Bagnoli Irpinio"	6.02	9.08
763	"Loma Prieta", 1989, "Gilroy - Gavilan Coll"	5.28	8.19
1013	"Northridge-01", 1994, "LA Dam"	7.69	11.48
1102	"Kobe_ Japan", 1995, "Chihaya"	14.83	22.98
1161	"Kocaeli_ Turkey", 1999, "Gebze"	9.60	14.84
2627	"Chi-Chi_ Taiwan-03", 1999, "TCU076"	19.71	29.15
4213	"Niigata_ Japan", 2004, "NIG023"	5.19	7.77
4472	"L'Aquila_ Italy", 2009, "Celano"	7.56	11.80
4858	"Chuetsu-oki_ Japan", 2007, "Tokamachi Chitosecho"	7.59	12.09
4864	"Chuetsu-oki_ Japan", 2007, "Yoitamachi Yoita Nagaoka"	5.99	9.44
5618	"Iwate_ Japan", 2008, "IWT010"	7.27	11.13
5809	"Iwate_ Japan", 2008, "Minase Yuzawa"	5.30	8.56
6928	"Darfield_ New Zealand", 2010, "LPCC"	9.55	14.31
8110	"Christchurch_ New Zealand", 2011, "MQZ"	8.81	14.15
	AVERAGE	**8.60**	**13.21**
	C.o.V.	**0.46**	**0.44**

Figure 4.28 is presented to help to clarify some of the concepts below. The relevant part of the displacement response to RSN 1161 – Kocaeli earthquake is presented together with the bridge responses at specific time instants. It includes equivalent total strain plots to describe the damage qualitatively and maximum principal stress plots to illustrate the cracking of masonry and stress relaxation.

It is possible to observe crack openings and their propagation time-histories in NDA. As the cracking occurs, the stiffness matrix is modified, and the strength of the cracked element is greatly reduced. Therefore, as the bridge displaces in the same direction, the crack tip continues to propagate, whereas stress relaxation is observed in the previously cracked parts. Cracks can close when the bridge starts moving in the opposite direction, and the compressive stresses may be observed at the already cracked locations. Depending on the earthquake characteristics, several different damage mechanisms might occur. For example, the most common damage type found in the early stages of the responses was the cracking at the middle arches. The bridge may fail if the mid-arch cracks develop too much, or it may survive the damage in which case the plasticity is further spread to the other arches, arch springing, and the spandrel walls as long as there is no excessive stiffness reduction. In this case, higher deformations are observed in the response.

Another phenomenon is that, in some instances, damage occurs in one of the displacement cycles as a response to a peak in the acceleration record, but the analysis continues for a few other cycles until another large peak happens in the same direction as the one damaging the bridge before. In some other instances, early damage due to high seismic intensity leads to lower acceleration response of the bridge even for the higher intensities in the later part of the record, possibly due to an increase in the structure's vibration period, and the bridge may survive the earthquake. In such cases, the difference stems from the pattern and timing of the acceleration and the damage rather than just the acceleration intensity [82].

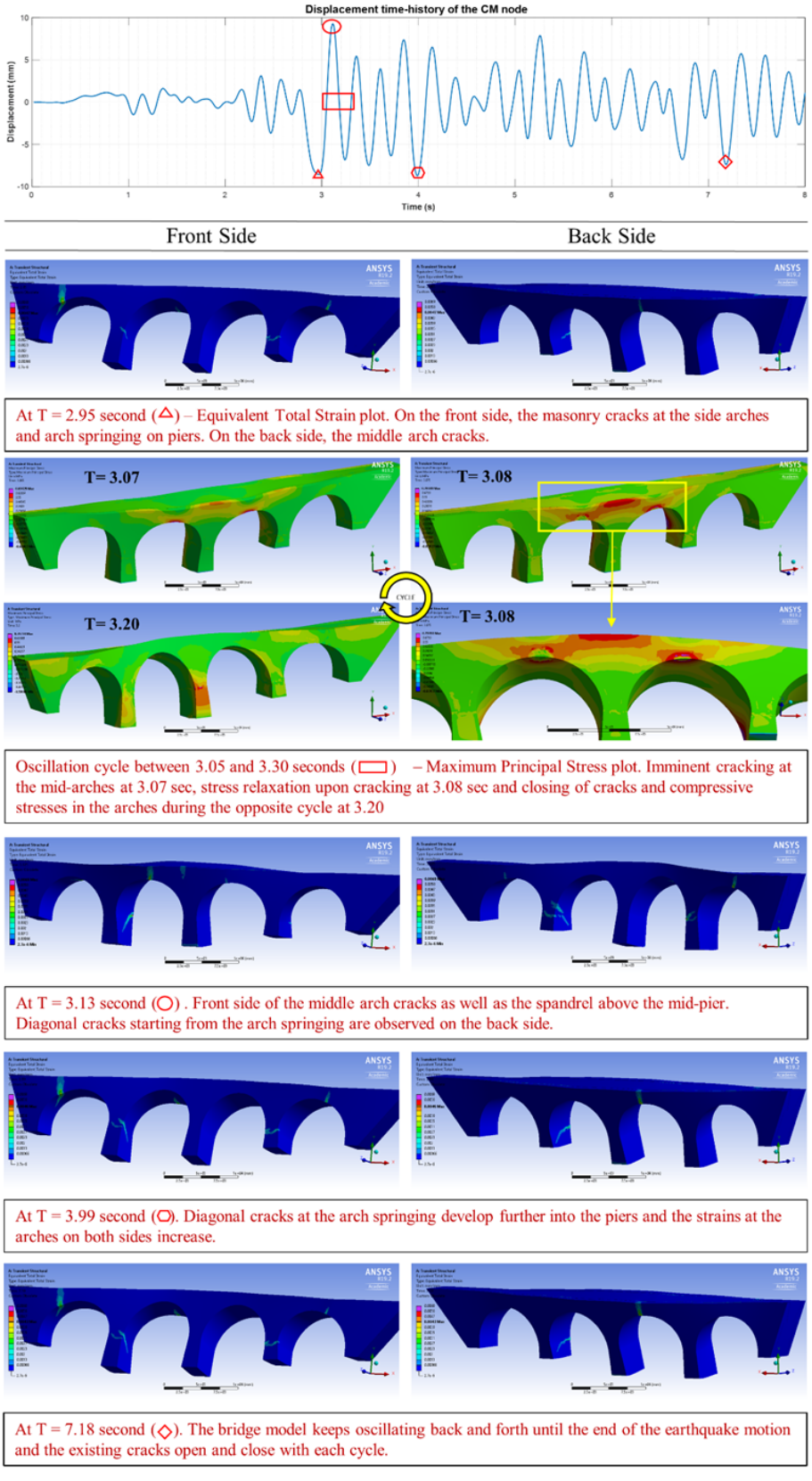

Figure 4.28. RSN 1161 – Kocaeli earthquake response at specific time instants.

Further investigation into the earthquake characteristics and their interaction with the superstructure reveals a curious case. From the comparison of the structure's fundamental vibration periods with the response spectra of each record, some records influence the higher modes in the structural response, whereas the response is dominated entirely by the first mode for the other records. This phenomenon can also be observed in Figure 4.29, where the maxima of the whole time-history of the NDA accelerations are compared to the first mode spectral acceleration values. Moreover, some damage mechanisms such as cracking in the mid-spandrel wall, transverse cracking of piers, and multiple cracking of arches and piers are only observed, as in Figure 4.30, when the higher modes are also dominant in the response.

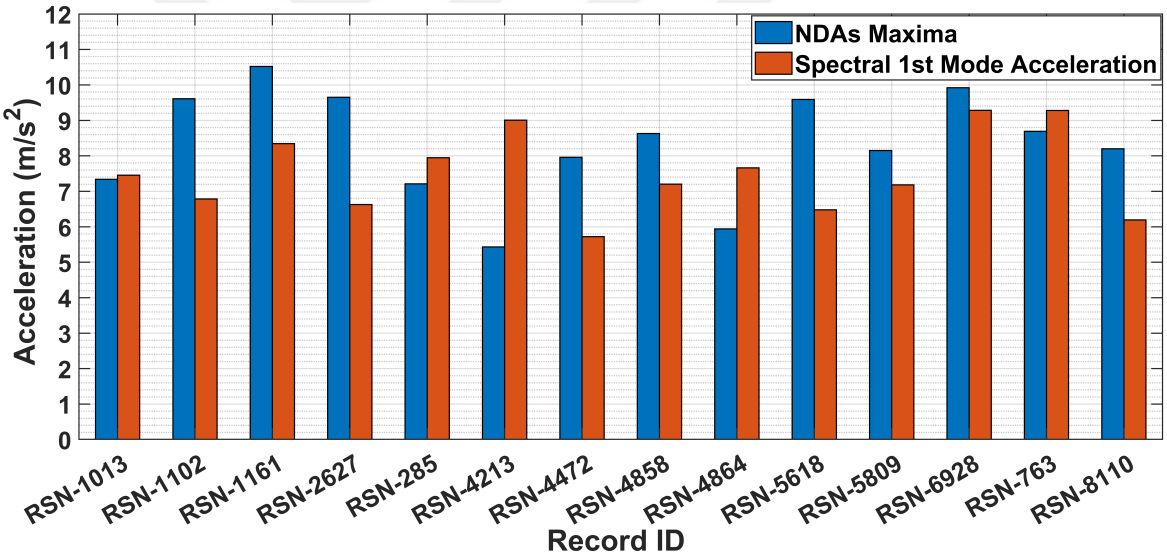

Figure 4.29. NDA maxima vs. spectral first mode accelerations.

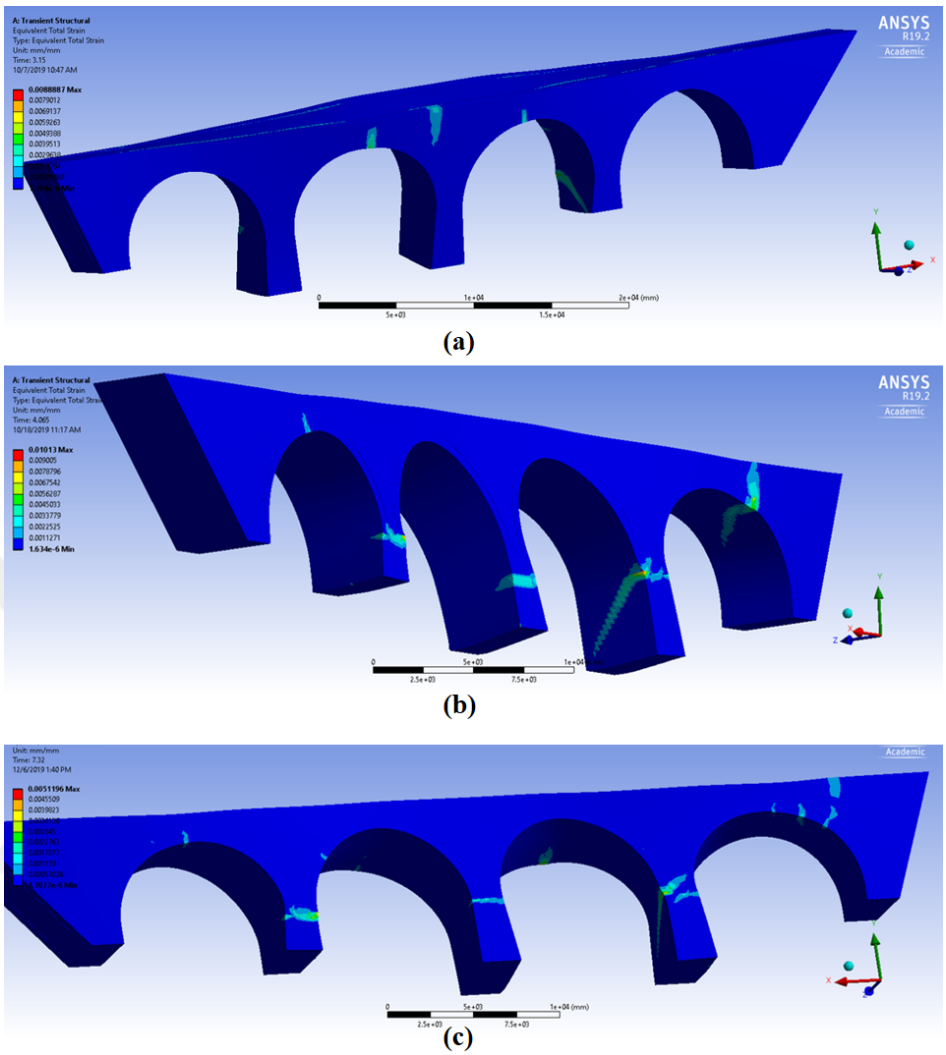

Figure 4.30. Examples for the effects of higher modes using qualitative total strain plots. Results from different earthquake motions and IDA analyses: (a) RSN1161-IDA2, (b) RSN 4213-IDA3, (c) RSN 6928-IDA6.

4.6.3.2. NDA in Horizontal and Vertical Directions Combined. One of the uncertainties in NDA mentioned earlier, i.e., the effects of the vertical component of an earthquake on the superstructure and effects of the interaction of horizontal components of ground motion were also investigated. When two- and tri-directional earthquake records were used, the NDA results generally showed an increase in the displacements and equivalent total strains. Change in the transverse and total displacements is rather small on average, approximately 3-6%, with some outliers that reach up to 23%,

whereas the change in vertical displacements is slightly more significant. Notably, the strain values increased significantly for most of the earthquake records: approximately 13-20% or additional plasticity occurred at different locations of the bridge. Hence, the increase in the displacements is generally smaller than the increase in the strains. The reason for this is the spreading of the plasticity along the bridge mentioned above. Quantitative comparison of these maxima does not reveal much; therefore, we recommend using the comparison of the dissipated energy together with displacements in order to better understand the effects of the horizontal and vertical components of earthquake records for future studies.

If behavioral differences are examined, earthquake analysis in transverse direction only seems to miss some of the damage mechanisms observed in two- and tri-directional analyses. For example, the horizontal component of the "RSN 285 Irpinia-Italy" creates a damage mechanism that is not observed when only the transverse component is used. An example of this phenomenon is demonstrated in Figure 4.31 and Figure 4.32, where the response of the structure to RSN 285- Irpinia earthquake record is shown. In some other cases, the bridge behavior improved due to the other components of the records such that the damage observed in the spandrel walls in unidirectional analyses decreased or completely disappeared. In contrast, in other cases, new damage occurred at different locations and/or the strains in the damaged locations of the unidirectional analysis increased.

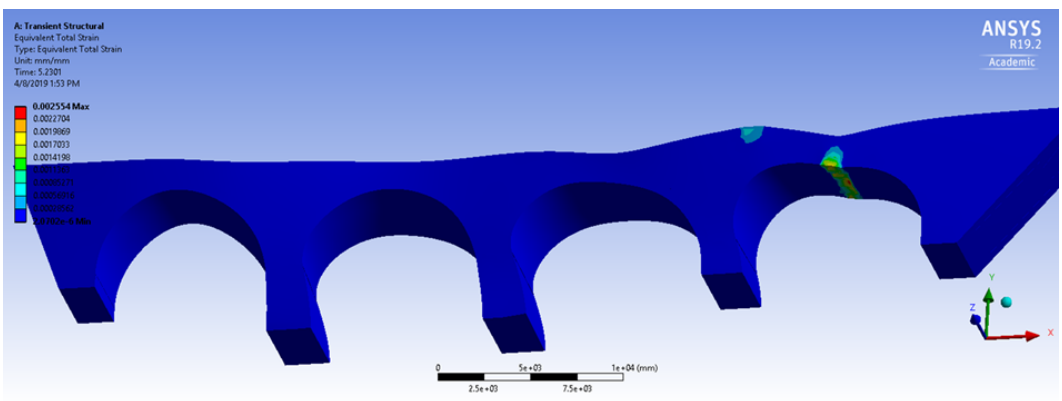

Figure 4.31. Equivalent total strain plot to show the damage distribution after RSN 285 Irpinia-Italy earthquake.

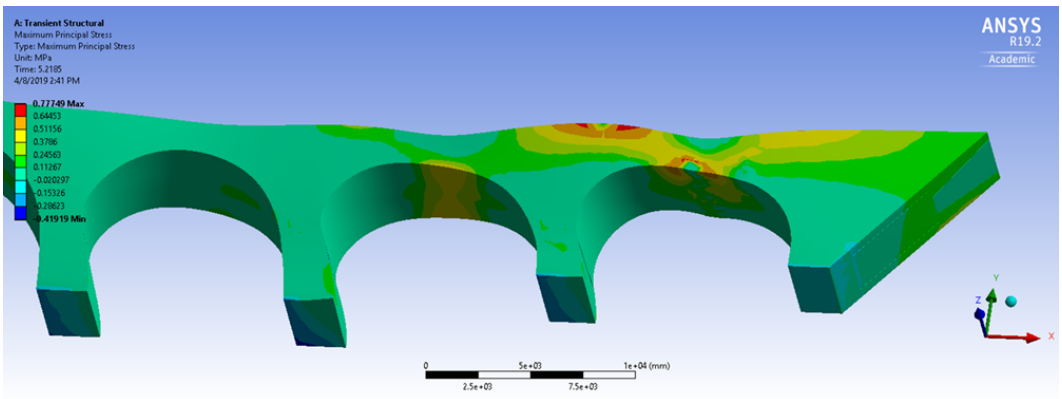

Figure 4.32. Principal stresses at the time of the damage occurred during RSN 285 Irpinia-Italy earthquake.

Last but not least, it is possible to say that the vertical component of the earthquake is not very effective. This was expected due to the reasons stipulated throughout the text. If we consider the effect of the geometry of the bridge and that the backing is masonry, it makes the bridge very stiff vertically, and there is little flexibility of the small part of the arch, which is encased in the fill. The vertical component of the earthquake would be more effective if the bridge had longer spans and shallow arches or more flexible backing material. Besides, the Bridge is not tall, and the vertical stresses in the piers are low. For tall piers, the vertical component of the earthquake would be more effective as well.

4.6.4. Comparison of NSA with NDA

There have been many comparisons between NSA and NDA results for common structures, especially for frame building systems. Similarly, there are some examples of comparisons that examine masonry structures of building typology [18, 83–85]. Examples of studies investigating masonry arch bridges [38, 65], however, are strikingly scarce, and they suggest similar results for both methods and the use of nonlinear static analysis for its simplicity. Thus, with this work, by comparing the results of the NDA and NSA in terms of structural behavior and numerically, we hope to contribute to the literature in this field.

In terms of behavior, both NSA and NDA present similar stress and strain distributions. The plasticity or the damage distribution seems to be fairly enveloped by the distribution observed in MPP analysis. This can be observed by comparing Figure 4.33 with Figure 4.19. This is generally true for the records where the effect of the first mode is dominant in the response. However, the damage distribution is different from the one observed in MPP analysis when the higher modes are dominant. Generally, we can say that the NDA gives a lot more information compared to the NSA since MPP analyses were not able to detect the damage mechanisms triggered by the higher modes of the Bridge.

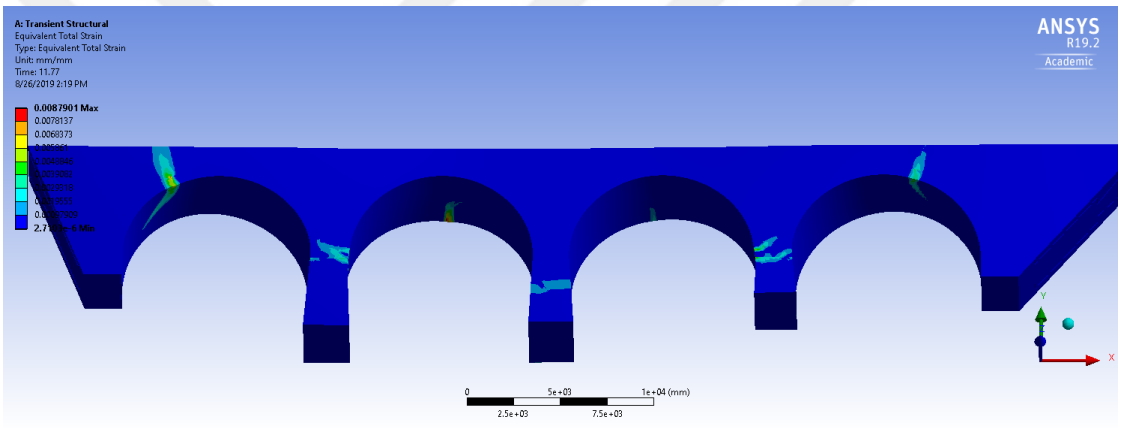

Figure 4.33. Results of the RSN1102 Kobe Japan earthquake.

In comparing the numerical results, the maximum accelerations and displacements obtained throughout the whole time-history are drawn together with the pushover curve in Figure 4.34. The comparisons are performed in terms of both displacements and accelerations. The use of the total mass in mass-proportional pushover analysis allows a direct comparison of the attained accelerations with the NDA results. As it is not feasible to compare the whole time-history results with the static analysis results, using the maxima of the displacement and acceleration time-histories seems appropriate. While the displacement demand is useful for ductile systems, accelerations are also important for massive and stiff structures. The earthquake determines the maximum lateral force for massive and stiff structures. In contrast, for ductile lumped-mass systems, the driver for the lateral force is the moment capacity of the structure [86].

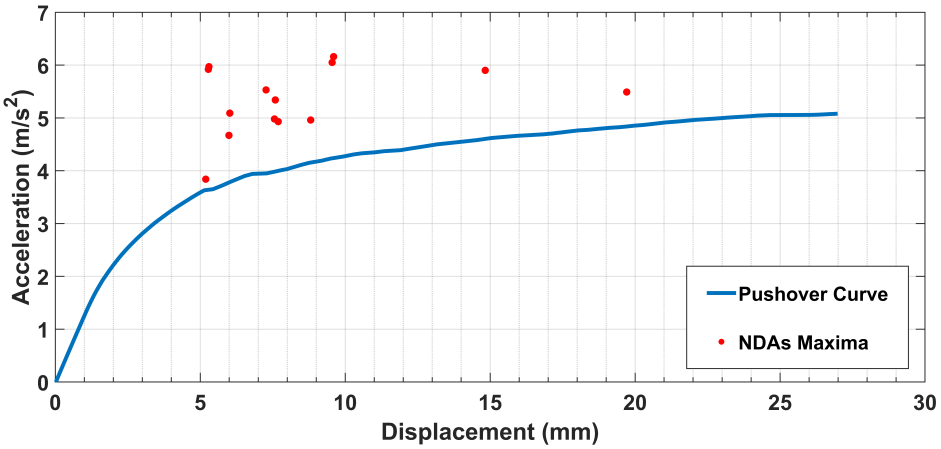

Figure 4.34. Pushover curve vs. NDA results for the CM node.

Our expectation that the PO curve would also envelop the results of the NDA falls short. Most of the NDA results are above the PO curve, and this becomes more prominent when the result comparison is made with respect to the TOP node. One reason might be the effect of higher modes causing NDA results to deviate from the NSA results since MPP analysis displacements are similar to the first mode shape, and the MPP analysis does not consider the higher modes. Indeed, when the first mode spectral accelerations are examined, they are much smaller than the maximum accelerations and closer to the MPP accelerations. Another reason is that most of the acceleration response spectra are above the target spectrum for the range of periods of interest, as seen in Figure 4.26. Finally, the complexity of the bridge's seismic response can be proposed as another reason. Similar results in terms of the differences between NSA and IDA analyses for masonry towers are reported in another research [87]. In the end, the average TOP and CM displacements obtained from NDA are 13.21 mm and 8.60 mm, whereas the performance displacements obtained from the NSA for TOP and CM control nodes are 11.61 mm and 7.78 mm, respectively. As the NSA predicts much lower accelerations for the bridge response (Figure 4.34), it might not be suitable even though the performance point displacement is close to the average NDA displacement.

Finally, the following comment may be made about the combination of the transverse earthquake component with the longitudinal and vertical components. The damage distributions obtained in the nonlinear dynamic analyses can be thought similar to

the distributions observed in nonlinear static analyses. However, the NDA give more information compared to the NSA. Moreover, MPP analyses were not able to detect the damage mechanisms triggered by the higher modes of the Bridge.

4.7. Incremental Dynamic Analysis

Since it was observed that the Mass Proportional Pushover analysis results were not reliable for the estimation of the structure's capacity, Incremental Dynamic Analysis (IDA) will be used as a credible tool to estimate the capacity curve. Incremental Dynamic Analysis [82] is a parametric analysis method that helps to describe the seismic performance of a structure exhaustively. The structural model is subjected to multiple ground motion records, each scaled to various levels of intensities, and then the responses are recorded as parametric curves of damage measure (DM) versus the intensity measure (IM). In this way, IDA provides a thorough understanding and a continuous picture of the structural response produced by the potential levels of ground motion records.

4.7.1. Intensity and Damage Measures

The 5% damped first-mode spectral acceleration is generally used as the intensity measure in building type structures as it is proven to be efficient and sufficient. Minimizing the scatter in the results and requiring only a few ground motion records to provide good demand and capacity estimates are related to efficiency, whereas sufficiency entails a complete characterization of the response without the need for magnitude or source-to-site distance information [82]. To the best of our knowledge, there is only one study carried out on the determination of suitable IMs to evaluate the seismic demand of masonry arch bridges, which is the work of Jahangiri *et al.* [88]. Also, the first-mode spectral acceleration is not the best choice. As demonstrated in the previous section, the maximum acceleration responses attained in NDA are generally much larger than the first-mode spectral accelerations, and structural response requires consideration of the higher modes. Considering the recommendation of Jahangiri *et al.* and in the

absence of a sensitivity study for IM, the maximum spectral acceleration is selected as the IM for the IDA conducted. As for the DM selection, it can be application-specific and we decided to use the maximum displacements attained in the analyses since they generally relate well to global dynamic instability and the structural performance limits we intend to define and focus on in future studies.

4.7.2. Record Selection and Scaling

As in the case of nonlinear time history analyses, the results of IDA are highly dependent on the selected record. In order to cover the full range of responses, a sufficient number of records are necessary. Thus, the same set of records presented in Table 4.2 was used for the IDA.

After determining the IM and DM, a similar algorithm to the hunt and fill algorithm [89] was used in conducting the nonlinear dynamic analyses. In order to cover the entire range of response, from elasticity to yielding and global dynamic instability, each record is generally scaled by 10% of the previous run. A maximum of fourteen runs was allowed for each record and more than 120 analyses were conducted in total, summing up to approximately 2300 hours of analysis duration. A 10% resolution on the collapse capacity was specified so that the collapse occurs at some intensity level, and this level is predicted within 10% of its IM level. When predicting the collapse, the numerical instability or attaining extreme values for the selected DM is evaluated as dynamic instability. This assumption implicitly considers that the numerical model is capable of representing the real structure in all ranges of the response. Therefore, the accuracy of the numerical model is of utmost importance. Notwithstanding this, the results are affected by the factors stated in the NDA section of the thesis, such as the quality of the numerical model, the step size of the time-integration, and even the round-off errors. After finding the collapse, the large gaps between the elastic response and the collapse are filled in with a manual intervention to ensure that an earlier collapse state was not missed.

As indicated, the process is not fully automated. Setting up the numerical model requires substantial time, but once it is done, it can be used for all the other analyses. On the other hand, the average analysis duration is very high, approximately 18 hours, and postprocessing the results require manual evaluation because the behavior of a 3D continuous system is much more complicated than the plane-frame structures.

4.7.3. Results

The IDA results are examined both qualitatively and quantitatively. The behavior of the bridge is complex, and each of the NDA presents a different story. Therefore, we start the analysis by examining the mode-shapes and the dictated behavior of the bridge, so that some of the damage observed in the analyses might give qualitative hints about the effect of specific structural modes.

4.7.3.1. Qualitative Observations. The first three mode shapes are in the form of a sinusoidal. The first mode has the highest mass participation ratio, cumulative 60.45%, the second mode has almost zero, cumulative 61.20%, and the third mode has 30% of the first mode, cumulative 78.00%. The first mode causes diagonal/inclined cracks in the side-piers and side arches, and transverse cracking in the mid-arch. The first three numerical mode shapes in plan-view are presented in Figure 4.35 to help visualizing the behavioral descriptions presented within the text.

The second mode has almost zero mass participation ratio. This might be a trivial thing stemming from two opposite vectors canceling out each other. It would cause transverse bending in the side-piers, i.e., horizontal cracks at the level of arch springing, cracks in the arch couples (left or right couples in plan-view) –which is only seen in the IDA for RSN 5618, and shear in the upper portion of the mid-pier – which is seen as a spandrel crack.

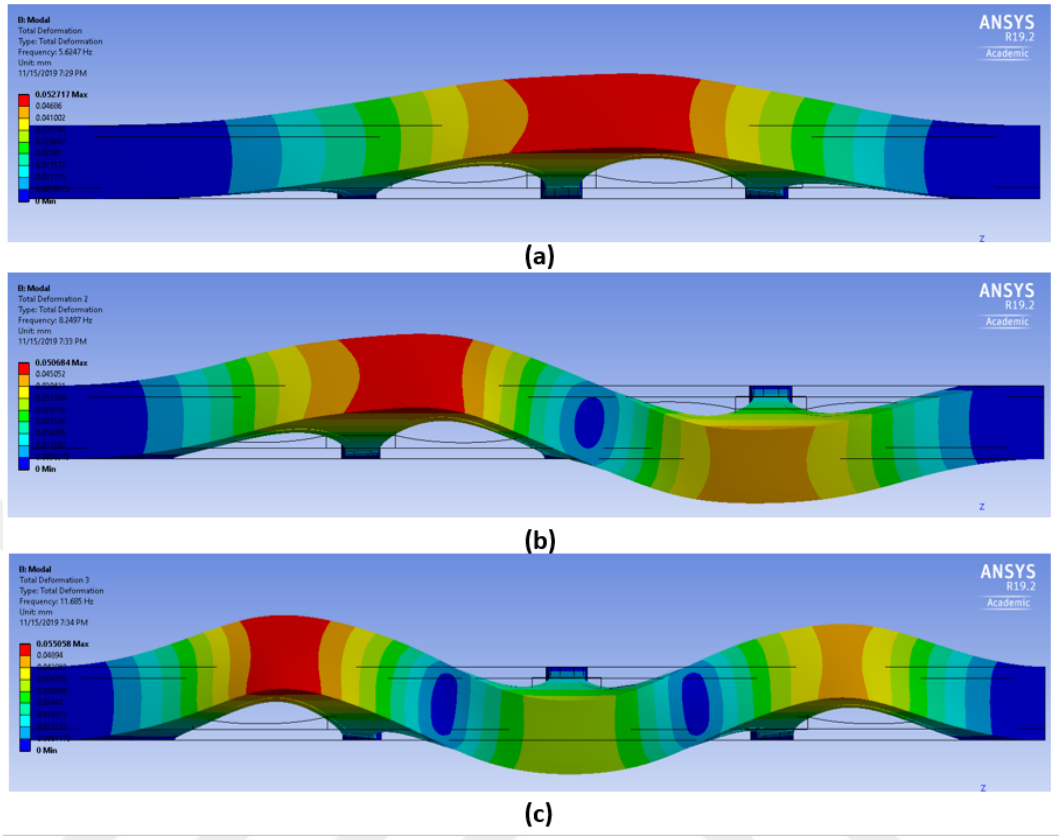

Figure 4.35. First three transverse mode shapes - plan view.

The third mode causes transverse bending of the mid-pier and possibly of the side-piers as well. It might be possible to observe spandrel cracking in the middle part of the Bridge, and side-arch cracking close to the arch springing or abutments. Mid-spandrel cracks and transverse cracks at the arch springing (top of the piers) due to mass proportional pushover analysis; therefore, the reason for observing such behavior should be the contribution of the second or the third mode. A pure third mode behavior is observed during the time-history analysis, and it is presented in Figure 4.36 below.

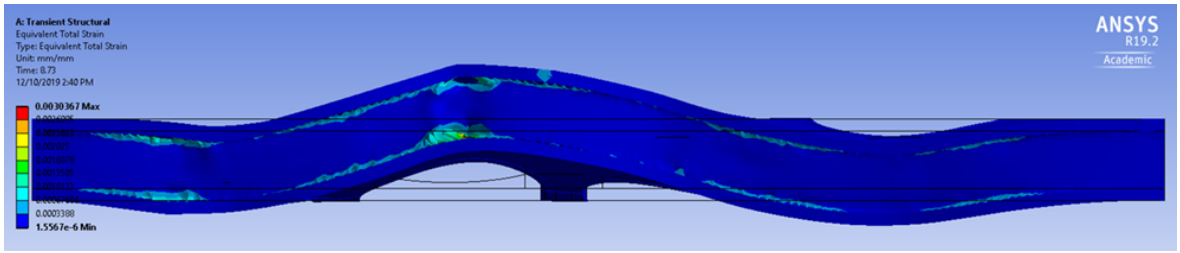

Figure 4.36. Third mode behavior observed during RSN 6928 IDA9 (plan view).

For the MPP behavior, the response seems to be dominated by the first mode (half-sine), but also it is not the same as the first mode obtained from the modal analysis. It looks like, in Figure 4.37, the first-mode behavior is stiffer than the MPP behavior. Two cases resemble a beam with fixed ends and pinned ends. This might explain why higher maximum accelerations are attained in NDA. It should be stated that the beam analogy is just an analogy. MPP behavior is not as natural as the mode shapes. That is why the first mode and MPP displacement shapes are different. Moreover, in the absence of a "right transformation," the MPP analysis cannot be expected to give results compliant with NDA.

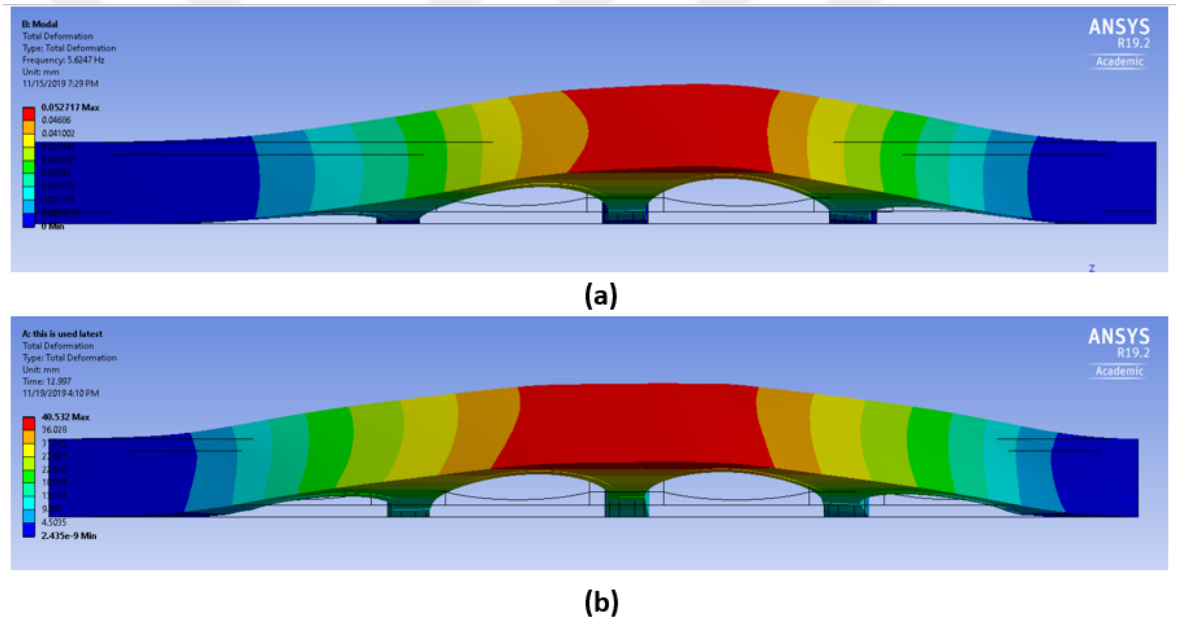

Figure 4.37. (a) First mode displacements, (b) MPP displacements.

The observations pertinent to the NDA behavior that was mentioned previously, such as the early damage altering the structural behavior completely, are also valid for the IDA, as IDA is essentially an NDA. Additionally, the first mode related plasticity is always dominant in all the responses, regardless of the earthquake records' frequency content, probably because of the first mode's high mass participation ratio. As the scale of the records increases, the second and third modes also show their effects and cracks occur in the mid-spandrel, mid-pier, and side-piers in the transverse direction, and in the mid-arches at the mid-heights, as seen in Figure 4.30. An example of multiple spandrel cracking due to higher mode effects is illustrated in Figure 4.38.

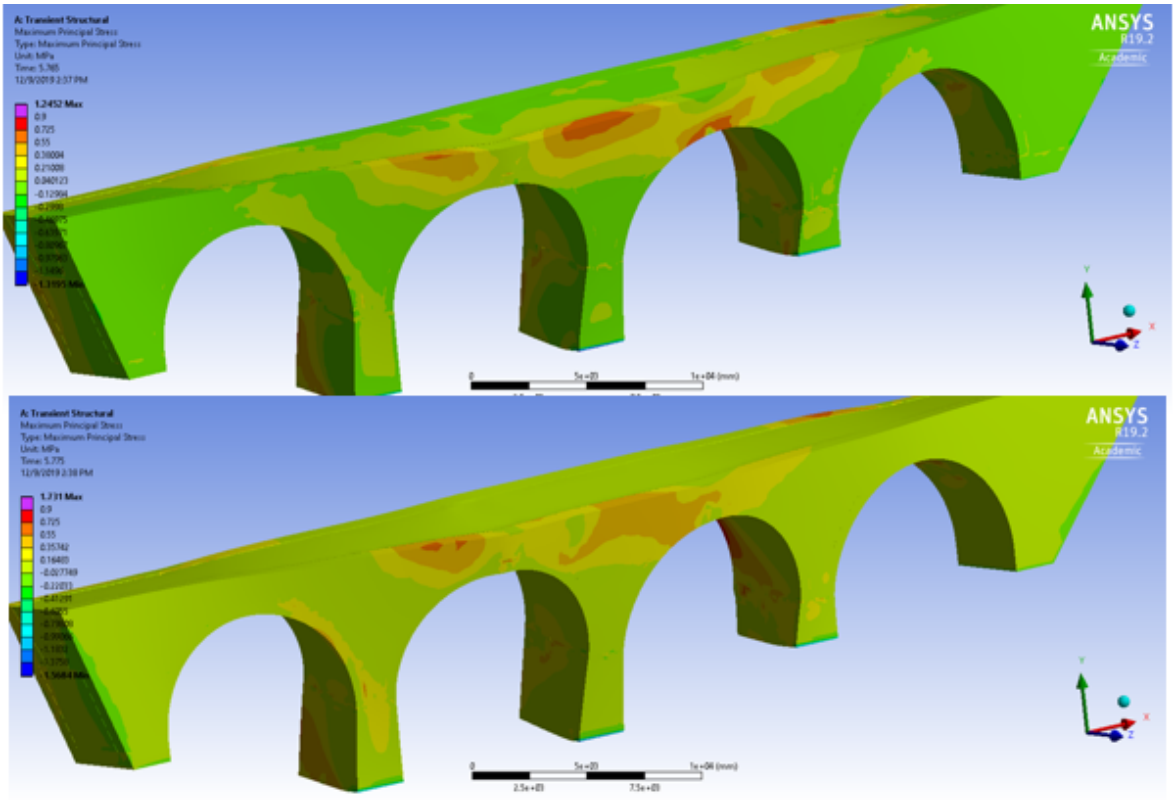

Figure 4.38. Multiple spandrel cracks from max principal stress plot - two subsequent steps (RSN 6928 IDA8).

In addition to those observations, we can add that in a single-record IDA, total strains usually increase dramatically, and the damage patterns change.

4.7.3.2. Quantitative Observations. The system's high response during an earthquake with a given intensity level may change due to damage. Consequently, the same or even lower response might be observed when the system is subjected to higher seismic intensities. With the scaling up of the accelerations, the weak response cycles observed in the early part of the response time-history get stronger, sometimes strong enough to cause damage, so that the properties of the structure and the response to the subsequent stronger cycles change. In addition, depending on the frequency content of the earthquake record, increasing fundamental periods of the system may resonate with the earthquake's dominant frequency and thus inflict more damage to the structure. There are several examples of this phenomenon, and some of them are demonstrated in the figures below. An increase in the structure's period and the behavior change

is observed in Figure 4.39, where the displacement responses of the CM node in the transverse direction are compared.

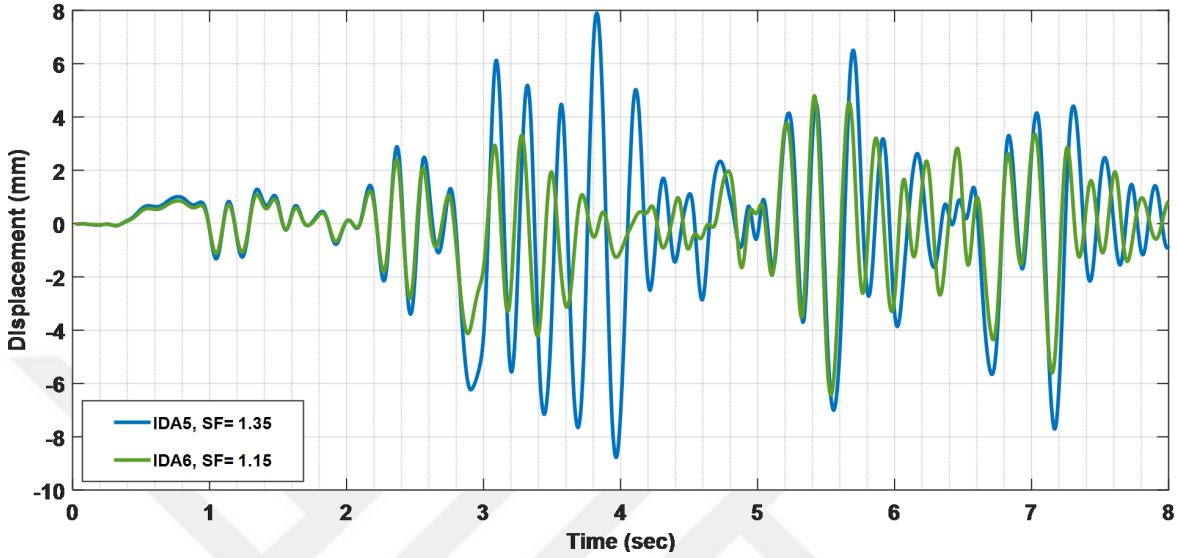

Figure 4.39. Change in the displacement time-history of "RSN 1161 Kocaeli" earthquake.

The location and timing of the maximum response quantity, such as displacement, acceleration, or strains, may change. The dominance of a particular mode in the response can also change. The shift in the responses, for example, the structural frequencies, can be tracked from the Fourier Amplitude Spectra of the acceleration responses. As the scale-factor increases, the FAS increase and shift to the left, as illustrated in Figure 4.40, because the inflicted damage cause the structure to lose stiffness. Moreover, the shape of the FAS remains similar, but separate peaks become more evident, as in Figure 4.41. Indeed, the fundamental frequencies shift and the dominant peaks in the behavior change. However, we cannot tell whether these correspond to the second and third modes or some new, and maybe local, modes occurring because of the damage. The FAS of the TOP and CM node responses are very similar.

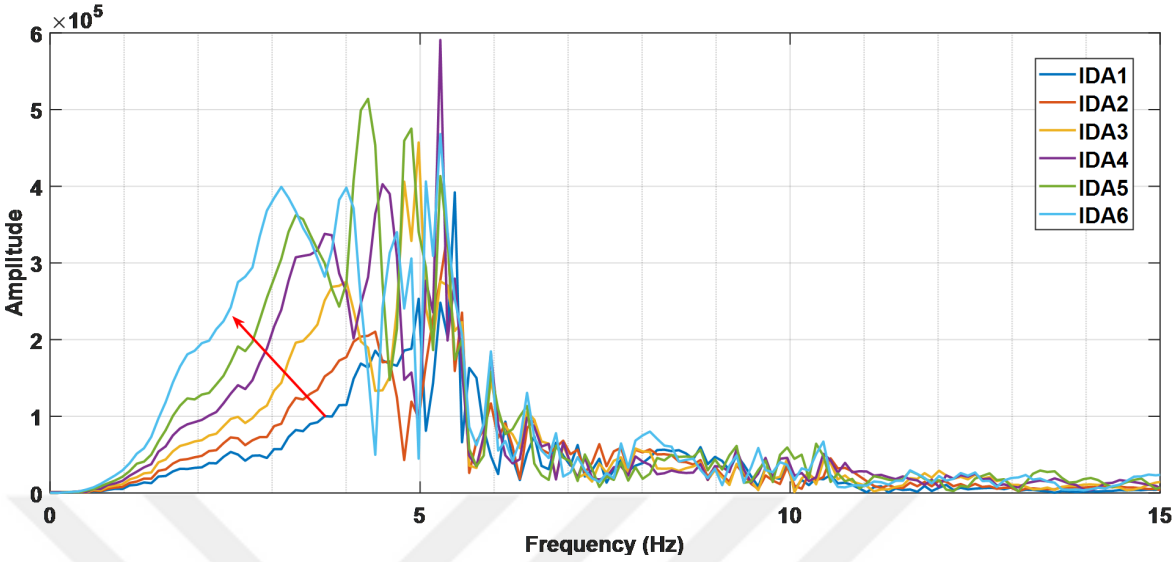

Figure 4.40. FAS of the acceleration responses of RSN 2627 IDA.

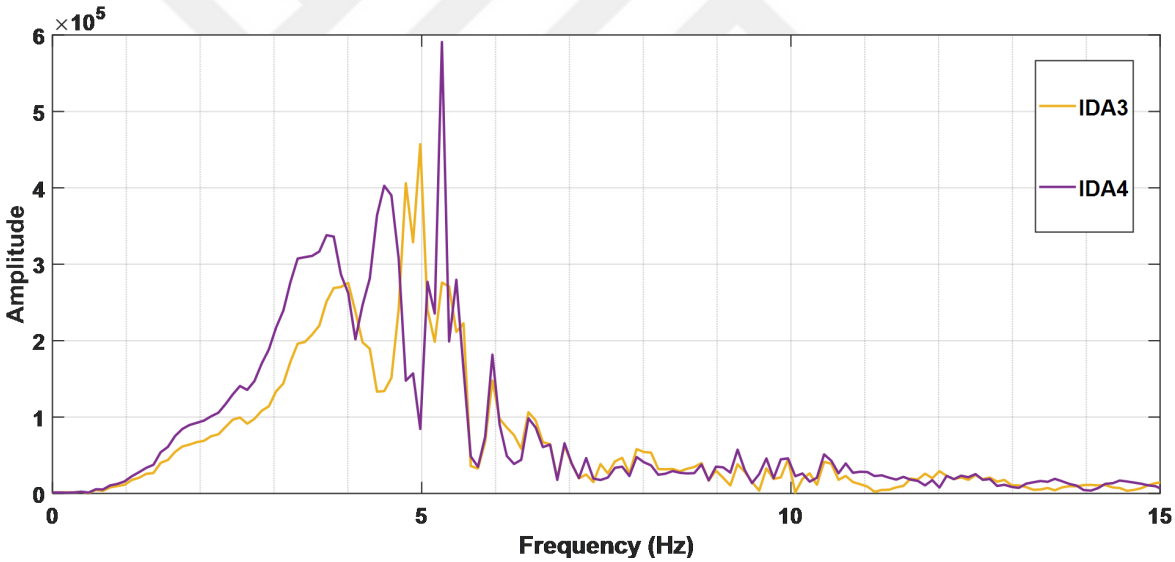

Figure 4.41. Peaks becoming more significant in RSN2627 IDA.

IDA curves for CM node and the corresponding pushover curve are drawn, in Figure 4.42, using maximum spectral accelerations as intensity measure and the maximum displacements as the damage measure. The comparison of average IDA and PO curves (Figure 4.43- RSN 6928 results are excluded) enables us to confirm the previous conclusions related to the difference between NDA and NSA results. Please recall that the NDA results were generally higher than the MPP results. The causes were stressed as *i*) the first mode spectral acceleration being smaller than the max spectral acceleration, *ii*) the most of the acceleration response spectra being high above the

target spectrum for the range of periods of interest and *iii*) the effect of higher modes causing NDA results to deviate from the NSA results as the MPP analysis does not account for the higher modes. Thus, the average IDA curve represents the capacity of the structure in a more reliable manner.

Notice that in Figure 4.42, the individual IDA curves differ from the PO curve even in the elastic range. This is contrary to what is assumed in the work of [82]. On the other hand, Figure 4.43 shows that the average of IDA curves and the PO curve overlap in the elastic range of the behavior.

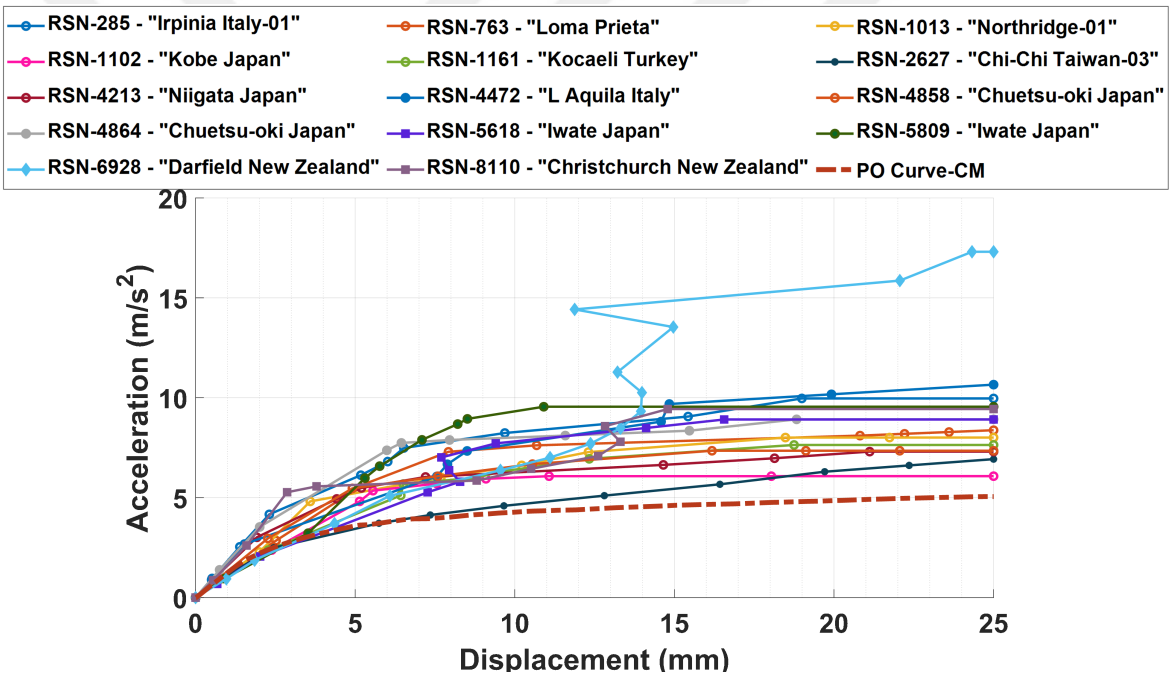

Figure 4.42. IDA curves for CM node using spectral acceleration as IM.

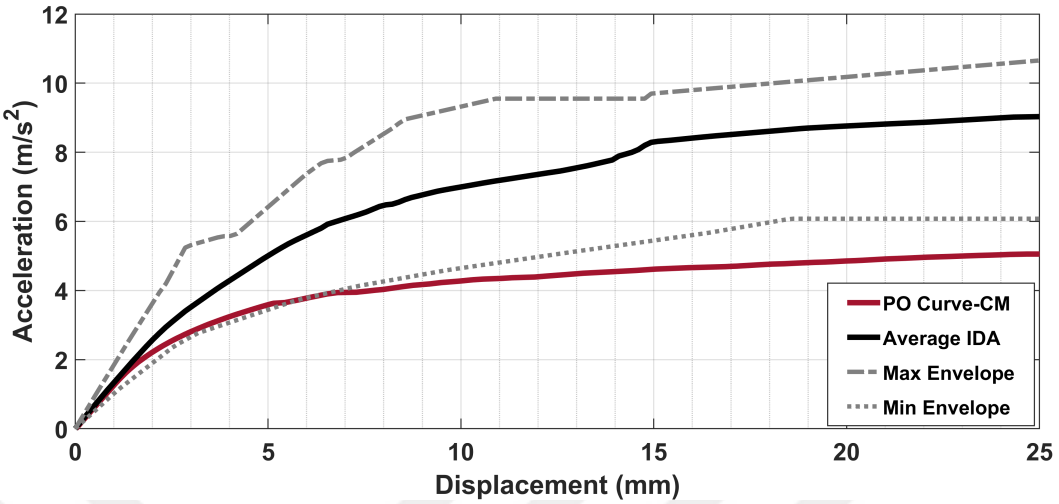

Figure 4.43. Characteristic IDA and PO curves for the CM node.

As a side note, the spectral acceleration is available only for the TOP node. Using the mean ratio of the TOP/CM acceleration, the spectral acceleration for the CM node is obtained. If the IDA curve is cut short, i.e., the non-convergence occurs, and no further analysis results are available, then the last point on the curve (i.e., the ultimate displacement) is connected to 25 mm and 39 mm displacements for the cases of CM and TOP nodes, respectively, with the same acceleration value. This is necessary because the IDA curves have different lengths, and they should be standardized to calculate the average curves.

Another remark is the choice of the intensity measure. As mentioned earlier, there is no previous work to determine the suitable IMs to evaluate the seismic behavior masonry arch bridges. However, a recent work by Jahangiri *et al.* [88] demonstrates the impact of IM selection on plain concrete bridges. In the present study, significant differences between the IDA curves were observed if the IM was selected as the maximum acceleration attained during the response time-history. Nevertheless, this IM does not comply with the IM definition of Vamvatsikos and Cornell [82], from whom the method originates, and the results are not presented.

Overall, each earthquake is a different scenario: different excitation, different behavior, and different damage evolution. Moreover, each IDA is another story: timing,

magnitude, and pattern of accelerations combined with the excitation characteristics may result in completely different behavior, which is not easily tracked by checking discrete pictures or values only. Therefore, in our opinion, research on the IDA of masonry structures must focus on the "whole movie" rather than just the snapshots.

5. LABORATORY EXPERIMENTS

"Nobody believes the analysis results except the person who devised it; everyone believes an experiment except the one who performed it."

An altered version of the quote from A. Einstein

In this chapter, the sources of uncertainties in determining the elasticity modulus of masonry are investigated and highlighted by using various non-destructive, minor-destructive, and destructive tests. A masonry panel wall is constructed with similar stone and mortar types to that of Bridge 41. First, the mechanical characterization of the masonry components is done. Their results are used in empirical equations provided by international standards to obtain the homogenized material properties. Masonry wallettes are also built and tested to calculate the elasticity modulus. Several non-destructive and minor-destructive tests are performed on the masonry panel wall. Next, the panel wall is tested under cyclic in-plane shear-compression loading. A 3D FE model of the wall is generated in order to determine the elasticity modulus by matching the experimental and numerical results. In this part of the thesis it was aimed at obtaining knowledge by laboratory testing to determine the uncertainty in the elasticity modulus value of Bridge 41.

Not only in the assessment of existing masonry structures but also for the design of new ones, only a few mechanical properties of masonry are used regardless of the chosen approach within the wide range of analysis techniques available. Amongst the mechanical properties, the compressive strength of masonry appears to be the primary parameter considered by the design codes and the researchers so far. It is used to derive the other mechanical properties, such as the modulus of elasticity, as it is relatively easier to obtain this parameter using the well-established test methods. Therefore, a

noteworthy amount of experimental and numerical research has been conducted regarding compressive strength. Consequently, the determination of the compressive strength of masonry is now rather a straightforward issue compared to the other mechanical properties. On the other hand, Elasticity Modulus (or Young's Modulus) still constitutes the most important uncertainty in the assessment and testing of masonry [39, 90, 91]. Evidence suggests its variability is due to the masonry composition and morphology, as well as to the assumptions made in the different test methods. The uncertainties caused by using different test methods and their direct influence on the numerical analysis results, however, have not been fully investigated.

There are various works of experimental characterization of masonry and its constituents in the published literature. The following examples include mostly the destructive laboratory and in-situ testing. Rao *et al.* [92] present one of the early examples that investigated the strength characteristics of stone masonry and how they change with different mortar properties. Corradi *et al.* [93] and Chiostrini *et al.* [94] conducted several compression, diagonal compression, and shear-compression tests on in-situ masonry wall panels and obtained strength and stiffness values. They also compared these values to those given in different standards. Sarangapani *et al.* [95] investigated the effect of the masonry bond strength on the compressive strength and failure pattern of masonry prisms. Oliveira *et al.* [90] performed cyclic uniaxial compression tests on stone and masonry specimens and highlighted their properties, such as the brittleness and the intrinsic variability of strength and elastic modulus. Gumaste *et al.* [96] focused on the compressive strength and elasticity modulus of brick masonry prisms and how these values change with different bonding arrangements and mortar strengths. Vasconcelos and Lourenço [97] pointed out the need for determining the mechanical parameters of stone masonry for the assessment and numerical analysis. Then, they implemented parametric experimental testing on masonry wallettes to determine their elasticity modulus and compressive and shear strength. Magenes *et al.* [98] examined the mechanical characteristics of stone masonry walls via vertical and diagonal compression tests and compared the results to the ones proposed in standards. Garcia *et al.* [99] carried out compression tests on stone masonry wallettes and compared the

results to those given in standards. Almeida *et al.* [100] studied the mechanical characterization of one-leaf stone masonry walls under compression, the relationship between compressive strength and elasticity modulus, and the effect of injection with mortar. Demir and Ilki [101] conducted an experimental campaign to characterize the single-leaf and multi-leaf masonry walls that are frequently observed in historical structures in Istanbul. Lumantarna *et al.* [102] investigated the compressive strength and stiffness of brick masonry prisms and the relationship between these two parameters. Drougkas *et al.* [103] carried out an experimental campaign on brick masonry with lime mortar joints and investigated the relationship between the compressive strength and stiffness of masonry prisms.

On the other hand, the experimental characterization of the masonry elasticity modulus using Non-Destructive Testing (NDT) and Minor-Destructive Testing (MDT) is very scarce. Until recently, NDT and MDT were used only for the qualitative investigation, monitoring and to obtain information locally due to the difficulty encountered in evaluating their results, whereas the input parameters for numerical models obtained by destructive testing [104, 105]. However, the trend is shifting towards more sophisticated use of NDT and MDT methods and of numerical approaches in estimating the elasticity modulus. Brencich and Sabia [48] conducted a series of NDT and MDT on a masonry bridge and compared the results to those obtained from destructive testing. Miranda *et al.* [106] proposed a new acoustic test method to characterize the elastic modulus of stone masonry walls. The method was later used on various stone masonry walls, and the modulus of elasticity values were compared to those found from compression tests [107]. Bartoli *et al.* [91] implemented in-situ flat-jack and dynamic tests in order to determine the mechanical parameters of the historical masonry tower. Drougkas *et al.* [108] worked on the numerical prediction of the behavior and mechanical characteristics of masonry in compression via the finite element micro-modeling technique. Makoond *et al.* [109] investigated the dynamic elasticity modulus of brick masonry components and the compatibility of the values obtained from the Impulse Excitation of Vibration and Ultrasonic Pulse Velocity tests.

The commonly used structural standards for masonry utilize the elastic stiffness of masonry walls [62] for in-plane shear loading and directly use the modulus of elasticity of masonry in stiffness calculations [77, 78]. Two of the most commonly utilized modeling strategies in research; continuum models such as Finite Element modeling and structural element models such as Equivalent Frame modeling require the definition of elasticity modulus of masonry [110]. Whether in practice or research, experimental tests are the main source for material characterization for the analytical models used in structural assessment and design. Testing the whole structure is often not physically possible or economically feasible, and the material properties obtained from local tests are often considered to be representative of the whole structure. However, the elasticity modulus, for example, can only represent the average deformability of the part of the structure that is measured and not the individual stones or mortar. The presented literature review suggests that most studies are limited to the comparison of only a couple of test methods, and there is not enough evidence on the similarity of results from distinct experimental campaigns on large samples. In contrast, significant variations in the results might be observed, depending on the experimental technique used. Such limitations encountered in testing can change the outcomes of the analytical approaches when analyzing the "global behavior" of the structure. The uncertainty in predicting the elasticity modulus is eventually carried to the structural analysis, as the elasticity modulus obtained from experimental tests are directly used in numerical models. Therefore, a considerable variation in the numerical analysis results might occur and jeopardize the reliability of the seismic assessment. That is why reliable estimation of elasticity modulus is of extreme importance.

The purpose of this study is to find the elasticity modulus of a stone masonry panel wall by several destructive, minor-destructive, and non-destructive tests as well as using numerical modeling and empirical equations from the standards. Masonry components, i.e., the stone and the mortar, were tested under compression and flexure at the laboratory first. Their results allowed the use of empirical homogenization equations obtained from the standards. Then, masonry wallettes were tested in compression, and the elasticity modulus was determined. Increasing the material scale

gradually, from the components to the size of a masonry panel wall constructed at the laboratory, vertical compression, flat-jack, ultrasound, and ambient vibration tests were carried out on the masonry wall. The comparison of the results helped to identify the uncertainties related to elasticity modulus estimation and the methods that enable determining the parameters representative of the global behavior of the structure. In addition, various range of parameter values obtained from different tests provided information for probabilistic structural analysis. This study also demonstrated the influence of the uncertainty in the elasticity modulus of masonry on the numerical analyses results. After obtaining the modulus of elasticity using various approaches, the cyclic shear-compression test result of the panel wall was compared to the nonlinear static pushover analyses results, which were carried out for different values of elasticity modulus. How the uncertainty in elasticity modulus of masonry propagated into the results of the analyses is illustrated using a simple and commonly used approach.

5.1. Masonry Component Tests

Masonry components, i.e., stone and mortar, were tested under compression and flexural loading in order to determine their compressive and flexural-tensile strength. These values are later used in empirical formulae to obtain homogenized material properties. Masonry components tests were performed at Boğaziçi University Construction Materials Laboratory. The ashlar stones were bought from Hantaş quarry in Çamkonak Village, Kandıra-Kocaeli. It is classified as "clayey-limestone," which has a composition of approximately 85% limestone and 15% clay. Its composition is similar to the stone used in Bridge 41. The stone is fine-grain and not uniform, and it has a pale-yellow tone color. It is used in new constructions as well as a replacement for old ones. The NHL mortar was prepared by mixing Teknorep 500 and natural sand in 1:3 weight proportions. The amount of water was determined on-site as per the consistency requirements for the ease of construction. Teknorep 500 is a special natural hydraulic lime mix that is developed for applications in historical structures, and it contains no cement.

5.1.1. Compressive Strength of Stone Units

Tests were carried out according to EN 772-1 [111], "Methods of test for masonry units. Determination of compressive strength" standard, which includes instructions for the preparation, storage, test setup, and the procedures. Twelve cubic specimens with an edge length of 100 mm were kept in laboratory conditions for more than 14 days, according to the standard. The choice of 100 mm edge length was the result of the desired shape factor (1.0) for the normalized compressive strength calculation. Loaded surface areas were calculated after the edges had been measured with a sensitive caliper. First, the specimens were loaded, using MTS servo-hydraulic test machines with 500 kN capacity, up to 5 kN to remove bedding effects between the loading platens and the surface, and then they were unloaded. Afterward, each specimen was loaded up to the point of failure with 0.3 $(N/mm^2)/s$ loading speed. Figure 5.1 shows the stone specimens before and after the tests, and Figure 5.2 displays the force-displacement behavior of the specimens. Note that some of the graphs do not start from the origin due to the initial calibration of the MTS loading machine. Still, the stiffness obtained from the first part of each graph is coherent, and we are only interested in the maximum load.



Figure 5.1. Stone specimen before and after the test.

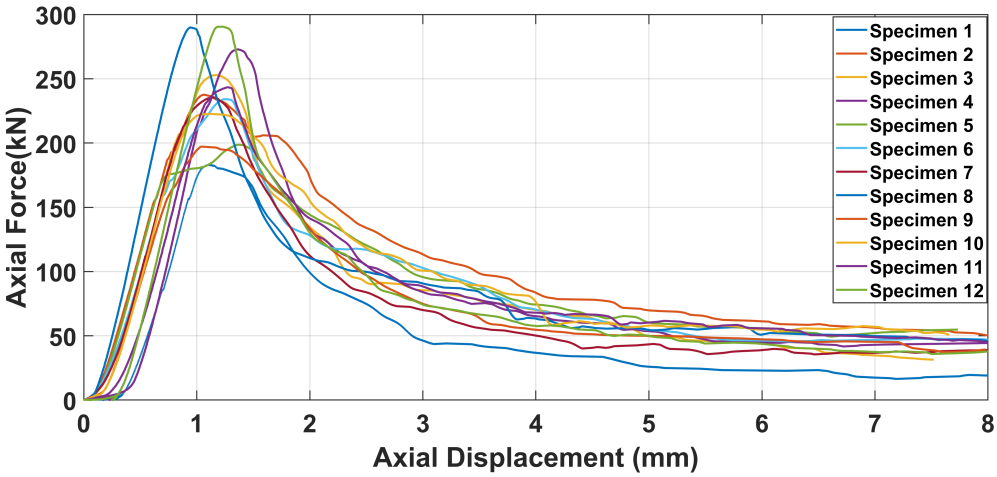

Figure 5.2. Force-displacement graphs of stone specimens under compression.

The maximum compressive stresses attained for each specimen are presented in Table 5.1. The average compressive strength of the stone was calculated as 23.3 MPa with a standard deviation of 3.2 MPa. The coefficient of variation is 0.14. The stones are taken from the same part of the rock quarry; thus, the obtained variation of results is relatively low.

Table 5.1. Compression tests results of stone specimens.

Specimen #	**Max Load (kN)**	**Surface Area (mm^2)**	**Stress, σ (MPa)**
1	183.17	10100.0	18.14
2	237.89	10302.0	23.09
3	253.14	10302.0	24.57
4	273.13	10049.5	27.18
5	199.03	10351.5	19.23
6	234.43	10201.0	22.98
7	235.92	10251.0	23.01
8	290.16	10609.0	27.35
9	197.54	9999.8	19.75
10	222.96	10200.0	21.86
11	243.70	10251.0	23.77
12	290.81	10302.0	28.23
Average	238.5	10243.2	**23.26**
Std. Dev.	34.9	158.7	**3.24**

5.1.2. Flexural-Tensile Strength of Stone Units

The EN 12372 [112] standard was used in order to determine the flexural strength of the stone units. Sixteen specimens with dimensions of 50x50x300 mm^3 were placed on roller supports 250 mm apart. Then, each specimen was concentrically loaded, with a 0.083 kN/s speed, in the middle until flexural tensile stresses at the middle portion of the stones caused tension crack and the failure of the specimens. Testing is shown in Figure 5.3, while the force-displacement behavior of the specimens is presented in Figure 5.4. Note that none of the cracks occurred more than 37.5 mm away from the middle of the specimens (15% of the distance between roller supports).

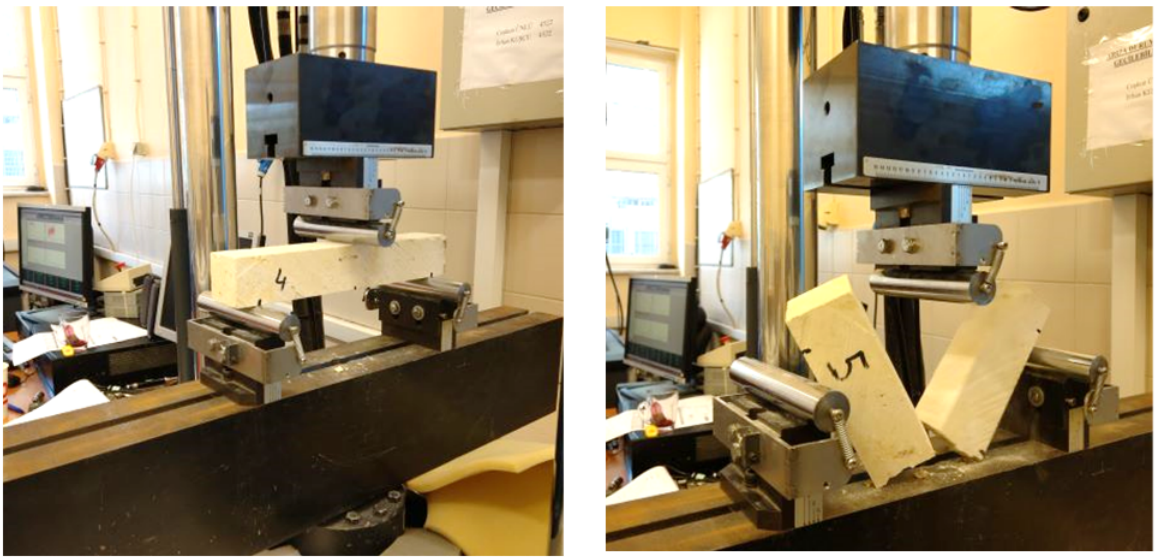

Figure 5.3. Stone specimens before and after the flexural tests.

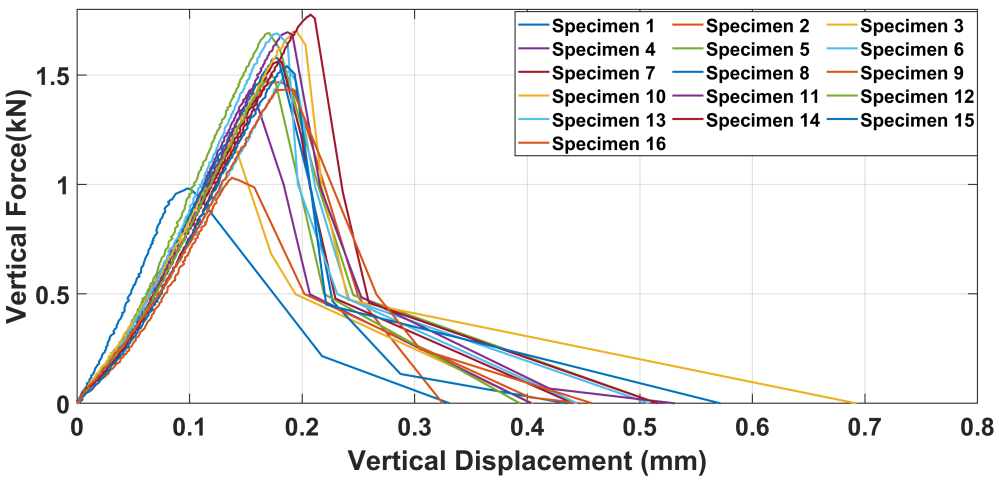

Figure 5.4. Force-displacement graphs of the prism specimens.

The maximum tensile stresses attained for each specimen are presented in Table 5.2. In the end, the flexural-tensile strength of stone specimens was calculated as 4.45 MPa with a standard deviation of 0.71 MPa. Besides, the lower expected value was calculated as 3.09 MPa. The ratio of the tensile strength of the stone to its compressive strength is 19.1%.

Table 5.2. Flexural-tensile tests results of stone specimens.

Specimen #	**Fmax (kN)**	**Stress (MPa)**
1	0.98	2.94
2	1.47	4.41
3	1.17	3.51
4	1.43	4.30
5	1.69	5.07
6	1.52	4.55
7	1.56	4.68
8	1.58	4.74
9	1.03	3.09
10	1.70	5.09
11	1.69	5.08
12	1.49	4.47
13	1.69	5.07
14	1.78	5.33
15	1.54	4.62
16	1.43	4.30
Average	**1.48**	**4.45**
Std. Dev.	**0.24**	**0.71**
C.o.V	**0.16**	**0.16**

5.1.3. Flexural-Tensile and Compressive Strength of Mortar

Flexural and compressive strength of mortar were found according to EN 1015 [113] standard. Mortar samples were taken during the construction of the panel walls, cast in 40x40x160 mm^3 molds, stored and cured according to the related standard.

Each sample consisted of three specimens. All specimens were tested under three-point-bending first, and the two pieces obtained from each bending test were tested in compression later.

Six specimens with dimensions of 40x40x160 mm^3 were placed on roller supports 100 mm apart, and loaded in the middle, as shown in Figure 5.5. The loading speed was 0.03 kN/s. The flexural tensile stresses at the middle portion of the mortar specimens caused tension crack and splitting of the specimens. The average flexural-tensile strength of NHL mortar specimens was calculated as 1.00 MPa with a standard deviation of 0.06 MPa. The force-displacement behavior of the specimens is presented in Figure 5.6, and the results are given in Table 5.3.

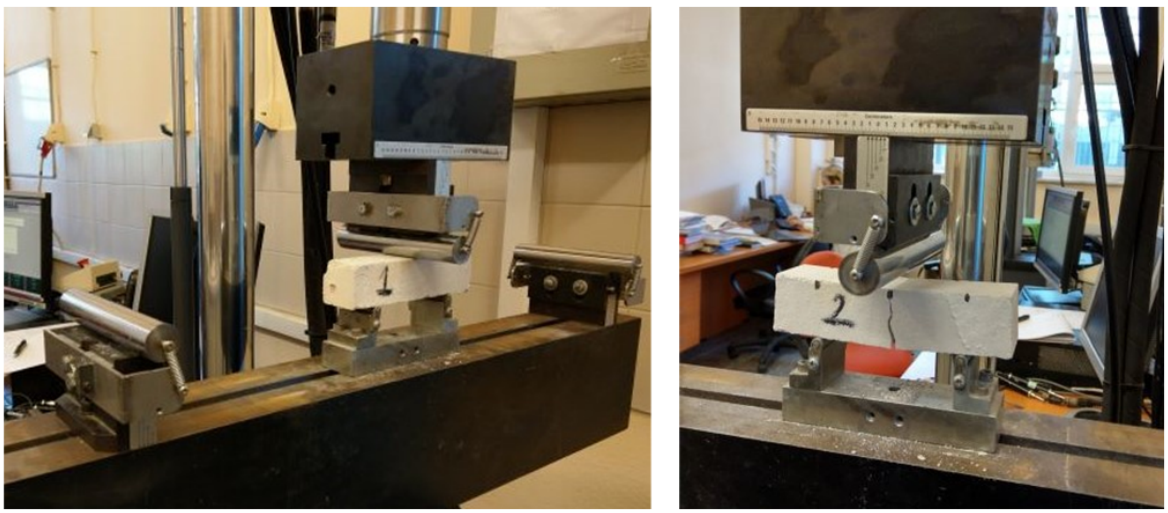

Figure 5.5. Mortar specimens before and after the bending test.

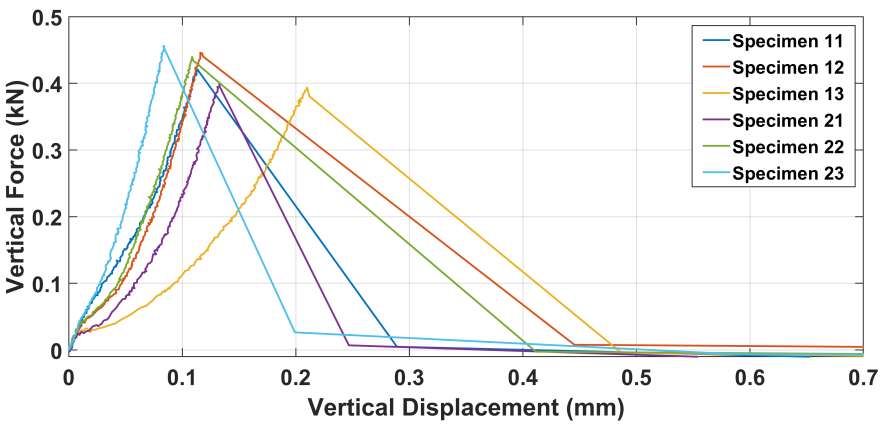

Figure 5.6. Force-displacement graphs of the NHL mortar prism specimens under bending.

Table 5.3. Flexural-tensile test results of NHL mortar specimens.

Specimen #	**Fmax (kN)**	**Stress (MPa)**
11	0.42	0.99
12	0.45	1.05
13	0.39	0.92
21	0.40	0.94
22	0.44	1.03
23	0.46	1.07
Average	**0.43**	**1.00**
Std.Dev	**0.03**	**0.06**

For the compression tests, pieces of the six specimens, i.e., 12 specimens, were used according to the standard. The specimens were loaded in compression between 40x40 mm^2 steel plates, with 0.1 kN/s loading rate, until the crushing occurred, as shown in Figure 5.7.



Figure 5.7. NHL mortar specimens before and after the compression test.

The average compressive strength of NHL mortar specimens was calculated as 2.74 MPa with a standard deviation of 0.14 MPa. Table 5.4 presents the results, and Figure 5.8 displays the force-displacement graphs of the specimens. The ratio of the tensile strength of the NHL mortar to its compressive strength is 36.5%.

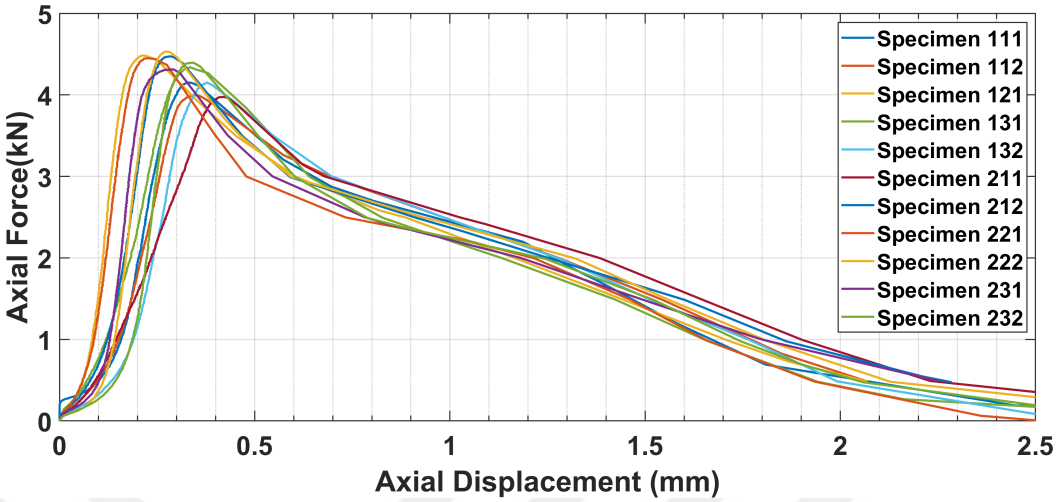

Figure 5.8. Force-displacement graphs of the NHL mortar specimens under compression.

Table 5.4. Compression test results of NHL mortar specimens.

Specimen #	**Max Load (kN)**	**Stress (MPa)**
111	4.05	2.53
112	4.10	2.56
121	4.59	2.87
131	4.44	2.78
132	4.25	2.66
211	4.08	2.55
212	4.59	2.87
221	4.56	2.85
222	4.64	2.90
231	4.42	2.76
232	4.50	2.81
Average	4.38	**2.74**
Std.Dev	0.22	**0.14**

The results do not present a significant scatter as expected. The reason behind this might be using only a few samples taken from the same batch (or the bucket) of mortar. On the other hand, the technical sheet of NHL mortar suggests a compressive

strength greater than 3.70 MPa and a tensile strength greater than 1.0 MPa. We see that the tensile strength value complies with the test results, whereas the compressive strength seems lower.

Tests on mortar samples were done after 28 days of curing. It would have been better to plan more tests on different curing ages, such as seven days, 60 days, and 90 days, in order to observe the strength evolution of the mortar. The common assumption is that the material reaches close to its peak resistance after 28 days, while it gains its full resistance after 60 days as the curing process is completed [98]. This might be important in our case because the wallette compressive strength turned out to be higher than expected, and it will be elaborated in the related section.

5.2. Empirical Equations

Exponential empirical models for predicting the masonry compressive strength have found wide application due to their simplicity. Compressive strengths of the individual masonry components are considered together with a coefficient that accounts for the regression analysis of the empirical results. They often have the following form in Equation 5.1:

$$f_{c,mas} = K \cdot f_{c,st}^{a} \cdot f_{c,mo}^{b} \tag{5.1}$$

The coefficients and the exponentials may vary according to different material types and standards. For example, EN 1996-1-1 (Eurocode 6) standard equation and "RIL 805 [114] - Structural safety of existing railway bridges" standard equation for natural stone masonry result in completely different values, as presented in Equation 5.2 and Equation 5.3, respectively:

$$f_{c,mas} = 0.45 \cdot 23.3^{0.70} \cdot 2.74^{0.30} = 5.51 MPa \tag{5.2}$$

$$f_{c,mas} = 0.80 \cdot 23.3^{0.80} \cdot 2.74^{0.20} = 12.15 MPa \tag{5.3}$$

Other standards also suggest empirical formulae, such as TMS 402/602 [115], NTC 2018 and NZSEE 2015 [116]. However, the equations are given for brick masonry type rather than natural stone masonry.

Using the approach that correlates the compressive strength and elastic modulus of masonry, one can obtain the Modulus of Elasticity for the masonry panel wall. Eurocode 6 uses the $E_{mas} = 1000 \cdot f_{c,mas}$ equation, but it should be stated that there exist different approaches in various international standards. For example, FEMA 356 recommends $E_{mas} = 550 \cdot f_{c,mas}$ and TBDY 2018 proposes $E_{mas} = 750 \cdot f_{c,mas}$. Generally, the coefficient changes between 300-1000.

5.3. Masonry Wallettes

Compression tests of masonry wallettes were carried out according to EN 1052-1 [117] European standard. MTS servo-hydraulic test machine with 500 kN capacity was used. Ten specimens were constructed, each using eight stones with dimensions 150x80x120 mm^3 and four stones of dimensions 75x80x120 mm^3 as well as the NHL mortar used for the construction of the panel wall. The same type of stone was used for the wallettes as the one used for the panel wall. The average mortar thickness is 10 mm, and the approximate dimensions of the wallettes are 320x440x120 mm^3, as shown in Figure 5.9a. The volumetric content of each constituent, Vstone and Vmortar, were determined as 85.23% and 14.77%, respectively.

Before the tests, each wallette specimen was built between 20 mm thick steel plates to facilitate transport. A fine layer of gypsum plaster was applied between the specimens and steel plates to provide smooth contact surface and to level the steel plates for even loading. Uniform loading is assured by the hinge of the upper loading platen of the MTS testing machine. Also, the net loading areas of wallettes were calculated using the edge lengths of each wallette. Two LVDT's were placed on each side of the wallettes to measure the vertical displacements as per the standard. Additionally, one horizontal LVDT was placed in the middle of the wallettes to determine the horizontal

deformations, and eventually, the Poisson's ratio. The instrumentation can be seen in Figure 5.9b.

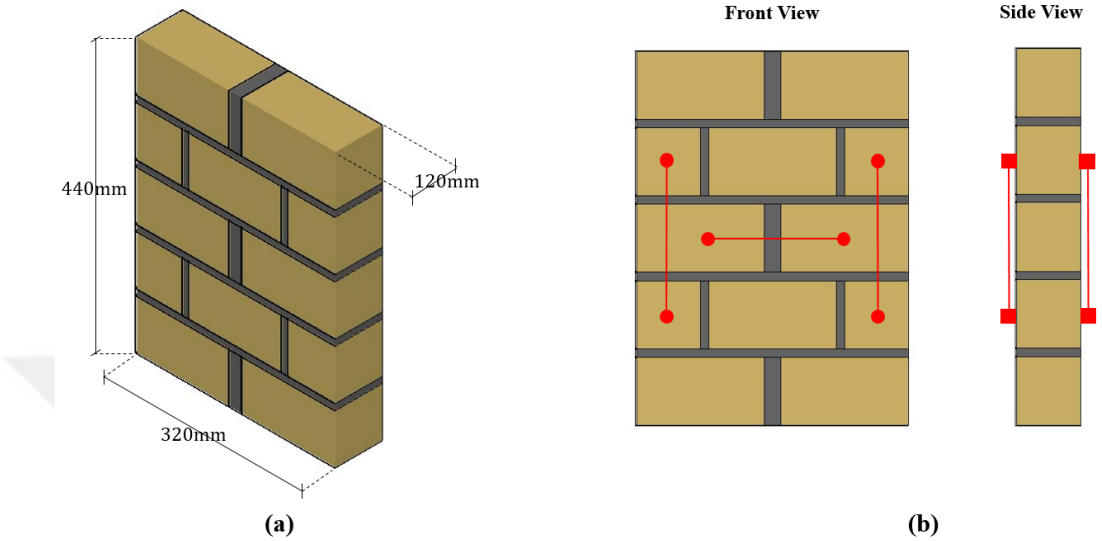

Figure 5.9. (a) dimensions, (b) displacement measurements as per EN 1052-1.

A total of 10 specimens were used in two separate campaigns. The specimens produced in the first and second experimental campaigns can be seen in Figure 5.10. A force-controlled loading was used (as the related standard specifies) for half of the specimens. In the first campaign, three specimens were used. It was not possible to completely crush the specimens under compression, as illustrated in Figure 5.11. The MTS machine has a maximum capacity of 500 kN, and the maximum compressive loads attained were close to the capacity of the machine. Vertical cracks appeared close to the end of the loading (approximately 85% of the ultimate load). At some point, the vertical pressure was unloaded automatically because the machine was not able to load the specimens anymore. During the removal of the tested specimens, it was observed that some of the stones were split, and the mortar was almost crushed and disintegrated. Apart from the lack of integrity and the residual strength of the mortar, stone-mortar adherence was almost non-existent due to the crushing of mortar. Figure 5.11c exemplifies the disintegration of the specimen during the removal.



(a) (b)

Figure 5.10. Specimens of (a) the first campaign; (b) the second campaign.

As the tests were force-controlled, it was also not possible to record the behavior of the specimens after the maximum load was reached. Therefore, a second experimental campaigned was planned.

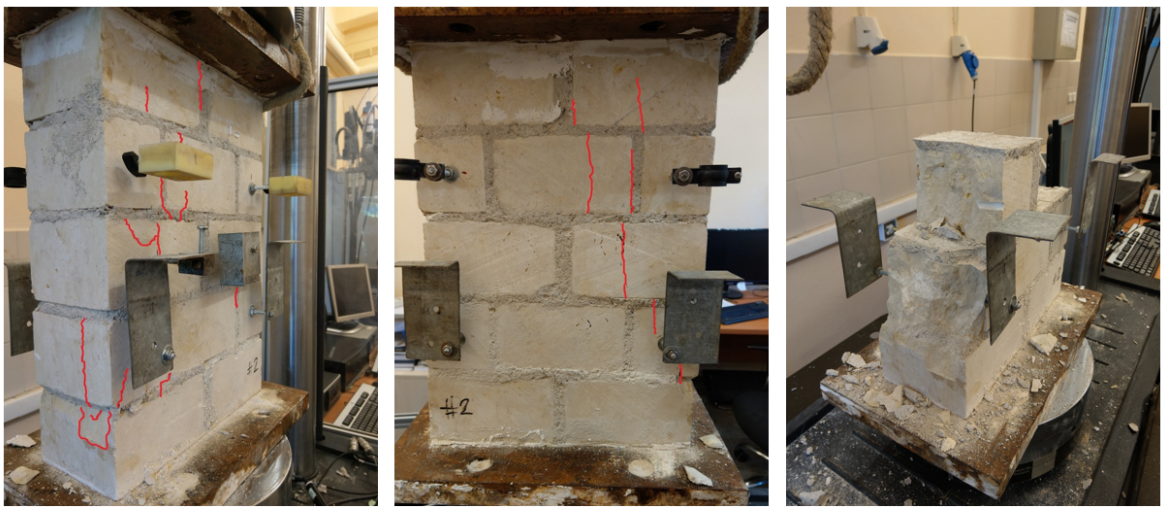

(a) (b) (c)

Figure 5.11. Cracks and spalls of the second specimen after the test: (a) front, (b) back, (c) disintegrating masonry constituents.

The displacement-controlled loading was preferred for the second half of the specimens to observe the post-peak behavior. In both campaigns, the specimens were preloaded up to 19 kN to eliminate the bedding down effect between the loading platens and the surface and then unloaded. Afterward, each specimen was loaded up to the

maximum load with 16 kN/min or 0.02 mm/s loading speed. Load history and crack pattern development were recorded. The test setup and the specimen after the tests are illustrated in Figure 5.12.

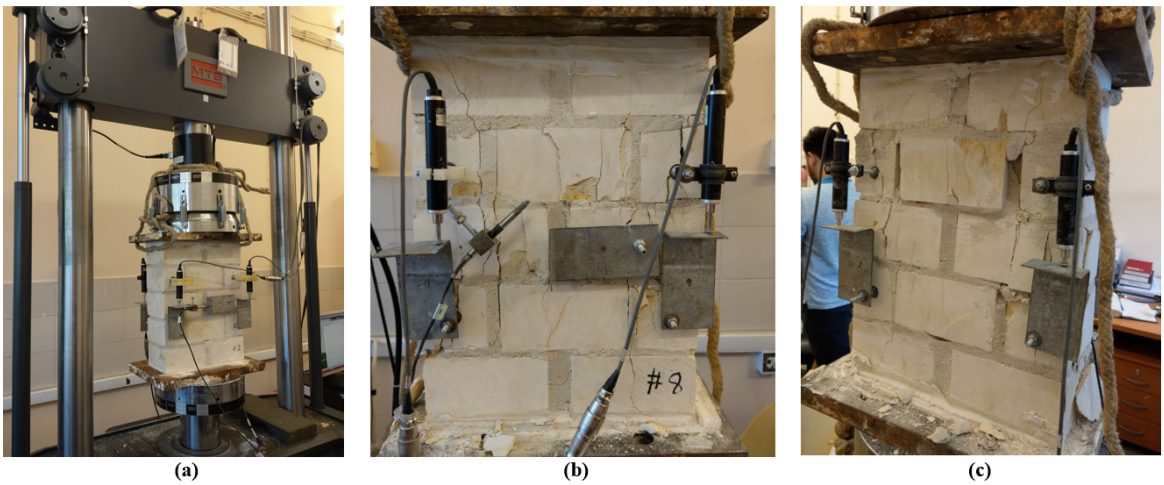

Figure 5.12. (a) The test setup used in compression tests, (b) crushed Specimen 8 front, (c) crushed Specimen 8 back.

The displacement measurements were converted to strains as the vertical load was converted to vertical stress. Then, for each masonry wallette, stress-strain graphs were drawn using the average of all four (or using only the proper data) strain graphs, and their average. It is illustrated in Figure 5.13. Occasionally, it was observed that the stress-strain curves of the prisms are almost linear until the peak stress. This was observed in other research as well [101].

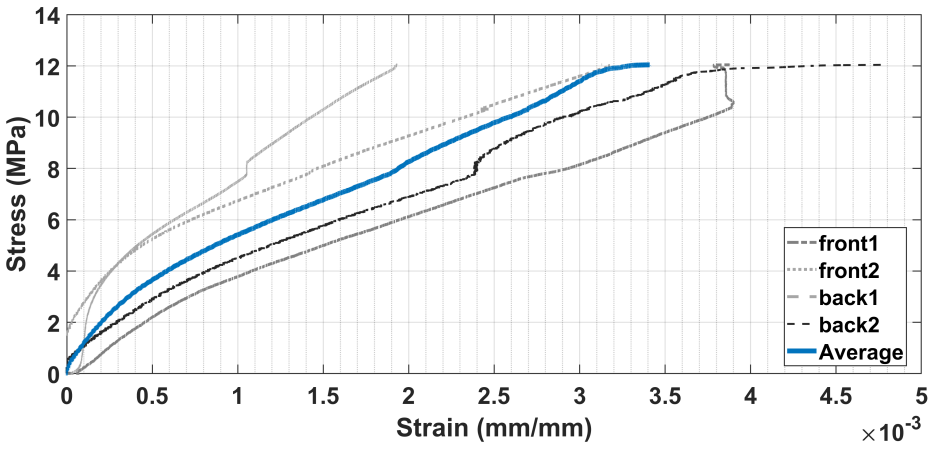

Figure 5.13. Stress-strain graphs obtained from LVDT measurements for the second specimen.

There is an important aspect that should be mentioned here: the strains obtained using the LVDTs are quite different from the strains found using the displacement between the loading platens of the MTS machine, i.e., the full height of the wallettes. This phenomenon can be seen in the Figure 5.14 below and probably results from the well known "bedding down effect" that is caused by the initial adjustment of the plaster and the wallette-loading platen connection. Another reason may be the difference between measurement lengths and the different numbers of stone and mortar layers along the length that compressive strength and modulus of elasticity values were obtained. The phenomenon is significant because it is directly related to the elasticity modulus calculation. In the end, the deformations obtained from the LVDT's are used for the calculations, as required by the standard.

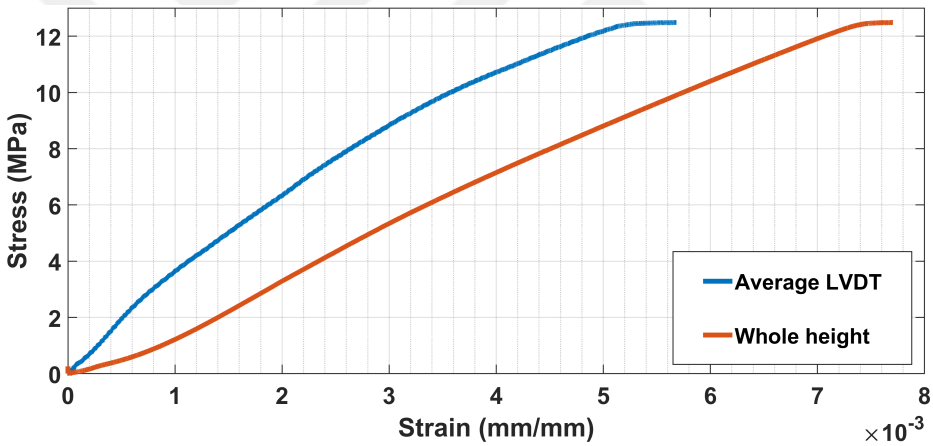

Figure 5.14. Comparison of stress-strain graphs obtained from LVDT and full height measurements (the third specimen).

Six out of ten wallettes were used in the calculations, which were carried out according to the related standard. The compressive strength of the specimens, average compressive strength, elasticity modulus values, and the average elasticity modulus were calculated. The compressive strength was simply obtained by dividing the maximum load to the cross-sectional area.

$$f_i = \frac{F_{i,max}}{A_i} \qquad , N/mm^2 \tag{5.4}$$

The characteristic compressive strength, f_k, was found by dividing the average compressive strength by 1.2. The average stress-strain graphs for the selected specimens were obtained using the average of all four strain values, and they are represented in Figure 5.15.

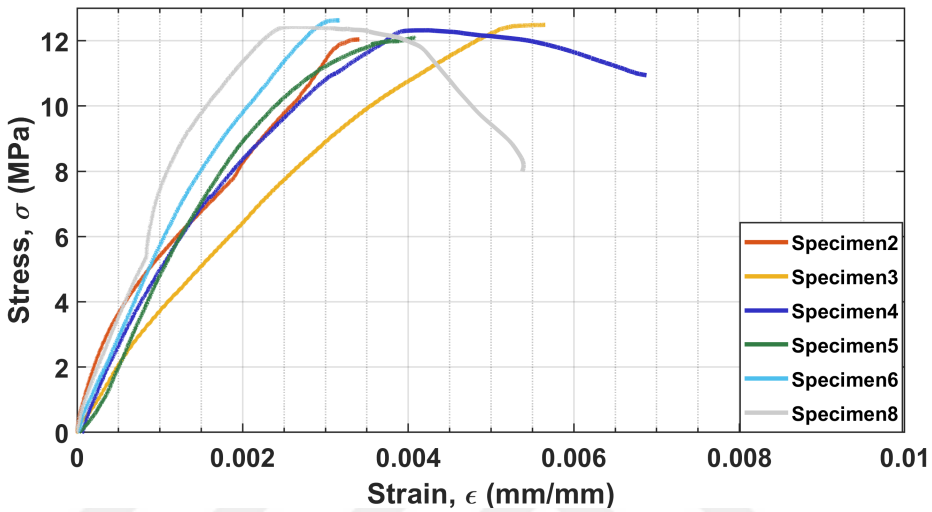

Figure 5.15. Stress-average strain graphs for the selected specimens.

In general, the secant modulus of the linear part of the masonry compression stress-strain curve, which is generally defined between 5%-33% of the ultimate compressive strength, is used to calculate the modulus of elasticity for masonry [102]. What is important here is the definition and use of elasticity modulus itself. If it is to be used in the linear analysis, then the chord should be the one that represents the linear portion of the curve the most. Otherwise, I don't think the chord drawn to 70% of the ultimate stress value can be used in nonlinear analysis, as proposed by Lumantarna *et al.*. [102] The true elastic modulus, by definition, is obtained by the cyclic tests and from the unloading part of the curves, as only the elastic deformations are recovered, i.e., it is the elastic deformations vs. force graph.

Modulus of elasticity was computed, using Equation 5.5, as a secant modulus from the mean of the strains of all four measuring positions occurring at stress equal to one-third of the maximum stress achieved ($E_{1/3}$). The calculated strength and modulus

of elasticity values are provided in Table 5.5 below.

$$E_i = \frac{F_{i,max}}{3 \cdot A_i \cdot \varepsilon_i} \qquad , N/mm^2 \tag{5.5}$$

Table 5.5. Compressive strength and modulus of elasticity values.

	Compressive Strength, $f_{c,mas}$ **(MPa)**	**Elasticity Modulus,** E_{mas} **(GPa)**
2nd Specimen	12.04	6.81
3rd Specimen	12.49	3.58
4th Specimen	12.32	5.16
5th Specimen	12.10	4.71
6th Specimen	12.63	5.81
8th Specimen	12.43	6.85
Average	**12.34**	**5.49**
$\mathbf{f_k}$	**10.28**	**N/A**
$\mathbf{E_{ave}/f_k}$	**N/A**	**534**

Looking at the results, we see that the average compressive strength is closer to the value obtained empirically from RIL 805 standard. In fact, the compressive strength value seems high – contrary to what is expected. Our expectation was that the compressive strength values would be closer to EN 1996-1-1 empirically found value, i.e., 5.51 MPa. However, it should be mentioned that the masonry wallettes were tested six months after the production. Recall that the technical sheet of NHL mortar suggests a compressive strength greater than 3.70 MPa and a tensile strength greater than 1.0 MPa, whereas the test results indicated average compressive strength after 28 days as 2.74 MPa. Therefore, mortar strength could have reached higher values in six months and affected the compressive strength of masonry wallettes. A considerable increase in the strength of the mortar after 28 days curing period has also been observed in other studies [103]. Significant effects of the bed-joint material (or the mortar type) on

the compressive strength, elasticity modulus, and the behavior of masonry wallettes were observed in previous studies as well [97]. Also, it is possible that the friction at the specimen-machine boundary is causing higher compressive stresses. On the other hand, it plausible that the coefficients of the empirical equations given in EN 1996-1-1 do not cover a wide range of tests required to include different natural stone types encountered in these tests.

Another important observation is about the elasticity modulus of masonry. The scatter in the elasticity modulus is more evident compared to the compressive strength values. Moreover, the relationship between the elasticity modulus and the characteristic compressive strength is represented by a ratio/coefficient. That coefficient was found much smaller than 1000, i.e., the ratio suggested in EN 1996-1-1. Based on the results and some other research [102, 103], it is evident that more experimental research is needed on this topic.

Last but not least, Poisson's ratio could not be reliably determined in the experiments. Its value either ranges between 0.10 and 0.45 during the tests or has a constant value for some portion of the test. Based on engineering judgment, the Poisson's ratio estimated from the tests is between 0.26 and 0.35. It should be stated that for elastic and isotropic materials, the increase in the Poisson's ratio drastically decreases the Shear Modulus (when the elasticity modulus is assumed constant). We think that the Poisson's ratio has been affected by the size effect significantly because the mortar thickness remains approximately the same as the panel walls' mortar thickness, whereas the size of the stones is much smaller.

A term in the literature, a ratio called "masonry efficiency", should also be mentioned. It is defined as the ratio of the normalized compressive strength of masonry specimens to that of the unit (stone/brick) and is presented by Equation 5.6.

$$\eta = \frac{f_{k,mas}}{f_{c,st}} \tag{5.6}$$

In our case, masonry efficiency was found 44%. However, it does not really represent the efficiency of masonry. First of all, even for the case of dry stack masonry, the compressive strength of masonry prism is much lower than that of stone. Second, if there is a significant variation in the unit strength, the crushing of the weakest unit in the specimen may determine the masonry strength. In this case, the interaction between brick and mortar may be less important. This might mask the influence of mortar strength on masonry strength. It may perhaps be useful to use indirect methods like natural frequency of vibration, or static deflection of specimens wherein the characteristics of all the bricks get averaged in the measurement [96]. On the other hand, the deformation capacity of masonry significantly increases when mortar is present, even though the compressive strength decreases. Therefore, it is not entirely logical to classify efficiency based on masonry compressive strength only.

5.4. Masonry Panel Wall

As a part of the experimental campaign, the masonry panel walls were tested under vertical loading and in-plane cyclic shear-compression loading separately, in order to investigate the mechanical properties and the walls' seismic performance. The experiments were conducted at Structures Laboratory of the Civil Engineering Department. Whole sets of results are not in the scope of this dissertation; however, findings related to the elasticity modulus values and the effects of uncertainties are presented. Only the benchmark wall (the first wall panel) was considered in this study.

5.4.1. Panel Wall Production

A wall specimen with 155x160x30 cm^3 dimensions was constructed using machine sawn and smooth stones, and natural hydraulic lime (NHL) mortar. For the construction, 55 stones were used, 45 of them with dimensions 30x30x15 cm^3 and the rest cut to half size at 15x30x15 cm^3. The stones are classified as "clayey-limestone," which has a composition of approximately 85% limestone and 15% clay.

In order to connect the wall specimens to the ground and move them easily in the laboratory, the wall was constructed on the readily available reinforced concrete foundation, as seen in Figure 5.16. High strength repair mortar connected the wall to the RC foundation, and the steel profiles prevented the lateral translation of the base. The panel wall was cured for 28 days and stored for 50 days before testing. The panel-wall was built with natural hydraulic lime mortar and ashlar stones. Figure 5.17 displays the wall right after its construction and during the curing process.



Figure 5.16. Panel wall construction in the laboratory.



(a) (b)

Figure 5.17. (a) Panel wall specimen right after its construction, and (b) during the curing process.

5.4.2. Tests

Different approaches were employed to find out the elasticity modulus of the wall panel. First, to determine the vertical elastic stiffness of the wall panel, the wall was loaded under cyclic vertical-compression so that the vertical stress levels corresponded to 0.45 MPa, 0.75 MPa, and 1.0 MPa, and the deformations under these stress levels were measured. The panel wall was not loaded further not to cause any damage because it was intended to be tested in shear-compression later. Thus, the maximum stress level attained was still much lower than the expected compressive strength. The modulus of elasticity calculated from the vertical compression test is 2.13 GPa. However, the lack of standard procedures defining the measurement length is a significant source of uncertainty in terms of comparing the results with other methods. In other words, there is no justification for the choice of the measurement length for the comparison with other methods. If we measured the vertical deformation at the middle third portion of the wall instead of its whole height, then the deformations would probably be different. Such choices are commonly encountered in vertical testing of masonry walls. Therefore, the elasticity modulus value obtained from the vertical compression test has its own uncertainties.

As another approach, cyclic shear-compression test results were used. The shear modulus of the panel wall was calculated and used to find the elasticity modulus. Because the vertical stresses are generally in between 0.2-1.0 in historical masonry structures [118], the vertical loading for the cyclic tests was determined as constant 23 tons as it corresponds to 0.5 MPa average stress. A lateral rig was used in order to apply the displacement-controlled lateral loading, which was determined using ASTM E2126-11 [119] standard as Test Method B. The vertical load was applied with the help of a system made of a jack connected to a steel beam and strands, all sitting on a reinforced concrete spreader beam to distribute the load to the masonry wall. The out-of-plane movement was prevented by using two roller supports on both sides of the walls. Therefore, the boundary conditions of the wall were similar to that of a pre-stressed cantilever beam. Strain gauges and potentiometers were installed on both

sides of the walls in order to measure the strains and displacements during the tests. The instrumentation is illustrated in Figure 5.18 and Figure 5.19 for the front and back sides of the wall. The test setup is shown Figure 5.20 from the front and back sides of the wall.

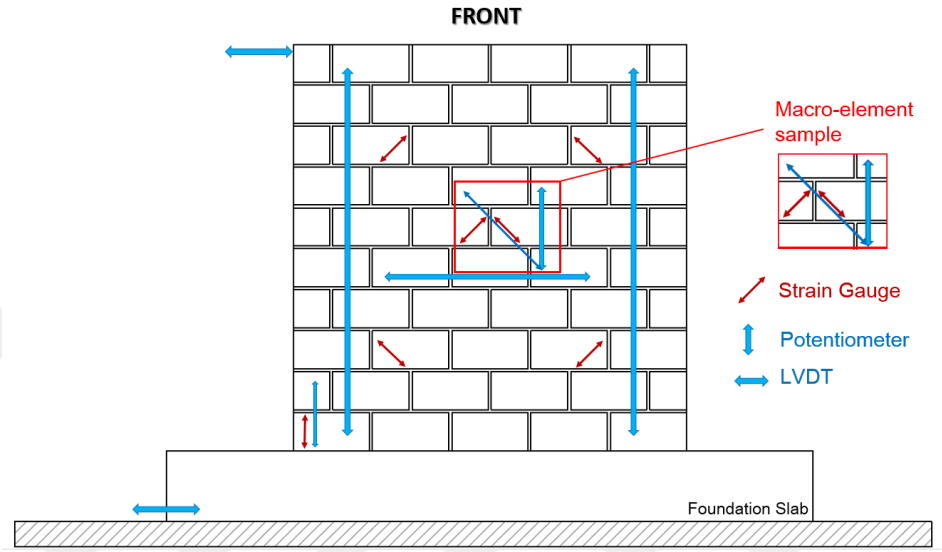

Figure 5.18. Instrumentation of the front face of the wall.

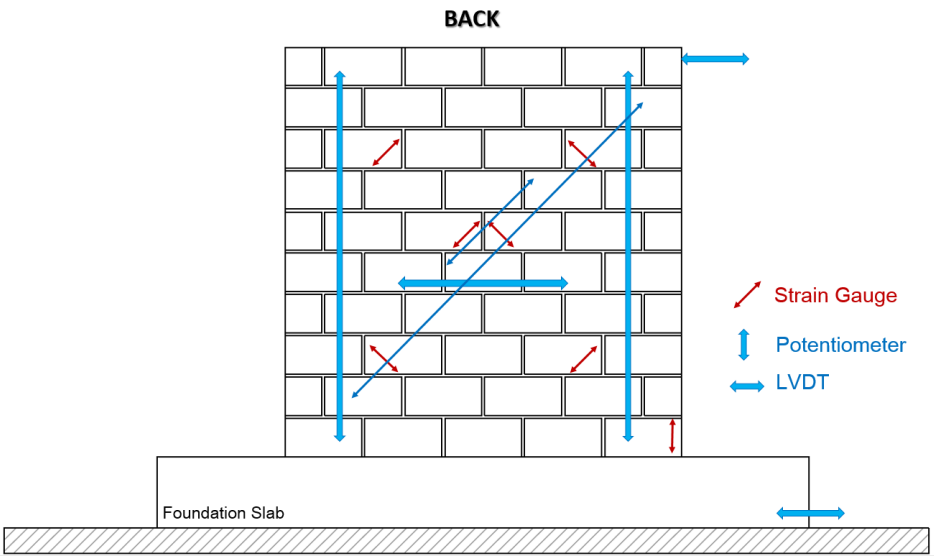

Figure 5.19. Instrumentation of the backside of the wall.



(a) (b)

Figure 5.20. (a) Front face of the wall specimen and the test setup, (b) backside of the wall, and the test setup.

The wall panel exhibited a mixture of flexural-rocking and shear-sliding behavior during the test. The first cracks occurred simultaneously at the lower part close to the right bottom corner, and a stepped crack developed from the right top to the left bottom corner at the stone-mortar interface. The upper left part slid and the crack widths grew significantly. Afterward, the compressive stresses at the lower portion of the wall increased significantly, and additional cracks at the stones occurred while the stones at the bottom corners of the wall were crushed. Figure 5.21 shows the wall panel after the test.



Figure 5.21. Front view of the wall panel after the test.

After the cyclic tests, the hysteresis curve and the average envelope curves were obtained from the data to determine the in-plane initial elastic stiffness. Figure 5.22 and Figure 5.23 show the hysteresis curve and the envelope curves, respectively.

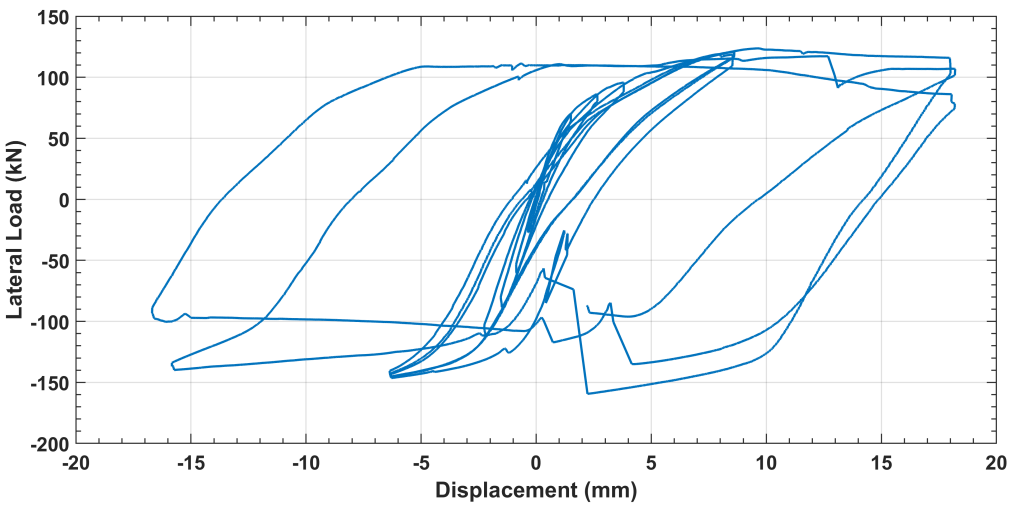

Figure 5.22. Lateral displacement-lateral load hysteresis curve.

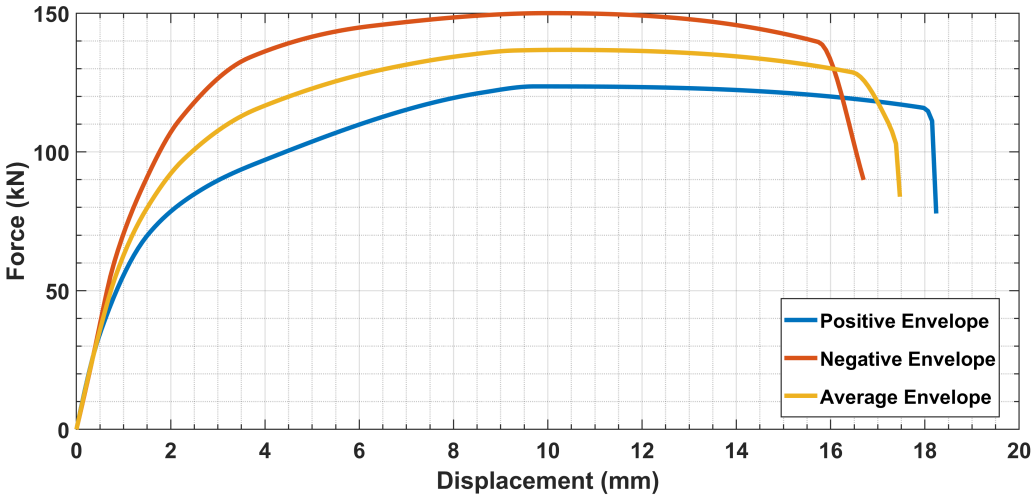

Figure 5.23. Positive, negative and the average envelope curves.

Bi-linearization of the average envelope curve was done using the ASTM E2126 standard, and the energy equivalent elasto-plastic (EEEP) curve was obtained, as shown in Figure 5.24. The initial elastic stiffness, i.e., the ratio of the lateral load to lateral displacement is called Shear Modulus, G. Eurocode 6 and ASCE/SEI 41-17 recommend a shear modulus value as 40% of the elasticity modulus. Thus, the shear modulus obtained as 228 MPa using the EEEP curve can be transformed as the equivalent of 570 MPa elasticity modulus value. Notice that the G/E ratio is usually smaller than 0.4 in different literature examples. Also, this relationship between G and E in both standards are derived from the theory of elasticity. Thus, physically it corresponds to the elastic behavior. With the damage such as cracking and crushing, the shear stiffness is known to decrease substantially. As these nonlinear effects cannot be related to the elastic modulus, the proposed G/E ratio is solely appropriate for uncracked unreinforced masonry.

In the construction of the panel walls, no surface treatment was applied to the stone surfaces so that the friction between the stone and mortar could be higher – as in real masonry structures, therefore, these stiffness values can be considered as the lower bound values.

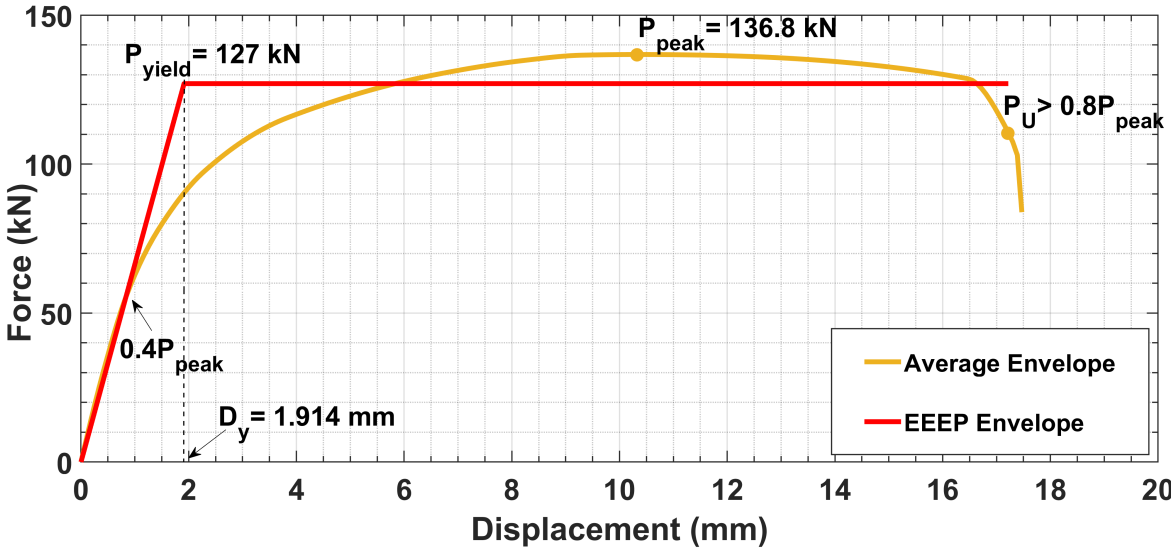

Figure 5.24. Average envelope curve and EEEP curve.

5.4.3. Modeling

The modeling of the masonry wall had three main objectives, *i*) to generate a 3D nonlinear finite element model of the panel wall using ANSYS software, which is commonly used by practitioners, *ii*) to simulate and match the results of the two experimental campaigns: cyclic shear-compression and the ambient vibration tests, in order to obtain the elasticity modulus, and *iii*) to demonstrate the influence of the uncertainty in elasticity modulus on the numerical analyses results.

The geometry of the model was determined using the panel wall dimensions, and the base of the wall model was assigned fixed-boundary conditions. Notice that these boundary conditions are slightly different from the actual case. Still, the difference in the results was found minimal when more complex restraints, such as compression-only supports or nonlinear springs, were used. Thus, fixed-boundary conditions were utilized for the ease of computations. The top surface of the wall was set free to rotate, but the out-of-plane movement was restrained, to simulate the physical conditions in the experiment. A maximum mesh size of 50 mm was used and resulted in 28057 nodes and 84171 degrees of freedom. The macro-modeling approach considering a homogenous

and isotropic wall material was used, and an elastoplastic material property was defined for the masonry. The density, the modulus of elasticity, the Poisson's ratio of the masonry, the compressive and tensile yield strength, and the tangent modulus after the yield are the only input parameters required for the material definition. The constitutive model used for masonry does not have a softening behavior to simulate cracking and crushing. This straightforward approach is widely used by practitioners and preferred in this study to fill the gap between the researchers and practitioners. It is sufficient because the aim is to determine the elasticity modulus of the wall, not to investigate the post-peak behavior.

Experimental average-envelope and the numerical nonlinear static pushover curves were compared for finding the elasticity modulus from cyclic test modeling. It was observed that if the compressive and tensile strength of masonry are set constant as 5.51 MPa and 1.2 MPa, respectively, the numerical pushover curve converges to the experimental average-envelope curve when the elasticity modulus is 1700 MPa. The comparison of the analytical and experimental curves is presented in Figure 5.25.

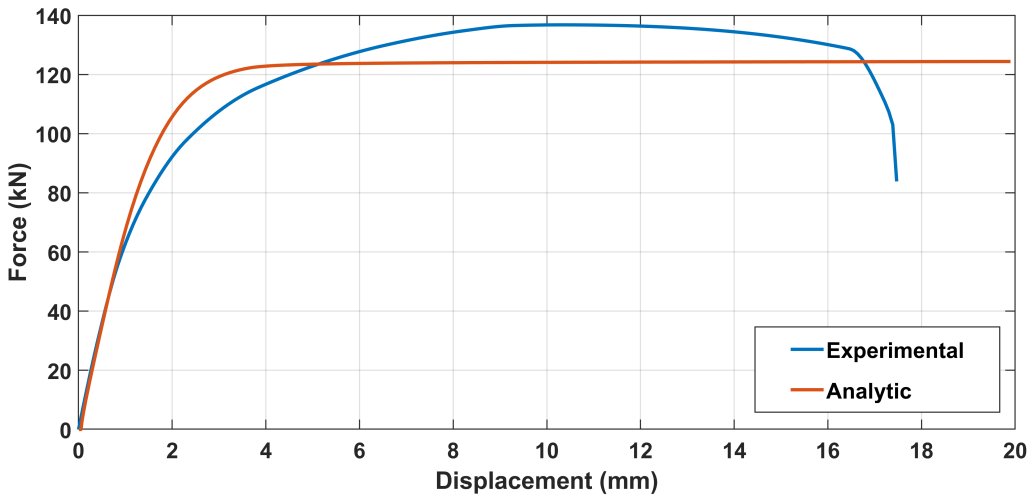

Figure 5.25. Comparison of the analytical and experimental curves.

The results of the model matching for ambient vibration tests are presented in Chapter 5.5.3, whereas the effects of the uncertainty in elasticity modulus on the numerical analysis results are demonstrated in Chapter 5.7.

5.5. Non-destructive and Minor-destructive Tests

There are various non-destructive tests (NDT) and minor-destructive tests (MDT) techniques including infrared thermography, vibration signatures, ultrasonic and magnetic methods, flat-jack test, Schmidt Hammer test, and many more. They are based on different theoretical principles; thus, they produce different sets of data related to the physical properties of the investigated structure. In the interpretation of these properties, some assumptions about the structure have to be made, and previously gathered information should be evaluated in conjunction with the structural features and conditions, as well as the engineering properties of the structure [105]. While some of these NDT and MDT methods allow only for qualitative evaluation, some others enable to obtain mechanical properties of masonry. Due to the difficulty in interpreting the NDT and MDT data, complementary testing is encouraged to provide more information and better knowledge [120]. In this study, an ultrasound test, flat-jack test, and ambient vibration test were carried out on the masonry wall panels. Ambient vibration survey was carried out using the equipment from the Structures Laboratory of Bogazici University Civil Engineering Department, whereas the other tests were conducted and the raw data were provided by KURAM Laboratories of Fatih Sultan Mehmet Vakif University. These raw data were then processed using the in-house developed codes.

5.5.1. Schmidt Hammer Test

Schmidt Hammer Test is one of the most widely used minor-destructive tests, and it is used to find the compressive strength of materials such as concrete, asphalt, rock, and mortar. The method is based on the relation between the surface hardness and the compressive strength of the material. It is applied directly to the material's surface. The rebound of the hammer that hits the surface with a known amount of energy is measured and used for calculating the compressive strength of the material. The surface hardness is representative of a layer only of 5 cm depth.

Empirical formulae exist for concrete material; however, such a relationship has not been reported for masonry or the stone type used in these experiments. ASCE/SEI 41-17 reports that the technique is sensitive to differences in masonry strength but cannot by itself be used to determine absolute strength. Therefore, it may be possible to relate the Schmidt Hammer test results to the compressive strength test results of the stone specimens. Such future studies on similar and different construction stone types might help build a catalog and even an empirical relationship between the surface hardness and the compressive strength, similar to that of concrete.

"Proceq SilverSchmidt" brand hammer was used in our tests. Measurements were taken at 19 different spots of the wall, respectively, with 20 measurements at each spot. Figure 5.26 illustrates the testing. The average value and the standard deviation for the 380 measurements taken are 46.1 and 3.97, respectively. These results correspond to the compressive strength of 23.3MPa with 3.2 standard deviation, for the clayey-limestone used in the experiments.



Figure 5.26. Schmidt Hammer test.

5.5.2. Ultrasound Test

The word “ultrasound” is used for the sound that is above the audible frequencies. Generally, sound frequencies above 20 kHz can be classified as ultrasound. The transmission and reflection of ultrasonic waves, which are generated by an ultrasonic transducer, form the basis of the ultrasonic methods. Longitudinal and transversal (P and S waves), as well as surface waves (R waves), can be generated and measured. Mechanical parameters of the structure and the properties of the interfaces between different materials determine the wave propagation velocity. Therefore, sonic or ultrasonic methods have been used for detecting detachment of leaves, locating voids and deteriorated areas, quantifying cracks, and correlating the wave velocities with the mechanical material properties. Application of sonic and ultrasonic methods on masonry has generally focused on the qualitative measurements; however, their use for determining the elasticity modulus has recently emerged [106].

“Proceq Pundit Lab” brand ultrasound testing device was used to obtain 13 measurements in the vertical direction. This commercial device has a signal generator and acquisition units, as well as a processing unit that returns the wave travel time without needing the intervention of an operator. The measurements were surface wave measurements (indirect tests), where the emitter and receiver were placed on the same side of the wall, as can be seen in Figure 5.27a. Of thirteen measurements, six were taken when the vertical loading was 15 tons, whereas the other seven measurements were taken under 25 tons vertical loading. Measurements were conducted in the vertical direction, the same as the loading path, as we would like to find out the elasticity modulus in the vertical direction.

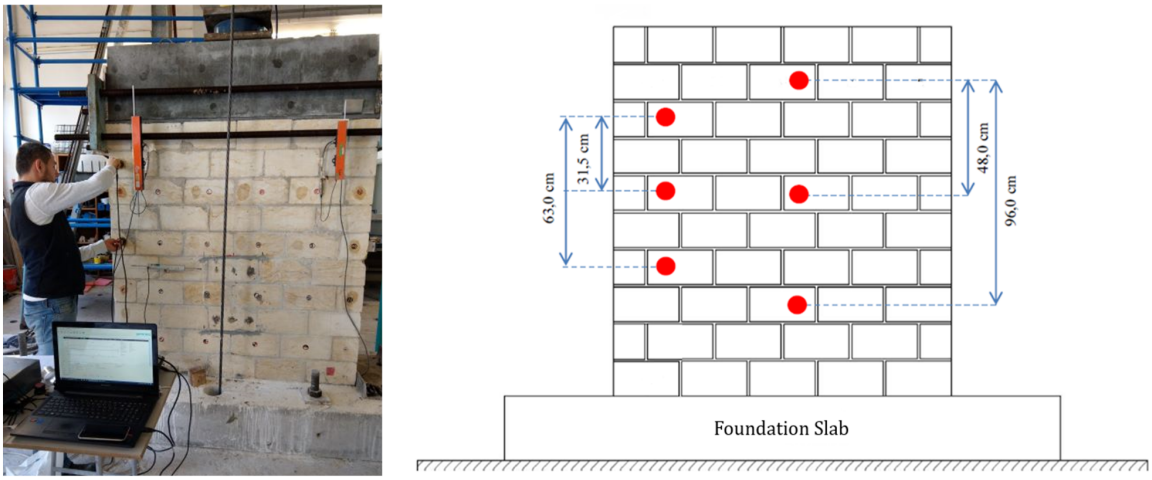

Figure 5.27. (a) Measuring the surface waves during ultrasound testing, (b) test points and distances for the indirect measurements.

The distances to measure the wave travel time were 31.5 cm, 48 cm, 63 cm, and 96 cm, as shown in Figure 5.27b. Moreover, P and S waves along the length of the wall (155-160 cm) could not be measured due to the ultrasound waves being filtered at the mortar interfaces. In that regard, using sound waves with lower frequency content might have been useful. In addition, the distance between the measurement points cover a significant portion of the wall; hence, it is plausible to think that the results represent a global behavior, which the stones, mortar and the joints are acting together.

The wave propagation equations for solid, elastic, isotropic, homogeneous, and semi-infinite media are well known and were used to find the mechanical properties of the walls. Knowing that the nature of masonry does not fulfill the assumptions, these simplifications have been widely used, and the results were deemed satisfactory for engineering use.

By measuring the velocities of P and S waves (V_P and V_S), one can calculate P-wave Modulus (M_p) and Shear Modulus (G) using Equation 5.7:

$$M_P = \rho V_P^2 \tag{5.7a}$$

$$G = \rho V_S^2 \tag{5.7b}$$

where ρ is the density of the material. One can calculate the Poisson's ratio by using Equation 5.8:

$$\mu = \frac{M - 2G}{2M - 2G} = \frac{V_P^2 - 2V_S^2}{2(V_P^2 - V_S^2)} \tag{5.8}$$

After finding the Poisson's ratio, the elasticity modulus can be calculated using Equation 5.9:

$$E = 2G(1 + \mu) \tag{5.9}$$

The equations mentioned above were used for each measurement taken from individual stones on the panel walls. Poisson's ratio, Shear Modulus, and the Elasticity Modulus were calculated as 0.174, 12.6 GPa and 29.4 GPa, respectively.

In order to determine the properties of the masonry wall panels, the surface wave velocity, the specific weight, and Poisson's ratio of the panel wall are required. The properties of the stone and the mortar were homogenized into a single uniform and isotropic material to calculate the specific weight and Poisson's ratio of the wall. The volumetric content of each constituent, V_{st} and V_{mo}, was determined as 91.58% and 8.42%, respectively. Afterward, the specific weight (γ) and Poisson's ratio (μ) of the homogenized wall were calculated as 2606 t/m^3 and 0.19 using Equation 5.10 and Equation 5.11 [54] below.

$$\gamma_{mas} = \gamma_{st} V_{st} + \gamma_{mo} V_{mo} \tag{5.10}$$

$$\mu_{mas} = \mu_{st} V_{st} + \mu_{mo} V_{mo} \tag{5.11}$$

The surface wave velocity, V_R, was determined using the travel time and distances according to EN 14579 [121] European standard. Instead of using the secant velocity of each reading, a linear regression was employed to represent all the recordings' travel

time vs. travel distance. The slope of the regression line, 1256 m/s, represents the surface wave velocity in Figure 5.28.

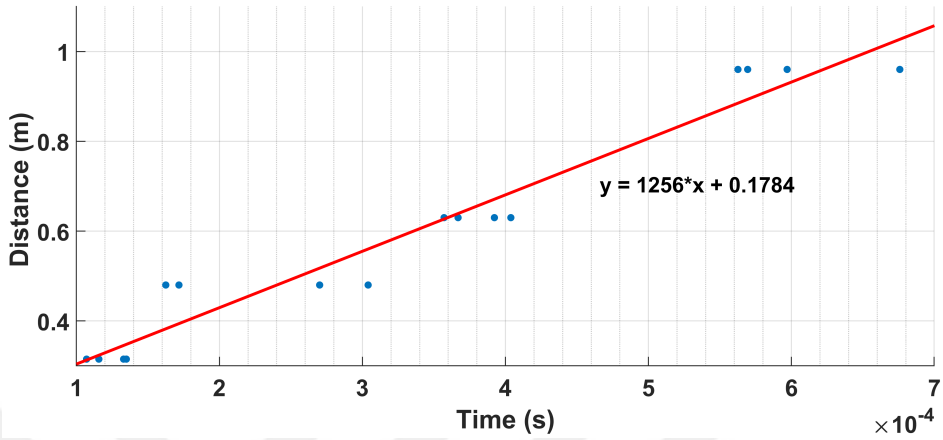

Figure 5.28. The best fit for the indirect pulse velocity transmission of the panel wall to determine V_R.

The indirect ultrasonic test was conducted for two different conditions: *i*) the vertical load was 15 tons, and *ii*) when the vertical load was 25 tons. The results for the two cases are different, as expected and presented in Table 5.6 and Table 5.7. The first case resulted in a lower wave velocity (1173 m/s) and elastic modulus (10.31 GPa). For the sake of consistency with other tests, the graphs and the calculations were presented only for the case when the vertical load was 25tons.

Modulus of Elasticity values can now be calculated using Equation 5.12:

$$V_R = \frac{0.87 + 1.12\mu}{1+\mu} \cdot \sqrt{\frac{E}{\gamma} \cdot \frac{1}{2(1+\mu)}} \tag{5.12}$$

Table 5.6. Elasticity modulus when the vertical loading is $P_v = 25$ tons.

Material Parameters	μ= 0.19	μ= 0.23	μ= 0.25
Specific weight (t/m^3),	2.606	2.606	2.606
Elasticity Modulus (GPa),	11.81	12.03	12.14
E_{max} **(GPa),**	25.81	26.28	26.52
E_{min} **(GPa),**	7.45	7.58	7.65

Table 5.7. Elasticity modulus when the vertical loading is $P_v = 15$ tons.

Material Parameters	μ= 0.19	μ= 0.23	μ= 0.25
Specific weight (t/m^3),	2.606	2.606	2.606
Elasticity Modulus (GPa),	10.31	10.49	10.59
E_{max} **(GPa),**	16.43	16.73	16.88
E_{min} **(GPa),**	5.80	5.91	5.96

From the results, elasticity modulus, E, was found as 11.81 GPa. It was observed that the elasticity modulus varies for different Poisson's ratio values and vertical loading conditions. Therefore, from the observed values in literature, the interval for the Poisson's ratio was determined as 0.19-0.25. Depending on the type of mortar, different values are recommended in Drougkas *et al.* [108]. For example, for weak natural lime mortar, a value of 0.25 was chosen, whereas 0.15 was adopted for Portland cement mortars. Also, the dependence of the elasticity modulus to vertical pressure was observed previously for rocks in a different study [122], but this phenomenon appears to hold true for the case of masonry as well.

The method itself includes uncertainty related to the measurement of ultrasound wave velocity. Under 25 tons of vertical loading, the average wave velocity and the standard deviation for the wall are 1297 m/s and 280 m/s. Therefore, the maximum and minimum values of elasticity modulus found from the wave propagation may differ from the average significantly.

The mechanical properties obtained using the ultrasound testing are called "dynamic mechanical properties", such as dynamic elasticity modulus. Static elasticity modulus is most often smaller than the dynamic one. The difference stems from the distinct conditions under which the static and dynamic tests are performed. The loading rate is high in the dynamic tests, but the exerted stress is much lower than the static tests. Thus, the applied strains are low, and they do not change the structure of the material. In static tests, the micro-cracks present in the material close upon loading, and the deformation increases, leading to lower elasticity modulus. It is also

possible to observe a nonlinear elastic response during the static tests contrary to the dynamic ones. In other words, the differences between static and dynamic moduli can be explained by the differences in the frequency and strain amplitudes used in measurements. Young moduli obtained from ultrasonic tests are higher than low-frequency (acoustic and seismic bandwidths) and static moduli: $E_{ultrasonic} > E_{lowfreq} > E_{static}$. Frequency dependence is similar to strain rate dependence. For example, concrete becomes stiffer as the frequency of the applied strain increase, which increases the elasticity modulus. For further details of the physical causes of having different elastic moduli for static and dynamic measurements, the reader is referred to Mashinsky's work [122].

In order to find the static elastic moduli of the panel walls, the conversion from the dynamic ones were made using the empirical equation given in the work of Eissa and Kazi [123]. The equation includes 342 observations with a coefficient of correlation equal to 0.84. The approach used here, i.e., considering the masonry wall like a rock specimen, is deemed applicable as the volumetric ratio of the stones in the panel wall is nearly 92%. Using Equation 5.13, the static elasticity modulus of the masonry wall was found as 7.92 GPa. Moreover, the maxima and minima of the static elasticity moduli are presented in Table 5.8.

$$E_S = 0.74E_D - 0.82 \qquad ,(GPa) \tag{5.13}$$

Table 5.8. Static elasticity moduli when the Poisson's ratio is 0.19.

	P_v**=15 tons**	P_v**=25 tons**
E_{ave} **(GPa)**	6.81	7.92
E_{max} **(GPa)**	11.34	18.28
E_{min} **(GPa)**	3.47	4.69

The use of dynamic and static elastic moduli depends on the situations encountered. For example, in rock mechanics, for stability problems of building works and

mining works, the static modulus is used. On the other side, dynamic elasticity modulus is used for short-term loadings such as rock disintegration at blasting works and earthquake effects.

It should be noted that the ultrasonic methods do not apply to the masonry of poor quality. They are susceptible to the surface conditions, the coupling material used between the transducer or receiver and the masonry, and the pressure applied to the transducer [78].

5.5.3. Ambient Vibration Tests and Model Matching

An ambient vibration test was conducted on the wall specimen before the shear-compression test to find its dynamic characteristics and use them in calibrating the FE model. In this way, it was aimed to find the elastic modulus of the wall. Vibration measurements were first conducted for the bare benchmark panel-wall. Then, the rest of the testing was done on the walls with the test setup. Acceleration measurements under ambient vibrations and uncontrolled impacts on the walls were taken using a 24-bit recorder and five force-balance accelerometers (FBA sensors), four of which are out-of-plane and the last one is in in-plane directions, as illustrated in Figure 5.29. Sensor properties include very-low self-noise, resulting in 155 dB dynamic range and user-selectable full g-scale range: from $\pm$ 0.25g to $\pm$ 4g. Approximately sixty minutes of data were taken in each set up with a sampling frequency of 200 Hz. Recorded data were pre-processed, and Enhanced Frequency Domain Decomposition [21] method was utilized to find the dynamic properties of the panel walls. It should be stated that instrumentation was determined with the aim of determining only the first three modal frequencies and mode shapes.

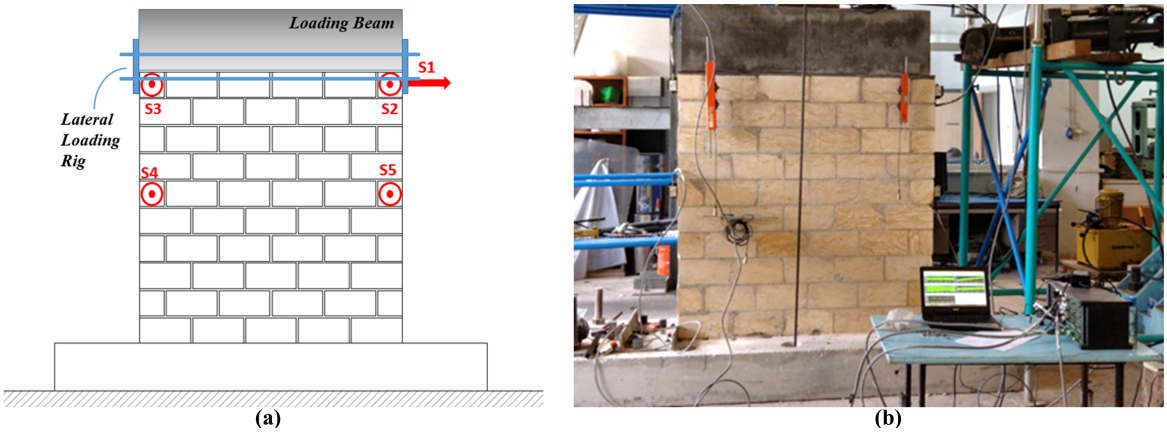

Figure 5.29. (a) the instrumentation and (b) the test setup.

EFDD method is used to determine modal frequencies, damping ratios, and mode shapes. In Figure 5.30 below, the PSD graph is represented, and the peaks corresponding to the first three modal frequencies were determined as 9.86 Hz, 32.03 Hz, and 51.12 Hz.

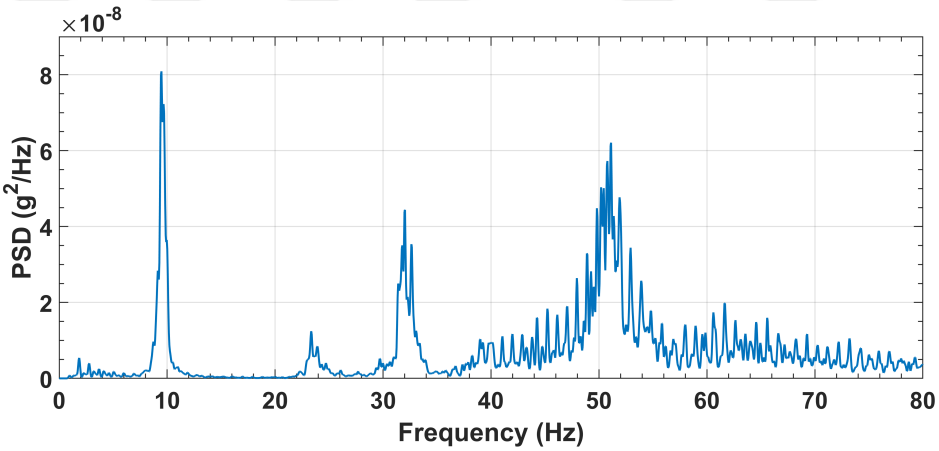

Figure 5.30. Auto-spectrum of the wall data before the cyclic test.

Modal frequencies and the mode shapes found after the experimental dynamic identification were compared to the ones obtained from the analytical model of the panel wall generated in the ANSYS platform. The intention was to manipulate the analytical model parameters so that its properties would converge to the experimental ones. The only updating parameter was the elastic modulus of the wall material, and it was updated manually since the analytical model had been generated using the macro-modeling approach and isotropic and homogenous wall material definition. After

the modal matching with respect to the first modal frequency, the analytical modal frequencies were obtained as 9.86 Hz, 25.03 Hz, and 37.16 Hz, whereas the elasticity modulus was determined as 2.36 GPa. If the modal matching were done for the third modal frequency-which is the in-plane mode, the elasticity modulus would then be found as 0.670 GPa. Moreover, if the empirical equations given in the standards were used, the structural frequencies could have been very different. For example, Eurocode 6 standard suggested value, 5.51 GPa, would result in 15.1 Hz, 38,3 Hz, and 56.8 Hz, as the first three fundamental structural frequencies.

Finally, experimental mode shape results are not presented here in order not to divert from the mainframe of this research. Nonetheless, we should mention that the mode shapes found experimentally and analytically enable deducing another set of important conclusions. Primarily, the second and the third mode shapes found from the numerical model, as shown in Figure 5.31, are interchanged in reality. Indeed, this phenomenon proves that the masonry is not isotropic at all, and the real in-plane stiffness of the wall is much lower compared to the stiffness of the isotropic model. This phenomenon also proves that the masonry wall is an orthotropic material and explains why the elasticity modulus found from the in-plane cyclic test is smaller than the values found from other tests. Another observation is that the wall is not symmetric and homogeneous; on the contrary, the material properties change throughout the wall.

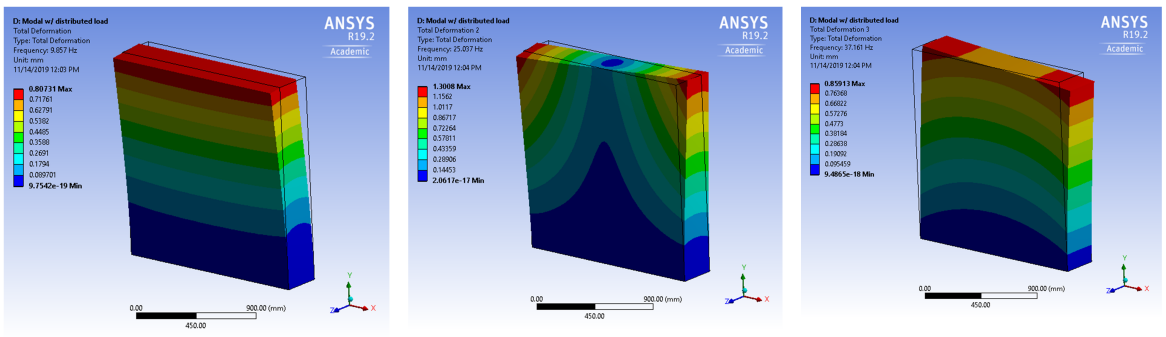

(a) 1st Mode **(b)** 2nd Mode **(c)** 3rd Mode

Figure 5.31. Mode shapes found using the analytical model.

5.5.4. Flat-jack Tests

Flat-Jack tests can be used to determine the compressive stress levels of masonry walls and also to determine the mechanical properties of the material. Flat-jacks are a thin envelope-like bladder, 1 to 6 mm width, with inlet and outlet ports which may be pressurized with hydraulic oil.

The single flat-jack tests are based on the following assumptions:

- the stress in place of the test is compressive
- the masonry surrounding the slot is homogenous
- the masonry deforms symmetrically around the slot
- the state of stresses in the place of the measurement is uniform
- the stress applied to the masonry by the flat-jack is uniform
- the value of stresses (compared to compressive strength) allows the masonry to work in an elastic regime

The single flat-jack test is based on the principle of partial stress release and involves the local elimination of stresses, followed by controlled stress compensation. First, the reference field of displacements is determined by measuring distances between gauge points fixed to the surface of the masonry. After a cut, local stresses are releases, and a thin flat jack is introduced into the slot. With the aid of this device, pressure (compressive stress) is applied to the masonry. This causes a partial restoration of the initial displacement field, which at some point they reach (approximately) previously pressure values. This procedure is shown in Figure 5.32.

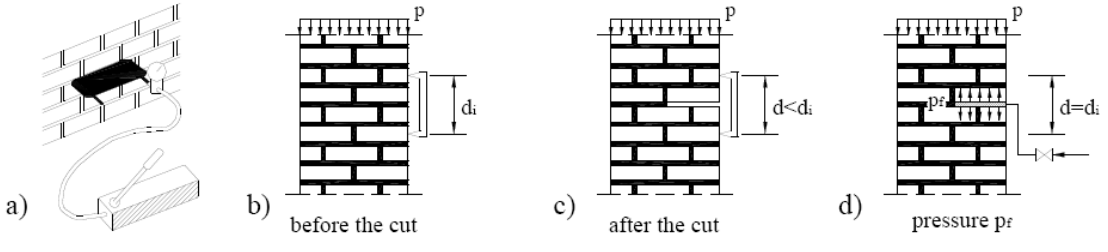

Figure 5.32. Single flat-jack test procedure.

The pressure level in the masonry wall is given by Equation 5.14.

$$\sigma_m = K_m \cdot K_a \cdot P \tag{5.14}$$

where K_m is the calibration factor taking into account the physical characteristic of the jacks ($0 < K_m < 1$); K_a is the ratio of the measured area of the flat-jack to the average measured area of the slot ($0 < K_a < 1$); P is the flat-jack pressure.

The double flat-jack test is similar to a standard compressive test. The difference is that it is performed in-situ, and two flat-jacks are used to apply the load. By cutting two parallel slots, part of the wall is isolated from the surrounding masonry forming a "specimen". Masonry between the flat-jacks is assumed to be unstressed. Flat-jacks are then introduced into both slots, as seen in Figure 5.33, and the initial distances between gauge points are measured. By gradually increasing the flat-jack pressure and measuring the deformation of the masonry between the flat-jacks, load-deformation (or stress-strain) properties may be obtained. From there, the modulus of elasticity can be obtained. A maximum compressive strength may be measured if the specimen is loaded up to failure. ASTM C1197-14a [124] standard was used for double flat-jack tests in this experimental campaign.



Figure 5.33. Preparation for the double flat-jack tests.

For the execution of the test, two semi-oval flat-jacks, hydraulic circular saw, hydraulic hand pump, and four LVDTs were used. The panel wall is under vertical loading during the experiment. Also, the vertical stress levels in historical structures are generally between 0.2-1.0 MPa. Therefore, the flat-jack tests were performed for the cases where the vertical stress level was 0.21 MPa, 0.42 MPa, 0.75 MPa, and 1.0 MPa. The execution of the flat-jack test is shown in Figure 5.34. In fact, we do not expect any changes in the results since the part of the wall between the jacks is assumed isolated. The vertical load had to be increased so that the flat-jacks could not lift the part of the wall above them.



Figure 5.34. Execution of the double flat-jack test.

As can be seen in Figure 5.35, the results for different vertical stress levels are quite similar. The differences are related to uncertainties involved with the test and the material, and these differences between flat-jack tests are known to reach up to 24%, as mentioned in ASTM 1197-14a standard.

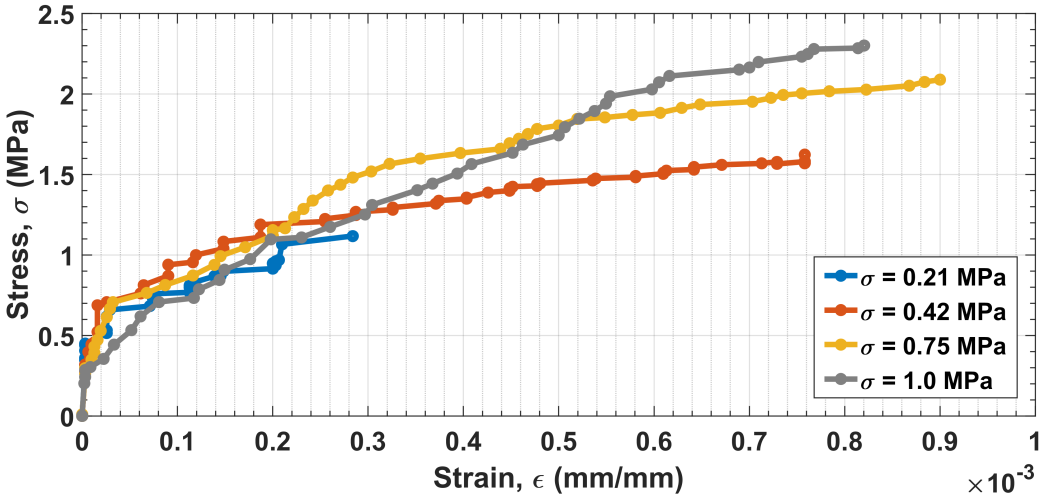

Figure 5.35. Stress-strain graphs under different vertical stress levels.

Two approaches are presented in the related standard to find the elasticity modulus. The first one is the Tangent Modulus calculated between any stress interval. Tangent modulus can also be calculated for each loading cycle; however, our tests were conducted under monotonic loading. Elasticity modulus can be found using Equation 5.15.

$$E_t = \frac{\delta f_m}{\delta \varepsilon_m} \tag{5.15}$$

where δf_m is the stress increment and $\delta \varepsilon_m$ the increment in the strains. Using this approach, initial deformation modulus, $E_{t,initial}$, for the very steep first part of the graphs, and the plastic deformation modulus, $E_{t,plastic}$, for the part following the drop in the stiffness were found as 21.32 GPa and 2.99 GPa, respectively. They can be seen in Figure 5.36 below.

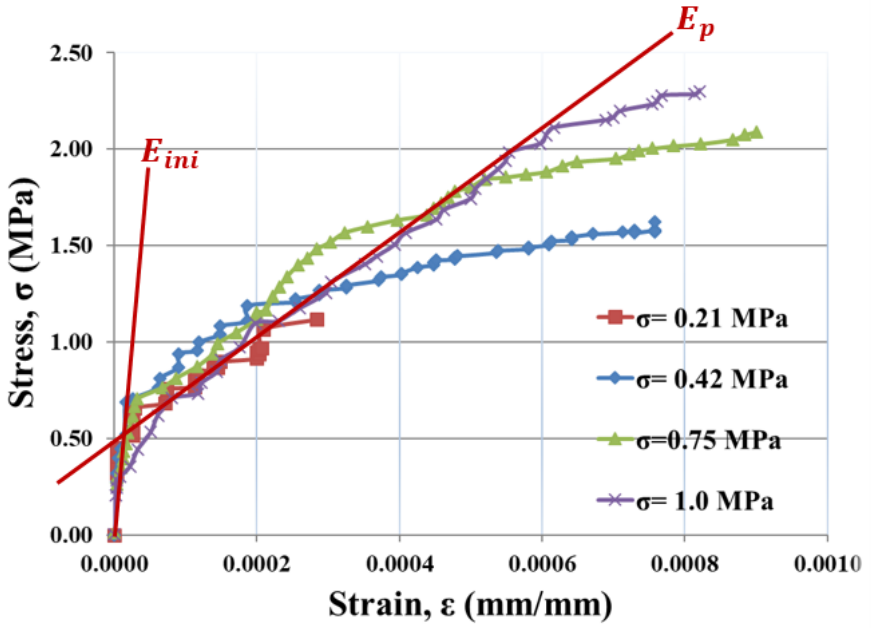

Figure 5.36. Initial and "plastic" tangent moduli.

The second approach is the Secant Modulus, found by using Equation 5.16, i.e., the slope of a line drawn from the origin to any point on the stress-strain curve.

$$E_{si} = \frac{\delta f_{mi}}{\delta \varepsilon_{mi}} \tag{5.16}$$

The related standard does not advise on which point should be used to draw the secant line. Secant modulus is mostly used for design purposes in civil engineering. Therefore, if we consult to EN 1996-1-1 (Eurocode 6) standard, it recommends using EN 1052-1 standard to determine the elasticity modulus. As recalled, EN 1052-1 standard defines the testing of masonry wallettes under compression. When finding the elasticity modulus, the slope of the line drawn to the 1/3 of the maximum stress attained during the test is used. However, in the flat-jack experiments, the specimen was not loaded up to failure, and the stress levels were much lower than the expected compressive strength. The compressive strength of the panel wall was found 5.51 MPa when the empirical homogenization equation in EN 1996-1-1 was used.

The maximum stresses attained at the flat-jack tests correspond to 1/3 of the expected compressive strength, except the case where the vertical stress level was 0.21

MPa. In another aspect, the correlation given in EN 1996-1-1 standard between the elasticity modulus and the compressive strength of masonry, $E_{mas} = 1000 \cdot f_{c,mas}$, presumes that the secant line passes from 0.001 strain. Considering these two aspects mentioned above, the graph for the 0.21 MPa stress level was discarded, and the maximum stresses and strains were used to obtain the secant modulus. Finally, the secant elasticity modulus was determined as 2.42 GPa.

5.6. Summary of the Results and Discussion

Summary of the elasticity modulus values obtained from the experiments, numerical models, and the empirical equations are presented in Table 5.9. Note that the comparison is only performed for the first wall panel. The encountered diversity in the elasticity modulus values was an expected phenomenon. It should be recalled that all the tests conducted include physical differences and various assumptions, as explained explicitly in the related sections of this research. For example, ultrasound and flat-jack tests were done under vertical loading, whereas the in-plane cyclic test was conducted under both vertical and lateral loading. This brings us to the obvious question: which value should be selected, and what type of tests should be carried out to estimate the elasticity modulus of masonry with an acceptable level of accuracy?

Primarily, knowing the assumptions and sources of uncertainties in these tests may help to reduce the associated uncertainties and to design the optimal experimental campaign for individual cases. Then, the choice of the test methods might be decided on an ad hoc basis, considering the physical circumstances of the encountered problem. For example, the elasticity modulus found from the ambient vibration test is remarkably similar to the one found from flat-jack and the vertical compression tests, and it seems to represent the overall global behavior of the structure. These two tests can be considered reliable, as the published literature indicates. Elasticity modulus found from the ambient vibration test is also in a similar range with the value found from the analytical macro-model of the wall. Therefore, the elasticity modulus obtained from ambient vibration tests can be used for the structural analysis of masonry

walls if the modeling approach is chosen as FE macro-modeling. In any case, as commonly encountered in experimental campaigns, engineering judgment is still required to choose the proper values from the experimental data set or the values provided by the empirical and numerical approaches. Finally, the range of the values obtained for this masonry property might be used in defining intervals and probability distributions, which in turn are used in probabilistic seismic assessment, reducing the uncertainty in the seismic capacity prediction [125].

Table 5.9. Summary of the results.

	Elasticity Modulus (GPa)
Ultrasound Test	7.92
Flat-jack Test	2.42
Ambient Vibration Test and Model Updating	2.36
Eurocode 6 empirical equation ($E = 1000 \cdot f_{cm}$)	5.51
RIL 805 empirical equation ($E = 1000 \cdot f_{cm}$)	12.15
Masonry Wallettes	5.49
Panel Wall – Vertical Compression	2.13
Panel Wall – Cyclic test	0.570
Panel Wall – Nonlinear macro-model	1.70

The relationship between the compressive strength and the elasticity modulus of masonry is a well-known phenomenon, especially for modern masonry, and various factors relating the two are provided in different international standards. However, this relationship seems to be more complicated when low-strength mortars, such as NHL mortar, is used. In this experimental campaign, empirical equations yielded higher elasticity modulus values when the Eurocode 6 approach, i.e., $E_{mas} = 1000 \cdot f_{c,mas}$ was applied. It should also be noted that there are other standards and design codes that propose lower ratios between the elasticity modulus and the compressive strength. Thus, it is clear that more research is needed on this topic. Some recent research efforts such as Magenes *et al.* [98]; Almeida *et al.* [100]; Lumantarna *et al.* [102]; Drougkas *et al.* [103, 108] also pointed out such a need. Generally, the empirical equation proposed by Eurocode 6 was found to overestimate the elastic modulus obtained experimentally.

Finally, we mentioned about the similarity between the elasticity modulus found from the cyclic in-plane shear-compression test and the one found from the ambient vibration test when the third mode is used for model updating instead of the first mode. In reality, the analytically found second and third modes are interchanged because the in-plane stiffness of the panel wall is much lower than the isotropic model. This phenomenon also proves that the masonry wall is an orthotropic material and explains why the elasticity modulus found from the in-plane cyclic test is smaller than the values found from other tests. Nonetheless, this value should not be used even if the analysis is conducted as an in-plane analysis because the results would be very different from the real ones. A better approach would be using this value in defining an orthotropic material model. However, it should be kept in mind that more complicated material models require more parameters, hence more experimental tests.

At this point, we should acknowledge that the number of samples used for NDT and MDT tests does not allow for quantification of variability encountered in masonry structures. However, it is a common drawback encountered in laboratory testing and will expectantly be overcome by collective knowledge in the future.

A disclaimer about the use of these results should also be added. Even though these results will be used in the reliability assessment stage of the methodology, they do not reflect the actual properties of the bridge parts and the true nature of the interactions between bridge parts.

5.7. A Simple Example

In order to demonstrate the influence of the uncertainty in elasticity modulus to the numerical analyses results, a simple comparison was made. For this, cyclic test results of the panel wall were compared to the nonlinear static pushover analyses results performed for different values of elasticity modulus. The results shown in Figure 5.37 indicate very different behavior before the “yielding”. It is acknowledged that the nonlinear model is rather rudimentary; however, it seems clear that implementing

a sophisticated damage-plasticity model would result in even more different behavior. That would certainly change the attained maximum displacements and forces, resulting in a more substantial difference in analysis outcomes. Such differences in a real-life problem may cause unsafe evaluations or over strengthening solutions.

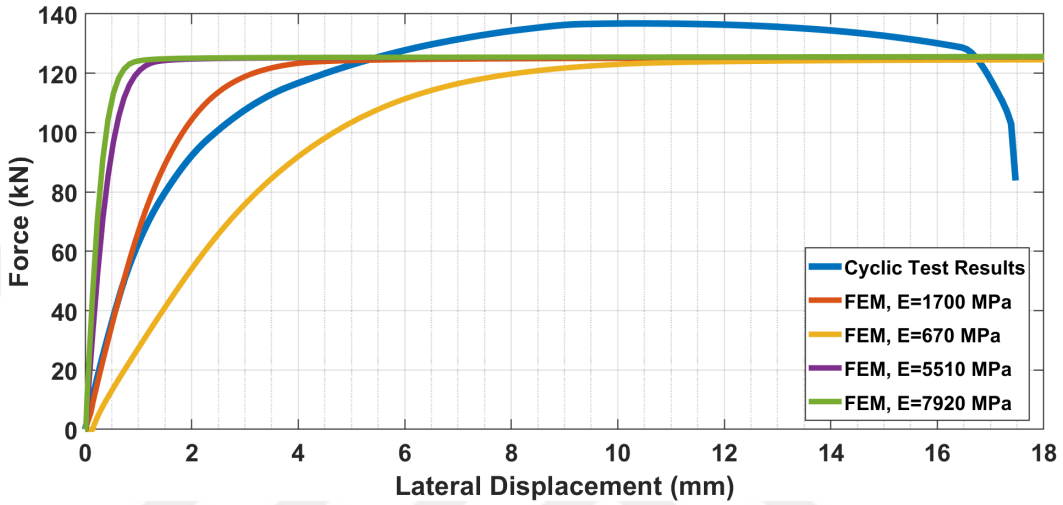

Figure 5.37. Pushover curve comparison for different elasticity modulus values.

6. RELIABILITY-BASED SEISMIC ASSESSMENT

"Every word or concept, clear as it may seem to be, has only a limited range of applicability."

Werner Heisenberg

The knowledge gained from laboratory testing about the uncertain material properties is carried on to the analytical study. In this chapter, the seismic reliability assessment of the Bridge is done, using all the information and knowledge obtained so far. Uncertainty in the elasticity modulus values is represented as a probability distribution and implemented to the FE model the Bridge to carry out the probabilistic nonlinear analyses. Next, the main aspects and principles of defining the limit states are discussed and combined with the probabilistic analysis results to determine the capacity distributions. Meanwhile, the demand distribution is obtained from the nonlinear dynamic analysis results in Chapter 4. The background information regarding the reliability analysis is presented before moving to the final part of the chapter. Eventually, the capacity and demand distributions are used together to calculate the probability of failure (or exceedance) for each performance limit state. Also, the reliability index for each limit state is calculated and compared to the values given in the international standards.

Available seismic assessment methods and procedures for masonry arch bridges are essentially deterministic. Even if the variability of the input ground motion is taken into account, these methods provide the seismic behavior of the structures considering deterministic parameters, which are probabilistic variables in nature. These variables inherently include uncertainties related to materials and loads, as well as the geometry of structures. Current technology allows reducing those uncertainties. For example, geometric uncertainties are greatly reduced with the effective use of photogrammetry and

terrestrial laser scanning techniques [52, 126]. Similarly, non-destructive and destructive testing provides more information in terms of material characteristics, structural morphology, and dynamic properties of the structure [29, 39, 48]. Nonetheless, uncertainties related to the structural behavior in inelastic range, modeling assumptions, and the assessment methods are not considered in the deterministic analysis. Despite being useful, deterministic models suffer from these limitations. In turn, the reliability of the decision-making process is affected as it can lead to unsafe bridges, strengthening measures that are not needed or to the replacement of the bridge. To avoid the drawbacks of the deterministic procedure, a reliability-based seismic assessment that explicitly takes the uncertainties into account is presented. It allows quantifying the performance of the bridges probabilistically and in terms of the reliability index. This results in a more robust decision-making criterion.

Several researchers have recently studied probabilistic seismic assessment of masonry structures considering the uncertainty in the material properties. Masonry buildings [125, 127, 128] and more complex typologies of historical structures [110, 129, 130] were the main focus of these studies. Even though there are a few examples of reliability-based assessment of masonry arch bridges [129, 131–134] these examples consider only the case of vertical loading. Reliability-based seismic assessment of masonry arch bridges is very rare due to the factors such as lack of performance criteria and statistical data on material properties, and the absence of verified and accurate theoretical models [132]. An example of a probabilistic seismic vulnerability assessment is Zampieri *et al.* [135], which takes the material uncertainty into account and uses a simplified limit analysis. Jahangiri and Yazdani [5] is another example that provides damage state probabilities of a plain concrete arch bridge, using 2D FE modeling and incremental dynamic analysis. As can be seen, there is almost no work considering the reliability-based seismic assessment of masonry arch bridges via 3D modeling. This study brings novelty by proposing limit states for the seismic assessment of masonry arch bridges and evaluating the probability of failure for each limit state through reliability-based analysis. It considers the uncertainties in the material properties (modulus of elasticity of masonry) and the earthquake loading. On the other hand,

the uncertainties related to the modeling assumptions such as boundary conditions; the ability of material models to predict the correct behavior, and the assessment methods like assumptions in PO analysis or NDA, have not been considered, although they have been recognized by the research community [136, 137]. These uncertainties will be a part of future research. One reason is that they were minimized when generating the deterministic model, and also there is not enough experimental data to characterize such uncertainty statistically. Epistemic uncertainties are dependent on human knowledge and can be reduced by increasing the knowledge about the parameter of interest [136]; therefore, those uncertainties are expected to be taken into account as our knowledge about them improves.

The performance-based earthquake engineering (PBEE) framework requires the consideration of uncertainties in the analysis and defining performance criteria. Thus, the first step to the reliability-based seismic assessment of masonry arch bridges is defining the performance limit states.

6.1. Performance Criteria Study

6.1.1. General Concept for Masonry Buildings

In this section, the performance criteria (PC) concept, in general, is explained, and the performance criteria available for masonry buildings and the research on them are outlined.

Performance objectives of the structures specify the expected seismic hazard and the level of seismic performance which the structure must achieve. The selection of those objectives is made by policy makers, property owners, and code developers. As there can be multiple performance objectives for a single analysis, they might also change depending on the context of each different case. Determining the performance objectives requires the definition of performance limits for structural components or systems first [78].

The majority of the existing standards define three performance limit states: Immediate Occupancy (IO), Life Safety (LS), and Collapse Prevention (CP). Other damage state definitions, such as Damage Limitation (DL), Significant Damage (SD), and Near Collapse (NC) are also used [138]. In general, performance limits are determined considering the "occupant safety". These performance limit states exhibit different criteria for distinct materials used in the structural system of the existing structures. In other words, the criteria corresponding to the above-mentioned limit states are different for reinforced concrete, steel, timber, or masonry structures. In the case of masonry, existing standards differentiate even the types of masonry, and mostly do not present any performance criteria for stone masonry buildings. Moreover, the basis for the criteria changes for the invaluable historical structures. The limit states for complex masonry structures, such as heritage structures, is a popular research topic. Several approaches for different types of masonry structures have been proposed so far [110, 130, 139].

ASTM E2126 [119] defines the limit state as "*an event that demarks the two behavior states, at which time some structural behavior of the specimen is altered significantly*". A specimen can be a single element or an entire line of resistance within a lateral force-resisting system. Also, FEMA 461 [140] defines a relevant damage state as "*any group of component conditions that result in similar consequence with regard to potential casualties, direct economic loss, or downtime, and are predictable on the basis of a common demand parameter*". Considering these descriptions, ASCE/SEI 41-17 performance limits and FEMA 356 (predecessor of ASCE 41-06) limit state definitions for masonry walls can be summarized as below:

- Immediate Occupancy (IO): the structure remains safe to occupy after the earthquake. Pre-earthquake strength and stiffness of structural members are retained. Minor cracks might be observed, but no or minor permanent drift is expected.

- Life Safety (LS): the structure has significant damage, but it still has a margin of safety against the onset of partial or total collapse. Extensive cracking in masonry

and noticeable in and out-of-plane offsets for the walls might be observed, but it is still possible to repair the structure.

- Collapse Prevention (CP): the structure sustains heavy damage and has limited residual strength and stiffness. It continues to support gravity loads but retains no margin against collapse. It may not be possible or feasible to repair the structure.

Turkish Building Seismic Code [77] uses three similar performance limits. However, capacity and demand comparison is made in terms of shear capacity of the walls and the earthquake demand instead of the drift-based assessment used in ASCE/SEI 41-17 and NTC 2018. Alternatively, ISMEP Guidelines [141] for the Seismic Risk Management of Historical Structures, which is a comprehensive document, defines those three performance limit states in terms of drift limits.

Once the performance objectives are set, the seismic performance assessment should be carried out. An appropriate assessment methodology should have the following properties stated by the FEMA P-58 description. FEMA P-58, Seismic Performance Assessment of Buildings [142], describes the seismic performance assessment methodology for individual buildings as "*The procedures are probabilistic, uncertainties are explicitly considered, and performance is expressed as the probable consequences, in terms of human losses (deaths and serious injuries), direct economic losses (building repair or replacement costs), and indirect losses (repair time, unsafe placarding, and environmental impacts) resulting from building damage due to earthquake shaking*".

There have been several attempts to define performance limits for masonry structures. Lagomarsino and Giovinazzi [143] defined limit states using the idealized bilinear capacity curve of the equivalent SDOF system of the building type structures. Four limit states defined were the functions of the yield and ultimate displacements. Saloustros *et al.* [130] followed the same approach for the performance assessment of a gothic masonry church. D'Ayala and Ansal [144] followed a similar approach and determined the performance states using the yield and ultimate displacements from pushover anal-

yses. Park *et al.* [127] adopted the FEMA 356 approach and defined the limit states of masonry buildings using the drift ratios. Mouyiannou *et al.* [145] carried out extensive research to identify the limit states of masonry structures from nonlinear dynamic analyses. They combined different indicators and parameters from the analyses results to determine four limit states representing global behavior. As a result of a comprehensive project work, Lagomarsino and Cattari [139] classified the performance limits according to different groups of safety and conservation requirements, considering human life, building conservation, and artistic assets conservation. Then, the definition of the damage limits was done using a multiscale approach employing both structural element and heuristic approaches. All the previous work mentioned here, also the ones that were not mentioned, generally defined the damage states based on a displacement-based approach. Energy-based approaches [146] or a hybrid approach combining both approaches [147, 148] are also considered for reinforced concrete structures. However, it is noticed that there has not been a consensus on the approach to quantify damage and determine the damage states.

6.1.2. Performance Criteria for Masonry Arch Bridges

Performance criteria for contemporary structures are usually defined in terms of drift ratio, strain values, and ductility values or determined using the capacity curve of the structures. Performance criteria for masonry walls exist even though they are dependent on factors such as vertical load level, geometry, material properties, and morphology. On the other hand, there are no criteria available for masonry arch bridges neither in national nor international standards. We reckon that seismic load testing of full-scale bridge models will remain unfeasible, and the number of post-earthquake observations regarding the masonry arch bridge failures will not produce statistically meaningful data in the near future. Therefore, the studies to determine the performance limits of masonry arch bridges will focus on the analytical modeling of structural behavior. The performance limits and the collapse modes will again depend on many factors such as the geometry of the bridge, mechanical properties of the masonry, boundary conditions, and morphology of the bridge.

Amongst the available modeling approaches, the FE macro-modeling approach seems to be the most common and feasible, and most researchers prefer it due to reasons stated in Chapter 4. The macro-modeling approach considers the masonry as a homogeneous and isotropic continuum, whereas the mechanical properties of the masonry are either determined by experimental tests or derived through homogenization techniques. Therefore, macro-modeling the masonry with a single material can provide the global system response, overall nonlinearity, and the capacity curve but may not give the local damage and deformation reliably; because the material, in reality, is inhomogeneous and consists of different materials. It would be more logical to look for global displacements and average deformation values in finite regions rather than the local deformations or strains. So, rather than the local stress or strain values that are highly dependent on the modeling strategy, it might be more logical to focus on the global indicators such as drift ratio, ductility, or the stiffness reduction in the capacity curve. Also, notice that it is almost impossible to divide the bridge behavior into different components.

In light of this information, the remarks below should be considered for determining the performance limits:

- A thorough investigation must be made in the beginning, revealing all the necessary geometrical, morphological, and mechanical information necessary for the robust numerical modeling of the masonry arch bridge.

- The analytical model should be verified in the nonlinear range, if possible. Otherwise, it should be able to predict the expected nonlinear behavior.

- Damage scenarios should be differentiated as “horizontal”, “transverse” and “vertical” damage, according to the dominant bridge behavior and the mode shapes. It might also be possible to add “scour” damage to the damage scenarios.

- In order to be able to differentiate the dominant bridge behavior, a 3D model taking the transverse effects into account is a must. It is not possible to distinguish

the behavior by simply checking the span length and height of the bridges. The number of piers, pier slenderness, and "arch slenderness" taking into account the span, height, and thickness of the arch play an important role in determining the behavior.

- Once the dominant behavior is determined as "transverse", the drift ratio for the center of mass (CM) of the bridge might be a good metric to track the damage evolution, because the CM location is directly related to the global geometry. For the piers, it indicates the in-plane drift, and it depends on the piers' slenderness. In the orthogonal direction, it may represent the out-of-plane capacity. Also, the out-of-plane drift between the CM and TOP nodes might be useful for spandrel wall failure. Transverse failure modes include flexure and shear damage, as well as the out-of-plane failure of the spandrels. Therefore, the drift ratio for the CM node might be able to represent all these failure modes. Note that the notion of drift ratio for the CM node is not applicable for single-span bridges.

6.1.3. Defining the Limit States

In the national standard for railroad bridges [149], performance objectives are defined according to the bridge importance classes. Three classes, i.e., special, normal, and simple bridges, require four different performance levels associated with three seismic hazard levels. Performance limit states are called Minimum Damage, Controlled Damage, Significant Damage, and Collapse limit states. Similar to the definitions for building type structures, these limit states are defined for components and structural systems and explained below.

- Minimum Damage (MD): there is either no damage or limited damage after the earthquake. Either the railroad traffic is not interrupted, or the damage is repaired in a couple of days.

- Controlled Damage (CD): medium and repairable damage is allowed in this limit state. The bridge might be expected to be dysfunctional for a short duration (a

few days or weeks).

- Significant Damage (SD): there is heavy and distributed damage. The bridge is near the collapse state. The long-term bridge closure is expected, and the bridge can even be out-of-service completely.

- Collapse (C): the structure collapses under the earthquake actions.

The performance limits in the DLH standard are provided for reinforced concrete bridges. The state of the existing bridge is determined after linear or nonlinear analysis, using earthquake load reduction factor or strain limits for concrete and steel, respectively.

Similarly, EN 1998-2 - Design of structures for earthquake resistance -Part 2: Bridges [150] classifies the bridges into three groups: Class I, II, and III. This classification is based on the consequences of their failure in terms of human life, economic losses, and their importance for maintaining communications, especially after the earthquake. AASHTO LRFD Specifications [151] and NZTA Bridge Manual [152] also classify the bridges according to importance levels. Then, the reliability of structural members is specified according to the importance levels and bridge permanence. Yet, all of these documents are intended for the design of new structures. In that sense, the performance objectives satisfy the Serviceability Limit State and the Ultimate Limit State, as well as the capacity design principles.

As can be seen from the summary provided above, there are no performance criteria for masonry arch bridges. There have been some attempts in the literature to define performance objectives for masonry arch bridges; however, there is still a need for significant research to distinguish the behavior of the bridge and determine the performance criteria. Therefore, this study aims at defining limit states for the seismic assessment of the investigated masonry arch bridge and hopes to contribute to the literature by proposing a methodology for the assessment.

The three limit states are defined in this study through the use of ad hoc rules. To be able to generalize them, these performance limits should be applicable to other similar masonry arch bridges. Noting that the expected performances of the masonry arch bridges will differ according to their importance and use, such as historical value and strategic importance, these considerations are not in the scope of this performance assessment study. The proposed limit state definitions are as explained below:

- Functionality (FunC) Limit State: this limit state marks the behavior state until which the behavior is mostly elastic, and there is either no or minor damage. There is still a considerable reserve of strength and stiffness after the earthquake. Either the railroad traffic is not interrupted, or the damage is repaired in a couple of days.

- Life Safety (LS) Limit State: before and after this limit state, the damage/plasticity starts increasing and spreading so that the maximum strength capacity is near and the initial stiffness has decreased significantly. Nonetheless, the structure still has a margin of safety against the onset of partial or total collapse. The bridge is expected to suffer medium to significant damage. Still, it should be feasible to repair, and it might be dysfunctional for a short duration—for example, a few days or weeks.

- Near Collapse (NC) Limit State: the damage is heavy and distributed to the extent that the bridge is near to collapse state. The long-term bridge closure is expected, and the bridge can even be out-of-service or replaced completely. The definition of this ultimate limit state in most codes also corresponds to the NC limit state. Also, NC limit state is used when estimating the seismic risk via probabilistic analyses as it is very difficult actually to simulate the physical collapse [79].

As it is evident, these descriptions are defined in qualitative terms and possibly vague after the analysis [153]. Translating these limit states into quantitative definitions to apply in numerical assessments is a must, even though it is not simple and smooth

[145]. As we are examining the global behavior of the bridge, a structural element approach that assumes attainment of a certain limit state in a part of the structure, as local damage, is not feasible. Thus, a heuristic approach is adopted in this study. Heuristics are logical assumptions that help to simplify or solve the problem, but ultimately they remain unjustified or unproven mathematically. Examples include, from common engineering practice, the yield strength definition for structural steel using 0.2% offset stress, equivalent static loads for wind loading, rectangular stress block assumption for reinforced concrete beam cross-sections, and distributed loading for live loads [136]. The performance limit states are defined directly on the pushover curve using the limits based on strength and displacement values, and also the decay in the initial stiffness. In addition, such heuristic definitions considering the global behavior enable comparing the limit states for other masonry arch bridges.

- Functionality (FunC) Limit State: is defined as the displacements corresponding to the 75% of the maximum acceleration (or Base Shear) value. The basis for this decision is merely the observation of the pushover curves and the engineering judgment to consider where the "yielding" approximately starts.

- Life Safety (LS) Limit State: is found when the initial stiffness of the pushover curve decreases to 7%. If there is more than one such point, then the last point is taken. It is difficult to quantify the repairable damage, but at the same time, the limit state is justified by not losing the strength capacity significantly. As the ductility of the bridge behavior is questionable, it is safer to track the decay in the stiffness. Similar approaches have been used by other researchers [5, 145].

- Near Collapse (NC) Limit State: corresponds to the 90% of the maximum displacement attained on the pushover curve. The reason for this choice correlates strongly to the definition above in terms of damage distribution and the failure simulation. The last point on the deterministic PO curve is evaluated as the physical collapse. Considering that the structural response parameters near collapse are highly dependent on the modeling technique, analysis method and software, as well as the stability and convergence issues [154], 90% of the maximum, attained

displacement is chosen.

With the definition of these heuristic functions, it was intended to translate the qualitative performance criteria into quantitative damage measures that are well correlated with the global structural behavior, so that performance-based analytical assessment of the bridges can be performed. Regardless of how well the heuristic functions perform, there may be other parameters or approaches to defining the limit states that describe the global damage better. Therefore, more research is necessary on this topic.

6.2. Seismic Reliability Assessment

Defining an explicit limit-state equation in terms of the probability distributions of input parameters is not possible due to the complexity of the problem and the nonlinearity involved. To be able to calculate the probability of failure, one must resort to simulation methods such as Monte Carlo Simulation (MCS). Crude MCS is, however, hardly applicable due to the high number of runs necessary to obtain a smaller variance and sufficient accuracy [132]. To this end, more advanced techniques ranging from variance reduction techniques such as Latin Hypercube Sampling (LHS) and Importance Sampling to surrogate methods like Response Surface method, are available [155, 156].

The probability of failure (or exceedance) associated with each limit state determined previously is calculated by using a four-step approach: *i*) taking the material uncertainty into account and using the Latin Hypercube Sampling method to produce samples, *ii*) mass-proportional pushover analyses with the uncertain material properties and application of the predetermined performance limits to those results to derive the capacity distributions, *iii*) implementing a probability distribution to the NDA results to determine the demand distribution, iv) the reliability assessment by using MCS or First Order Reliability Method (FORM).

The next step in conducting the reliability-based seismic assessment is the statistical definition of the input variables. Then, applying the performance criteria derived in Chapter 6.1 to the MPP analyses results, we obtain the (capacity) distributions for each limit state. Together with the demand distribution obtained from the NDA results, both capacity and demand distributions are used in MCS and FORM to determine the probability of failure for each limit state.

6.2.1. Material Uncertainty

In the experimental campaign presented in Chapter 5, a similar type of stone to the one used in Bridge 41 was used, and several non-destructive and destructive tests were carried out. Based on the results it was observed that the ratio of elasticity modulus to compressive strength (E/f_c) is between 500-700, the compressive strength of the homogenized masonry from the empirical equations is 5.51 MPa, and the range of elasticity modulus values is 1.70 – 3.86 GPa. By assuming a normal distribution for the compressive strength and the elasticity modulus of masonry, these limit values were set as the lower and upper bounds of the distribution. Since the mean ± three standard deviation covers 99.996% of the whole data space of the normal distribution, parameters of the distribution of the elasticity modulus were decided as N(2.78,0.36) MPa. These parameters result in a coefficient of variation of 0.13, and this value is considered the same for the masonry material of Bridge 41. Also, the elasticity modulus values used for the deterministic analyses were considered as the mean value. Back propagating from these values, the standard deviations were calculated for the masonry elements and arches, resulting in normal distributions as N(6.2,0.81) and N(6.7,0.87), respectively. Several researchers chose to use a normal distribution for the compressive strength and elasticity modulus of masonry [4, 129, 134, 135], whereas some others preferred lognormal distribution [127, 130, 157]. Haciefendioglu *et al.* [158] found the effect of the distribution type on the probabilistic response negligible while also highlighting that the elasticity modulus has a considerable impact on the response of masonry bridges.

As a side note, it should be stated that the ranges for the elasticity moduli should be updated as 1.70-5.49 GPa, considering the results of the new wallette tests. Because of the Covid19 pandemic, the wallette tests could not be performed as planned, and the previously given range above was used in the reliability-based seismic assessment.

Once the statistical distributions were determined, the Latin Hypercube Sampling method [159] is used to derive sample values for the simulations. The Latin hypercube sampling method, a stratified variance reduction technique, is a variation of Monte Carlo simulation. This technique reduces the variance in the MCS samples, and thus, lower the number of required runs. It works by segmenting the variable's probability distribution into a number of equal-probability and non-overlapping intervals [160]. Samples are taken within those intervals; thus, they fill the sample space more effectively and reduce the variance of statistical estimators computed from the samples [161]. The LHS technique has been used as a tool to improve the efficiency of sampling methods for structural reliability analysis and shown to produce significant savings on computational cost [162].

The LHS technique is used to generate 45 simulations. The number of simulations is decided by observing the relative difference between the mean values after a number of simulations with the prescribed mean values in Table 4.1. This relative difference is expressed in terms of percent error. The magnitude of the error after "j" simulations can be tracked in Figure 6.1. The final values of the errors are all smaller than 0.5% for both random variables. Therefore, 45 simulations were deemed reasonable even though the common practice employs more simulations.

Dependency between the random variables is considered through the covariance or the correlation coefficient, which is a linear dependency ratio. Elasticity moduli for the masonry and arches are assumed to have a 95% correlation between them. Forty-five samples from each distribution were used. The distributions and histograms are presented in Figure 6.2.

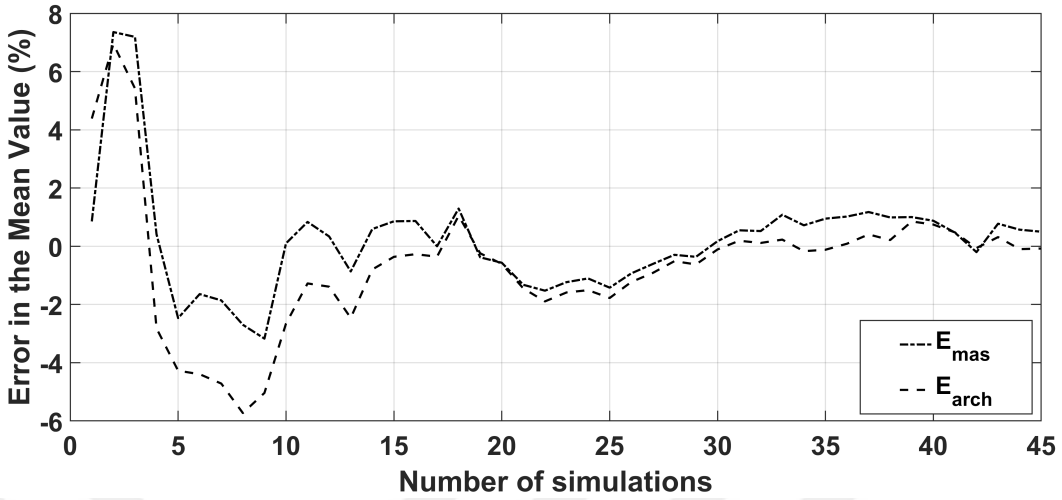

Figure 6.1. The relative error between the prescribed mean and the mean of first j realizations.

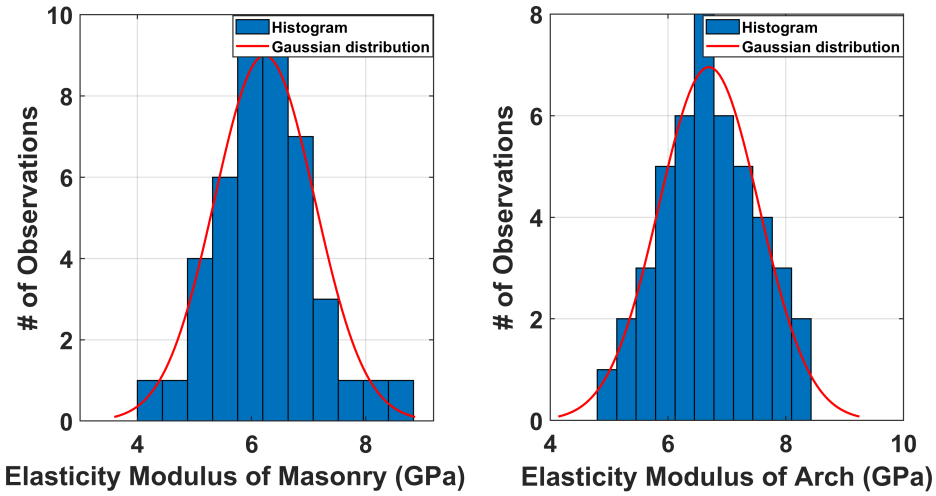

Figure 6.2. Histograms and distributions for the elasticity modulus values for masonry and arch.

Mass proportional pushover analyses were conducted for the set of 45 pairs of samples. Considering the findings from the laboratory tests, E/f_c and f_c/f_t ratios were revised as 700 and 0.10, respectively. The results are presented as the center of mass displacement versus the applied mass proportional acceleration in Figure 6.3. Please note that the PO curves are presented based on the definition of failure explained in Chapter 4.5. The curves end when it becomes flat and the damage distributions indicate physical collapse.

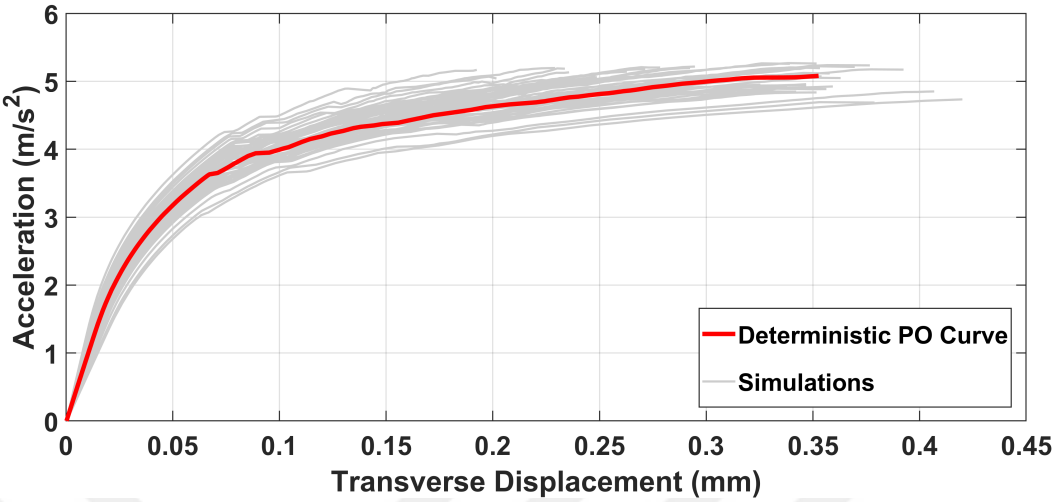

Figure 6.3. Acceleration-CM displacement results of the probabilistic and deterministic pushover analyses.

6.2.2. Capacity Distributions

Applying the performance criteria defined in Chapter 6.1 to the MPP analyses results, we obtain the set of values, to which normal distributions are fit in order to determine the capacity distributions for each limit state. The corresponding limit states for each simulation are marked on the pushover curves and presented in Figure 6.4. Summary of the distributions and the bridge response at the limit states are presented in this section.

It is observed that the coefficient of variation (C.o.V) in any of the limit states does not exceed 0.2; thus, indicating the behavior is relatively predictable, and the damage state would initiate within a small range of potential damage parameters. If the dispersion were high, then it would indicate that the demand parameter being used to predict the limit state is not an appropriate one. The transverse drifts of the CM node at the mean of various limit states are presented on the deterministic PO curve in Figure 6.5 below.

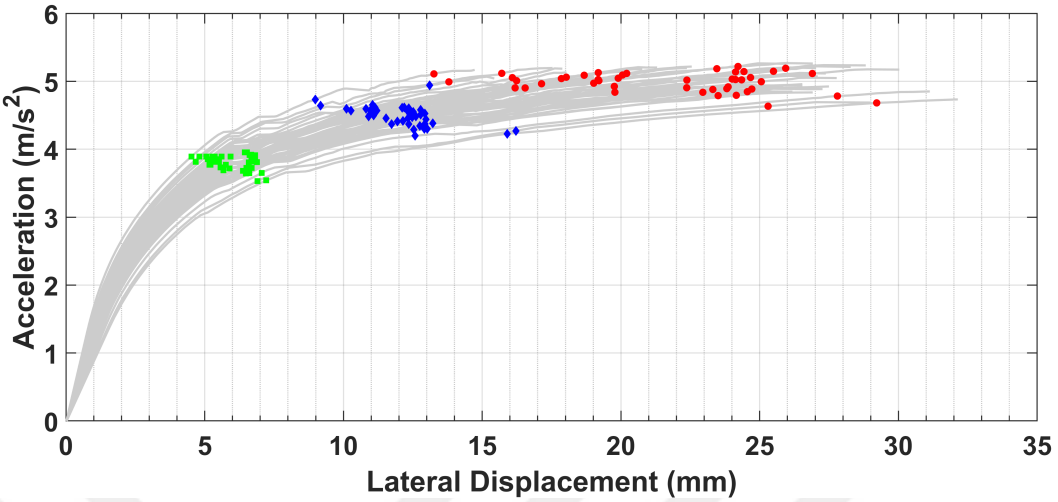

Figure 6.4. MPP analyses results and the limit states (green: FunC, blue: LS, red: NC).

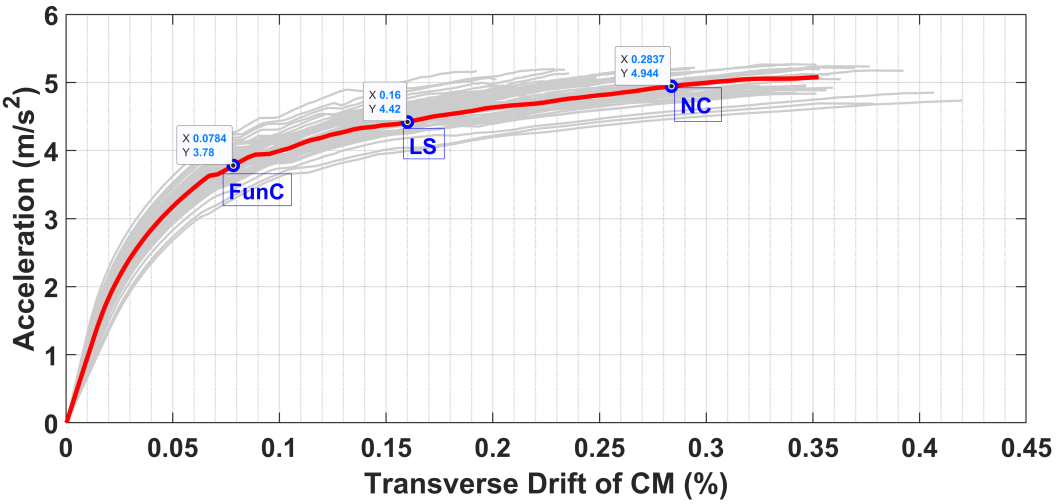

Figure 6.5. Transverse drift of the CM node at the performance limit states.

6.2.2.1. Functionality (FunC) Limit State. A normal distribution, $N(6.02,0.74)$ mm, is assigned to the set of limit state values as the capacity distribution. In compliance with its description, there is very little damage observed at the FunC limit state. Figure 6.6 displays the total strains at mean plus one standard deviation CM displacement. The bridge remains completely functional before this damage state.

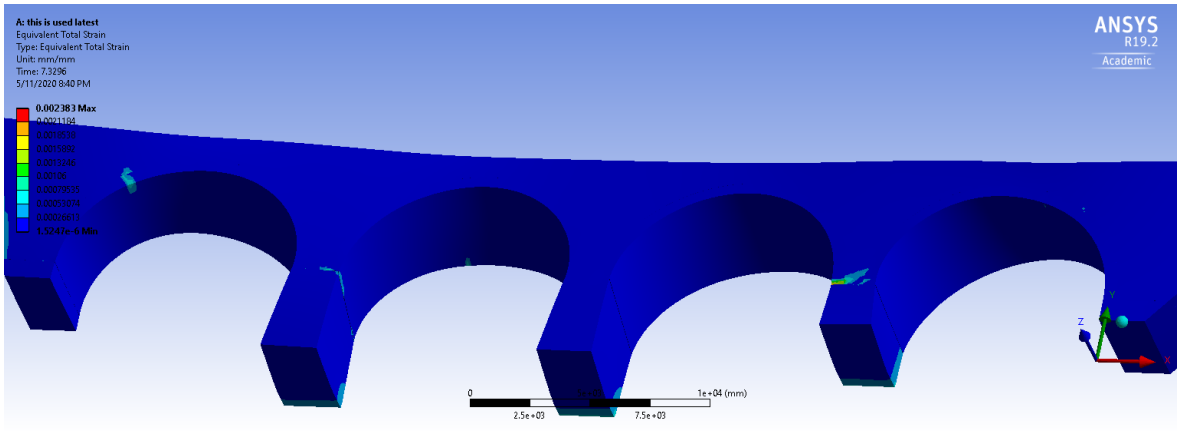

Figure 6.6. Bridge response to MPP at the FunC limit state – equivalent total strains.

6.2.2.2. Life Safety (LS) Limit State. A normal distribution is assigned to the set of limit state values. The capacity distribution is a normal distribution with $N(12.03,1.34)$ mm. As the definition of LS limit state implies, and as can be observed in Figure 6.7, there is significant damage on the bridge in the form of cracking at the arches - diagonally on the sides and transversely in the middle, and at the arch springing. The bridge has lost the majority of its initial stiffness, but there is no strength degradation, and the damage can be repaired.

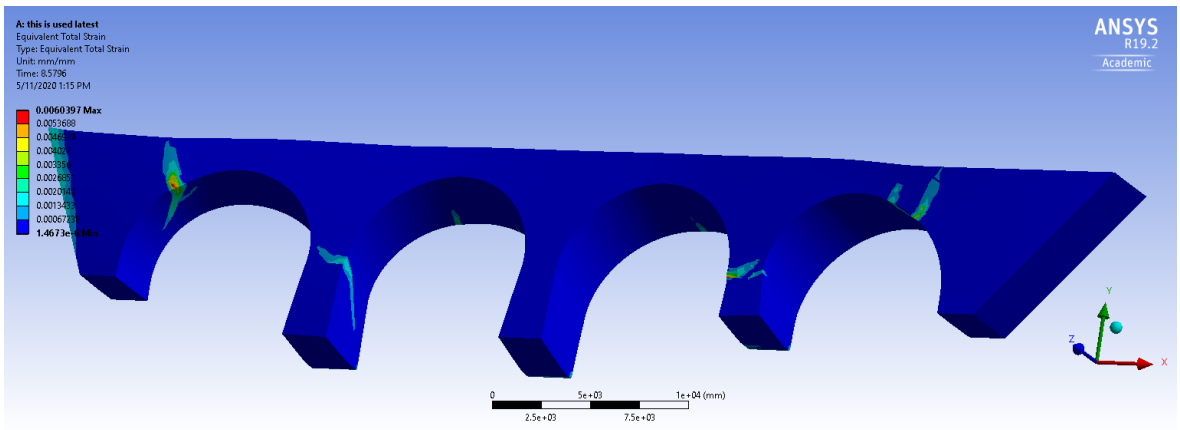

Figure 6.7. Bridge response to MPP at the LS limit state – equivalent total strains.

6.2.2.3. Near Collapse (NC) Limit State. A normal distribution, $N(21.57,3.86)$ mm, is assigned to the set of limit state values as the capacity distribution. In this limit

state, nonlinearity increased, new cracks were formed, and the damage propagated to an extent where instability is imminent. Figure 6.8 illustrates that there is heavy and distributed damage. Forming of new cracks close to the existing ones may indicate local collapse mechanisms, whereas propagation of the existing ones through the whole width of the bridge implies global physical failure. Therefore, the bridge is near to collapse state, and it might be out-of-service completely.

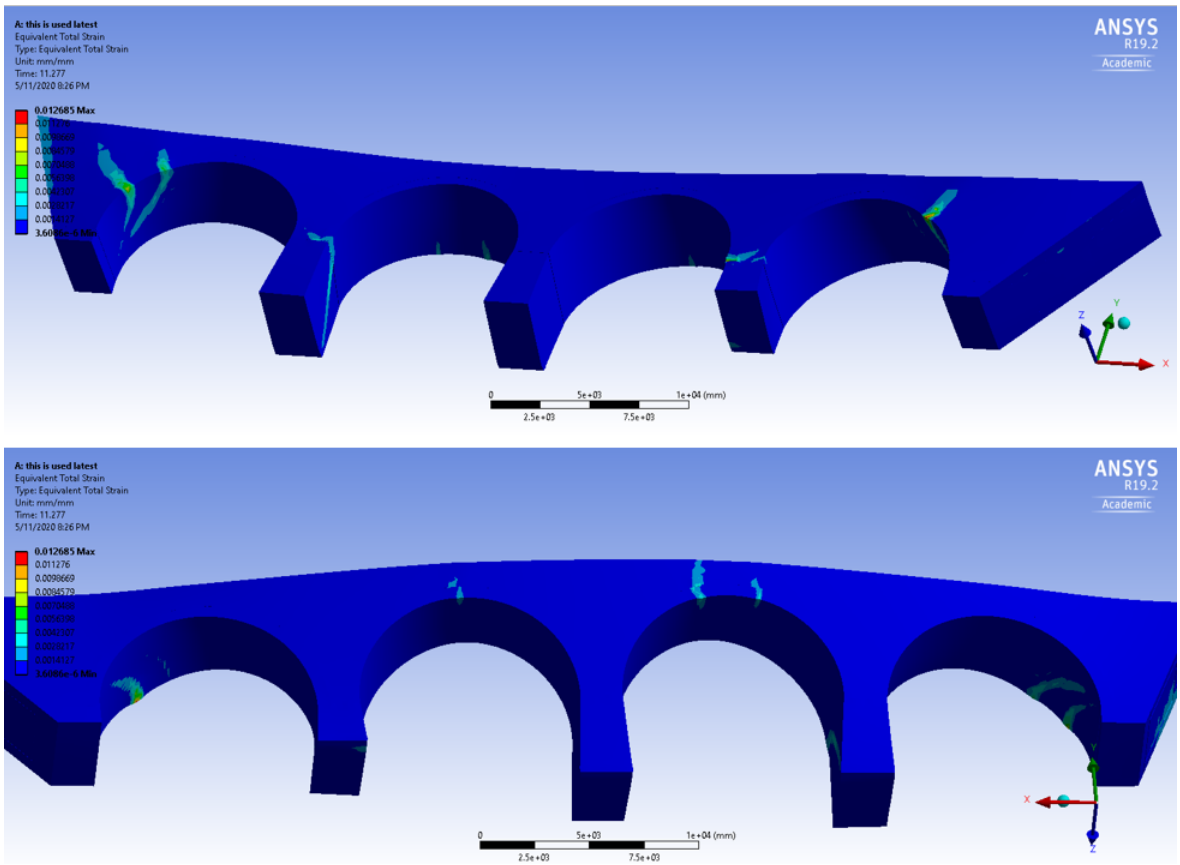

Figure 6.8. Bridge response to MPP at the NC limit state – equivalent total strains.

In terms of the behavior in the simulations, it is observed that the failure mode does not change significantly. Yet, the sensitivity of the crack pattern to the elasticity moduli can still be appreciated.

6.2.3. Demand Distribution

The uncertainty in the earthquake input to the structure is a well-known phenomenon by the earthquake engineering community. The main factors affecting the

structural response are the earthquake duration, the frequency content, and the magnitude [24]. In order to represent the uncertainty in the earthquake demand, a number of strong ground-motion records compatible with the design spectrum were selected from the PEER NGA-West2 database and scaled according to the procedure defined in the Turkish Building Seismic Code. For the scaling parameters, the soil type of the location was determined as ZC, and the intensity of seismic ground motion was chosen as DD-2, representing a 10% probability of exceedance in 50 years (or 475 years return period). The distance to the fault was measured as 80 km, and S_s and S_1 values were obtained. Finally, a set of 14 earthquake records compliant with the design response spectrum was selected and used in the nonlinear time-history analyses. The selected records and the NDA results were presented in Chapter 4.6; therefore, they will not be repeated here.

A lognormal distribution is fit to the maximum CM displacements (Table 4.3) obtained from the nonlinear response time-histories, such that $S = LN(2.07, 0.39)$. The corresponding histogram and the distribution are shown in Figure 6.9 below. Chi-square goodness-of-fit test was used to confirm that the data in the vector of CM displacements, $\{D\}$, come from a lognormal distribution with a lognormal mean, μ_{lnx}=2.07 and standard deviation, σ_{lnx}=0.39, estimated from $\{D\}$.

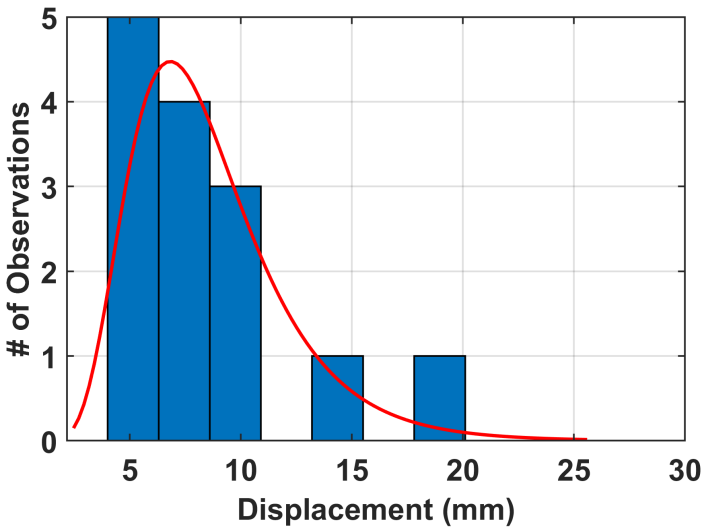

Figure 6.9. Histogram of the CM max displacements of NDA and the lognormal distribution fit.

The CM displacement data vector $\{D\}$ has the first and second moments (8.60, 4.08), and they are used in calculating the lognormal mean and standard deviation.

$$\mu_{lnx} = ln\left(\frac{\mu_x}{\sqrt{1+\delta_x^2}}\right) = ln\left(\frac{8.60}{\sqrt{1+0.474^2}}\right) = 2.05 \tag{6.1}$$

$$\sigma_{lnx} = \sqrt{ln(1+\delta_x^2)} = \sqrt{ln(1+0.474^2)} = 0.45 \tag{6.2}$$

Transformed (Equivalent Normal) distribution of demand, S, should be determined so that it can be used in FORM analysis.

$$U_S = \frac{ln(S) - 2.05}{0.45} \rightarrow ln(S) = 0.45U_S + 2.05 \tag{6.3}$$

$$S = e^{\mu_{lnx} + u\sigma_{lnx}} = e^{2.05+0.45U_S} \tag{6.4}$$

6.2.4. Reliability Analysis Background

Reliability can be defined as the assurance of performance that is defined probabilistically. The traditional methods of engineering achieved reliability via using the factors of safety and conservative assumptions, such as minimum resistance and maximum load. Those methods were insufficient in terms of addressing the uncertainty. In contrast, state-of-the-art methods model the load and resistance (or demand and supply) as random variables to explicitly consider the effect of uncertainties [155]. If we call the resistance, R, and the load, S, then the objective of reliability analysis is to ensure that the safety margin M is greater than zero, i.e., $R - S > 0$.

In order to model the uncertainties in a problem, a vector of random variables $X = [X_1, X_2, ..., X_n]^T$ with joint probability density function (PDF), $f_X(x)$ can be used. These uncertainties may be the loads, yield strength, geometry, material property, etc., in physical (such as structural analysis) problem. Each realization of the random variable X is denoted as $x = [x_1, x_2, ..., x_n]^T$, which is a point in n-dimensional space.

6.2.4.1. Limit State Functions. Identifying failure modes is the first step in reliability analysis. The failure modes should be represented in a mathematical form and involve the random variables that define the load and resistance. Such a mathematical representation is called a "limit state function". The limit state function is defined as a function of the random variables, $G(x) = G(x_1, x_2, ..., x_n) = 0$, and it divides the space of the random variables into two regions: the safe region and the failure region [163].

$$G(x) = \begin{cases} > 0, & x \in \text{“safe region”} \\ \leqslant 0, & x \in \text{“failure region”} \end{cases} \tag{6.5}$$

In its most basic form, the limit state function, G, can be defined as $G(R, S)$ and the corresponding failure probability is represented as $P_F = P\left[G(R, S) \leq 0\right]$, in general [164]. The mathematical forms of the failure and safety probability are given in the equations below.

$$P_F = P\left(G(x) \leq 0\right) = \int_{G(x)\leq 0} f_x(x)dx \tag{6.6}$$

$$P_S = P\left(G(x) > 0\right) = \int_{G(x)>0} f_x(x)dx \tag{6.7}$$

From Equations 6.6 and 6.7, it is realized that the limit state represents an n-dimensional failure surface and the probability of safety is calculated via the volume integral of $f_x(x)$ over the safe region $G(x) > 0$. For a two-dimensional case, an example is provided in Figure 6.10.

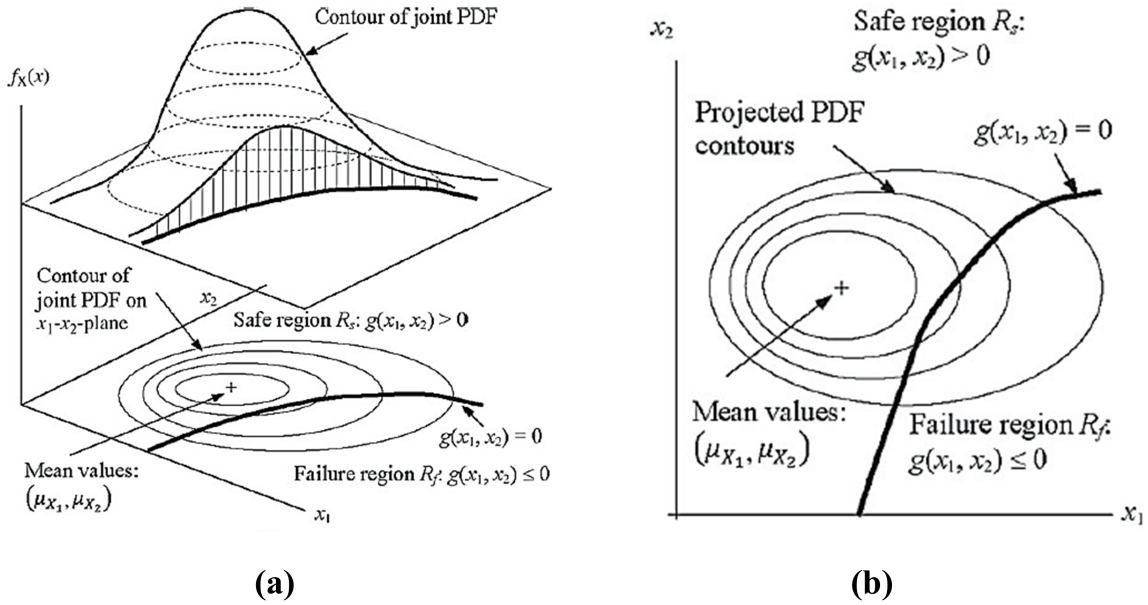

Figure 6.10. Probability integration using a two-dimensional example: (a) isometric view and (b) projected view on the $x_1 - x_2$ plane (Retrieved from [163]).

6.2.4.2. The first expression of the Probability of Failure, P_F. The probability of failure of the event which represents loads ranging between $x+dx$ and the resistance being smaller than x is a joint probability of the two events: I) the event at which the load $S \in [x, x+dx]$, and II) the event where the resistance $R < x$. Thus, the probability of failure, $P(S-R>0)$, is represented by $P(I \cap II)$ [165]. Figure 6.11 below is presented to help visualizing these two events.

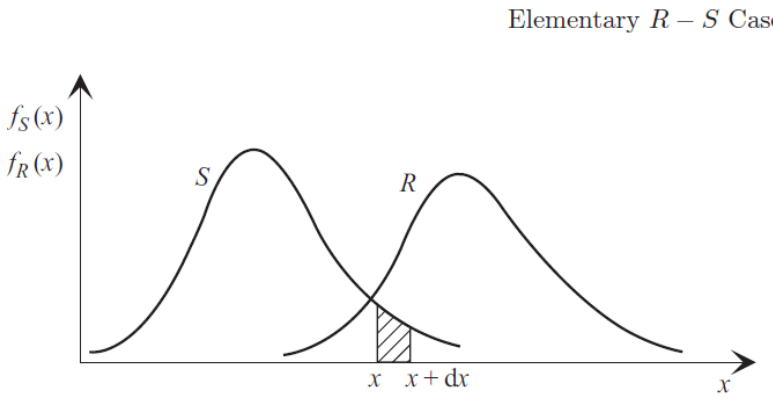

Figure 6.11. Densities of R and S: the first form of P_F (Retrieved from [165]).

Then, the probability of these individual events is presented in the equations below.

$$P(I) = f_S(x)dx \tag{6.8}$$

$$P(II) = \int_{-\infty}^{\infty} f_R(x)dx = F_R(x) \tag{6.9}$$

where $P(I)$ is the probability density function (PDF) of the load variable S and $P(II)$ is the cumulative distribution function (CDF) of the resistance variable R.

Assuming the events are independent, the following Equation 6.10 is obtained. Note that if the events are not independent, then the calculation of their joint probability requires introducing the covariance matrix.

$$dP_F = P(I \cap II) = P(I) \cdot P(II) = f_{R,S}(R,S) = f_S(x)dxF_R(x) \tag{6.10}$$

If all the possible loads are included, Equation 6.10 now becomes Equation 6.11 and gives the probability of failure.

$$P_F = \int_{-\infty}^{\infty} f_S(x)F_R(x)dx \tag{6.11}$$

The use of Equation 6.11 is limited because its analytical solution is very difficult. The marginal distributions of R and S, or the joint distribution function $f_{(R,S)}(R,S)$, are often not available. Even if they are, the integration is most often multi-dimensional due to the multiple random variables included in the process. The limit state function $G(x)$ is frequently nonlinear and even without an analytical form when numerical methods such as the FE method is employed [163]. These aspects render numerical integration impractical. For this reason, other methods employing simulation techniques such as Monte Carlo Simulation and the Response Surface Method, and methods employing the "reliability index" like the First-Order Reliability Method (FORM) and the Second-Order Reliability Method (SORM) have been developed to estimate the probability of failure. In this study, the MCS method and FORM are employed to

calculate the failure probabilities.

6.2.4.3. The Concept of Reliability Index. In general, the available information regarding the random variables is only sufficient to evaluate the first and second moments, i.e., the mean and the standard deviation (μ, σ). In the absence of the probability distributions of the random variables, the reliability can be measured by using the second-moment approach. This approach utilizes the reliability index, β, which is a function of the first and second moments.

In the case where the load and the resistance have normal distributions, the safety margin (M) has a normal distribution. Therefore, the standard normal probability (Φ) can be used to calculate the P_F.

Recall that, $M = R - S$ and

$$P_F = P(R - S \leq 0) = P(M \leq 0) \tag{6.12}$$

Then the mean and standard deviation of the safety margin can be obtained using Equation 6.13 and 6.14.

$$\mu_M = \mu_R - \mu_S \tag{6.13}$$

$$\sigma_M = \sqrt{\sigma_R^2 + \sigma_S^2} \tag{6.14}$$

The reliability index is determined using Equation 6.15.

$$\beta = \frac{\mu_M}{\sigma_M} \tag{6.15}$$

Using the reliability index (β) and the standard normal probability (Φ), one can obtain the failure probability and the reliability (or probability of safety) by employing

Equations 6.16 and 6.17, respectively.

$$P_F = \Phi(\frac{0 - \mu_M}{\sigma_M}) = \Phi(-\beta) = 1 - \Phi(\beta) \tag{6.16}$$

$$P_S = 1 - P_F = \Phi(\beta) \tag{6.17}$$

As it is evident by the above formulations, the reliability is a function of the relative positions of the probability distributions of R and S, and their respective dispersions. The reliability index described until here is called the "Rjanitzyne and Cornell index" in literature, and it is only correct in the case of Gaussian (Normal) random variables and a linear limit-state function. Even then, different representations of the safety margin may result in a different value of the index. The "Hasofer and Lind index" overcomes the non-invariance of the Rjanitzyne and Cornell index by transforming the variables of the physical space to a new space of independent Gaussian variables with zero mean and unit standard deviation [165]. The conversion is achieved by the iso-probabilistic transformation, such that $\Phi(u) = F_x(x)$. After the transformation, the reliability index has the interpretation of being the minimum distance between the origin and the "most probable point/ or design point", in the standard Gaussian space of variables u_i. More detailed information on the reliability index can be found in various textbooks [155, 163–165].

6.2.4.4. Monte Carlo Simulation. The MCS consists of three basic steps: *i*) generating the random input variables by random sampling, *ii*) evaluating the limit state function $G(x)$, and *iii*) determining the probability of failure via statistical analysis of the outcome of the $G(x)$. From these steps, it is evident that the cumulative distribution functions of the random variables should be known. The MCS does not necessitate the assumption of Gaussian and independent random variables, while it can be computationally very costly for complex structural problems involving finite element analysis.

6.2.4.5. First-Order Reliability Method (FORM). The FORM is an iterative procedure and provides an estimate for the integral form of the failure probability given in Equation 6.11. It is achieved basically in two steps: I) the joint PDF of the random variables is simplified and transformed into a standard normal distribution function of independent random variables of the same dimensions, II) the limit-state function $G(x) = 0$ is approximated by using the first terms of its Taylor Series expansion. This method can still be used even if the limit-state function is nonlinear. In such a case, the reliability index β represents the shortest distance from the origin in the standardized normal space to the hyperplane, which is tangent to the failure surface. In the case of non-normal distributions, "equivalent normal distributions" should be obtained using Rosenblatt or Nataf transformations. A more comprehensive explanation of this method and the algorithm for the numerical approximation can be found in various sources [155, 163–165]. Figure 6.12 presents a graphical explanation of the transformation, whereas Figure 6.13 illustrates the first-order approximation of the probability of failure.

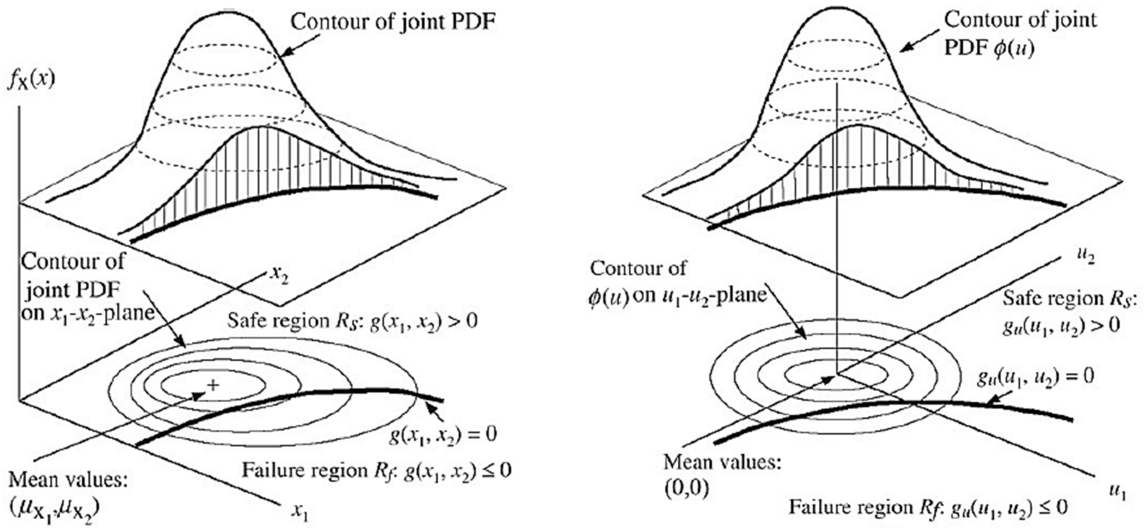

Figure 6.12. Transformation of random variables from X to U space, using a two-dimensional example: (a) PDF and projected contours in X-space, and (b) standard normal distribution in U-space (Retrieved from [163]).

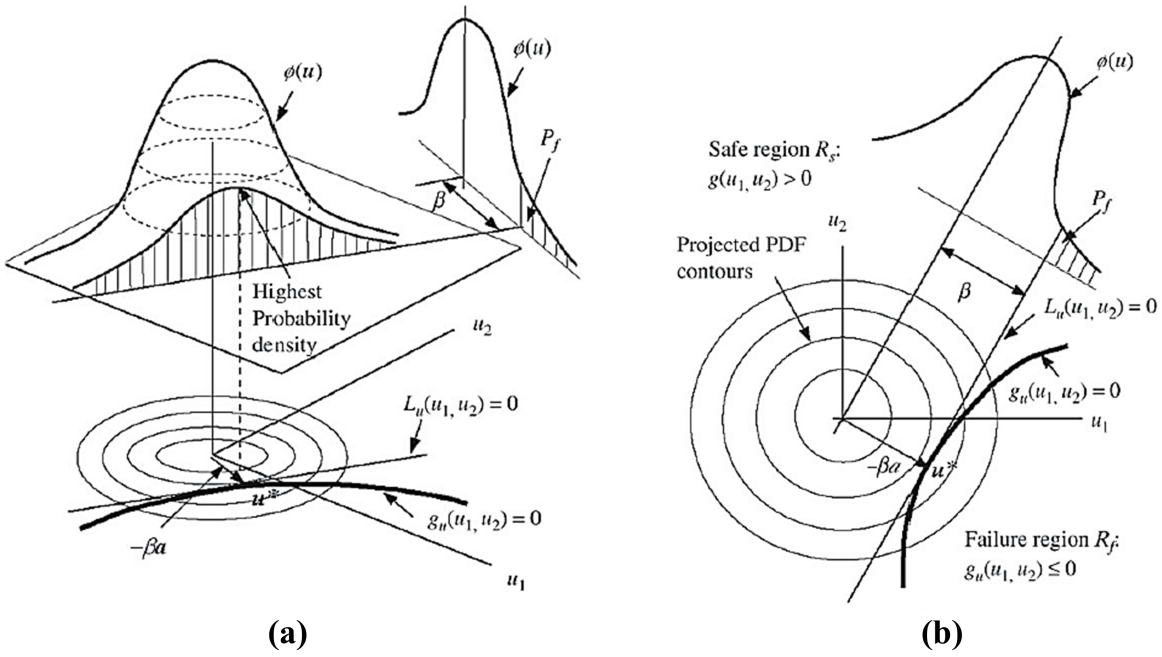

Figure 6.13. Approximation of failure probability integration using a two-dimensional example: (a) PDF and projected contours in U-space and (b) projected view on the $u_1 - u_2$ plane (Retrieved from [163]).

6.2.5. Probability of Failure Calculation

The probability density graphs of the demand and capacity distributions obtained so far are presented below in Figure 6.14.

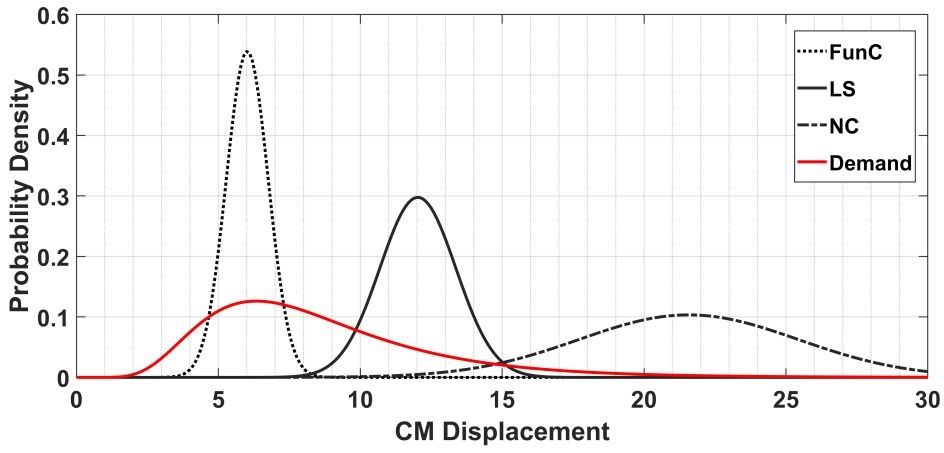

Figure 6.14. Probability Density Distributions of the demand and capacity.

For each limit state, the normal distributions are standardized as follows:

$$R1 = FunC = N(6.02, 0.74) \rightarrow U_{R1} = \frac{R_1 - 6.02}{0.74} \rightarrow R_1 = 0.74U_{R1} + 6.02$$

$$R2 = LS = N(12.03, 1.34) \rightarrow U_{R2} = \frac{R_2 - 12.03}{1.34} \rightarrow R_2 = 1.34U_{R2} + 12.03$$

$$R3 = NC = N(21.57, 3.86) \rightarrow U_{R3} = \frac{R_3 - 21.57}{3.86} \rightarrow R_3 = 3.86U_{R3} + 21.57$$

In the end, the limit state functions become a nonlinear function of normal and non-normal, uncorrelated variables.

$$G_{FunC} = 0.74U_{R1} + 6.02 - exp(2.05 + 0.45U_S) = 0 \tag{6.18}$$

$$G_{LS} = 1.34U_{R2} + 12.03 - exp(2.05 + 0.45U_S) = 0 \tag{6.19}$$

$$G_{NC} = 3.86U_{R3} + 21.57 - exp(2.05 + 0.45U_S) = 0 \tag{6.20}$$

In order to calculate the probability of failure, numerical integration is necessary, and FORM is going to be used. Another option is using a Monte Carlo Simulation. Both methods are going to be used and compared in this part of the study.

It should be noted that when calculating the P_F, we assume that R and S are independent random variables. This independence assumption is not correct in the case of earthquake load and system resistance. It is known that the masonry properties such as the elasticity modulus, the compressive and tensile strength (E, f_c and f_t) are correlated, but we do a simplification here.

6.2.5.1. Monte Carlo Simulation. The MCS was carried out using the variables and limit state functions presented previously. A total of one million simulations were carried out. The number of simulations was determined by monitoring the change in

the calculated probability of failure for each limit state, as presented in Figure 6.15. The probability of failure for each limit state, i.e., probability of the demand displacement exceeding the capacity displacement for each limit state ($S > R$), is found by dividing the number of cases in which $S > R$ to the total number of simulations. The value of the probability of failure for each limit state is presented in Table 6.1.

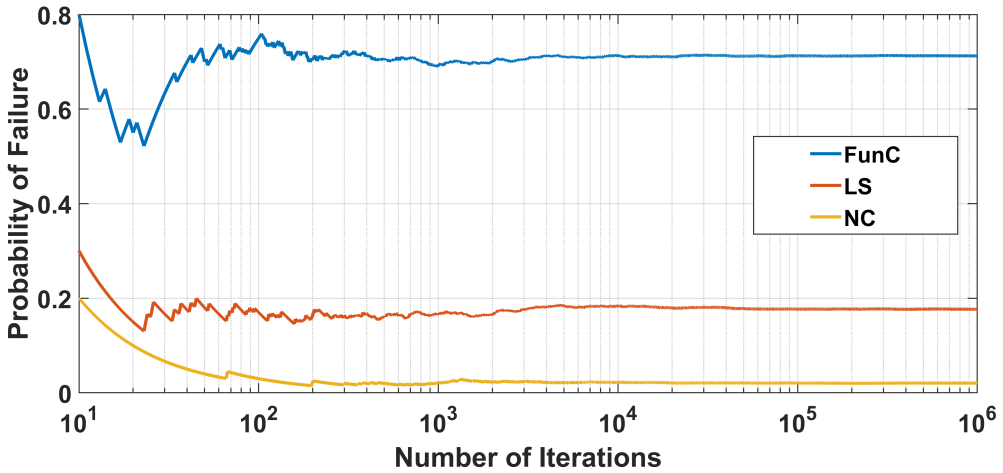

Figure 6.15. Probability of failure for each limit state vs. number of iterations.

6.2.5.2. First-Order Reliability Method (FORM). FERUM v.4.1 software [166] was used to calculate the reliability index and the probability of failure using FORM. FERUM software uses "Nataf transformation" to calculate transformed variables and offers "direct differentiation" and "forward finite differences" for the numerical calculation of limit state derivatives. The direct differentiation option was used in this study. The P_F and β index are calculated and presented below in Table 6.1. Notice that they match with and are verified by the MCS results.

Table 6.1. Probability of Failure and Reliability Index values.

	MCS	**FORM**	
Limit State	**Probability of Failure, P_F**	**Probability of Failure, P_F**	**Reliability Index, β**
FunC	71.3 %	70.8 %	-0.547
LS	17.7 %	17.3 %	0.941
NC	2.07 %	1.87 %	2.081

Illustration of the basic R-S problem for the calculation of the probability of failure is indicated in Figure 6.16.

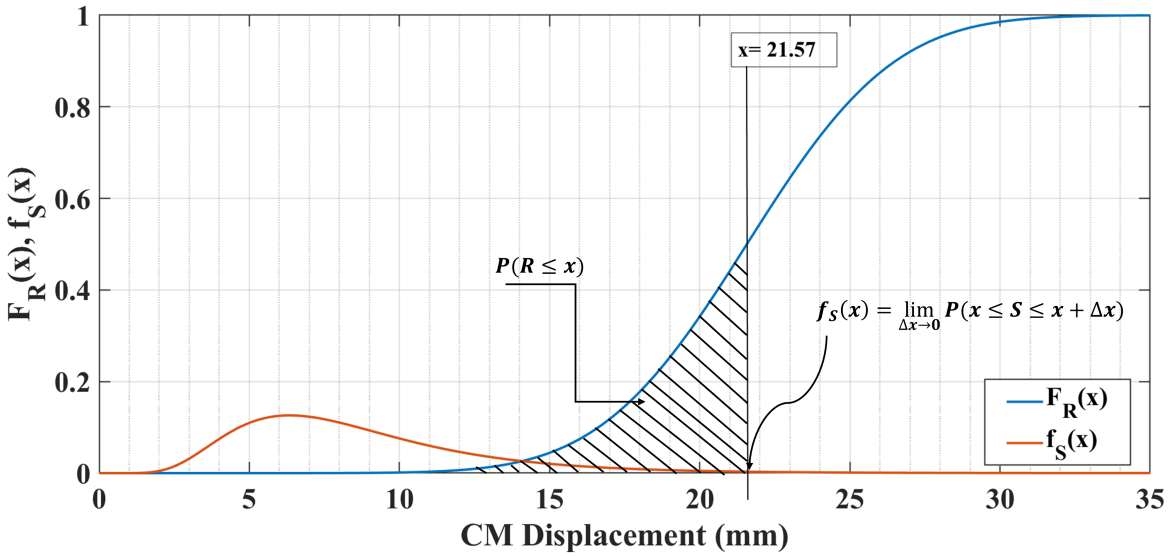

Figure 6.16. R and S distributions for the Near Collapse limit state and demand, $F_R(\cdot)f_S(\cdot)$ representation

6.3. Discussion

Selecting the safety level of bridges depends on many factors such as the type and age of the bridge, consequences of failure, and associated cost of the safety measures. While the safety levels significantly vary throughout the world, the safety indexes are expected to be lower in the assessment of existing structures compared to the design of new ones. Unsurprisingly, there are no guidelines to choose a suitable target reliability index for the seismic performance assessment of masonry arch bridges. To the author's knowledge, the available literature example belongs to the Sustainable Bridges Project [131] and is limited to a few actions other than seismic.

The level of safety can be defined in member and system levels. Most structural codes are based on the failure of structural members, and there is no consensus on

how the system failure should be defined. Intuitively, the safety of a structural system should be greater and equal to that of a structural member. If the failure of the member leads to a system failure, then the probability of safety (or the safety index) for both the member and the system are the same. In contrast, the safety index is larger for a system in case of a higher redundancy.

Table 6.2 shows various target reliability index values in different countries and international standards, for member level at ultimate limit state, moderate consequences of failure, and reference period of one year. As can be seen, the target reliability index ranges between 2.5 and 4.7. The low values of the beta index are associated with relatively low consequences of failure, whereas the high values correspond to very high consequences. In that regard, the failure of railroad bridges results in high consequences, thus should be associated with high beta values. Considering this and comparing the table values with the beta indexes obtained in the previous section, the results indicate that the probability of exceedance of each limit state is very high. Please note that it may not be a theoretically sensible comparison because of the underlying assumptions, especially in terms of the seismic hazard definition and bridge typology. Although these beta values do not represent the same thing and we have not defined a target safety index in this study, the table values are provided for the reader to have an opinion about the order of magnitude of beta values for such structures.

Table 6.2. Proposed target reliability index values in different countries and international bodies (at member level for ultimate limit state, moderate consequences of failure and reference period of one year, adapted from [130].

	Canada	**USA**	**Eurocode**	**Denmark**	**ISO**
Design	3.75	3.75	4.7	4.2	4.7
Assessment	3.25	2.50	-	4.2	4.7

The main criticism of the approach followed during the reliability assessment is that the capacity distributions are obtained from the nonlinear static analyses, whereas the demand distribution is obtained from the nonlinear dynamic analyses, and these two types of analysis methods are combined to find the probability of failure. Also, the

relationship between the parameters were 700 and 0.10, for the E/f_c and f_c/f_t ratios, respectively. In this case, how to justify that the change in the capacity is due to not only elasticity modulus but also the compressive and tensile strength as well?

Recall that in order to demonstrate the effect of the change in the elasticity modulus, three pushover analyses were done. In each of these analyses, the compressive and tensile strength of the masonry were fixed, i.e. f_c=6.2 MPa, and f_t=0.8 MPa, and the elasticity modulus was set E=6200 MPa, E=3100 MPa, and E=12400 MPa in each case. As can be seen in Figure 4.11, the pushover curves are significantly affected by the change in the elasticity modulus of the masonry. The approach followed in this study was an inverse methodology, as mentioned previously. In other words, we obtained the dynamic properties of the structure, and calibrated the FE model through model updating, considering the global behavior of the bridge. The main updating parameter was the modulus of elasticity of the masonry. The compressive and tensile strength of the masonry were predicted using this parameter and its relationship with the material strength. Therefore, the approach where the compressive and tensile strength changes with the value of the elasticity modulus is more logical and conforms to the physical reality better.

In terms of combining different analysis methods, the following justifications are made. At the beginning of the research, it was presumed that the uncertainty in the earthquake demand is associated with the elasticity modulus of masonry, and the uncertainty in the seismic capacity of the bridge is related to the variations in the tensile and compressive strength of masonry. In fact, all these three parameters are correlated with each other, as can be observed in various published literature. For that reason, the most accurate approach would be considering all the material properties as random variables and then conducting several nonlinear time-history analyses using the combination of each strong-ground motion record with different realizations of material properties (considering enough number of simulations to cover up the whole statistical distribution). Unfortunately, this approach is not feasible for large FE models, as it would take several months to conduct those analyses. Surrogate models or simplified

models are necessary to follow the above-mentioned approach.

We step back from this approach by not showing the change in the demand for all elasticity modulus values. However, to illustrate the phenomenon, a series of NDA was performed for one of the selected strong-ground motion records. RSN-763 Loma Prieta record was chosen, and 14 different values of elasticity modulus were sampled using Latin Hypercube Sampling. All the other parameters except the moduli of elasticity of masonry and arch were fixed to their values given in Table 4.1, as in the deterministic analysis. The ratio of the elasticity modulus of the masonry to that of the arch, E_{mas}/E_{arch} was set constant as 0.925 in all of the analyses. The ratios E/f_c=1000 and f_c/f_t= 0.129 ratios were kept constant in the analyses, the same as the deterministic analyses.

The results presented as acceleration versus absolute displacements in Figure 6.17 yielded interesting observations. There were two groups and an outlier. Two groups were formed for two cases: *i*) when the elasticity modulus value was higher than or close to its deterministic value, i.e., 6.2 GPa, and *ii*) the modulus of elasticity values were in the range of 5-5.9 GPa. The outlier was observed in the case where E=4.5 GPa, as the displacement was bigger than 12 mm. These differences stem from both the decrease in the natural frequencies of the system and the low value of the tensile strength. If the elasticity modulus value is low, then the higher mode effects are more prominent in the response, changing both the behavior and the displacements. However, high values of the elasticity modulus of masonry do not cause a significant change in the behavior.

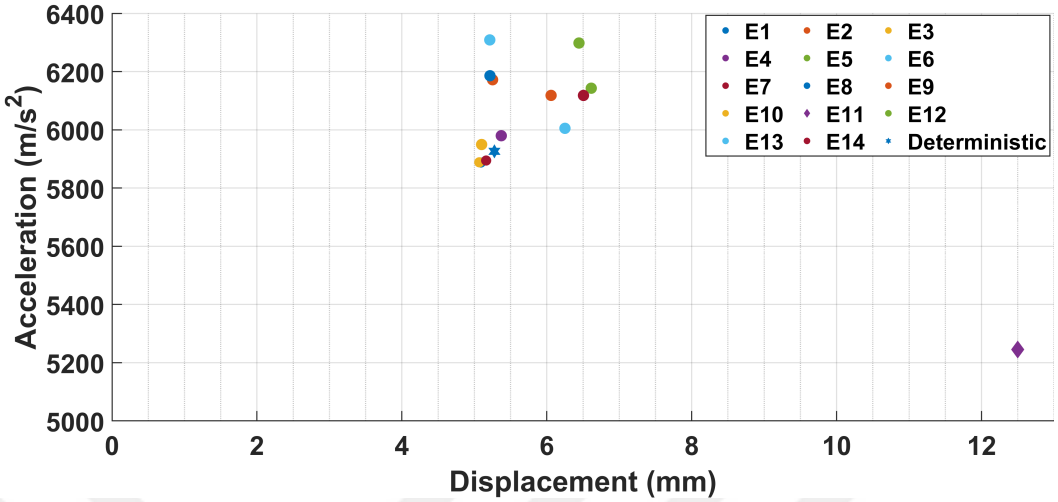

Figure 6.17. NDA results for RSN 763 Loma-Prieta earthquake record.

Different displacement time-history records of the Bridge 41, obtained for three different values of elasticity modulus is represented in Figure 6.18. As can be observed, the displacements are amplified, and the period of the displacement cycles increases when the elasticity modulus is 4456 MPa. On the other hand, the difference is subtle for values of the elasticity modulus larger than 8000 MPa. In Figure 6.19, the dominant first mode behavior, and the effects of higher modes are illustrated.

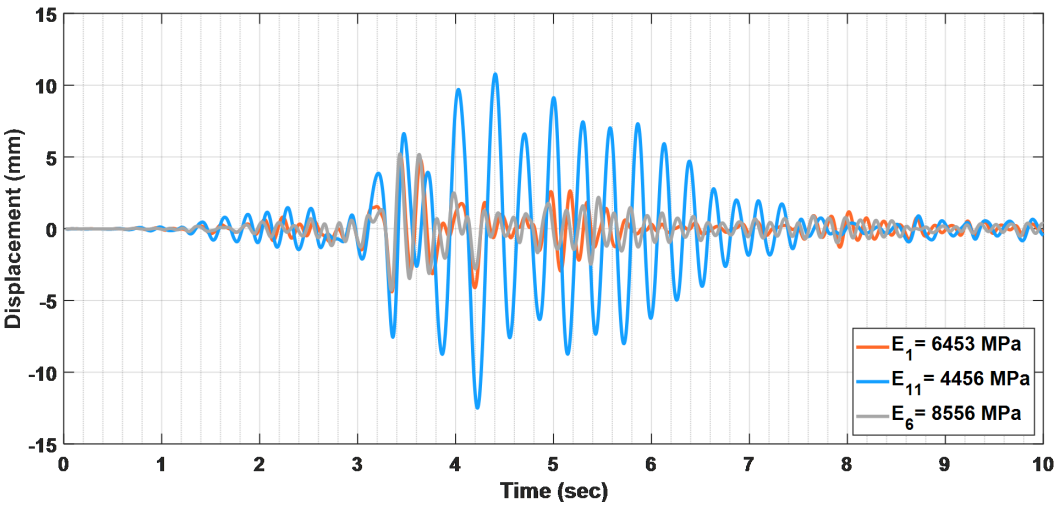

Figure 6.18. Displacement time-histories obtained for different elasticity modulus values.

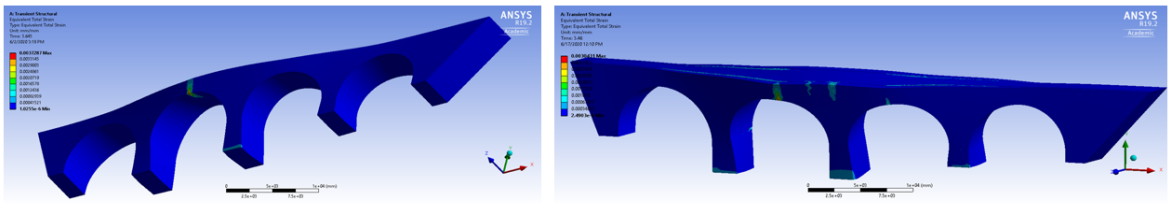

Figure 6.19. (a) The first mode dominant behavior and (b) the higher mode effects.

Finally, another important criticism should be the approach followed in determining the uncertainty in the elasticity modulus. The reason we used all the different laboratory tests, and not a single type, such as the masonry wallette tests, to obtain the uncertainty in the elasticity modulus is because it represents the common practice better. Generally, a mixture of tests is conducted before the assessment of masonry arch bridges, as observed in the literature examples.

7. CONCLUSIONS

This research started by outlining the importance of masonry arch bridges for road and rail networks all around the world and the need for further research and an overarching reliability-based methodology for the seismic performance assessment of masonry arch bridges. Following this, a comprehensive seismic assessment methodology of masonry arch bridges was presented. Considering that there are no performance criteria available for seismic assessment of masonry arch bridges, the principles and important aspects to be taken into account when defining performance criteria for such structures were outlined. The ad hoc rules described in this study should be seen as the first humble step towards defining common performance criteria for masonry arch bridges. Probably, the criteria that will find their place in the codes will require substantial work, and they will be different for bridges with different materials and dominant behavior. Hopefully, this study will be of assistance in the process.

The initial conditions of the bridge investigated offered very little information and many unknowns, as the assessment of historic masonry structures includes significant uncertainties. Therefore, initial tests to characterize the bridge geometry and material properties were conducted. Rigorous dynamic identification using ambient vibrations was carried out to find the global dynamic characteristics of the structure. Subsequent finite element model updating helped to reduce the uncertainties associated with the masonry arch bridge under investigation. In addition, reasonable assumptions were made for the unknown factors to obtain a reliable FE model of the structure for seismic assessment.

As the information sought lies in the nonlinear behavior range of the bridge, a nonlinear FE macro-model was generated in ANSYS v19.2 software. Seismic structural analyses of the bridge were carried out utilizing nonlinear static (pushover), nonlinear dynamic (time-history), and incremental dynamic analyses. First, the assumptions in performing the NSA were examined, and a mass-proportional pushover analysis was

used to determine the seismic performance of the bridge. Then, NDA was implemented for the set of 14 earthquake records in the transverse direction and the combination of all directions as well. The effects of horizontal and vertical components of earthquake records were investigated. Afterward, the results of NDA and NSA were compared to each other, revealing both similarities and differences.

In addition to analytical modeling work, extensive laboratory and field testing were conducted to provide necessary information to the analytical model. For example, ambient vibration testing was conducted, and the data was used to determine the dynamic properties of the Bridge, which later were utilized to update the finite element model of the structure. In order to obtain the data for reliability-based seismic assessment, various laboratory experiments were implemented. The modulus of elasticity of a masonry wall constructed in the laboratory was determined using numerous destructive and non-destructive approaches, as well as the empirical equations provided by the standards. The destructive tests included the masonry components, wallettes, and the cyclic in-plane shear testing of the wall, whereas the flat-jack, ultrasound, ambient vibration, and vertical loading tests were used as the non-destructive tests. Afterward, the in-plane shear-compression experiment of the wall was simulated using the 3D finite element macro-model of the structure. The analytical results were matched with the experimental ones, and this enabled deriving further information. The results were compared to each other, with international standards and with similar research. As a result, the sources of uncertainties in various experimental methods used for determining the elasticity modulus of masonry were investigated and highlighted. Also, the knowledge acquired from experimental testing on the elasticity modulus of masonry is then applied in the seismic reliability assessment of the bridge. The major aspects of the limit states for masonry arch bridges were defined. They were combined with probabilistic nonlinear analyses results to obtain the limit state distributions. Ultimately, the reliability index corresponding to each limit state was calculated and compared to the values given in the international standards. The reliability for each limit state was significantly low compared to the new structures. All this study thus presented a comprehensive methodology, combining both the experimental and analytical work for

the seismic assessment of masonry arch bridges.

As the work described in this study is extensive and detailed, the following example is provided for the reader seeking to use this methodology on their bridges. Suppose that the target reliability index, or the safety level, is provided by the bridge owner, and the user is required to determine the subsequent actions. The first thing to do is acquiring as much information as possible. This is done mostly in terms of searching the historical records, obtaining the geometry description, and performing visual inspection and evaluation on the bridge. Then, a preliminary analytical model should be generated and used to plan in-situ and laboratory testing. In order to obtain the global parameters of the structure, a dynamic identification study is performed. Notice that the analytical model feeds the initial experimental stage, and the results of the experiments help to update the analytical model and provide the uncertainty in modeling parameters. After having a reliable model in hand, the nonlinear dynamic analysis should be carried out. Using the performance criteria provided in this study or obtaining them specifically for the case study (as done in this research), the seismic reliability assessment is performed. If the safety level is below what is required, then strengthening applications can be designed. Accordingly, future maintenance and health monitoring planning can be done.

Detailed discussions and conclusions were given at the end of each chapter previously. In order to present the overall impression of the outcomes of this study, the highlights and novelties are presented below.

- The results of this study highlight the importance of determining the modal parameters of the structure via ambient vibration testing and using them for FE model updating to obtain a reliable model that describes the accurate behavior of masonry arch bridges.

- The results also highlight the similarities and differences between the results of NSA and NDA. Mass-proportional nonlinear static pushover procedure may produce more conservative displacement results and predict the seismic behavior

of the masonry arch bridge in general. However, it still falls short in predicting the behavior and the damage mechanisms triggered by the higher vibration modes of the structure. Nonlinear dynamic analyses provide more reliable results and information, but they suffer from the computational cost when large and detailed FE models are used. Notwithstanding this, they remain the better choice in this study for the safety assessment of the bridge. IDA promises the highest amount of information while the computational drawback is more prominent, and it may even not be feasible to use IDA in some cases.

- In addition to the NDA in the main transverse direction, including the horizontal and vertical components of the earthquakes in the analysis strongly indicates the need for their consideration. They increase the displacements and strains and alter the damage mechanisms as well as the bridge behavior. Even though the effect of the vertical earthquake component was found to be minimal in this instance, due to the particular conditions stressed in the text, it would have significant effects for bridges with different morphologies or whose behavior is dominated by flexure. We recommend a different parameter for future studies, together with displacements, to check the differences with one-dimensional NDA. Energy dissipation should be more useful when the plasticity spreads and the bridge behavior changes.

- The laboratory test results present a considerable scatter as the applied methods are based on different theories and assumptions. A comparison of various test methods based on different theoretical principles highlighted their advantages and drawbacks while also advising for future experimental campaigns.

- The comparison of the results helped to identify the sources of uncertainties related to elasticity modulus estimation and the methods that enable determining the parameters representative of the global behavior of the structure.

- The disparity of the elasticity modulus values from different approaches calls attention to its implications in structural assessment and design.

- The need for further research on the relationship between the compressive strength and elasticity modulus of masonry is underlined.

- The mechanical properties of the masonry type, which is common in Turkey's historic structures, are characterized.

- Seismic performance criteria for masonry arch bridges, which do not exist but are extremely necessary, are proposed for bridges with dominant transverse behavior. Also, the important aspects of defining performance limit states that will assist in future studies are discussed.

- By combining the knowledge obtained from the laboratory testing and analytical modeling, the probabilistic nonlinear pushover analyses on a 3D FE model of the bridge are conducted. The results are then used in obtaining the limit state distributions and, eventually, the reliability indexes. Even though the reliability-based analysis framework has been widely used on various structures, to the author's knowledge, it is the first time this method is used on the seismic assessment of masonry arch bridges. Therefore, this study presents a contribution to the reliability-based seismic assessment framework.

This research used and evaluated the available methods pertinent to system identification, model updating, seismic analysis, laboratory testing, and reliability analysis of structural systems. It combined them all to come up with an overarching assessment methodology. While doing so, several handicaps and possible research areas were highlighted within each chapter. Emanating from these limitations, diverse topics for future research can be recommended.

- The damping ratio is a very intricate subject. The complexity is even more when damping mechanisms in masonry structures are considered. The damping ratio of the masonry arch bridges under ambient vibration, impact, and train passing will be investigated. Moreover, the cyclic test results of the masonry wall panel will be used to examine the energy dissipation and damping properties of the

wall.

- Several parameters are affecting the FE model behavior, such as the tensile strength of masonry, shear transfer coefficients, and the others, as demonstrated in Chapter 4. They should be investigated more in detail if the FE macro-modeling strategy is used. Their effects on the results should be explored for bridges with different geometry and morphology. Also, their values ought to be compared to and confirmed by using laboratory tests.

- Nonlinear static pushover procedure appears to have shortcomings when used for distributed-mass systems. There are no generally accepted procedures to calculate the participation factor, which controls the transformation from MDOF to the SDOF model and vice versa. The approach proposed in this study should be applied and verified, if possible, for different cases.

- The comparison of nonlinear static and dynamic analyses revealed the drawbacks of the static analysis that contradicts all the limited number of findings in the literature. More cases comparing these two methods should be investigated for different bridges, in order to identify under which circumstances both methods differ from each other.

- The effect of horizontal and vertical components of earthquakes should be investigated more in detail, especially for those bridges with significant vulnerability to those scenarios. Also, to better realize the differences with one-dimensional NDA, we recommend a different parameter for future studies. Energy dissipation, particularly the fracture energy in tension, will be more useful when the plasticity spreads and the bridge behavior changes.

- Performance-based earthquake engineering (PBEE) requires estimating the structural performance under seismic loads. Specifically, expressing the probability of exceeding a specified level of structural demand or a specific limit state capacity (e.g., global dynamic instability) is essential [89]. In order to be able to do the performance calculations needed for PBEE, limit-states should be well de-

fined and established. Then, they can be used with the IDA curves to derive the fragility curves, or in the reliability assessment like in this study. The mainframe of the performance criteria studies is depicted in this study and applied to a case study example, but the generalization of those limit states is essential. For this purpose, various masonry arch bridges with different geometry, morphology, material properties, and boundary conditions should be analyzed.

- A part of the masonry arch bridge or its members can be modeled separately by using discontinuum models, such as DEM, to observe how these parts/members behave and what their status is at the defined limit states. Then, a comparison can be made to confirm the assumptions in defining the limit sates.

- The comparison of several test methods on the same specimen provided valuable insight into the elasticity modulus of masonry. While the findings of the elasticity modulus and its disparity in different tests might be restricted to the masonry and the wall's characteristics, they provide knowledge for a better understanding of the elasticity modulus concept. Similar future research on large-scale masonry structures and different materials is recommended.

- The ongoing degradation in the masonry structures is a major issue, which should be managed in a structural health monitoring framework. Time-dependent material properties, changes in the loads acting on structures and the environmental factors should be monitored.

- Simplified models should be generated to conduct reliability analyses efficiently. For this purpose, methodologies are to be developed to generate efficient and accurate simplified models. Also, the use of surrogate models, such as the Response Surface method, for reliability assessment, should be studied further.

- The reliability analysis is essentially an optimization problem. The goal is to find the minimum distance to the hyperplane (or surface), which represents the limit state function. Even though they were not used in this study, the machine learning algorithms, such as Support Vector Machines, have recently been used

in reliability analysis. The author believes that more advanced applications such as Deep Learning will become more common soon.

- Future studies should also include uncertainties in the modeling parameters and verification of them by large scale tests. Like any scientific theory, we generate our computer models to describe our observations and make future predictions. In the absence of nonlinear behavior of the structure, it is not possible to observe the "true behavior," as in most cases. So, should we discard our findings/model predictions? The answer is no because *i*) the computer model behavior matches our expectations and comply with the engineering judgment; *ii*) the distinction between the science and technology in our time comes forth into play; that is, the usefulness is what matters rather than the truth.

REFERENCES

1. Brian, B., *D1.2 European Railway Bridge Demography, WP1, Network Rail*, Sustainable Bridges – Assessment for Future Traffic Demands and Longer Lives, 2004.

2. Helmerich, R., E. Niederleithinger, C. Trela, J. Bień, T. Kamiński and G. Bernardini, "Multi-tool inspection and numerical analysis of an old masonry arch bridge", *Structure and Infrastructure Engineering*, Vol. 8, No. 1, pp. 27–39, 2012.

3. UIC, *Improving Assessment, Optimization of Maintenance and Development of Database for Masonry Arch Bridges*, International Union of Railways, 2005.

4. Kamath, A., *Seismic Risk Assessment of Masonry Arch Bridges in the United States*, M.Sc. Thesis, Clemson University, 2017.

5. Jahangiri, V. and M. Yazdani, "Seismic reliability and limit state risk evaluation of plain concrete arch bridges", *Structure and Infrastructure Engineering*, pp. 1–21, 2020.

6. Caballero, V. R., *Chile Earthquake 2010: Collapsed Bridge*, 2010, `https://www.nationalgeographic.com/news/2010/3/100227`, accessed in July 2020.

7. Oliveira, D. P. L. and J. Lemos, "Geometric issues and ultimate load capacity of masonry arch bridges from the northwest Iberian Peninsula", *Engineering Structures*, Vol. 32, No. 12, pp. 3955–3965, 2010.

8. *Trains of Turkey. TCDD History*, 2018, `http://www.trainsofturkey.com/`, accessed in May 2018.

9. Lourenço, P., "Computations on historic masonry structures", *Progress in Struc-*

tural Engineering and Materials, Vol. 4, No. 3, pp. 301–319, 2002.

10. Costa, C., A. Arede, A. Costa, E. Caetano, A. Cunha and F. Magalhaes, "Updating Numerical Models of Masonry Arch Bridges by Operational Model Analysis", *International Journal of Architectural Heritage*, Vol. 9, No. 7, pp. 760–774, 2015.

11. Aoki, T., D. Sabia, D. Rivella and T. Komiyama, "Structural Characterization of a Stone Arch Bridge by Experimental Tests and Numerical Model Updating", *International Journal of Architectural Heritage*, Vol. 1, No. 3, pp. 227–250, 2007.

12. Andersen, P., R. Brincker, B. Peeters, G. Roeck, L. Hermans and C. Krämer, "Comparison of System Identification Methods using Ambient Bridge Test Data", *17th International Modal Analysis Conference (IMAC)*, pp. 1035–1041, 1999.

13. Magalhães, F. and A. Cunha, "Explaining operational modal analysis with data from an arch bridge", *Mechanical Systems and Signal Processing*, Vol. 25, No. 5, pp. 1431–1450, 2011.

14. Gentile, C. and A. Saisi, "Operational modal testing of historic structures at different levels of excitation", *Construction and Building Materials*, Vol. 48, pp. 1273–1285, 2013.

15. Ramos, L., L. Marques, P. B. Lourenco, G. D. Roeck, A. Campos-Costa and J. Roque, "Monitoring historical masonry structures with operational modal analysis: Two case studies", *Mechanical Systems and Signal Processing*, Vol. 24, No. 5, p. 1291–1305, 2010.

16. Formisano, A., F. Gilda, L. Raffaele and F. Mazzolani, "Numerical calibration of an easy method for seismic behaviour assessment on large scale of masonry building aggregates", *Advances in Engineering Software*, Vol. 24, No. 5, pp. 116–138, 2015.

17. Sesigür, H., G. Erol, S. Soyöz, K. Kaynardağ and S. Gönen, "Repair and Retrofit

of Ketchaoua Mosque", *Proceedings of the 10th International Conference on Structural Analysis of Historical Constructions*, Leuven, Belgium, 2016.

18. Demirlioglu, K., S. Gonen, S. Soyoz and M. Limongelli, "In-Plane Seismic Response Analyses of a Historical Brick Masonry Building Using Equivalent Frame and 3D FEM Modeling Approaches", *International Journal of Architectural Heritage*, Vol. 14, No. 2, pp. 238–256, 2020.

19. Kaya, Y. and E. Safak, "Real-time analysis and interpretation of continuous data from structural health monitoring (SHM) systems", *Bulletin of Earthquake Engineering*, Vol. 13, No. 3, pp. 917–934, 2015.

20. Brincker, R., L. Zhang and P. Andersen, "Modal identification of output-only systems using frequency domain decomposition", *Smart Materials and Structures*, Vol. 10, No. 3, pp. 441–445, 2001.

21. Brincker, R., L. Zhang and P. Andersen, "Damping Estimation by Frequency Domain Decomposition", *Proceedings of the 19th International Modal Analysis Conference (IMAC)*, 2001.

22. Allemang, R. and D. Brown, "A correlation coefficient for modal vector analysis", *Proceedings of the 1st International Modal Analysis Conference (IMAC)*, pp. 110–116, Orlando, Florida, 1982.

23. Peeters, B., *System Identification and Damage Detection in Civil Engineering*, Ph.D. Thesis, Katholieke Universiteit Leuven, 2000.

24. Clough, R. and J. Penzien, *Dynamics of Structures*, McGraw-Hill Book Company, Berkeley, USA, 1993.

25. Safak, E., "Identification of linear structures using discrete-time filters", *Journal of Structural Engineering*, Vol. 117, pp. 3046–3085, 1991.

26. Loeve, M., *Probability Theory. Graduate Texts in Mathematics*, Vol. II, 4th edition, Springer-Verlag, 1978.

27. Moon, T. and W. Stirling, *Mathematical methods and algorithms for signal processing*, Prentice Hall, Upper Saddlle River, NJ, 2000.

28. Safak, E., "Analysis of real-time data from instrumented structures", *Proceedings of the 13th World Conference on Earthquake Engineering*, Vancouver, Canada, 2004.

29. Orbán, Z. and M. Gutermann, "Assessment of masonry arch railway bridges using non-destructive in-situ testing methods", *Engineering Structures*, Vol. 31, No. 10, pp. 2287–2298, 2009.

30. Heyman, J., *The Stone Skeleton : Structural Engineering of Masonry Architecture*, Cambridge University Press, 1997.

31. Friswell, M. and J. Mottershead, *Finite Element Model Updating in Structural Dynamics*, Vol. 38 of Solid Mechanics and Its Applications, Springer Science & Business Media, 2013, 1995.

32. *SAP2000 v19*, Computers and Structures Inc. (CSI), Berkeley, USA, 2017.

33. Bowles, J., *Foundation Analysis and Design*, Vol. 4th edition, McGraw Hill, 1998.

34. *ANSYS Academic Research Mechanical, Release 19.2*, Swanson Analysis System, Houston, TX, USA, 2018.

35. Pelà, L., A. Aprile and A. Benedetti, "Seismic assessment of masonry arch bridges", *Engineering Structures*, Vol. 31, No. 8, pp. 1777–1788, 2009.

36. Leprotti, L., L. Pelà, A. Aprile and A. Benedetti, "Control node identification in nonlinear seismic analysis of masonry arch bridges", *Proceedings of the 8th*

International Masonry Conference, pp. 1113–1122, Dresden, Germany, 2010.

37. Milani, G. and P. Lourenço, "3D non-linear behavior of masonry arch bridges", *Computers & Structures*, Vol. 110-111, pp. 133–150, 2012.

38. Pelà, L., A. Aprile and A. Benedetti, "Comparison of seismic assessment procedures for masonry arch bridges", *Construction and Building Materials*, Vol. 38, pp. 381–394, 2013.

39. Domede, N., A. Sellier and T. Stablon, "Structural analysis of a multi-span railway masonry bridge combining in situ observations, laboratory tests and damage modelling", *Engineering Structures*, Vol. 56, pp. 837–849, 2013.

40. Zampieri, P., M. Zanini and C. Modena, "Simplified seismic assessment of multi-span masonry arch bridges", *Bulletin of Earthquake Engineering*, Vol. 13, No. 9, pp. 2629–2646, 2015.

41. Modena, C., G. Tecchio, C. Pellegrino, F. da Porto, M. Donà, P. Zampieri and M. Zanini, "Reinforced concrete and masonry arch bridges in seismic areas: typical deficiencies and retrofitting strategies", *Structure and Infrastructure Engineering*, Vol. 11, No. 4, pp. 415–442, 2015.

42. Deng, L., W. Wang and Y. Yu, "State-of-the-Art Review on the Causes and Mechanisms of Bridge Collapse", *Journal of Performance of Constructed Facilities*, Vol. 30, No. 2, p. 04015005, 2016.

43. Karaton, M., H. Aksoy, E. Sayın and Y. Calayır, "Nonlinear seismic performance of a 12th century historical masonry bridge under different earthquake levels", *Engineering Failure Analysis*, Vol. 79, pp. 408–421, 2017.

44. Aydin, A. and S. Özkaya, "The finite element analysis of collapse loads of single-spanned historic masonry arch bridges (Ordu, Sarpdere Bridge)", *Engineering Failure Analysis*, Vol. 84, pp. 131–138, 2018.

45. Zampieri, P., M. Zanini, F. Faleschini, L. Hofer and C. Pellegrino, "Failure analysis of masonry arch bridges subject to local pier scour", *Engineering Failure Analysis*, Vol. 79, pp. 371–384, 2017.

46. Pulatsu, B., E. Erdogmus and P. Lourenço, "Comparison of in-plane and out-of-plane failure modes of masonry arch bridges using discontinuum analysis", *Engineering Structures*, Vol. 178, pp. 24–36, 2019.

47. Fanning, P. and T. Boothby, "Three-dimensional modelling and full-scale testing of stone arch bridges", *Computers & Structures*, Vol. 79, pp. 2645–2662, 2001.

48. Brencich, A. and D. Sabia, "Experimental identification of a multi-span masonry bridge: The Tanaro Bridge", *Construction and Building Materials*, Vol. 22, No. 10, pp. 2087–2099, 2008.

49. de Felice, G. and S. de Santis, "Experimental and Numerical Response of Arch Bridge Historic Masonry Under Eccentric Loading", *International Journal of Architectural Heritage*, Vol. 4, No. 2, pp. 115–137, 2010.

50. Pellegrino, C., M. Zanini, P. Zampieri and C. Modena, "Contribution of in situ and laboratory investigations for assessing seismic vulnerability of existing bridges", *Structure and Infrastructure Engineering*, Vol. 11, No. 9, pp. 1147–1162, 2015.

51. Sarhosis, V., G. de Felice and S. de Santis, "A review of experimental investigations and assessment methods for masonry arch bridges", *Structure and Infrastructure Engineering*, Vol. 12, No. 11, pp. 1439–1464, 2016.

52. Conde, B., L. Ramos, D. Oliveira, B. Riveiro and M. Solla, "Structural assessment of masonry arch bridges by combination of non-destructive testing techniques and three-dimensional numerical modelling: Application to Vilanova bridge", *Engineering Structures*, Vol. 148, pp. 621–638, 2017.

53. Roca, P., M. Cervera, G. Gariup and L. Pela, "Structural Analysis of Masonry Historical Constructions. Classical and Advanced Approaches", *Archives of Computational Methods in Engineering*, Vol. 17, No. 3, pp. 299–325, 2010.

54. Proske, D. and P. Gelder, *Safety of historical stone arch bridges*, Springer Berlin Heidelberg, 2009.

55. Reccia, E., G. Milani, A. Cecchi and A. Tralli, "Full 3D homogenization approach to investigate the behavior of masonry arch bridges: The Venice trans-lagoon railway bridge", *Construction and Building Materials*, Vol. 66, pp. 567–586, 2014.

56. Oliveira, D., *Experimental and numerical analysis of blocky masonry*, Ph.D. Thesis, University of Minho, 2003.

57. Milani, G. and M. Valente, "Failure analysis of seven masonry churches severely damaged during the 2012 Emilia-Romagna (Italy) earthquake: Non-linear dynamic analyses vs conventional static approaches", *Engineering Failure Analysis*, Vol. 54, pp. 13–56, 2015.

58. Scheibmeir, E., *Nonlinear Seismic Analysis of a Masonry Arch Bridge*, Master's Thesis, Advanced Masters in Structural Analysis of Monuments and Historical Constructions (SAHC), 2012.

59. Lourenço, P., J. Rots and J. Blaauwendraad, "Continuum Model for Masonry: Parameter Estimation and Validation", *Journal of Structural Engineering*, Vol. 124, No. 6, pp. 642–652, 1998.

60. Boothby, T., Y. Yurianto and E. Erdogmus, "Experimental replication of masonry arch bridge spandrel wall collapse", *TMS Journal*, pp. 37–46, 2005.

61. Chácara, C., N. Mendes and P. Lourenço, "Simulation of Shake Table Tests on Out-Of-Plane Masonry Buildings. Part (IV): Macro and Micro FEM Based Approaches", *International Journal of Architectural Heritage*, Vol. 11, No. 1, pp.

1–15, 2016.

62. *EN 1996-1-1. Eurocode 6 —Design of masonry structures. Part 1-1: General rules for reinforced and unreinforced masonry structures*, European Committee for Standardization, 2005.

63. *ANSYS Academic Research Mechanical, Release 19.2, Help System, Theory Reference Manual*, Swanson Analysis System, Houston, TX, USA, 2018.

64. Wang, J., *Numerical Modelling of Masonry Arch Bridges: Investigation of Spandrel Wall Failure*, Ph.D. Thesis, University of Bath, 2014.

65. Aytulun, E., S. Soyoz and E. Karcioglu, "System Identification and Seismic Performance Assessment of a Stone Arch Bridge", *Journal of Earthquake Engineering*, pp. 1–21, 2019.

66. Rots, J. and J. Blaauwendraad, "Crack Models for Concrete: Discrete or Smeared? Fixed Multi-directional or Rotating?", *HERON*, pp. 5–59, 1989.

67. William, K. and E. Warnke, "Constitutive model for the triaxial behavior of concrete", *Proceedings of the International Association for Bridge and Structural Engineering*, Bergamo, Italy, 1975.

68. Eslami, A., H. Ronagh, S. Mahini and R. Morshed, "Experimental investigation and nonlinear FE analysis of historical masonry buildings – A case study", *Construction and Building Materials*, Vol. 35, pp. 251–260, 2012.

69. Bertolesi, E., G. Milani, F. Lopane and M. Acito, "Augustus Bridge in Narni (Italy): Seismic Vulnerability Assessment of the Still Standing Part, Possible Causes of Collapse, and Importance of the Roman Concrete Infill in the Seismic-Resistant Behavior", *International Journal of Architectural Heritage*, Vol. 11, No. 5, pp. 1–30, 2017.

70. Chapra, S. and R. Canale, *Numerical Methods for Engineers*, McGraw-Hill Education, New York, 2014.

71. Bhatti, A. Q., *Seismic Vulnerability of Historical Arch Type Bridge Structures in Italy*, Master's Thesis, Advanced Masters in Structural Analysis of Monuments and Historical Constructions (SAHC), Barcelona, 2009.

72. Ghosh, S., "Observations from the Bhuj earthquake of January 26, 2001", *PCI Journal*, pp. 34–43, 2001.

73. Kawashima, K., Y. Takahashi, H. Ge, Z. Wu and J. Zhang, "Reconnaissance Report on Damage of Bridges in 2008 Wenchuan, China, Earthquake", *Journal of Earthquake Engineering*, Vol. 13, No. 7, pp. 965–996, 2009.

74. Fajfar, P., "A Nonlinear Analysis Method for Performance Based Seismic Design", *Earthquake Spectra*, Vol. 16, No. 3, pp. 573–592, 2000.

75. FEMA(356), *Prestandard and Commentary for the Seismic Rehabilitation of Buildings*, Federal Emergency Management Agency, 2000.

76. Kim, S. and Y. Kurama, "An alternative pushover analysis procedure to estimate seismic displacement demands", *Engineering Structures*, Vol. 30, No. 12, pp. 3793–3807, 2008.

77. TBDY(2018), *Türkiye Bina Deprem Yönetmeliği*, Afet ve Acil Durum Yönetimi Başkanlığı, 2018.

78. *ASCE/SEI 41-17. Seismic Evaluation and Retrofit of Existing Buildings*, American Society of Civil Engineers, 2017.

79. Fajfar, P., "Analysis in seismic provisions for buildings: past, present and future: The fifth Prof. Nicholas Ambraseys lecture", *Bulletin of Earthquake Engineering*, Vol. 16, No. 7, pp. 2567–2608, 2018.

80. Elmenshawi, A., M. Sorour, A. Mufti, L. Jaeger and N. Shrive, "Damping mechanisms and damping ratios in vibrating unreinforced stone masonry", *Engineering Structures*, Vol. 32, No. 10, pp. 3269–3278, 2010.

81. Lee, H.-H., *Finite Element Simulations with ANSYS Workbench 18*, SDC Publications, 2017.

82. Vamvatsikos, D. and C. Cornell, "Incremental dynamic analysis", *Earthquake Engineering & Structural Dynamics*, Vol. 31, No. 3, pp. 491–514, 2002.

83. Lourenco, P., N. Mendes, L. Ramos and D. Oliviera, "Analysis of Masonry Structures Without Box Behavior", *International Journal of Architectural Heritage*, pp. 369–382, 2011.

84. Endo, Y., L. Pela, P. R. F. da Porto and C. Modena, "Comparison of seismic analysis methods applied to a historical church struck by 2009 L'Aquila earthquake", *Bulletin of Earthquake Engineering*, Vol. 13, No. 2, pp. 3749–3778, 2015.

85. Endo, Y., L. Pela and P. Roca, "Review of Different Pushover Analysis Methods Applied to Masonry Buildings and Comparison with Nonlinear Dynamic Analysis", *Journal of Earthquake Engineering*, Vol. 21, No. 8, pp. 1234–1255, 2017.

86. Sozen, M., *The Velocity of Displacement*, Springer Netherlands, 2003.

87. Marra, A., L. Salvatori, P. Spinelli and G. Bartoli, "Incremental Dynamic and Nonlinear Static Analyses for Seismic Assessment of Medieval Masonry Towers", *Journal of Performance of Constructed Facilities*, Vol. 31, No. 4, p. 04017032, 2017.

88. Jahangiri, V., M. Yazdani and M. Marefat, "Intensity measures for the seismic response assessment of plain concrete arch bridges", *Bulletin of Earthquake Engineering*, Vol. 16, No. 9, pp. 4225–4248, 2018.

89. Vamvatsikos, D. and C. Cornell, "Applied Incremental Dynamic Analysis", *Earthquake Spectra*, Vol. 20, No. 2, pp. 523–553, 2004.

90. Oliveira, D., P. Lourenço and P. Roca, "Cyclic behaviour of stone and brick masonry under uniaxial compressive loading", *Materials and Structures*, Vol. 39, No. 2, pp. 247–257, 2007.

91. Bartoli, G., M. Betti and s. Giordano, "In situ static and dynamic investigations on the "Torre Grossa" masonry tower", *Engineering Structures*, Vol. 52, pp. 718–733, 2013.

92. Rao, V., R. Venkatarama and K. Jagadish, "Strength characteristics of stone masonry", *Materials and Structures*, Vol. 30, No. 4, pp. 233–237, 1997.

93. Corradi, M., A. Borri and A. Vignoli, "Experimental study on the determination of strength of masonry walls", *Construction and Building Materials*, Vol. 17, No. 5, pp. 325–337, 2003.

94. Chiostrini, S., L. Galano and A. Vignoli, "In Situ Shear and Compression Tests in Ancient Stone Masonry Walls of Tuscany, Italy", *Journal of Testing and Evaluation*, Vol. 31, No. 4, pp. 289–303, 2003.

95. Sarangapani, G., R. Venkatarama and K. Jagadish, "Brick-Mortar Bond and Masonry Compressive Strength", *Journal of Materials in Civil Engineering*, Vol. 17, No. 2, pp. 229–237, 2005.

96. Gumaste, K., K. Rao, R. Venkatarama and K. Jagadish, "Strength and elasticity of brick masonry prisms and wallettes under compression", *Materials and Structures*, Vol. 40, No. 2, pp. 241–253, 2007.

97. Vasconcelos, G. and P. Lourenço, "Experimental characterization of stone masonry in shear and compression", *Construction and Building Materials*, Vol. 23, No. 11, pp. 3337–3345, 2009.

98. Magenes, G., A. Penna, A. Galasco and M. Rota, "Experimental characterisation of stone masonry mechanical properties", *Proceedings of the 8th International Masonry Conference*, pp. 247–256, Dresden, Germany, 2010.

99. García, D., J. San-José, L. Garmendia and P. Larrinaga, "Comparison between experimental values and standards on natural stone masonry mechanical properties", *Construction and Building Materials*, Vol. 28, No. 1, pp. 444–449, 2012.

100. Almeida, C., J. Guedes, A. Arêde, C. Costa and A. Costa, "Physical characterization and compression tests of one leaf stone masonry walls", *Construction and Building Materials*, Vol. 30, pp. 188–197, 2012.

101. Demir, C. and A. Ilki, "Characterization of the materials used in the multi-leaf masonry walls of monumental structures in Istanbul, Turkey", *Construction and Building Materials*, Vol. 64, pp. 398–413, 2014.

102. Lumantarna, R., D. Biggs and J. Ingham, "Uniaxial Compressive Strength and Stiffness of Field-Extracted and Laboratory-Constructed Masonry Prisms", *Journal of Materials in Civil Engineering*, Vol. 26, No. 4, pp. 567–575, 2014.

103. Drougkas, A., P. Roca and C. Molins, "Compressive strength and elasticity of pure lime mortar masonry", *Materials and Structures*, Vol. 49, No. 3, pp. 983–999, 2016.

104. Binda, L., A. Saisi and C. Tiraboschi, "Investigation procedures for the diagnosis of historic masonries", *Construction and Building Materials*, Vol. 14, No. 4, pp. 199–233, 2000.

105. McCann, D. and M. Forde, "Review of NDT methods in the assessment of concrete and masonry structures", *NDT & E International*, Vol. 34, No. 2, pp. 71–84, 2001.

106. Miranda, L., J. Rio, G. Miranda and A. Costa, "Sonic Impact Method – A new technique for characterization of stone masonry walls", *Construction and Building*

Materials, Vol. 36, pp. 27–35, 2012.

107. Miranda, L., L. Cantini, G. Miranda and A. Costa, "Assessment of mechanical properties of full-scale masonry panels through sonic methods. Comparison with mechanical destructive tests", *Structural Control and Health Monitoring*, Vol. 23, No. 3, pp. 503–516, 2016.

108. Drougkas, A., P. Roca and C. Molins, "Numerical prediction of the behavior, strength and elasticity of masonry in compression", *Engineering Structures*, Vol. 90, pp. 15–28, 2015.

109. Makoond, N., L. Pelà and C. Molins, "Dynamic elastic properties of brick masonry constituents", *Construction and Building Materials*, Vol. 199, pp. 756–770, 2019.

110. Kržan, M., S. Gostič, S. Cattari and V. Bosiljkov, "Acquiring reference parameters of masonry for the structural performance analysis of historical buildings", *Bulletin of Earthquake Engineering*, Vol. 13, pp. 203–236, 2015.

111. *EN 772-1. Methods of test for masonry units. Determination of compressive strength*, European Committee for Standardization, 2015.

112. *EN 12372. Natural stone test methods - Determination of flexural strength under concentrated load*, European Committee for Standardization, 2006.

113. *EN 1015-11. Methods of test for mortar for masonry- Part 11: Determination of flexural and compressive strength of hardened mortar*, European Committee for Standardization, 1999.

114. *RIL 805. Tragsicherheit bestehender Eisenbahnbrücken*, Deutsche Bahn, 1999.

115. *TMS 402/602. Building Code Requirements and Specification for Masonry Structures*, TMS Publications, 2016.

116. NZSEE(2015), *Assessment and Improvement of the Structural Performance of Buildings in Earthquake*, New Zealand Society for Earthquake Engineering, 2015.

117. *EN 1052-1. Methods of test for masonry - Part 1: Determination of compressive strength*, European Committee for Standardization, 1999.

118. Demir, C., *Seismic Behavior of Historical Stone Masonry Multi-Leaf Walls*, Ph.D. Thesis, Istanbul Technical University, 2012.

119. ASTM(E2126-11), *Standard Test Methods for Cyclic (Reversed) Load Test for Shear Resistance of Vertical Elements of the Lateral Force Resisting Systems for Buildings*, ASTM International, 2018.

120. Binda, L., A. Saisi and L. Zanzi, "Sonic tomography and flat-jack tests as complementary investigation procedures for the stone pillars of the temple of S. Nicolò l'Arena (Italy)", *NDT & E International*, Vol. 34, No. 6, pp. 215–227, 2003.

121. *EN 14579. Natural Stone Test Methods - Determination of Pulse Velocity.*, European Committee for Standardization, 2004.

122. Mashinsky, E., "Differences between static and dynamic elastic moduli of rocks: Physical causes", *Russian Geology and Geophysics*, Vol. 44, No. 9, pp. 953–959, 2003.

123. Eissa, E. and A. Kazi, "Technical Note: Relation Between Static and Dynamic Young's Moduli of Rocks", *International Journal of Rock Mechanicsand Mining & Geomechanics Abstracts*, Vol. 25, No. 6, pp. 479–482, 1988.

124. ASTM(C1197-14), *Standard Test Method for In Situ Measurement of Masonry Deformability Properties Using the Flatjack Method*, ASTM International, 2014.

125. Parisi, F. and N. Augenti, "Uncertainty in Seismic Capacity of Masonry Buildings", *Buildings*, Vol. 2, No. 3, pp. 218–230, 2012.

126. Acikgoz, S., M. DeJong, C. Kechavarzi and K. Soga, "Dynamic response of a damaged masonry rail viaduct: Measurement and interpretation", *Engineering Structures*, Vol. 168, pp. 544–558, 2018.

127. Park, J., P. Towashiraporn, J. Craig and B. Goodno, "Seismic fragility analysis of low-rise unreinforced masonry structures", *Engineering Structures*, Vol. 31, No. 1, pp. 125–137, 2009.

128. Bosiljkov, V., D. D'Ayala and V. Novelli, "Evaluation of uncertainties in determining the seismic vulnerability of historic masonry buildings in Slovenia: use of macro-element and structural element modelling", *Bulletin of Earthquake Engineering*, Vol. 13, No. 1, pp. 311–329, 2015.

129. Moreira, V., J. Fernandes, J. Matos and D. Oliveira, "Reliability-based assessment of existing masonry arch railway bridges", *Construction and Building Materials*, Vol. 115, pp. 544–554, 2016.

130. Saloustros, S., L. Pelà, F. Contrafatto, P. Roca and I. Petromichelakis, "Analytical Derivation of Seismic Fragility Curves for Historical Masonry Structures Based on Stochastic Analysis of Uncertain Material Parameters", *International Journal of Architectural Heritage*, Vol. 13, No. 7, pp. 1142–1164, 2019.

131. Casas, J., D. Wisniewski, J. Cervenka, E. Bruwhiler, G. Holm, M. Olsson, P. Bengtsson and M. Plos, *Safety and Probabilistic Modelling Background document D4.4*, Tech. rep., 2007.

132. Casas, J., "Reliability-based assessment of masonry arch bridges", *Construction and Building Materials*, Vol. 25, No. 4, pp. 1621–1631, 2011.

133. Moreira, V., J. Matos and D. Oliveira, "Probabilistic-based assessment of a masonry arch bridge considering inferential procedures", *Engineering Structures*, Vol. 134, pp. 61–73, 2017.

134. Conde, B., J. Matos, D. Oliveira and B. Riveiro, "Probabilistic-based structural assessment of a historic stone arch bridge", *Structure and Infrastructure Engineering*, pp. 1–13, 2020.

135. Zampieri, P., M. Zanini and F. Faleschini, "Derivation of analytical seismic fragility functions for common masonry bridge types: methodology and application to real cases", *Engineering Failure Analysis*, Vol. 68, pp. 275–291, 2016.

136. Bulleit, W., "Uncertainty in Structural Engineering", *Practice Periodical on Structural Design and Construction*, Vol. 13, No. 1, pp. 24–30, 2008.

137. Atamturktur, S., F. Hemez and J. Laman, "Uncertainty quantification in model verification and validation as applied to large scale historic masonry monuments", *Engineering Structures*, Vol. 43, pp. 221–234, 2012.

138. EN(1998-3), *Eurocode 8: Design of Structures for Earthquake Resistance Part 3: Assessment and Retrofitting of Buildings*, European Committee for Standardization, 2005.

139. Lagomarsino, S. and S. Cattari, "PERPETUATE guidelines for seismic performance-based assessment of cultural heritage masonry structures", *Bulletin of Earthquake Engineering*, Vol. 13, No. 1, pp. 13–47, 2015.

140. FEMA(461), *Interim Testing Protocols for Determining the Seismic Performance Characteristics of Structural and Nonstructural Components*, Federal Emergency Management Agency, 2007.

141. IPCU, *Seismic Risk Management of Historical Structures*, Istanbul Seismic Risk Mitigation and Emergency Preparedness Project (ISMEP), 2017.

142. FEMA(P-58), *Seismic Performance Assessment of Buildings*, Federal Emergency Management Agency, 2012.

143. Lagomarsino, S. and S. Giovinazzi, "Macroseismic and mechanical models for the vulnerability and damage assessment of current buildings", *Bulletin of Earthquake Engineering*, Vol. 4, No. 4, pp. 415–443, 2006.

144. D'Ayala, D. and A. Ansal, "Non-linear pushover assessment of heritage buildings in Istanbul to define seismic risk", *Bulletin of Earthquake Engineering*, Vol. 10, No. 1, pp. 285–306, 2012.

145. Mouyiannou, A., M. Rota, A. Penna and G. Magenes, "Identification of Suitable Limit States from Nonlinear Dynamic Analyses of Masonry Structures", *Journal of Earthquake Engineering*, Vol. 18, No. 2, pp. 231–263, 2014.

146. Wong, K. and Y. Wang, "Energy-based damage assessment on structures during earthquakes", *The Structural Design of Tall Buildings*, Vol. 10, No. 2, pp. 135–154, 2001.

147. Rodriguez, M. and J. Aristizabal, "Evaluation of a seismic damage parameter", *Earthquake Engineering & Structural Dynamics*, Vol. 28, No. 5, pp. 463–477, 1999.

148. Park, Y. and A. Ang, "Mechanistic Seismic Damage Model for Reinforced Concrete", *Journal of Structural Engineering*, Vol. 111, No. 4, pp. 722–739, 1985.

149. DLH(2008), *Kıyı ve Liman Yapıları, Demiryolları, Hava Meydanları İnşaatlarına İlişkin Deprem Teknik Yönetmeliği*, Ulaştırma Bakanlığı, 2008.

150. EN(1998-2), *Eurocode 8: Design of Structures for Earthquake Resistance -Part 2: Bridges*, European Committee for Standardization, 2005.

151. AASHTO, *LRFD Bridge Design Specifications*, American Association of State Highway and Transportation Officials, 2017.

152. NZTA, *Bridge Manual*, New Zealand Transport Agency, 2018.

153. Krawinkler, H., "Challenges and progress in performance-based earthquake engineering", *Proceedings of the International Seminar on Seismic Engineering for Tomorrow- In Honor of Professor Hiroshi Akiyama*, Tokyo, Japan, 1999.

154. Zareian, F. and H. Krawinkler, *Simplified Performance Based Earthquake Engineering*, J. A. Blume Earthquake Engineering Center, Stanford University, 2009.

155. A.Ang and W. Tang, *Probability Concepts in Engineering Planning and Design, Vol. 2: Decision, Risk, and Reliability*, John Wiley & Sons Inc., 1984.

156. Hurtado, J., *Structural reliability, statistical learning perspectives. Lecture Notes in Applied and Computational Mechanics*, 17, Springer, 2013.

157. Sykora, M. and M. Holicky, "Probabilistic Model for Masonry Strength of Existing Structures", *Engineering Mechanics*, Vol. 17, No. 1, pp. 61–70, 2010.

158. Hacıefendioğlu, K., H. Başağa and S. Banerjee, "Probabilistic analysis of historic masonry bridges to random ground motion by Monte Carlo Simulation using Response Surface Method", *Engineering Mechanics*, Vol. 134, pp. 199–209, 2017.

159. Stein, M., "Large sample properties of simulations using latin hypercube sampling", *Technometrics*, Vol. 29, No. 2, pp. 143–151, 1987.

160. Boussabaine, A. and R. Kirkham, *Whole Life-Cycle Costing: Risk and Risk Responses*, Blackwell Publishing, 2004.

161. Shields, M., K. Teferra, A. Hapij and R. Daddazio, "Refined Stratified Sampling for efficient Monte Carlo based uncertainty quantification", *Reliability Engineering and System Safety*, Vol. 142, pp. 310–325, 2015.

162. Olsson, A., G. Sandberg and O. Dahlblom, "On Latin hypercube sampling for structural reliability analysis", *Structural Safety*, Vol. 25, No. 1, pp. 47–68, 2003.

163. Chang, K., *Product Performance Evaluation using CAD/CAE*, Elsevier Inc., 2013.

164. Melchers, R. and A. Beck, *Structural Reliability Analysis and Prediction*, John Wiley & Sons Ltd, 2017.

165. Lemaire, M., A. Chateauneuf and J. Mitteau, *Structural Reliability*, ISTE, London, UK, 2009.

166. Bourinet, J., C. Mattrand and V. Dubourg, "A review of recent features and improvements added to FERUM software.", *Proceedings of the 10th International Conference on Structural Safety and Reliability (ICOSSAR'09)*, Osaka, Japan, 2009.